



**HAL**  
open science

# Design, modeling and evaluation of a thermo-magnetically activated piezoelectric generator

Adrian Abdala Rendon Hernandez

► **To cite this version:**

Adrian Abdala Rendon Hernandez. Design, modeling and evaluation of a thermo-magnetically activated piezoelectric generator. Micro and nanotechnologies/Microelectronics. Université Grenoble Alpes, 2018. English. NNT : 2018GREAT070 . tel-02013549

**HAL Id: tel-02013549**

**<https://theses.hal.science/tel-02013549>**

Submitted on 11 Feb 2019

**HAL** is a multi-disciplinary open access archive for the deposit and dissemination of scientific research documents, whether they are published or not. The documents may come from teaching and research institutions in France or abroad, or from public or private research centers.

L'archive ouverte pluridisciplinaire **HAL**, est destinée au dépôt et à la diffusion de documents scientifiques de niveau recherche, publiés ou non, émanant des établissements d'enseignement et de recherche français ou étrangers, des laboratoires publics ou privés.

## THÈSE

Pour obtenir le grade de

### **DOCTEUR DE LA COMMUNAUTÉ UNIVERSITÉ GRENOBLE ALPES**

Spécialité : **NANO ÉLECTRONIQUE & NANO TECHNOLOGIES**

Arrêté ministériel : 25 mai 2016

Présentée par

**Adrián Abdalá RENDÓN HERNÁNDEZ**

Thèse dirigée par **Skandar BASROUR**

Préparée au sein du **Laboratoire Techniques de l'Informatique et de la Microélectronique pour l'Architecture des systèmes Intégrés (TIMA)** dans l'École Doctorale **Électronique, Électrotechnique, Automatique et Traitement du Signal (EEATS)**

## **Design, modeling and evaluation of a thermo-magnetically activated piezoelectric generator**

Thèse soutenue publiquement le **27 septembre 2018**,  
devant le jury composé de :

**M. Vittorio FERRARI**

Professeur, Università degli Studi di Brescia, Président

**M. Mickaël LALLART**

Professeur, INSA Lyon, Rapporteur

**M. Alain GIANI**

Professeur, Université Montpellier, Rapporteur

**M. Adrien BADEL**

Professeur, Université Savoie Mont Blanc, Examineur

**M. Jérôme DELAMARE**

Professeur, Université Grenoble Alpes, Examineur

**M. Skandar BASROUR**

Professeur, Université Grenoble Alpes, Directeur de thèse



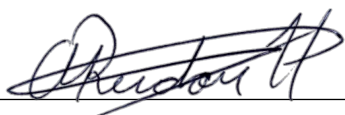


## Declaration of Authorship

I, Adrián Abdalá RENDÓN HERNÁNDEZ, declare that this thesis titled, “Design, modeling, and evaluation of a thermo-magnetically activated piezoelectric generator” and the work presented in it are my own. I confirm that:

- This work was done wholly or mainly while in candidature for a research degree at this University.
- Where any part of this thesis has previously been submitted for a degree or any other qualification at this University or any other institution, this has been clearly stated.
- Where I have consulted the published work of others, this is always clearly attributed.
- Where I have quoted from the work of others, the source is always given. With the exception of such quotations, this thesis is entirely my own work.
- I have acknowledged all main sources of help.
- Where the thesis is based on work done by myself jointly with others, I have made clear exactly what was done by others and what I have contributed myself.

Signed: \_\_\_\_\_



Date: September 27, 2018  
\_\_\_\_\_

*“For those who want some proof that physicists are human, the proof is in the idiocy of all the different units which they use for measuring energy”*

– Richard P. FEYNMAN (1918-1988)

# Abstract

Thermal energy harvesting can be realized by numerous techniques of energy transduction. Direct conversions of thermal to electrical energy are typically the most popular technologies used. When miniaturized generators are required, direct conversion methods present difficulties, including the need of bulky heat sinks or the strong dependence to rapid temperature fluctuations. Therefore, indirect conversion methods, like thermal-to-mechanical-to-electrical energy are presented as an alternative to thermal energy harvesters towards powering autonomous sensors. This disruptive technology opens up a new approach to overcome the limitations of miniaturized thermal energy harvesting systems. Even if having a relatively low efficiency due to losses linked to energy conversion steps, energy harvesters based on thermo-magnetic effect show a large power density upon miniaturization. Nevertheless, little research on thermo-magnetic energy harvesting at miniature scale has been conducted and no competitive electrical output has been reported until now. This work presents the design of a generator able to convert small and slow ambient temperature fluctuations into electricity. It exploits the thermo-magnetic effect of a soft magnetic material, namely, iron nickel alloy (FeNi) and piezoelectricity. Thermo-magnetization of FeNi is driving the conversion of thermal energy, in the form of temporal fluctuations, into mechanical vibrations of a structure. The structure consists in a piezoelectric bimorph (PZT) cantilever beam. The generator has two stable positions; open position and closed one. Curie temperature of FeNi being near to ambient temperature, applications like wearable connected devices may be targeted. By changing the temperature of the soft magnetic alloy, the interaction between counterbalance forces (magnetic and mechanical forces) leads the generator to one of its two commutations. Analytical model is developed in order to predict generator performance. Making use of this model, a rapid design of generator is conducted to fit custom requirements such as: temperature of operations, temperature range of operation, thermal response, piezoelectric energy conversion capabilities, etc. Additionally, main design rules were derived from the design parameters of the generator. Special attention was paid on how scaling down size affects the generator performance by using the analytical model. Finite element models are developed through ANSYS software in order to validate the analytical simplified model. They couple the thermal to magnetic field and then mechanical to electrical energy conversion is solved. This model allows designers to explore other materials and do improvements by using design optimization processes. First generation energy harvesting demonstrators achieve power densities of  $0.88\mu\text{W cm}^{-3}$  during opening commutations around  $41^\circ\text{C}$  and  $0.03\mu\text{W cm}^{-3}$  at closing commutations around

24°C. By reducing the generator's size, opening commutations at 32°C and closing commutations at 29°C, are achieved. By modifying design parameters such as initial distance of separation between the permanent magnet and soft magnetic alloy is identified as a key to boost the energy conversion capability of the generator. Finally, electrical equivalent model of this thermo-magnetically activated piezoelectric generator is developed to design an energy extraction circuit and power management module. This circuit is developed in a unique software PSpice, to implement losses linked to materials (mechanic and dielectric losses). Making use of curve fitting processes, this model is able to find losses values. A variability analysis of the design is conducted by using the analytical model through Matlab in order to explore the feasibility of producing such a generator industrially. Thus, thermo-magnetic energy harvesting can compete for the first time with the state-of-the-art thermoelectrics.

# Résumé

La récupération d'énergie thermique peut être réalisée par de nombreuses techniques de transduction d'énergie. Les techniques directes de conversion d'énergie thermique en énergie électrique sont généralement les technologies les plus utilisées. Lorsque des générateurs miniaturisés sont requis, des méthodes de conversion directe présentent des difficultés, y compris la nécessité des dissipateurs de chaleur volumineux ou la forte dépendance aux fluctuations de température rapides. Par conséquent, les méthodes de conversion indirecte, comme la conversion d'énergie thermique vers la mécanique et puis la mécanique vers l'électrique, sont présentées comme des alternatives aux récupérateurs d'énergie pour alimenter des capteurs autonomes. Cette technologie ouvre un nouvel axe de recherche pour surmonter les contraintes des systèmes de récupération d'énergie thermique à petite échelle. Même si leur rendement est relativement faible en raison des pertes liées aux étapes de conversion d'énergie, les capteurs d'énergie basés sur l'effet thermo-magnétique présentent une densité de puissance élevée lors de leur miniaturisation. Néanmoins, peu de recherches sur la récupération d'énergie thermo-magnétique à petite échelle ont été menées et aucune étude de faisabilité industrielle n'a été signalée jusqu'à présent. Ces travaux présentent la conception d'un générateur capable de convertir de faibles et lentes fluctuations de température ambiante en électricité. Ce générateur exploite l'effet thermo-magnétique d'un matériau magnétique doux, à savoir l'alliage de fer et de nickel (FeNi) ainsi que la piézoélectricité. Lorsqu'un matériau présentant une thermo-aimantation est soumise à un champ magnétique externe et constant ainsi qu'à des variations temporelles de température, une force magnétique dépendante de la température est produite; cette force déclenche le mouvement mécanique d'une structure. La structure consiste en un bimorph piézoélectrique (PZT) en configuration poutre encastrée-libre. Le générateur a deux positions stables : la position ouverte et la position fermée. En modifiant la température de l'alliage magnétique doux, l'interaction entre deux forces du système (forces magnétique et mécanique) amène le générateur à l'une de ses deux positions. La température de Curie du FeNi étant proche de la température ambiante, des applications comme des dispositifs connectés portables peuvent être ciblées. Un modèle analytique est développé afin de prédire les performances du générateur. En utilisant ce modèle, une conception rapide du générateur est réalisée pour répondre aux cahiers des charges tels que : la température d'opération, la plage de températures de fonctionnement, la réponse thermique, les capacités de conversion piézoélectrique, etc. De plus, des règles de conception principales ont été

dérivées à partir des paramètres de conception du générateur. Une attention particulière a été accordée à la manière dont la réduction de la taille du générateur affecte le comportement du générateur. Des modélisations par éléments finis sont développés sous ANSYS afin de valider notre modèle analytique simplifié. Ces modèles numériques prennent en compte le système multi-physique. Ces modèles permettent aux concepteurs d'explorer d'autres matériaux et de faire des améliorations en utilisant des processus d'optimisation de la conception. Des prototypes des récupérateurs d'énergie atteignent des densités de puissance de  $0.88\mu\text{W cm}^{-3}$  pendant des commutations d'ouverture à  $41^\circ\text{C}$  et  $0.03\mu\text{W cm}^{-3}$  pendant des commutations de fermeture à  $24^\circ\text{C}$ . En réduisant la taille du générateur, des commutations d'ouverture à  $32^\circ\text{C}$  et des commutations de fermeture à  $29^\circ\text{C}$ , sont atteints. Des paramètres de conception tels que la distance initiale de séparation entre l'aimant permanent et l'alliage magnétique doux sont identifiés comme une piste d'amélioration pour augmenter la capacité de conversion d'énergie du générateur. Enfin, un modèle équivalent électrique de ce générateur piézoélectrique à déclenchement thermo-magnétique est développé afin de concevoir un circuit d'extraction d'énergie ainsi qu'un module de gestion d'énergie. Ce circuit est développé sous PSpice, permettant de mettre en œuvre des pertes liées aux matériaux (pertes mécaniques et diélectriques). En utilisant des processus d'ajustement de courbe, ce modèle est capable de retrouver les valeurs de pertes. Une analyse de la variabilité de la conception est réalisée en utilisant le modèle analytique sous Matlab afin d'explorer la faisabilité industrielle d'un tel générateur. Pour conclure, la collecte d'énergie thermo-magnétique peut concourir, pour la première fois, avec les thermo-générateurs les plus modernes.

# Acknowledgements

During the time I have spent in Grenoble and other cities (Brescia, Lyon, Barcelona, etc...) where I had the chance to learn valuable experiences in pursuing this degree, I have been very fortunate to meet incredible people through academic and social interactions. I can only hope this section can convey how thankful I am for their continuing support, invaluable friendship and great memories.

First, I would like to thank my research advisor, Professor Skandar BASROUR, for his continuing support, guidance and valuable suggestions. With his aid I was able to overcome most of the difficulties that are common in Microsystems research. I will always admire and remember his passion for research, dedication and willingness to help in every aspect of this research project. I am profoundly indebted to him, Skandar has been more than a mentor, helping me both in my research and personal life. His constructive criticism was essential to overcome the stages of my research. Skandar's support and guidance truly went beyond my graduate student life. I will always remember that day when we had our first skype call and we agreed to conduct this thesis project. I could only hope that one day I can acquire some of his skills as a scientific leader, being able to cover the many areas of research his collaborators perform. I thank you once again for the confidence that you have expressed me, which allowed me to acquire an intellectual autonomy to conduct this research project.

Second, I have only gratitude towards Professor Vittorio FERRARI, for accepting me in his research group as a visiting PhD candidate. I am as well indebted to him, Vittorio's continuing encouragement and valuable discussions based on his expertise on the topic, helped me to better understand the multiphysics involved in the microsystems field. I will always remember that workshop in Paris where I met Vittorio, his scientific talk really inspired me and it motivated me to maintain a scientific rigor on my research work. Thank you Vittorio for honoring me by coming to Grenoble and chairing the thesis committee. I also thank to the members of his research group for sharing with me their knowledge and passion for research. Particularly, I thank to Professor Marco FERRARI for helping me during my research stay at Brescia. I extend my gratitude to my colleague Alessandro NASTRO, for introducing me to this research group in Brescia. Their valuable support and willingness made of my days in Brescia, one of the best research internship that a PhD student would expect to live.

Third, I would also like to extend my gratitude to Professor Mickaël LALLART for the time and energy dedicated in reviewing this thesis. I greatly appreciate his feedback at critical points of my research work. I will always be grateful for his willingness to accept to review this thesis despite some unexpected but necessary modifications in the composition of the thesis committee. Thank you Mickaël for kindly giving to my work the qualifier "la quintessence" of multiphysics at the end of my thesis defense.

Fourth, I am grateful to Professor Alain GIANI for generously offer his time, energy, support and good will throughout the review of this document. I really appreciate all his helpful feedback in improving this manuscript. Thank you Alain for all your constructive criticism, questions and suggestions that highly helped me to better prepare my thesis defense.

I also wish to extend my gratitude to Professor Adrien BADEL and Professor Jérôme DELAMARE for honouring me by examining this work. It was my great pleasure and privilege receiving your comments and questions on very specific points of my research. Thank you Adrien for coming to Grenoble and for your brilliant comments, questions and suggestions on my work. Thank you Jérôme for serving as my committee, your discussion, ideas, and feedback have been absolutely invaluable.

Fifth, I wish to thank Dr. Isabelle SCHUSTER, PhD School program director for KIC InnoEnergy, for accepting me in the program. I wish also thank her staff, Christine DOMINJON and Fabien GAUTHIER for their continuous support and guidance through my experience on the KIC InnoEnergy PhD School program. It was a great honor to me being part of this community, thank you for motivating me to experience different academic environments. This experience has been invaluable and it motivated me to continue on the sustainable energy field.

It was a great honor to me working in TIMA laboratory. I thank Professor Domonique BORRIONE and Professor Salvador MIR for have welcomed me in TIMA during my thesis work. They provided me with all the required means to conduct my research work in highly competitive conditions. I thank to the TIMA laboratory staff for all the support provided to me for administrative procedures. I am grateful to Dr. Libor RUFER for his constructive feedback throughout our team meetings.

I thank my friends, colleagues and classmates at the TIMA laboratory and CIME (Centre Interuniversitaire de Micro Electronique et nanotechnologies) who made life as a graduate student a much enjoyable experience. I have been very fortunate to have met such a great group of people down the road to name them all here, but I must thank especially

Quentin MORTIER, Emilie TRIoux, Gaëtan “GD” DEBONTRIDE, Achraf KACHOUDRI, Vincenzo MASTRONARDI, Mickaël COTTIN BIZONNE, François BERNARD, and Tom ROUIL-LARD. They were always there to provide insight and to help solve much of the design issues, but also made life at the laboratory a fun experience. I would like to thank Alexandre CHAGOYA for his availability in providing me support and help in setting up the numerical calculation tools. I will always remember our discussions and I could only hope that one day I can adopt some of your attentiveness and service in helping colleagues.

I also thank to Thierry ALVARO, Beatriz BETANCOURT-HERNANDEZ and Silvère COLLET. Their friendship and support have gone far beyond of what I would had ever expected. *Merci beaucoup à vous tous!*

It is to my family that I owe the least articulated but most profound thanks. I would like to thank my twin brother, Alberto for being always there and always supporting me. Thank you Alberto for inspiring me in life. I also wish to thank my mom, Emilia. Despite the geographic barriers, her thoughts and prayers had always been here with me. All this time far from her was worth it. There are no words to express my eternal gratitude and admiration to my dad, Pedro. Despite his early departure, He knew and fueled my dream of becoming a scientist. I am still wondering: *“what a smile God would have had when he saw you to arrive there early?”*

This research project would not have been possible without the support by the scholarship No. 315444 granted me by the National Council on Science and Technology (CONACyT) of México.

I would like to extend my gratitude to Schneider Electric, especially to Ignacio DAPIC and Agustin ARROYO, former director and current director, respectively, of the Design and Innovation Center of Schneider Electric in Monterrey, for giving me the opportunity to realize my dream in pursuing my PhD without leaving the company. I would like to thank Fabiola GUTIERREZ, Susan COLSH, and Benjamin PULIDO, for their belief in my work. Thank you for the time and energy you have put into our meetings we had during these years.

Finally, I am very grateful to my wife, Arlene -*te amo*-. Arlene has been my source of inspiration, joy and support. Her smile, patience, confidence and love are just a few things I will eternally be grateful for. Thank you “mi amor” for always believe in my dreams.

Adrián Abdalá RENDÓN HERNÁNDEZ



# Contents

<b>Declaration of Authorship</b>	<b>iii</b>
<b>Abstract</b>	<b>v</b>
<b>Résumé</b>	<b>vii</b>
<b>Acknowledgements</b>	<b>ix</b>
<b>List of Figures</b>	<b>xvii</b>
<b>List of Tables</b>	<b>xxiii</b>
<b>Abbreviations</b>	<b>xxv</b>
<b>Physical Constants</b>	<b>xxvii</b>
<b>Nomenclature</b>	<b>xxix</b>
<b>1 Introduction</b>	<b>1</b>
1.1 Background application	2
1.1.1 Energy harvesting for autonomous systems	2
1.1.1.1 Energy consumption of a wireless sensor node	3
1.1.2 Statement of the problem	5
1.1.2.1 Alternative techniques to thermal energy harvesting for slow and small ambient temperature variations	5
1.1.3 Research goals	5
1.1.4 Motivation	6
1.1.4.1 Human body temperature variations for energy harvesting	7
1.1.5 Research justification	7
1.1.6 Thesis organization	8
<b>2 Review on energy harvesting</b>	<b>11</b>
2.1 Ambient energy sources	12
2.1.1 Mechanical vibrations	13
2.1.2 Radiant energy	14
2.1.2.1 Solar radiation	14
2.1.2.2 Radio waves	15

2.1.3	Thermal energy	16
2.1.3.1	Spatial thermal gradients	16
2.1.3.2	Temperature variations	20
2.2	Energy transduction techniques	21
2.2.1	Electromagnetic transduction	22
2.2.2	Electrostatic generators	23
2.2.3	Piezoelectric transducers	24
2.2.4	Discussion	27
2.3	Thermal energy harvesting review	28
2.3.1	Direct conversion of thermal to electrical energy	29
2.3.1.1	Thermo-electric generators	29
2.3.1.2	Pyro-electric generators	30
2.3.2	Indirect conversion of thermal to electrical energy	32
2.3.2.1	Thermo-acoustic generators	32
2.3.2.2	Electrical generators based on shape memory alloys	34
2.3.2.3	Thermal buckling generators	35
2.3.2.4	Thermo-magnetic generators	36
2.3.3	Discussion	38
2.4	Proposed solution review	43
<b>3</b>	<b>Designing and modeling</b>	<b>45</b>
3.1	Thermal magnetization	46
3.2	Working principle	47
3.3	Analytical modeling	50
3.3.1	Thermal model	51
3.3.2	Thermo-magnetic model	55
3.3.3	Magnetic force model	57
3.3.4	Mechanical model	61
3.3.4.1	Mechanical modeling of the static behavior	61
3.3.4.2	Mechanical modeling of the transient behavior	65
3.3.5	Electro-mechanical model	67
3.3.6	Dynamic behavior of the generator	72
3.4	Design rules of the generator	77
3.5	Discussion	79
<b>4</b>	<b>Finite element method</b>	<b>81</b>
4.1	Three dimensional model of the generator	82
4.1.1	Heat transfer simulation	83
4.1.2	Modeling of the temperature-dependent magnetization	89
4.1.3	Study of the piezoelectric energy conversion	96
4.1.3.1	Implementing piezoelectric effect	96
4.1.3.2	Mechanical contact	99
4.1.3.3	Harmonic simulation	102
4.1.3.4	Transient simulation	106
4.2	Discussion	111

<b>5</b>	<b>Prototyping and testing</b>	<b>113</b>
5.1	First generation prototypes	114
5.1.1	Mounting fixture	114
5.1.2	Transducer system assembly	114
5.1.3	Soft magnetic material	116
5.1.4	Permanent hard magnets	117
5.1.5	Characterization of first generation prototypes	117
5.1.6	Discussion	127
5.2	Second generation energy harvester	128
5.2.1	Portable test prototype 1	128
5.2.2	Optimal load resistor per commutation	133
5.2.3	Output voltage rectification	135
5.3	Second portable test prototype	139
5.4	Equivalent electrical model	144
5.4.1	Electrical representation of the generator	144
5.4.2	Curve fitting and parameters estimation	147
5.4.3	Influence of magnetic breaking on the generator performance	150
5.5	Power management module	151
5.6	Discussion	154
<b>6</b>	<b>Design optimization</b>	<b>157</b>
6.1	Design optimization	158
6.1.1	Second optimization design attempt	166
6.1.2	Discussion	172
6.2	Variability analysis	173
6.3	Discussion	178
<b>7</b>	<b>Conclusions and future work</b>	<b>179</b>
7.1	Conclusions	179
7.1.1	Thesis contributions	181
7.2	Future work	182
<b>A</b>	<b>Piezoelectricity generalities</b>	<b>183</b>
<b>B</b>	<b>Mounting fixture design</b>	<b>187</b>
<b>C</b>	<b>Implementing losses in PSpice</b>	<b>191</b>
	<b>Bibliography</b>	<b>193</b>
	<b>List of Publications</b>	<b>203</b>
	<b>Résumé en français</b>	<b>205</b>
	<b>Vita</b>	<b>227</b>



# List of Figures

1.1	Basic components of a wireless sensor node. . . . .	3
1.2	Human body temperature variations in a normal day . . . . .	7
2.1	Energy sources and their respective transducers for powering autonomous sensors . . . . .	12
2.2	Schematic representation of vibration based energy harvesting. . . . .	13
2.3	Schematic representation of solar light energy harvesting and a solar wireless sensor node. . . . .	15
2.4	(a) Schematic of a single pair of a p- and n-type semiconductor block.Examples of thermoelectric materials and a thermoelectric based generator. (b) Photograph of a thermoelectric module. . . . .	17
2.5	Schematic of a thermionic emission energy conversion. . . . .	19
2.6	Schematic of Johnson Thermo Electrochemical converter. . . . .	19
2.7	(a)Schematic of a thermophotovoltaic energy harvester system. (b) Photograph of a thermophotovoltaic device . . . . .	20
2.8	Schematic of electromagnetic transduction . . . . .	22
2.9	Schematic of an electrostatic transduction energy harvesting. . . . .	24
2.10	Schematic of a piezoelectric transducer system . . . . .	25
2.11	Block diagram of a self-powered temperature sensor. . . . .	30
2.12	Electrical model of a thermoelectric generator. . . . .	30
2.13	(a) Schematic model of electric energy harvesting process using pyroelectric cells directly driving a load resistance $R_L$ . (b) Photograph of a pyroelectric cell	31
2.14	(a) Schematic of standing-wave thermoacoustic engine integrated with a piezoelectric element. (b) Photograph of a thermoacoustic energy harvester . . . . .	33
2.15	Concept of thermal energy harvesting using Shape Memory Alloy. . . . .	34
2.16	Schematic of the SMA based thermal energy harvesting . . . . .	35
2.17	(a) Schematic of the bimetal based thermal energy harvester showing its two stable positions in a thermal gradient set up. (b) Photograph of the prototype of the array of thermal energy harvester based on thermal buckling energy conversion . . . . .	35
2.18	SEM images of thermal buckling MEMS energy harvester . . . . .	36
2.19	Heat engine device representation . . . . .	37
2.20	Representation of the low cost thermomagnetic generator . . . . .	37
2.21	Representation of the thermomagnetic devices; (a) side view of a thermal switch using thermomagnetic effect, (b) schematic of a thermomagnetic generation due to fluctuating magnetic force and restoring spring forces . . . . .	38
2.22	Schematic representation of proposed solution . . . . .	43

3.1	Representation of transition between ferromagnetism and paramagnetism . .	46
3.2	Representation of the principal electromagnetic characteristics of FeNi alloys.	47
3.3	Representation of the principal magnetic characteristics of FeNiCr alloys. . . .	48
3.4	Schematic of the proposed solution for thermal energy harvesting . . . . .	48
3.5	Schematic of the generator's transient behavior . . . . .	50
3.6	ProposedSolution . . . . .	50
3.7	Temperature response of soft magnetic material . . . . .	54
3.8	Schematic representation of the model for the calculation of flux density along the axis of a cylindrical magnet. . . . .	55
3.9	Thermomagnetic curve . . . . .	56
3.10	Magnetic force against gap distance on triggering system. . . . .	58
3.11	Magnetic force as function of both temperature of soft magnetic material and gap distance. . . . .	59
3.12	Magnetic force as function of magnet dimensions. . . . .	60
3.13	Representation of the function $M_{FeNi}(z)$ for a given initial gap and thickness of magnet . . . . .	62
3.14	Parametric study of the Magnetization $M_{FeNi}(z)$ for a constant spring magnet- mass system . . . . .	63
3.15	Comparison of experimental results and analytical predictions of operating temperatures as a function of initial position $z_0$ . . . . .	64
3.16	Schematic of the configuration of the piezoelectric bimorph. . . . .	66
3.17	Schematic representation of possible architecture of piezoelectric transducer considered for the analytic electro-mechanical model . . . . .	67
3.18	Effect of the generator's dimension reduction on resonance frequency and energy density. . . . .	72
3.19	Temperature response of the generator when dimension reduction is consid- ered. . . . .	73
3.20	Tip beam displacement during 1 thermal cycle (closing to opening commu- tation) in transient simulation . . . . .	74
3.21	Velocity of the tip beam during 1 thermal cycle (closing to opening commu- tation) in transient simulation . . . . .	75
3.22	Output voltage response during transient simulation . . . . .	75
3.23	Instantaneous power dissipated during one thermal cycle . . . . .	76
4.1	Schematic view of the three dimensional model of the generator. . . . .	82
4.2	Three-dimensional model for thermal analysis. . . . .	83
4.3	Representation of the boundary conditions of the three-dimensional model.	84
4.4	Schematic representation of the pinball region for thermal contact analysis. .	85
4.5	Representation of the temperature distribution on the FeNi alloy for contact and contactless states. . . . .	86
4.6	Temperature response of the generator by finite element simulation consid- ering the thermal contact. . . . .	87
4.7	Photograph of the top view of the PCB serpentine-shape . . . . .	87
4.8	Thermal transient results of first prototype of FeNi. . . . .	88
4.9	Comparison of the thermal response of the generator between finite element model, analytical model and measured data. . . . .	88

4.10	Three-dimensional model of the generator used for the magneto-static analysis	89
4.11	Representation of the surface force density acting over the FeNi alloy and the permanent magnet by finite element method, (a) isometric view and (b) lateral view of the model. . . . .	90
4.12	Schematic representation of the variable sweep analysis for the horizontal alignment of the FeNi with respect to the permanent magnet, (a) shows the FeNi alloy with a maximum misalignment while (b) depicts the maximum misalignment. . . . .	91
4.13	(a) Finite element results showing the influence of the horizontal alignment of the FeNi alloy on the magnetic attraction force within the triggering system, (b) lateral view of the system illustrating the magnetic field strength magnitude for the optimum position of the FeNi. . . . .	91
4.14	Magneto-static result of the magnetic attraction force as a function of temperature and distance of separation within triggering system . . . . .	92
4.15	Representation of the interaction between mechanical and magnetic force as a function of temperature of FeNi and separation distance by finite element method. . . . .	93
4.16	Representation of the interaction between mechanical and magnetic force as a function of temperature of FeNi and separation distance by finite element method. . . . .	94
4.17	Representation of the benchmark study to validate the finite element model and the analytical model for the magnetic attraction force between a permanent magnet and a magnetized material. . . . .	95
4.18	Validation of the magnetic model and the benchmark case with the force calculation magnet. . . . .	95
4.19	Schematic representations of the three-dimensional models of prototypes studied through finite element method. . . . .	97
4.20	Representation of the contact surfaces in finite element model. . . . .	100
4.21	Results comparison in static domain of finite element modeling of three different prototype of generators. . . . .	101
4.22	Schematic representation of boundary conditions for harmonic analysis. . . . .	102
4.23	Finite element simulation results in harmonic regime of the prototype 1. . . . .	103
4.24	Finite element simulation results in harmonic regime of the prototype 2. . . . .	104
4.25	Finite element simulation results in harmonic regime of the prototype 3. . . . .	105
4.26	Schematic representation of general transient response of the generator. . . . .	106
4.27	Transient result during 1 thermal cycle of the prototype 2 . . . . .	108
4.28	Instantaneous power representation in a transient simulation for prototype 2. . . . .	109
4.29	Validation of the finite element model and analytical simplified model in transient simulation with measured data of a generator, vertical displacement of the tip beam. . . . .	110
4.30	Validation of the finite element model and analytical simplified model in transient simulation with measured data of a generator, generated voltage during operating commutations. . . . .	110
5.1	Schematic representation of the fixture for mounting the generator prototypes. . . . .	114
5.2	Photograph of the three prototype architectures of transducer beams. . . . .	116
5.3	Photograph of the pair of magnets used for the prototype generator . . . . .	117

5.4	Photograph of the testbed developed for first generation energy harvesters. . . . .	118
5.5	Experimental measurements of the temperature response of first generation prototypes. . . . .	119
5.6	Comparison of experimental results of output voltage and vertical displacement . . . . .	121
5.7	Comparison of instantaneous power output of three first test prototypes of first generation energy harvester. . . . .	122
5.8	Experimental results of the temperature evolution of prototypes 2b and 3b . . . . .	124
5.9	Experimental results of the vertical displacement of the tip of the beam and output voltage, when a smaller magnetic volume for prototype 2 and 3 is considered (i.e., Prototype 2b and 3b). . . . .	125
5.10	Instantaneous power per commutation of test prototypes of generator using smaller permanent magnets. . . . .	126
5.11	Photograph of the first portable test prototype of a second generation energy harvester. . . . .	129
5.12	Evolution of the temperature of the first portable test prototype of energy harvester. . . . .	130
5.13	Experimental results of the first portable test prototype of second generation energy harvester, dynamic behavior characterization. . . . .	131
5.14	Instantaneous power of the portable test prototype of second generation energy harvester. . . . .	132
5.15	Operating temperatures of the first portable prototype as a function of load resistor. . . . .	134
5.16	Output average power and energy density as function of load resistor of the first portable teste prototype of second generation energy harvester. . . . .	134
5.17	Schematic representation of the energy harvester with a full wave rectifier bridge. . . . .	135
5.18	Evolution of temperature during 4 thermal cycles of operation of first portable test prototype with a full wave rectifier bridge connected to the output. . . . .	136
5.19	Experimental results of the first portable test prototype of second generation energy harvester, when full wave rectifier bridge is connected to output. . . . .	136
5.20	Evolution of temperature during 3 thermal cycles of operation of first portable test prototype with a full wave rectifier bridge connected to the output. . . . .	138
5.21	Experimental results of the first portable test prototype of second generation energy harvester, when full wave rectifier bridge and a capacitance $C_{Load} = 2\text{nF}$ is connected to output. . . . .	138
5.22	Photographs of the second portable test prototype of second generation energy harvester . . . . .	140
5.23	Thermal response of second portable test prototype of second generation energy harvester. Two thermal cycles are depicted on the graph. . . . .	140
5.24	Experimental results of the second portable test prototype of second generation energy harvester, dynamic behavior characterization. . . . .	141
5.25	Operating temperatures of the second portable prototype as a function of load resistor. . . . .	142
5.26	Output average power and energy density as function of load resistor of the second portable teste prototype of second generation energy harvester. . . . .	143
5.27	Circuit representation of the piezoelectric generator. . . . .	144

5.28	Schematic representation of the electric equivalent model of our generator in mode generation mode. . . . .	147
5.29	Photograph of the test prototype of generator using to validate equivalent electrical circuit of the generator. . . . .	148
5.30	Schematic representation of the electric equivalent model of our generator in mode actuator mode. . . . .	148
5.31	Validation of the electric equivalent model through admittance measurements of a prototype. . . . .	149
5.32	Second validation of equivalent electric model. . . . .	150
5.33	Experimental measurements of the rotation of phase of electrical impedance showing the magnetic breaking. . . . .	151
5.34	Schematic representation of electric equivalent circuit of the generator with a full wave rectifier bridge. . . . .	152
5.35	Output voltage of the electrical equivalent model of the generator when a full wave rectifier bridge is connected. . . . .	153
5.36	Schematic representation of electric equivalent circuit of the generator with a power management module LTC3108. . . . .	153
5.37	Output voltage of the electric equivalent circuit using the LTC3108 chip. . . . .	154
6.1	Schematic representation of the architecture of the generator to be optimized through Simulink . . . . .	159
6.2	Implementation of the first step time model of the energy harvester in Simulink. . . . .	160
6.3	Schematic representation of the transducer system. . . . .	160
6.4	Schematic representation of signal bound as a requirement on first design optimization of generator. . . . .	161
6.5	Typical response of the generator during a thermal cycle (closing and opening commutations) of operation (input force, tip beam displacement, output voltage and velocity). . . . .	162
6.6	Typical response of the generator during a thermal cycle (closing and opening commutations) of operation (instantaneous power and output energy) . . . . .	163
6.7	Evolution of the energy over iterations on design optimization process. . . . .	164
6.8	Typical response of the optimum design of the generator during a thermal cycle (closing and opening commutations) of operation for input force, velocity, tip beam displacement and output voltage . . . . .	165
6.9	Typical response of the optimum design of the generator during a thermal cycle (closing and opening commutations) for power and output energy. . . . .	165
6.10	Implementation of energy harvester model in Simulink . . . . .	166
6.11	Implementation of triggering system of the model in Simulink . . . . .	167
6.12	Representation of the dashboard implemented on the step time model of the energy harvester. . . . .	168
6.13	Custom requirement representation for second attempt of design optimization of energy harvester model implemented on Simulink. . . . .	169
6.14	Typical response of the initial design generator for the second attempt of design optimization (temperature response, vertical displacement, velocity and output voltage of the cantilever beam). . . . .	170
6.15	Typical response of the initial design generator for the second attempt of design optimization (power and energy output). . . . .	170

6.16	Typical response of the optimum design generator for the second attempt of design optimization (temperature response, velocity, vertical displacement and output voltage). . . . .	171
6.17	Typical response of the optimum design generator for the second attempt of design optimization (power and output energy). . . . .	171
6.18	Histograms of the generator parts obtained by Monte Carlo simulation, when a tolerance of $\pm 5\%$ is considered. . . . .	175
6.19	Simulation results of the output energy for the 10000 generators sample. . . . .	175
6.20	Histograms of the generator parts obtained by Monte Carlo simulation, when a tolerance of $\pm 2\%$ is considered. . . . .	177
6.21	Simulation results of the output energy for the 10000 generators sample when a tolerance of $\pm 2\%$ is considered on the design variables. . . . .	177
A.1	Reference system representing polarization of a piezoelectric material and its polarization cycle. . . . .	184
A.2	Schematic representation of principals modes of operation of ceramic piezoelectric materials. . . . .	186
B.1	Design drawings of the fixture for mounting the first generation prototypes . . . . .	187
B.2	Base support design drawing . . . . .	188
B.3	Support bar design drawing . . . . .	188
B.4	Support block design drawing . . . . .	189
B.5	Jaws design drawing . . . . .	189
B.6	Central bar design drawing . . . . .	190
B.7	Vertical support bar design drawing . . . . .	190

# List of Tables

1.1	Characteristics of some popular wireless sensor nodes. . . . .	4
1.2	Summary of power density of various energy ambient sources . . . . .	6
1.3	Typical waste heat temperature range from different sources . . . . .	8
2.1	Summary of maximum energy density . . . . .	28
2.2	State of the art on thermal energy harvesting. . . . .	40
3.1	General parameters for the temperature response of the generator. . . . .	54
3.2	Identification results for saturation magnetization against temperature. . . . .	56
3.3	General parameters for the temperature response of the generator. . . . .	58
3.4	General parameters of the initial design of the generator for calculating the operation temperatures. . . . .	71
3.5	Energy densities per commutation of the initial design of generator. . . . .	76
3.6	Scaling laws for a thermo-magnetically activated piezoelectric generator towards miniaturization. . . . .	77
3.7	Design guidelines of a thermo-magnetically triggered piezo-electric generator. . . . .	78
4.1	General parameters of the 3D model of the generator for the transient thermal analysis. . . . .	85
4.2	General parameters of three prototypes studied through finite element method. . . . .	98
4.3	Material parameters of the finite element models. . . . .	99
4.4	Summary of the main static and modal characteristics of the prototypes. . . . .	100
5.1	Comparison of different piezoelectric materials and their characteristics. . . . .	115
5.2	General parameters of permanent hard magnets. . . . .	118
5.3	Thermal characterization of the test prototypes. . . . .	119
5.4	General characterization of the test prototypes. . . . .	123
5.5	General characterization of the test prototypes when smaller magnets are considered. . . . .	127
5.6	General dimensions of the main parts of the first portable test prototype of the second generation energy harvester. . . . .	129
5.7	Characterization values of the first portable prototype of second generation energy harvester. . . . .	133
5.8	Main features of the first portable prototype of second generation energy harvester with a full wave rectifier bridge connected as a load. . . . .	137
5.9	General dimensions of the main parts of the second portable test prototype of the second generation energy harvester. . . . .	139

5.10	Main features of the second portable prototype of second generation energy harvester. . . . .	142
5.11	Material parameters of the electric equivalent model. . . . .	148
5.12	Material parameters of the electric equivalent model, when FeNi is heated up to 80°C. . . . .	149
6.1	Design variables of the first design optimization attempt. . . . .	159
6.2	Initial design of the generator for the first design optimization attempt. . . . .	162
6.3	Optimum design of the generator for the first design optimization attempt. . . . .	164
6.4	Design variables of the second design optimization attempt. . . . .	168
6.5	Summary of the design variables of the initial design and the optimum design of the second attempt of design optimization process. . . . .	172
6.6	Design parameter values and uncertainty. . . . .	174
6.7	Probability of fail and process capability of optimum design of generator depending on tolerances. . . . .	178
7.1	Test prototypes performance comparison. . . . .	181
A.1	Variables involved on piezoelectric equations. . . . .	183
A.2	Relation between tensor subscript and Voigt representation. . . . .	184
A.3	Summary of mechanical, electrical and piezoelectrical coefficients. . . . .	185
A.4	Constitutive equations of piezoelectric effect. . . . .	185

# Abbreviations

<b>AlN</b>	<b>Aluminum Nitride</b>
<b>CMOS</b>	<b>Complementary Metal-Oxide-Semiconductor</b>
<b>ECG</b>	<b>ElectroCardioGraphy</b>
<b>ECO</b>	<b>European Communications Office</b>
<b>IoT</b>	<b>Internet of Things</b>
<b>JTEC</b>	<b>Johnson Thermo Electrochemical Converter</b>
<b>MEMS</b>	<b>Micro Electro Mechanical Systems</b>
<b>PVDF</b>	<b>Polyvinylidene Fluoride</b>
<b>RF waves</b>	<b>Radio Frequency waves</b>
<b>SMA</b>	<b>Shape Memory Alloy</b>
<b>SMA</b>	<b>Shape Memory Effect</b>
<b>TB</b>	<b>Thermal-Buckling</b>
<b>TEG</b>	<b>Thermo-Electric Generator</b>
<b>TM</b>	<b>Thermo-Magnetic</b>
<b>TGS</b>	<b>Triglycine Sulfate</b>
<b>TMPEG</b>	<b>Thermo-Magnetically triggered Piezoelectric Generator</b>
<b>WSN</b>	<b>Wireless Sensor Network</b>



# Physical Constants

Permeability of free space  $\mu_0 = 4\pi \times 10^{-7} \text{ H m}^{-1}$

Permittivity of free space  $\epsilon_0 = 8.8541 \times 10^{-12} \text{ F m}^{-1}$

Elementary electric charge  $e = 1.602 \times 10^{-19} \text{ C}$



# Nomenclature

<b>Symbol</b>	<b>Name</b>
$h_B$	Thickness of shim layer
$h_P$	Thickness of piezoelectric layer
$h_{mag}$	Height of permanent magnet
$h_{FeNi}$	Height of FeNi alloy
$F_{mec}$	Mechanical force
$F_{mec}$	Mechanical force
$k$	Mechanical stiffness
$\kappa$	Thermal conductivity
$L_B$	Length of cantilever beam
$L_P$	Length of piezoelectric layer
$\lambda$	Heat transfer coefficient
$r_{FeNi}$	Radius of FeNi alloy
$r_{mag}$	Radius of permanent magnet
$S_L$	Cross-sectional area of material
$\theta$	Temperature
$\theta_{opening}$	Temperature of opening commutation
$\theta_{closing}$	Temperature of closing commutation

$\theta_C$	Temperature of Curie
$w_B$	Width of cantilever beam
$w_P$	Width of piezoelectric layer

*This dissertation is dedicated to the memory of my father*

*Pedro Florencio RENDON SALINAS (1936-2008)*

*El último tren se ha parado en el último andén,  
y aún seguimos  
Fuiste el tronco invulnerable y no  
por e*

*Nunca no*

*pero de pronto llegó un aviso de Dio  
el tiempo se ha acabado, el tren avanza lentamente,  
nunca hubo hora más larga que cuando te dije adios*

*El último tren se ha parado en el último andén,  
el silbato del tren me preocupó por alguno  
hoy sé que e  
E  
pero sabemos*



# Chapter 1

## Introduction

### Contents

---

<b>1.1 Background application</b> .....	<b>2</b>
1.1.1 Energy harvesting for autonomous systems .....	2
1.1.1.1 Energy consumption of a wireless sensor node .....	3
1.1.2 Statement of the problem .....	5
1.1.2.1 Alternative techniques to thermal energy harvesting for slow and small ambient temperature variations .....	5
1.1.3 Research goals .....	5
1.1.4 Motivation .....	6
1.1.4.1 Human body temperature variations for energy harvesting	7
1.1.5 Research justification .....	7
1.1.6 Thesis organization .....	8

---

*This first chapter is meant to briefly set the scope covered in this thesis, its motivation and justification. Furthermore, it outlines the research objectives as the structure of this document. It starts with a non-exhaustive review about background application of autonomous sensor systems. In addition, this first chapter will allow readers to be familiar with the context of this research work. Most popular ambient energy sources and their principal transduction techniques for energy conversion as well as a literature review on thermal energy harvesting are presented in [Chapter 2](#). It will then provide a much more detailed and specific overview.*

## 1.1 Background application

This section summarizes the background of thermo-magnetic effect of soft magnetic materials for energy harvesting applications, mainly in the research field of powering autonomous sensor nodes.

### 1.1.1 Energy harvesting for autonomous systems

Although the term “*wireless autonomous system*” may include devices as diverse as mobile phones, entertainment devices, and other consumer electronics, it is usually used to describe devices used in the industrial, building, or environmental setting. This term is also used to describe wireless sensor nodes.

Autonomous sensors are devices able to interact with physical sensing hardware, perform some processing on the sampled data, and communicate this information wirelessly (in most of cases via a radio transceiver) to another device. In general, these kinds of sensor do not use cables neither for transmitting data nor for powering electronics. These devices can be deployed to monitor parameters of interest and to report these observations back, in most of cases to a central data collector. Sets of these wireless sensor nodes, known as wireless sensor networks (WSNs), can communicate and cooperate with one another.

WSNs may be used to monitor vibration of machines in the industrial setting in order to detect the development of faults and to react to a possible permanent damage [1], to monitor biomedical signals including ECG, pulse rate, blood pressure or temperature [2], in building applications, WSNs may also be used as part of a system to control heating or lighting [3]. The cost of installing wired sensors in a commercial building has been estimated at \$100 per sensor + \$1.6 per linear foot wiring [4]. Hence, when applications require hundred or thousands of these sensor nodes, it becomes impractical and too expensive.

In the field of electronic systems, the term “*energy harvesting*” designates techniques for capturing the environmental energy and convert it into electricity. And since the past decade there has been a growing interest on energy harvesters using piezoelectric materials [5–7]. The ongoing miniaturization and increase of functionality enable the development of systems including smart sensors for the internet of things, wearable and implantable devices. And such small volumetric devices are very limited in the amount of energy that a battery can store. In addition, the wireless sensor nodes are usually deployed in hostile environments, they can be not easily reached for the purpose of replacing their batteries. Therefore, alternatives in powering sensor nodes, like energy harvesting technologies are attractive as they offer the potential to sustain the operation of sensor nodes indefinitely, depending on the available energy sources (i.e., mechanical vibrations, radiant energy, thermal energy).

The main parts comprising a basic wireless sensor node are depicted in [Figure 1.1](#). The energy resources in [Figure 1.1](#) relate to the available energy sources. It can be either a primary battery storing a limited amount of energy or an energy harvesting system. The power management block has the function of matching the power source to the power supply requirements of the load such as the micro processor and the communication transceiver. In this dissertation, we are mainly interested in the energy resource block as well as its power

management system. We aim at developing both an energy harvester system and its power management system. The goal is to power a commercial available sensor node.

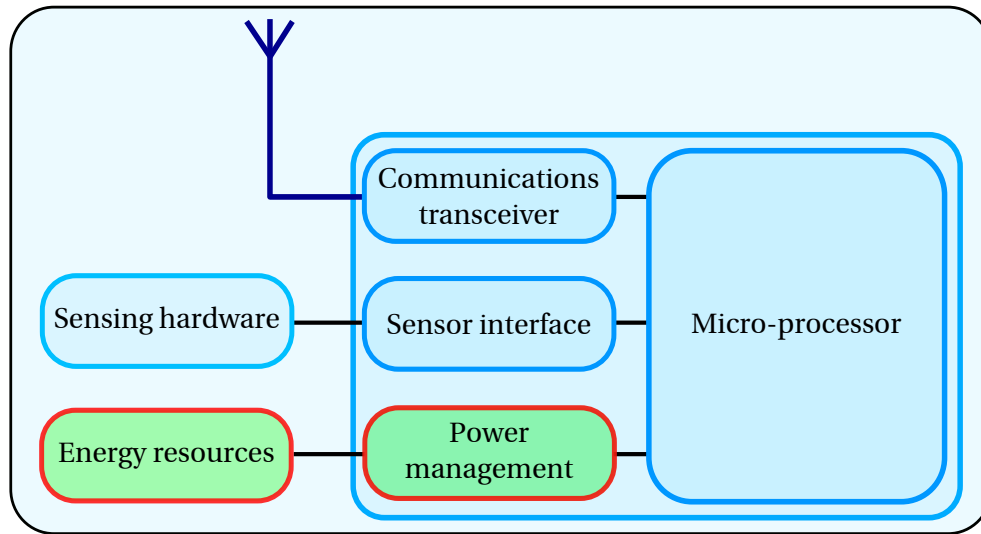


FIGURE 1.1: Block diagram of the basic components of a wireless sensor node.

A significant amount of research works are reported in the literature that discuss about harvesting small-scale environmental energy for powering wireless sensor nodes. A substantial part of the research work realized by Roundy *et al.* in [8] details the extraction of energy from kinetic motion. They present an extensive examination on vibration energy scavenging aiming at powering wireless sensor nodes.

#### 1.1.1.1 Energy consumption of a wireless sensor node

Estimating the energy consumption of a wireless sensor node is very important in order to have an idea of the amount of energy that can be useable for powering such a kind of devices. And powering of wireless sensor node can be a barrier to the uptake of this technology.

Among some commercial wireless sensors we detected the next ones as potential candidates to be powered:

- Wireless temperature sensor from Linear Technology [9]. It offers a wireless temperature sensor which is formed by connecting a wireless radio module to an ADC, reference and thermistor. In this case, the circuitry is powered by an energy harvester that can take power from a battery or solar panel. Typical power consumption for a sensor node reporting once per 10 seconds is less than  $20\mu\text{A}$  for the sensor system and can be  $20\mu\text{A}$  for the wireless communication, giving a total average load current of  $40\mu\text{A}$ . The information about the size of this device is not provided.
- STM 330 from enOcean [10]. A commercial solution for realization of wireless and maintenance free temperature sensors. Power supply is provided by a small solar cell

or by an external 3V battery. An energy management circuit is installed to bridge periods of darkness. The charge needed for one measurement and transmit cycle is about 130 $\mu$ C. Calculations are performed on the basis of electric charges because of the internal linear voltage regulator of the module. Energy consumption varies with voltage of the energy storage while consumption of electric charge is constant. The current consumption for continuous operation may be at 130 $\mu$ A. The size of this module is 0.688cm<sup>3</sup>.

- Wireless Temperature Sensor from Monnit [11]. The current consumption for transmission mode is 35mA while for the sleep mode can be 0.7 $\mu$ A. The size of this module is 32.54cm<sup>3</sup>.

Compact form factor and low power consumption of a wireless sensor node make them highly suitable for many applications, including medicine, environmental monitoring, ambient intelligence, and wireless multimedia sensor networks. A summary of commercial wireless sensor nodes is summarized in Table 1.1

TABLE 1.1: Characteristics of some popular wireless sensor nodes.

Current draw	sunSPOT [12]	LOTUS [13]	TelosB [14]	MicaZ [15]
Consumption Tx (mA)	18	17	18	17.4
Consumption Rx (mA)	23	16	23	19.7
Consumption sleep ( $\mu$ A)	33	10	6	15

It can be concluded that the current consumption of such wireless sensor nodes is dependent on their duty cycle. The power consumed by a wireless sensor node is typically few tens of mW and the power sources of the same volume space as the sensor node are much smaller, concretely in the range of tens of  $\mu$ W. Therefore, the energy harvesters, are eventually not able to power continuously the operation of the autonomous sensor node. To overcome this problematic, it can be reduced the power consumption of the sensor node by reducing its duty cycle into an intermittent way. Generally, wireless sensor nodes are designed to operate at very low duty cycles. This implies moderated power consumption in active mode (tens of mW), and very low power consumption in sleep mode (tens of  $\mu$ W).

To maintain sustainable operation of the autonomous sensor through energy harvester, the average generated power,  $P_{g,av}$  must fulfill the condition of:

$$P_{g,av} \geq P_{c,av} \quad (1.1)$$

Where,  $P_{c,av}$  represents the average power demanded from the power source. It also includes the average power losses of the different parts such as the conditioning block. Due to the variability of the ambient energy source, the harvested electrical energy would also change accordingly and so there would be times where  $P_{g,av} \leq P_{c,av}$ . Therefore, a storage unit is required in most of cases. This storage unit must supplement the power transferred to the load whenever the generated power is less than the demanded one. Supercapacitors and rechargeable secondary batteries can be used as energy storage units. Actually, secondary batteries and supercapacitors are sometimes used in hybrid devices because of their complementarity [16].

### 1.1.2 Statement of the problem

Among the classical techniques for converting thermal energy, either in the form of spatial gradients or temporal variations include, respectively, thermo-generators and pyro-electric generators. And these techniques offer a relatively low efficiency when small size of devices is required (because of the direct link with the area of electrodes or the active surface of thermo-electric materials) and when small thermal gradients or slow temperature rates are the input energy for such a systems. Therefore, we are proposing a new generator able to convert small and slow temperature variations into electricity.

We focus on the multiphysics modeling of such a system and its characterization to show the feasibility of powering a wireless sensor node with this kind of micro-power generator. This dissertation has per goal to propose the design guidelines of such a system, in addition, an analytical model is proposed to better understand the static and dynamic behavior of the generator. Finite element simulation have been conducted to explore different and complex architectures. Experimental prototypes have been built in order to validate the models and to show the feasibility and operability of thermal energy harvesting using thermo-magnetic effect coupled with piezoelectric transduction.

Finally, a power management circuit adapted to the generator is presented in order to extract from the generator the maximum energy and to power a wireless sensor device.

#### 1.1.2.1 Alternative techniques to thermal energy harvesting for slow and small ambient temperature variations

It is possible to convert thermal energy into electricity without using pyroelectric materials nor thermoelectric ones, but using other materials having a reversible and temperature-dependent property. The key principle behind conversion of thermal into mechanical power lies in having a reversible, thermally dependent property, just to name a few, gas expansion (thermoacoustics energy harvesting [17]), strain (shape memory alloy [18]), thermal-buckling [19, 20], and ferromagnetism (thermo-magnetisation [21–23]).

Recently, within our research group, thermo-magnetic effect has been coupled with piezoelectric transduction in order to harvest thermal energy [24, 25]. These devices have high power output compared with those using classical direct thermal energy conversion (i.e., therm-generators or pyro-electric based generators), low cost, and wider choice of materials for fabrication. The detailed working mechanism of these devices is explained in [Chapter 3](#). Coupled thermo-magnetic materials with piezoelectric transductions harvesters are more commonly termed as Thermo-Magnetically triggered Piezoelectric Generator (TMPEG).

### 1.1.3 Research goals

The long term goal of this work is to develop an energy harvester to power a wireless sensor node. The energy harvester converts temperature variations into electricity throughout

combining thermo-magnetic effect with piezoelectricity. The first converting thermal energy into mechanical energy while the latter transforming mechanical vibrations into electricity.

This dissertation presents the initial steps in the design and modeling to fully predict the dynamic behavior of such a energy generator. The specific thesis aims are:

1. To provide the theory and methodology for analysis of the design space using piezoelectric bimorph structures, permanent magnets and iron nickel alloys. The soft magnetic alloy and the permanent magnet forming the triggering system to convert temperature variations into mechanical energy. The piezoelectric bimorph comprising the transducer system, which converts mechanical energy into electricity.
2. To provide a rapid design tool for such a type of thermo-magnetically activated piezoelectric generator to enhance dynamic performance of the device.
3. To develop a suitable power management circuit able to extract the maximum energy from the generator. This circuit should be able to store the harvested energy and to provide it to power a wireless sensor node.
4. To experimentally verify the design theory and approach within dispoible materials; Iron-nickel alloy with a Curie point near to the room temperature and PZT 5H piezoelectric bimorph with steel reinforcement layer.

#### 1.1.4 Motivation

The main goal of this dissertation is to develop an alternative to direct conversion of thermal energy in the form of temperature variations into electrical energy. This solution should be able to overcome the problematic of dependency on the rate of change of temperature, for which we opted to combine the thermo-magnetic effect of soft magnetic alloys with piezoelectric transduction. Moreover, it is desirable to operate at temperature ranges near to the room temperature for general purpose applications.

Table 1.2 lists power density of some energy source available. From a general point of view, it can be noted that thermal energy sources do not offer the higher power density among all the energy source available. However, its ubiquity make them highly attractive in energy harvesting systems.

TABLE 1.2: Summary of power density of various energy ambient sources

Energy source	Power density	Reference
Radiant energy (direct sun)	100mW cm <sup>-2</sup>	[26]
Radiant energy (office light)	0.1mW cm <sup>-2</sup>	[26]
Thermal energy (temperature gradients)	17μW cm <sup>-3</sup>	[27]
RF waves (at 25m from GSM base station)	1mW m <sup>-2</sup>	[28]
Mechanical energy (vibrations)	309mW cm <sup>-3</sup>	[29]

Our motivation comes from the vision of providing alternatives to direct conversion of thermal energy into electricity. This alternative should be able to overcome the dependance of rapid changes of temperature and large thermal gradients, as requirements for classical solutions, like pyroelectricity and thermoelectric generators, respectively.

#### 1.1.4.1 Human body temperature variations for energy harvesting

The human body regulates the temperature according to different external factors and seasons. Typically, normal body temperature is  $37^{\circ}\text{C}$  and the normal fluctuation in this temperature may be from  $36^{\circ}\text{C}$  to  $37.8^{\circ}\text{C}$ . These temperature variations can be considered as a part of body's defense mechanism or even as a response adaptation the environment. In hot conditions, heat loss is observed in the form of sweating and at the time for cold conditions heat gain by the human body takes place through shivering. In a normal activity day, the core body temperature variations may range about  $35^{\circ}\text{C}$  and  $37^{\circ}\text{C}$  as shown in [Figure 1.2](#). These data suggest that slow and small temperature variations are present in human bodies.

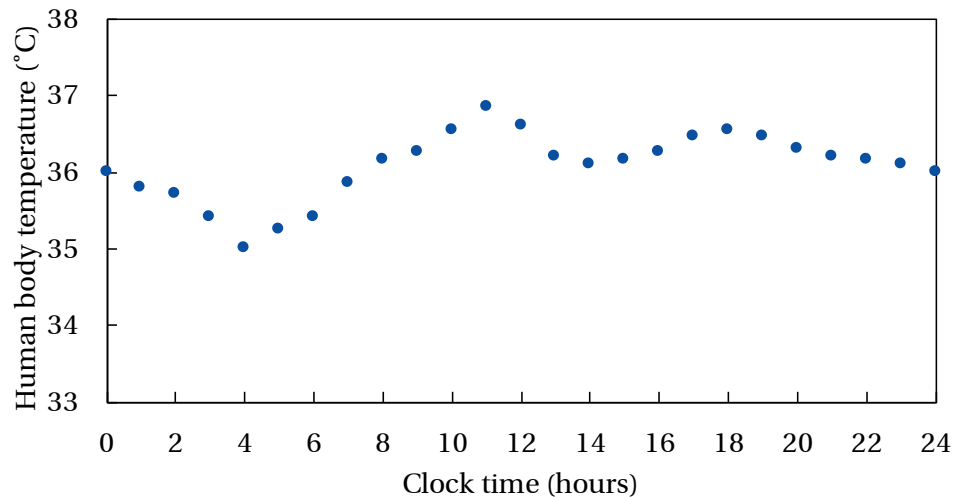


FIGURE 1.2: Human body temperature variations in a normal day [30].

The potential thermal energy is there, so when thinking in powering wearable sensors or some other portable devices, a need on thermal energy harvesting is evident. In addition, we believe that if new solutions for harvesting thermal energy are able to operate near to the human body range of temperature, they may be convenient for wearable devices. In addition, miniaturization of such a energy harvesters may open a large window of applications in where connected devices need to be powered.

#### 1.1.5 Research justification

Reported empirical evidence has supported the energy harvesting from thermal ambient energy in the form of temperature variations [31–33]. Ultimately, disruptive companies, including [Perpetuum](#), [SolePower](#), [EnOcean](#), [greenTEG](#), and [Pavegen](#) pursue energy harvesting to satisfy the growing demand of alternatives in powering wireless sensor networks.

Many authors have emphasized the importance of the exploiting renewable energies to fulfill the requirements of our modern world [8, 34]. Energy harvesting provides numerous benefits, it is suitable for Wireless Sensor Networks. Energy harvesting technologies can:

- Reduce or eliminate the dependency on batteries as main power for autonomous sensor nodes.
- Reduce installation costs on sensing systems as energy harvesting avoid power cables wiring and their conduits.
- Offer sensing and actuation capabilities deployed in dangerous human-access environments.
- Eliminate the need for millions on batteries and energy costs. They also can reduce maintenance cost on wireless sensor networks as once deployed it is no longer needed to retrieve all sensing nodes for replacing their batteries.

Particular attention is paid on thermal energy harvesting in the form of temperature variations at low range of temperature as listed in Table 1.3. from industrial or even human sources. It is evident that at low temperature range, temperature variations would be

TABLE 1.3: Typical waste heat temperature range from different sources. Adapted from [34]

Source or environment	Temperature (°C)
Industrial process using steam	55 - 88
Ball bearings	32 - 55
Welding machines	30 - 88
Injection molding machines	32 - 88
Forming dies	27 - 88
Air conditioning and refrigeration compressors	32 - 45
Industrial switching and controlling	27 - 80
Variable frequency drives in pumping and irrigation	30 - 90

present on industrial filed in an intermittent way when these machineries operate in a non-continuous time period. And the need of having connected devices or even monitoring some physical parameter such as humidity or temperature on these kinds of environment is increasing. Therefore, we decided to undertake this research work on thermal energy harvesting but with a different approach. For the sake of modularity, the first conversion stage of thermal-to-mechanical energy let open a wide band of combining different conversion techniques for mechanical vibration-to-electricity.

### 1.1.6 Thesis organization

The remainder if this thesis is organized as follows. Chapter 2 presents a review of most popular ambient energy sources and their principal transduction techniques. It also introduces the state of the art on thermal energy harvesting. As the main focus of this thesis

is using thermal energy harvesting, special attention has been paid to the thermal energy harvesters. Most recent devices for converting thermal ambient energy into electricity are listed and presented to point out the advances on this field. This study allowed us to define the research aims and to provide new design tools towards rapid design of thermal energy harvesters. The outcomes are shown the need of having alternatives for thermal energy conversion when small and slow temperature variations are considered as the ambient energy source. It ends presenting our proposed solution.

In order to conduct design and develop thermo-magnetically activated piezoelectric generators, an understanding of the working principle and device operation is necessary. Keeping this objective in mind, a detailed study was conducted to investigate the effect of the temperature on the spontaneous magnetization of soft magnetic materials when these later are exposed to cycled temperature variations and constant external magnetic flux density as described in [Chapter 3](#). It describes the theory and methodology for the design of a thermo-magnetically triggered piezoelectric generator. By coupling thermo-magnetization of soft magnetic materials with piezoelectric transduction, it is possible to convert small and slow temperature variations into electricity that can be useful to power a wireless sensor node. A general formulation is derived for the different subsystems comprising the multiphysics device. Moreover, a simplified global model, developed using software Matlab/Simulink. A mathematical model is built to describe the transducer characteristics as a function of temperature variations. This information is necessary to understand the data coming from the transducer and to correlate the results given by finite element analysis tools. After an introduction to working principle of such a device, a design parameters study is explained in detail.

[Chapter 4](#) presents the Finite Element Analysis of the generator. Multiple simulations are conducted to better understanding the physics involved on the system. The two main subsystems of the generator are modeled by using commercially available software ANSYS/Electronics Desktop. Coupling finite element analysis was conducted in order to establish the design rules for material selection and dimensioning of the generator. An electric equivalent model developed using LTSpice is presented to introduce losses of dielectric and mechanical origin. The essential electronic components for the model are frequency-sensitives.

[Chapter 5](#) introduces an experimental engineering testbed to prove the performance of the thermo-magnetically activated piezoelectric generator using joule heat as temperature variations. The set of bench tests and experiments presented provide information to demonstrate the energy harvesting capabilities of the generator. A material with known ferromagnetic properties subjected to an external magnetic field and a variety of temperature variations applied by Joule heat help characterize the generator's ability to detect thermal thresholds. Consequently, by piezoelectric transduction, mechanical energy is converted into electricity. A power management module has been utilized to store and provide this generated electricity to a wireless sensor node.

In [Chapter 6](#), exploration of the design optimization issue is detailed to investigate the design parameters and the production feasibility. It is also presented a detailed variability analysis of the generator. More important tolerance of the design are defined and described.

[Chapter 7](#) concludes and summarizes with a list of potential applications of such a generator as well as main contributions of this research work.



## Chapter 2

# Review of energy harvesting technologies and state of the art of thermal energy harvesting

### Contents

---

<b>2.1 Ambient energy sources</b> .....	<b>12</b>
2.1.1 Mechanical vibrations .....	13
2.1.2 Radiant energy .....	14
2.1.2.1 Solar radiation .....	14
2.1.2.2 Radio waves .....	15
2.1.3 Thermal energy .....	16
2.1.3.1 Spatial thermal gradients .....	16
2.1.3.2 Temperature variations .....	20
<b>2.2 Energy transduction techniques</b> .....	<b>21</b>
2.2.1 Electromagnetic transduction .....	22
2.2.2 Electrostatic generators .....	23
2.2.3 Piezoelectric transducers .....	24
2.2.4 Discussion .....	27
<b>2.3 Thermal energy harvesting review</b> .....	<b>28</b>
2.3.1 Direct conversion of thermal to electrical energy .....	29
2.3.1.1 Thermo-electric generators .....	29
2.3.1.2 Pyro-electric generators .....	30
2.3.2 Indirect conversion of thermal to electrical energy .....	32
2.3.2.1 Thermo-acoustic generators .....	32
2.3.2.2 Electrical generators based on shape memory alloys .....	34
2.3.2.3 Thermal buckling generators .....	35
2.3.2.4 Thermo-magnetic generators .....	36
2.3.3 Discussion .....	38
<b>2.4 Proposed solution review</b> .....	<b>43</b>

---

*This chapter presents the literature review and the state of the art in thermal energy harvesting. This chapter then progressively narrows the field down to vibration based devices and the associated challenges for ambient temperature changes before discussing the main strategies currently pursued in research to overcome them.*

## 2.1 Ambient energy sources

Several ambient energy sources can be exploited for powering systems in small scale [35]. We have categorized these energy sources into three principal types: mechanical energy (vibrations and kinetic motion), radiant energy (solar light and RF waves), and thermal energy (spatial thermal gradients and temperature variations). The choice of which energy source to harvest from depends in its availability and also on the final application.

Most popular energy sources and their possible transduction techniques are depicted in Figure 2.1.

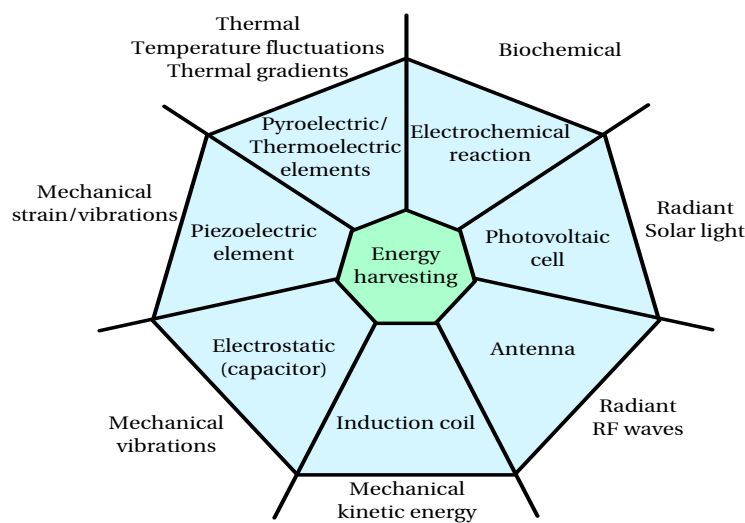


FIGURE 2.1: Energy sources and their respective transducers, adapted from [35].

In this dissertation, we are going to study an alternative approach to direct conversion of thermal energy into electricity; the indirect conversion of thermal energy into electricity by coupling thermo-magnetic effect and piezoelectric transduction. The main objective is to provide, in a long term, an energy harvesting technique able to be used in a human environment, where the temperature variations are slow and small (i.e., some Celsius degrees near to room temperature during several hours per day). With this in mind, radiant energy as the most popular energy source for energy harvesting in large and small scale, thermal energy in both temperature variations and thermal gradients, and mechanical energy as vibrations are outlined on the following sections.

### 2.1.1 Mechanical vibrations

Mechanical energy is one of the most ubiquitous sources of energy around us. It can be available in several forms, including human movement, heartbeat, vehicle motion and vibration. It can be a result of conversion of some other kind of energy; energy stored in fuel is converted to mechanical energy by burning the fuel in case of vehicle motion. This mechanical energy is generated through activities that are performed as part of daily lives to serve a specific purpose, for instance to move from one place to another, to pump blood to different body organs, to lift object, and so on.

The frequency of the mechanical excitation depends on the vibration source. It can range from less than 10Hz up to 200Hz, for the cases of human motion and industrial environments, respectively [36]. Roundy *et al.* [8] have undertaken several works on this energy source and they have demonstrated that a combination of theory and experiments suggest that about 300 $\mu$ W could be generated from vibration sources.

In order to determine how much power can be converted from vibrations, a general vibration to electricity model presented by Williams and Yates [37] can be used. The model is shown in Figure 2.2. This model takes into account the conversion of the kinetic energy of a vibrating mass to electrical power based on linear system theory without specifying the mechanism of energy transduction.

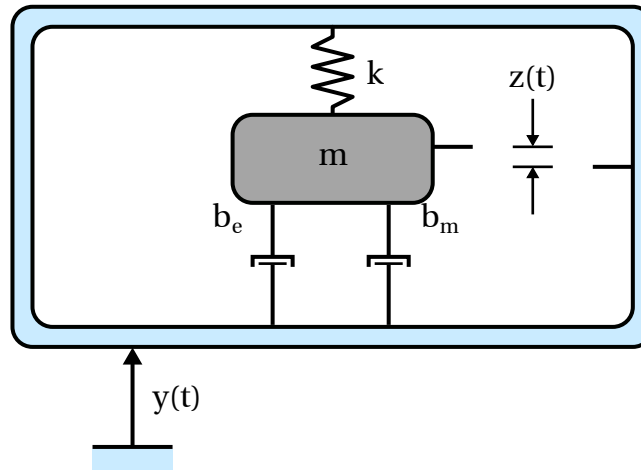


FIGURE 2.2: Schematic representation of vibration based energy harvesting.

This model is described by the Equation 2.1

$$m\ddot{z} + (b_e + b_m)\dot{z} + kz = -m\ddot{y} \quad (2.1)$$

where,  $z$  is the spring deflection,  $y$  is the input displacement,  $m$  is the mass,  $b_e$  is the electrically induced damping coefficient,  $b_m$  is the mechanical damping coefficient, and  $k$  is the spring constant. The principle behind this model is the conversion of energy from the oscillating mass into electricity by means a transduction technique like electromagnetic transduction. When using other type of vibration to electricity transduction, like piezoelectricity

for instance, this model has to be adapted because of the effect of the electrical system on the mechanical system may not be linear. Moreover, it may not be proportional to velocity but to mechanical strain. In addition, the mechanical damping is highly dependent on the medium where the system is operated and it not be necessarily linear and proportional to velocity.

The analytical expression for the magnitude of the output power is the following expression:

$$P = \frac{m\zeta_e\omega_n\omega^2\left(\frac{\omega}{\omega_n}\right)^3 Y^2}{\left(2\zeta_T\frac{\omega}{\omega_n}\right) + \left(1 - \left(\frac{\omega}{\omega_n}\right)^2\right)^2} \quad (2.2)$$

where,  $\zeta_e$  is the unitless electrical damping ratio according to the relationship  $b = 2m\zeta_e\omega_n$  with  $\omega_n^2 = \frac{k}{m}$ ,  $\omega_n$  and  $\omega$  are the angular frequency of the mass spring system and the angular frequency of the driving vibrations, respectively.  $Y$  is the Laplace transform of input displacement, and  $\zeta_T$  is the combined damping ratio ( $\zeta_T = \zeta_e + \zeta_m$ ).

In most of cases, the spectrum of the target vibrations is characterized in advance. Hence, the device can be designed to resonate at the frequency of the input vibrations. In this case, when the resonant frequency of the spring mass system matches the input frequency, the output power expression can be reduced to:

$$P = \frac{m\zeta_e A^2}{4\omega_n\zeta_T^2} \quad (2.3)$$

where  $A$  is the acceleration magnitude of the input vibrations. It is evident to note that if accelerations magnitude of the vibrations is considered as constant, the output power is inversely proportional to frequency.

## 2.1.2 Radiant energy

Radiant energy is generally emitted as electromagnetic waves. Solar energy is a kind of radiant energy, it is also referred as optical energy. This kind of energy accounts to the portion of the electromagnetic spectrum spanning infrared energy to ultraviolet light. In the following section the most popular radiant energies are outlined: solar radiation and RF waves.

### 2.1.2.1 Solar radiation

The incident solar light can holds a power density of  $100\text{mW cm}^{-2}$ . This is the most popular energy source for energy harvesting either in large scale, for instance in solar farms, or in small scale such as small photovoltaic cells. Standard solar cells have energy conversion efficiencies of between ten and twenty percent. The lighting power density on indoor environments such as illuminated offices drops dramatically to almost  $100\mu\text{W cm}^{-2}$  [35].

There are two different technologies to generate electricity from the solar light; photovoltaic and solar-thermal. Photovoltaic conversion is the direct conversion of sunlight

into electricity without any heat engine to interfere. Photovoltaic devices are rugged and simple in design requiring very little maintenance and their biggest advantage being their construction as stand-alone systems to give outputs from micro-watts to megawatts. Solar cells are small, squared-shaped semiconductors manufactured in thin film layers. They are made using some conductive materials, in general silicon. Figure 2.3(a) shows the schematic representation of the main parts of a solar light based energy harvester. It comprises a photovoltaic cell, that converts the solar energy into electrical energy. As the output of this kind of energy transducers is in DC, it can directly power a load. Furthermore, the photovoltaic cells can be plugged into the bulk electricity grid. Figure 2.3(b) illustrates a wireless sensor node powered by a photovoltaic cell.

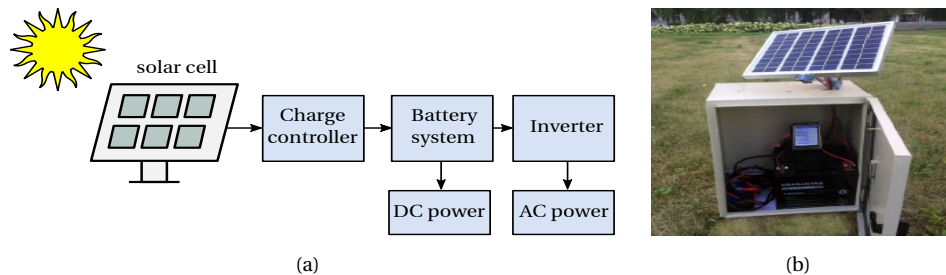


FIGURE 2.3: Schematic representation of solar light energy harvesting and a solar wireless sensor node. (a) Schematic representation of a photovoltaic based energy harvester. (b) Photograph of a photovoltaic based powering wireless sensor node [38].

Solar-thermal technologies use the sun's heat to create steam or pressurized gas to drive a turbine generator. Parabolic dish systems concentrate sunlight to heat gaseous hydrogen in a pipe system, which in turns drives a turbine to generate electricity. However, the portability of this kind of energy harvesters is scarified with the bulky pipes and elements needed to operate. Therefore, it is not suitable for powering autonomous sensor nodes.

A big advantage of these two kind of solar technologies is that they generate zero emissions themselves. However, some photovoltaic cell manufacturers generate some hazardous materials that need to be treated carefully in order to minimize the risks of exposure to humans and the ambient.

Traditional silicon solar cells are rigid, heavy and opaque [39]. The more solar energy produced, the more solar panels needed as we want to collect as much sunlight as possible to convert it to solar energy. Solar panels require a lot of space, since some roof tops aren't big enough to fit all, another alternative way is to install the solar panels in a place or area which gets enough access to sunlight [40]. In addition, the brittleness of silicon limits its uses. Furthermore, solar energy panels require additional equipment, such as inverters to convert direct electricity (DC) to alternating electricity (AC) for it to be passed onto and used by the national grid [41]. Photovoltaic panels require not only inverters but also storage batteries, increasing the investment cost for PV panels considerably

### 2.1.2.2 Radio waves

Radio frequency energy is present on environment in the form of signals that are deliberately radiated by broadcasting station antennas and cellular phone antennas. As increasing

the number of wireless communication technologies, the number of transmitters scattered around the modern world make abundantly this kind of radiant energy. These transmitters are able to generate strong electromagnetic fields. Consequently, RF energy harvesters can convert this radiant waves into electricity. Nevertheless, the very low power density levels is a major limitation. The expected power density around 25m from a Global System for Mobile communications (GSM) base station is less than  $1\text{mW m}^{-2}$  [28].

The available ambient power density, generally designated as  $S$  and it can be obtained from the following expression:

$$S = P_{erp} \frac{1}{4\pi d^2} \quad (2.4)$$

where  $P_{erp}$  is the effective radiated power, that is related to the isotropic radiator or ideal antenna, and  $d$  is the distance from the transmitter. It can be seen that the power density decays rapidly as the distance increases. The maximum value of the effective radiated power is regulated by European Communications Office (ECO). For example, for the 868MHz band, the maximum effective radiated power is 0.5W.

### 2.1.3 Thermal energy

Thermal energy is present all around us either in the form of spatial thermal gradients or temporal changes of temperature. And every energetic process, regardless of its initial nature, namely, kinetic, electrical or chemical, often it ends as heat that is then returned to environment. Therefore, thermal ambient energy is attracting the interest of researchers in developing new methods for converting thermal energy into electricity. Many techniques for converting directly thermal energy into electricity have been studied, including thermoelectric generation (Seebeck effect needing a heat sink facing a problematic to maintain an exploitable thermal gradient) and pyro-electricity [27, 42–45]. Even if these techniques have the advantage of being direct conversion methods that suggests fewer conversion losses (because having less energy conversion stages), they have some inconveniences when miniaturization is one of the design premises.

Several methods are currently used to harvest thermal energy, for instance direct energy conversion of thermal-to-electrical, and multistep energy conversion of thermal-to-mechanical-to-electrical. Below are presented the two most popular forms of thermal energy available on the environment.

#### 2.1.3.1 Spatial thermal gradients

Thermal energy in the form of spatial thermal gradients can be converted into electrical energy by several methods including Seebeck generators (i.e., thermoelectric generators), thermionic generators (also known as Edison effect), Johnson thermo-electrochemical converters, and Infrared photovoltaic harvesters.

Thermoelectric generators exploiting the Seebeck effect are comprised of several pairs of alternating p- and n-type semiconductor blocks (Figure 2.4(a)) arranged thermally in parallel and connected electrically in series (Figure 2.4(b))

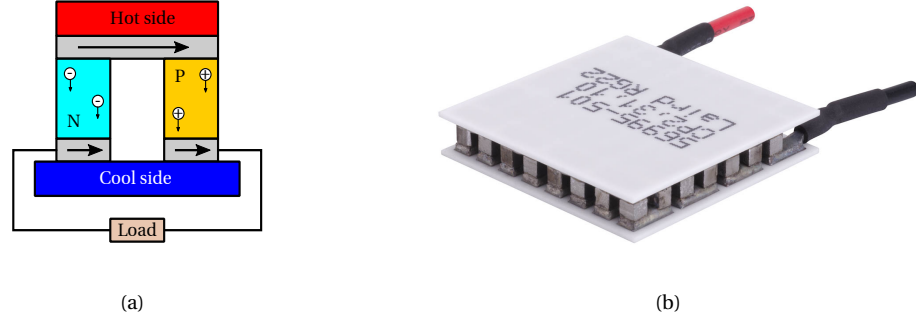


FIGURE 2.4: (a) Schematic of a single pair of a p- and n-type semiconductor block. Examples of thermoelectric materials and a thermoelectric based generator. (b) Photograph of a thermoelectric module.

These generators can be modeled as a DC voltage source connected in series with a resistance. The output voltage,  $V_s$ , of each element depends on the temperature difference,  $\Delta\theta$ , between the hot side and cool side, and on the Seebeck coefficients,  $\alpha_n$  and  $\alpha_p$ , which are material dependent.

$$V_s = (\alpha_n - \alpha_p)(\Delta\theta) \quad (2.5)$$

Thermoelectric materials are typically  $\text{Bi}_2\text{Te}_3$  or Poly-SiGe. p- and n-type semiconductors have Seebeck coefficients of opposite sign, that provides maximum voltage. In order to maximize the output harvested voltage in a thermoelectric generator, the thermal resistance of the generator should be matched of that of the thermal source. Optimizing the extracted power requires additional elements, including heat sinks for efficient dissipation of heat into the environment, and thermal shunts that direct the heat that passes between the hot and the cold plate into the thermocouple pair.

When using thermoelectric generators, and because thermoelectric devices are heat engines, their efficiency is limited by the Carnot efficiency. The maximal efficiency is given by the Carnot efficiency expression:

$$\eta = \frac{\theta_H - \theta_C}{\theta_H} \quad (2.6)$$

where  $\theta_H$  and  $\theta_C$  are the hot and cold temperatures measured in Kelvin, respectively. One key parameter that determines the efficiency of a thermoelectric generator is called figure of merit,  $Z$ , which is defined as:

$$Z = \frac{\sigma S^2}{\kappa} \quad (2.7)$$

where  $\sigma$  is electrical conductivity,  $\kappa$  is thermal conductivity, and  $S$  is the Seebeck coefficient.

Commonly, this figure of merit if multiplied by the average temperature,  $\theta = (\theta_H + \theta_C)/2$ , giving the dimensionless figure of merit  $Z\theta$ :

$$Z\theta = \frac{\sigma S^2 \theta}{\kappa} \quad (2.8)$$

$Z\theta$  is a method for comparing the potential efficiency of devices using different materials. The maximum efficiency,  $\eta_{max}$  of a thermoelectric device for electricity generation is defined as the ratio between the energy provided to the load and the heat energy absorbed at the hot junction. This can be described as:

$$\eta_{max} = \eta \frac{\sqrt{1 + Z\theta} - 1}{\sqrt{1 + Z\theta} + \frac{\theta_c}{\theta_H}} \quad (2.9)$$

Alternatively, when taking into consideration the thermoelectric capacity of both thermoelectric materials being used on the device, the maximum efficiency can be defined as:

$$\eta_{max} = \frac{(S_p - S_n)^2 T}{[(\rho_n \kappa_n)^{1/2} + (\rho_p \kappa_p)^{1/2}]^2} \quad (2.10)$$

where  $\rho$  is electrical resistivity,  $\theta$  is average temperature between the hot and cold surfaces, and the subscripts n and p denote the properties related to the n- and p-type semiconducting thermoelectric materials, respectively. Regardless materials, the coefficients of performance of currently available commercial thermoelectric refrigerators are in the range from 0.3 to 0.6, which are only one-sixth the value of traditional vapor-compression refrigerators [34]. This is why one of the the key to the applications of thermoelectric materials is to increase their figure of merit.

Another direct method for converting thermal energy into electricity is thermionic emission. It is also known as the Edison effect. Thermionic energy converter is a heat engine that generates electricity directly using heat as its source of energy and electron as its work function. As the electrons of a heated material are imparted with thermal energy, they gain the ability to escape from the material's surface. The energy lost in this process is termed the work function. The work function is a property of the emitting surface, and is generally in the order of several electron volts in magnitude [46].

Figure 2.5 outlines the basic concept of thermionic energy conversion. As heat is added to the emitter (cathode) and the emitter temperature rises, electrons have sufficient energy to escape the solid and move freely in the vacuum (i.e., interelectrode space), a process likened to evaporation or boiling off of electrons. These electrons then move across an electrode gap to a collector (anode), and completing the circuit with a load produces electrical power. To be emitted, electrons in the emitter must be energized to be above the vacuum potential barrier of the emitter, where the difference between the vacuum potential and the Fermi energy is called the work function.

The efficiency of a thermionic emission converter ( $\eta_{TEC}$ ) can be described as its the power density ( $jV_{out}$ ) divided by the heat flux supplied to the emitter, ( $\dot{q}_e$ ):

$$\eta_{TEC} = \frac{jV_{out}}{\dot{q}_e} = \frac{j}{\dot{q}_e} \left( \frac{\phi_e - \phi_c}{e} \right) \quad (2.11)$$

where  $j$  is thermionic current density described by the Richardson-Dushman equation [46],  $\phi_e$ , and  $\phi_c$  are, respectively, work functions of the emitter and collector and  $e$  is the elementary charge.

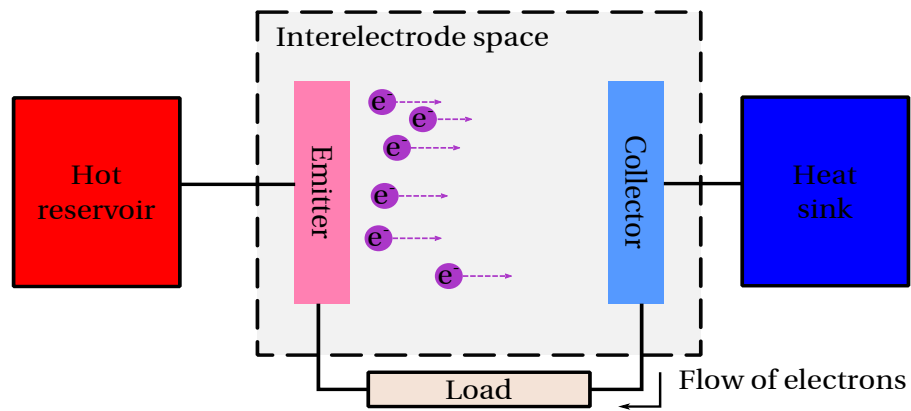


FIGURE 2.5: Schematic of a thermionic emission energy conversion.

It is trivial to see that current density increases when the emitter work function is small. However, to generate high power, large work function differences between the emitter and collector are needed, and thus the work function of the collector must be even smaller than that of the emitter, which is a significant materials challenge. Practically, the collector work function should be 0.5 eV, which is extremely small compared with the work function of most natural materials. In addition, to generate sufficient current for conventional emitter materials, the temperature of the emitter must be very high and typically much greater than 1500 K. However, this leads to greater thermal losses due to both radiation and conduction, decreasing the efficiency of the thermionic convertor.

Other method of thermal energy conversion is the the Johnson Thermo Electrochemical Converter (JTEC) developed by the Johnson Electro Mechanical Systems company [47]. In the JTEC, a pressure differential caused by heat is used to drive cations (hydrogen ions/protons) through a membrane, thus creating an electrical charge across the membrane.

The high-pressure hydrogen used in JTEC is forced through a membrane electrode assembly. It is comprised of a proton exchange membrane sandwiched between two electrodes. JTEC operates using Ericsson cycle but does not have mechanical parts. The amount of energy the device can generate is the difference in electrical energy required to compress the hydrogen at low temperature, and the electrical energy generated by the hydrogen passing through the membrane at high temperature. A schematic of this device is outlined in Figure 2.6

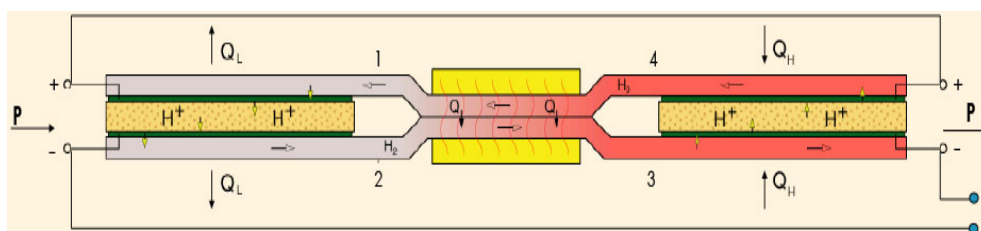


FIGURE 2.6: Schematic of Johnson Thermo Electrochemical converter [47].

JTEC generates power as hydrogen is continuously compressed at low temperature and expanded at high temperature. A portion of output power is consumed during low temperature pumping of hydrogen to high pressure as heat is rejected. High output power is generated during high temperature expansion of hydrogen to low pressure with heat input.

Lastly, we can use thermophotovoltaic systems to convert thermal energy into electricity via thermally radiating photons.

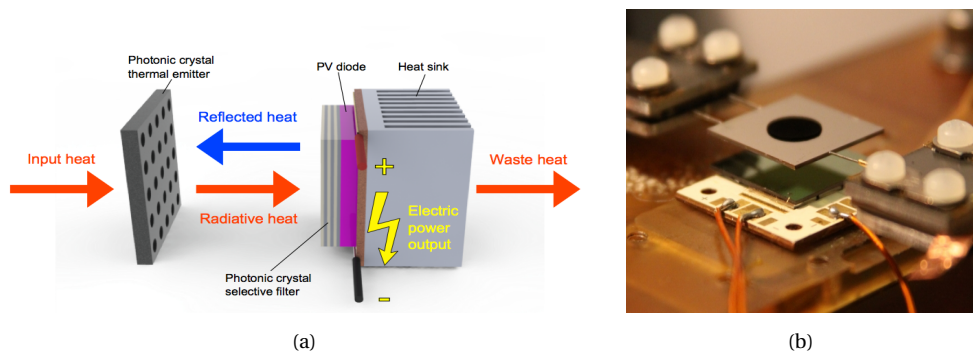


FIGURE 2.7: (a) Schematic of a thermophotovoltaic energy harvester system. (b) Photograph of a thermophotovoltaic device [48].

The schematic of a thermophotovoltaic cell is outlined in Figure 2.7(a). Figure 2.7(b) illustrates a built thermophotovoltaic energy harvester developed by the MIT. The heat source emits photons, which are absorbed by a photovoltaic cell and converted to electricity. When used with a combustible fuel, the advantages of thermo-photovoltaics include portability, the absence of moving parts, compatibility with a variety of fuels, low-noise operation, and scalability to both small and large power applications.

One limitation of the photovoltaic effect is due to the specific band gap of photovoltaic materials. The band gap determines both the minimum energy required for a photon to promote an electron into the conduction band, and the electrical energy that a single electron can expend on a load. However, the largest drawback is the very low efficiency with which these devices typically operate, which is exacerbated by the low amounts of power expected to be available at the MEMS scale. Thermophotovoltaic devices tend to lose a portion of their thermal energy to exhaust gases and insulation losses [48].

In conclusion, large thermal gradients are necessary to produce practical voltage and power level. Nevertheless, temperature differences greater than 10°C are rare in a micro-system, consequently producing low voltage and power level.

### 2.1.3.2 Temperature variations

Temperature variations can be converted into electrical energy using materials sensitive to time-varying temperature. Those materials are referred to pyroelectric materials. A subgroup of piezoelectric materials. The prefix “pyro-” is a word originating from the Greek word “pyr,” meaning “fire,” that implies a relation to fire or heat.

Electrical current generation from time-dependent temperature variations has revealed useful in sensing applications [44]. Pyroelectric converters, like piezoelectric transducers,

can be modeled as an AC current source connected in parallel with a capacitor. The pyroelectric current  $i_p(t)$  changes with the rate of change of the pyroelectric coefficient  $p$  as described by

$$i_p(t) = pA \frac{d\theta}{dt} \quad (2.12)$$

where  $A$  denotes the electrode surface area and  $\frac{d\theta}{dt}$  is the temperature change over time. It is trivial to see that the higher the electrode surface the higher is the pyroelectric current. In addition, by having rapid temperature changes over time higher pyroelectric current are obtained. These factors can sacrifice the efficiency of a pyroelectric energy harvester when size or input scenario are a limit. Indeed, one of the major drawbacks to practical devices that harvest energy using pyroelectric materials is that to generate an electric field, the device's temperature must change over time.

Few practical solutions will provide an external temperature that varies sufficiently to generate sufficiently to generate a significant voltage from a pyroelectric device. Therefore, to overcome this problematic, a temperature gradient is converted to a temperature variable through the use of a working fluid pumping between hot and cold reservoirs [49].

When considering pyroelectric generators, firstly, they do not require the high source temperatures that a traditional thermoelectric power generator needs. Secondly, the combination of relatively low operation temperatures provide the potential for a power generating system with good reliability. Great progress has been made in creating artificial pyroelectric materials which are lead-free, for example polymers or ceramics with perovskite type structure, compared with thermoelectric materials, pyroelectric materials show be more environmentally friendly.

Although wasted heat more likely creates spatial gradients rather than time variations, the conversion efficiency, which is defined as the ratio of net harvested energy to the heat taken from the hot reservoir, is much higher when using pyroelectric energy harvesting. In theory, it could reach the conversion ratio of the Carnot cycle, regardless of the materials properties [50].

In [Chapter 2](#), a detailed list of recent works on pyroelectric and thermoelectric generators is presented.

## 2.2 Energy transduction techniques

To convert an ambient energy source that we aforementioned, it is used an energy transduction technique. It depends on the source energy availability. As we are interested in converting thermal energy in the form of temperature variations, also we focus on mechanical energy in the form of vibration and strain, we will describe most classical transduction techniques for those energy sources.

### 2.2.1 Electromagnetic transduction

Electromagnetic vibration energy harvesters convert mechanical vibrations into electrical energy using electromagnetic transduction. Their basic design consists of a magnetic core and a coil, one of which is coupled to the mechanical resonator and the other remains static. The principle is the Faraday's induction law, when the resonator vibrates, the relative movement of the magnet to the coil induces an AC voltage on the coil.

Electromagnetic transduction represents an effective way of harnessing mechanical vibrations. Figure 2.8 shows a schematic of electromagnetic transduction.

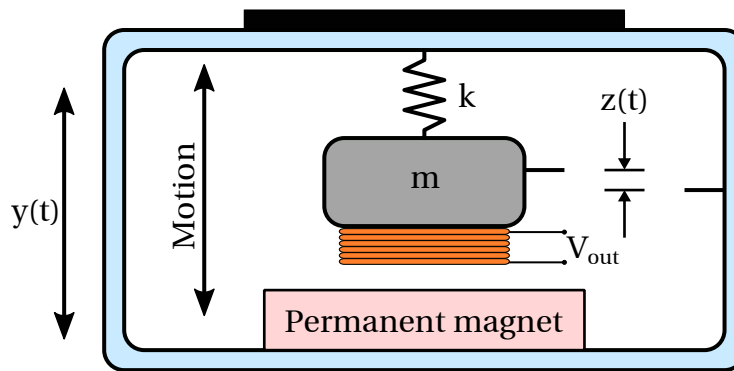


FIGURE 2.8: Schematic of electromagnetic transduction for mechanical vibrations.

The advantages of this kind of energy transduction is that it does not require external voltage source, it has high robustness as well. However, it has difficulties to implementing in micro-scales and its low output voltage can be a problematic.

The magnitude of the induced voltage,  $v_{out}$  can be defined by the equation

$$v_{out}(t) = -N \frac{d\Phi_B}{dt} \quad (2.13)$$

where  $N$  is the number of turns in the coil,  $\frac{d\Phi_B}{dt}$  is the time rate of change of the magnetic flux,  $\Phi_B$  is the product of the magnetic field  $B$  (assuming that  $B$  is uniform or constant) and the area of the coil. Considering,  $R$  as the combined resistance of the coil and the load, the magnitude of the current is defined by Ohm's law:

$$i(t) = \frac{v_{out}}{R} \quad (2.14)$$

The Len's law states that the direction of current induced in a conductor by a changing magnetic field due to induction is such that it creates a magnetic field that opposes the

change that produced it. It establishes a magnetic flux, which opposes the change in flux linkage that gives rise to the induced voltage.

At the MEMS scale, various limitations are imposed due to processes commonly used for MEMS coil manufacturing, for instance electrodeposition. Sometimes, the manufacturing process can limit the number of coils that can be included in a space, due to a minimum thickness and spacing that can be fabricated [51], or even increase the resistance of the coil [52]. Another challenge in producing an electromagnetic generator at the MEMS scale is the batch manufacturing of a strong permanent magnet to produce the magnetic flux required for an efficient generator. Furthermore, the operation of electromagnetic transducers is limited by temperature. Hence, when used as a mechanical-to-electrical conversion technique in heat engines, electromagnetic transducers have to be designed to generate energy over the expected temperature range the heat engine will endure. These material lose their magnetization above the Curie temperature.

Nevertheless, if care is taken in the design, efficiency can remain relatively high; for example, Beeby *et al.*, [53] claim 30% conversion efficiency was achievable from their micro-electromagnetic vibration generator.

In summary, electromagnetic generators have two main challenges: low voltage generation, and the limiting maximum operating temperatures of present magnet technologies. They have the advantages of potentially high efficiency and low cost of production.

### 2.2.2 Electrostatic generators

Other kind of energy transducers for mechanical vibrations is based on electrostatic effect. These devices can convert mechanical energy into electrical energy by using the input mechanical energy to change capacitance of the generator between a high and low value. The capacitance is most commonly reduced by increasing the distance (i.e., gap) between the capacitor plates, or by reducing the overlapping area of the plates. Electrostatic transducers operate in one of two modes. The first is constrained charge mode, in which the charge and electric field remain constant on the capacitor plates, causing an increase in voltage as the capacitance reduces. The second is constrained voltage mode, which causes charge to move from the capacitor to a storage device as the capacitance decreases. [Figure 2.9](#) shows the schematic of an electrostatic transduction system.

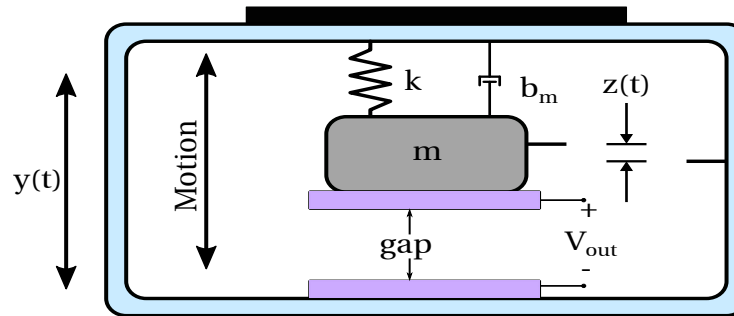


FIGURE 2.9: Schematic of an electrostatic transduction energy harvesting.

The major disadvantage of electrostatic converters is that they require a separate voltage source to initiate the conversion process because the capacitor must be charged up to an initial voltage for the conversion process to start. In addition, for many design configurations mechanical limit stops must be included to ensure that the capacitor electrodes do not come into contact and short the circuit. However, a primary advantage of electrostatic energy transduction is their potential for integration with microelectronics and micro-systems.

Energy can be extracted via charge-constrained or voltage-constrained approaches. In an electrostatic harvester, charge and voltage are related through capacitance ( $Q = CV$ ); therefore, a change in capacitance produces variations in either voltage (i.e., charge constraint) or current (i.e., voltage constraint). The harvested energy can be quantified using the equation below:

$$E = \frac{1}{2} Q^2 \left( \frac{1}{C_{min}} - \frac{1}{C_{max}} \right) \quad (2.15)$$

where  $Q$  is the charge and  $C_{min}$  and  $C_{max}$  correspond to the minimum and maximum capacitances achieved. Unlike the electromagnetic transducers, electrostatic ones can be driven with appropriate voltages for microelectronics, on the order of two to ten volts.

### 2.2.3 Piezoelectric transducers

The word “piezoelectricity” is derived from the Greek “piezein”, which means to “squeeze”. Piezoelectric transduction is one of the most popular strategies to harvest ambient mechanical energy. It is based on the well known material property called piezoelectricity. Some materials presenting this property are lead zirconate titanate (PZT) and zinc oxide (ZnO). These materials have been used to fabricate microelectromechanical systems MEMS based and also macro scale piezoelectric energy harvesting devices [54].

The direct piezoelectric effect links a mechanical action (mechanical stress or strain) with an electrical response (electric field, electric displacement or polarisation). This effect was first studied by brothers P. Curie and J. Curie in experimental work (1880) on the behavior of quartz single crystals subjected to an external mechanical stress [55].

Piezoelectric energy harvesting is based on the direct piezoelectric effect at which electrical charge (or polarisation of a piezoelectric element) is generated from an external mechanical stress, strain, acoustic wave, vibration sources and so on. Piezoelectric materials are anisotropic: their properties varying according to the direction of force, and the orientation of the polarization. Piezoelectric materials have been used for many years to convert mechanical energy into electrical energy. Piezoelectrics contain dipoles, which cause the material to become electrically polarized when subjected to mechanical force. The degree of polarization is proportional to the applied strain. Conversely, an applied electric field causes the dipoles to rotate, which results in the material deforming. Piezoelectric materials are therefore used in a variety of commercial sensors and actuators and are also a candidate for kinetic energy-harvesting applications.

In a majority of scenarios, piezoelectric harvesters operate in the lateral 31 mode. This is because the piezoelectric element is often bonded to the surface of a mechanical spring element that converts vertical displacements into a lateral strain across the piezoelectric element. Some designs can operate in the compressive 33 mode and these have the advantage of exploiting the 33 constants, which are typically greater than the 31 equivalents. Among the operational modes that can be employed employed for piezoelectric harvesters, mode 31 is more suitable for piezoelectric cantilever beams with a proof mass at the free end as shown in Figure 2.10.

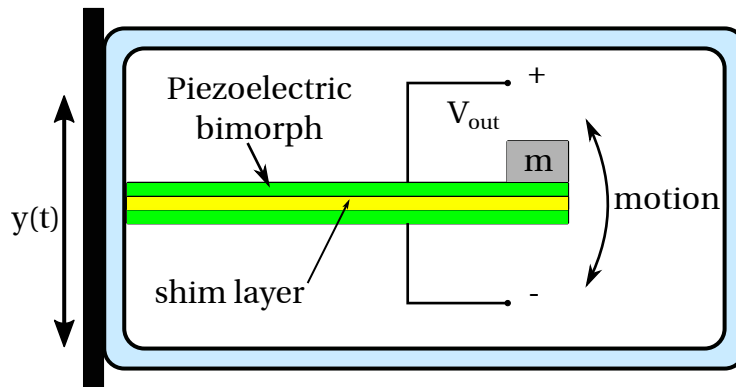


FIGURE 2.10: Schematic of a piezoelectric transducer system.

A very common architecture of transducer used in piezoelectric devices is the bimorph cantilever beam, which consists in two piezoelectric layers bound together, with a shim layer between them. The inertial frame transmits the vibrations to a suspended inertial

mass to produce a relative displacement between them. Systems like this usually have resonant frequencies, which can be designed to match the characteristic frequency of the environmental motions. In our research group, previous work have been performed implementing piezoelectric energy harvesters [56–58].

Using Equation 2.2 the dissipated power of a piezoelectric transducer can be obtained. And the piezoelectric damping coefficient can be estimated by using the following expression:

$$b_e = \frac{2m\omega_n^2 K^2}{2\sqrt{\omega_n^2 + \left(\frac{1}{(R_{load} C_{piezo})^2}\right)}} \quad (2.16)$$

where  $K$  is the piezoelectric coupling factor of the materials,  $R_{load}$  and  $C_{piezo}$  are load resistance and capacitance. Hence, there is an optimal load resistance value at maximum power given by

$$R_{opt} = \frac{1}{\omega_n C} \frac{2m\omega_n^2 K^2}{\sqrt{4\zeta_p^2 + K^4}} \quad (2.17)$$

where  $\zeta_p$  is the constant damping ratio of the piezoelectric material.

The constitutive equations describing the mechanical and electrical behaviors of piezoelectric transducers are:

$$S_{ij} = s_{ijkl}^E T_{kl} + d_{kij} E_k \quad (2.18)$$

$$D_i = d_{ikl}^E T_{kl} + \epsilon_{ik}^T E_k \quad (2.19)$$

The subscripts  $i$ ,  $j$ ,  $k$ , and  $l$  can be values of 1, 2, and 3.  $S$  and  $T$  are strain and stress tensors, respectively. The stresses represented by  $T$  with a unit of  $\text{N m}^{-2}$  are induced by the mechanical and electrical effects.  $D$  and  $E$  are the electric displacement and electric field vectors, with a unit of  $\text{C m}^{-2}$  and  $\text{V m}^{-1}$ , respectively.  $s^E$  is the elastic compliance matrix evaluated at a constant electric field with a unit of  $\text{m}^2 \text{N}^{-1}$ ,  $d$  is a matrix of piezoelectric strain coefficients with a unit of  $\text{m V}^{-1}$  and  $\epsilon^\sigma$  is a matrix of permittivity values that are evaluated at a constant stress with a unit of  $\text{N V}^{-2}$ .

Another important parameter for piezoelectric materials is the effective electromechanical coupling factor,  $K_{eff}$  given by

$$K_{eff} = \sqrt{1 - \left(\frac{f_r}{f_a}\right)^2} \quad (2.20)$$

whereby  $f_r$  and  $f_a$  are the resonance frequency and antiresonance frequency of the piezoelectric cantilever beam in Hertz, respectively.

The amount of energy stored in a piezoelectric device,  $E_c$  is given by

$$E_c = \frac{1}{2} C V^2 \quad (2.21)$$

where  $C$  depicts the capacitance of piezoelectric element and  $V$  is the voltage produced.

#### 2.2.4 Discussion

Great efforts have been done in vibration-to-electricity transduction techniques. Nowadays, depending on the application either of the three aforementioned transducers can be highly appropriate to use in energy harvesters. While electromagnetic converters may be useful for larger systems, or systems exhibiting vibrations of far greater acceleration magnitude than those under consideration, they are not as suitable in the context under consideration. In contrast, piezoelectric transducers exhibit all of the advantages of electromagnetic converters. Additionally, they provide useful voltages and exhibit higher practical energy densities.

Roundy *et al.*, [8] derived the expression describing the maximum energy densities of these three energy transduction techniques. First consider piezoelectric transducers. If an open circuit load situation is assumed, the constitutive relationship given in equation 2.18 reduces to the expression in equation 2.22

$$dT = -\epsilon E \quad (2.22)$$

The energy density of a dielectric material may be expressed as  $\frac{\epsilon E^2}{2}$ . Multiplying each side of equation 2.22 by  $\frac{E}{2}$  or its equivalent  $\frac{dT}{2\epsilon}$  yields the following expression

$$\epsilon E^2 = \frac{T^2 d^2}{\epsilon} \quad (2.23)$$

Equation 2.23 gives energy density both in terms of the electrical state of the material ( $E$ ) and the mechanical state of the material ( $T$ ). If the yield strength of the material ( $T_y$ ) is substituted for  $T$ , then the maximum possible energy density is given by

$$E_{max} = \frac{T_y^2 d^2}{2\epsilon} \quad (2.24)$$

The piezoelectric coupling coefficient ( $K$ ) is related to the strain coefficient ( $d$ ) by the equation 2.25. If  $K$  is used rather than  $d$ , the expression for maximum energy density is as shown in equation 2.26

$$d = K \sqrt{\frac{\epsilon}{Y}} \quad (2.25)$$

$$E_{max} = \frac{T_y^2 K^2}{2Y} \quad (2.26)$$

This may be a more intuitive form because the coupling coefficient is often used as a measure of the quality of a piezoelectric material. Substituting in physical data for a common piezoelectric material (PZT-5H), yields a result of  $35.4\text{mJ cm}^{-3}$ . As a practical number, assuming the properties of PZT-5H and a factor of safety of 2, the maximum energy density would be  $17.7\text{mJ cm}^{-3}$ .

The energy density of a capacitive device is  $\frac{\epsilon E^2}{2}$ . In the case of an electrostatic variable capacitor, the dielectric constant used is that of free space ( $\epsilon_0$ ). If  $100\text{ MV m}^{-1}$  is used as a maximum electric field, the resulting energy density is  $44\text{mJ cm}^{-3}$ , or a little more than PZT-5H. However, if a more realistic 30 volts over a  $1\mu\text{m}$  gap were assumed (or  $30\text{MV m}^{-1}$ ), the resulting energy density would be  $4\text{mJ cm}^{-3}$ .

The maximum energy density of an electromagnetic sensor is  $\frac{B^2}{2\mu_0}$  where B is the magnetic field, and  $\mu_0$  is the magnetic permeability. By using 0.1 Tesla as a maximum value for magnetic field, the resulting energy density is  $4\text{mJ cm}^{-3}$ . If an extremely high value of 1 Tesla were used as a maximum magnetic field, the resulting energy density would be  $400\text{mJ cm}^{-3}$ . Table 2.1 summarizes the maximum energy density for all three types of converters.

TABLE 2.1: Summary of maximum energy density [8].

Type	Equation	Practical Max.	Theoretical Max.
Piezoelectric	$u = \frac{\sigma_y^2 K^2}{2Y}$	$17.7\text{mJ cm}^{-3}$	$335\text{mJ cm}^{-3}$
Electromagnetic	$u = \frac{B^2}{2\mu_0}$	$4\text{mJ cm}^{-3}$	$400\text{mJ cm}^{-3}$
Electrostatic	$u = \frac{1}{2}\epsilon E^2$	$4\text{mJ cm}^{-3}$	$44\text{mJ cm}^{-3}$

The coupling coefficients of piezoelectric generators depends mainly on the piezoelectric materials used. The coupling coefficient of electromagnetic converters is dependent upon the magnetic circuit of the device. In the case of electrostatic generators, the coupling coefficient varies with position and device design.

Electrostatic and piezoelectric transduction are compatible with MEMS, they are convenient for micro- and nano-scale systems, while electromagnetic transducers are more suitable for macro-scale generators.

Since piezoelectric transducers have the same advantage over electromagnetic converters and as they exhibit higher output voltages we opted for using this transduction technique for converting the mechanical energy into electricity once thermal energy has been converted into mechanical vibrations as described in Chapter 3.

## 2.3 Thermal energy harvesting review

Several methods are currently used to harvest thermal energy. In this section, some of both direct conversion of thermal energy into electricity and indirect conversion, namely, thermal-to-mechanical-to-electrical energy conversion, are detailed.

### 2.3.1 Direct conversion of thermal to electrical energy

Most classical energy conversions for thermal energy are thermoelectric generators and pyroelectric converters. Both of them are direct methods of thermal to electricity conversion. However, the ambient energy source is not necessarily in the same form. While for thermoelectric generators thermal energy in the form of thermal gradients are required, for pyroelectric generators temperature fluctuations are the source energy of interest.

#### 2.3.1.1 Thermo-electric generators

Thermoelectric generators are devices governed by the Seebeck effect. This effect is the conversion of temperature differences directly into electricity. The physicist Thomas Johann Seebeck discovered this phenomena in 1821. This principle of transduction can be used in a thermocouple to measure a temperature difference.

Several works have recently employed this technology to develop thermoelectric generators. For instance Yang *et al.* [43] used a commercial CMOS process to built an array of 33 thermocouples in series. Each thermocouple consisted of p-type and n-type polysilicon strips. The output power of the generator depended on the temperature difference between the hot and cold parts in the thermocouples. The hot part of the generator located on a suspended plate for reducing the heat-sinking. The experimental results showed that the output power of the thermoelectric generator was about  $9.4\mu\text{W}$  as the temperature difference of 15K.

Later, Wahbah *et al.* [59] presented measured data of thermal and vibration energy harvested from human body using off-the-shelf thermoelectric generators and piezoelectric harvester, respectively. The measured data showed that the maximum peak voltage of the piezoelectric harvester is 7.68V at  $3.12\text{ms}^{-1}$ . At the same speed, the maximum generated current with  $1\mu\text{F}$  output capacitor is  $1\mu\text{A}$ . They also claim a power density of  $2.2\mu\text{W cm}^{-2}$  and  $7.4\mu\text{W cm}^{-3}$  for thermoelectric generator and piezoelectric energy harvester, respectively. This is an example of works coupling thermo-electric generators and piezoelectric converters but not in the same device.

A fully solution for powering wireless sensor using thermoelectric generators was recently presented by Prijic *et al.* [27]. In this work, a self-powered telemetric wireless sensor node for temperature measurement was presented. They managed to design an autonomous sensor node powered by thermoelectric conversion. Figure 2.11(a) shows the block diagram of the entire system. The Seebeck voltage provided by the thermoelectric generator is boosted by a step-up converter and power management circuitry to charge primary and backup capacitors. It is a full solution of energy harvester for autonomous sensor nodes. In this case, a temperature sensor measures the temperature of the same heat source which powers up the thermoelectric generator. Measured data are periodically acquired by the micro controller and transmitted wirelessly by the RF module. The backup capacitor is used to supply the system when the heat source is not capable of generating Seebeck voltage necessary for functioning of the step-up circuitry. Figure 2.11(b) illustrates the schematic diagram of the electric circuitry of the generator.

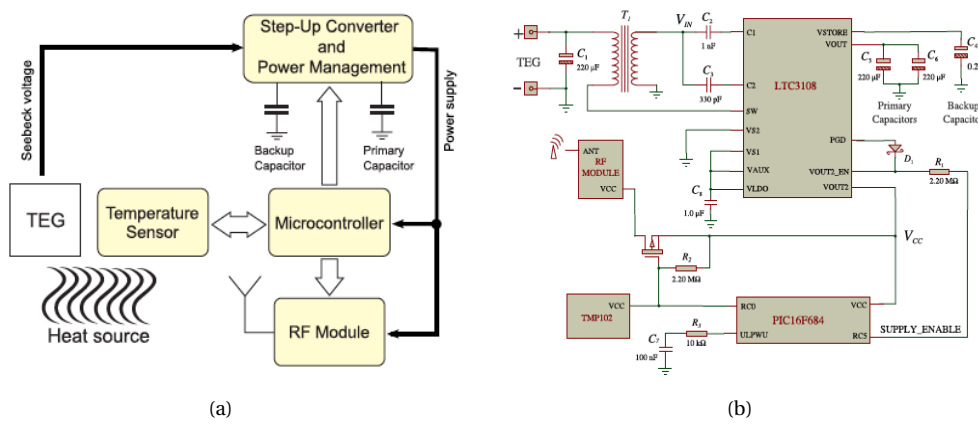


FIGURE 2.11: (a) Block diagram of the self-powered temperature sensor. (b) Schematic diagram of the autonomous sensor node powered by thermoelectric generator. Both figures taken from [27]

The thermoelectric generators can be electrically described as a voltage source in series with an internal resistance [60], as shown in Figure 2.12. The values of both the voltage produced and the internal resistance vary with temperature.

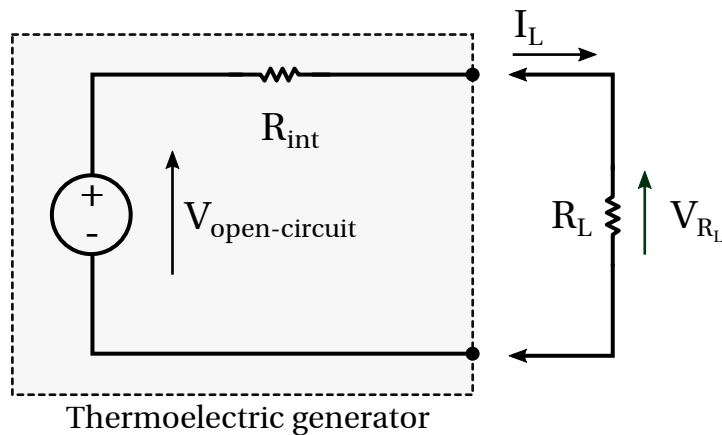


FIGURE 2.12: Electrical model of a thermoelectric generator.

An equivalent circuit is a convenient tool for electronic engineers. It helps to present the problem in electronic circuit terms, helps to understand its functionality, and facilitates the solving of cooling or power generation problems without the need for expertise in thermal engineering.

### 2.3.1.2 Pyro-electric generators

We can define pyroelectricity as resulting from a permanent electric dipole in the primitive unit cell of a crystal in thermal equilibrium. There are two subgroups of pyroelectrics: linear

pyroelectrics for which the spontaneous polarisation cannot be reversed by application of an electric field (i.e., ZnO, CdS, CdSe, tourmaline, lithium sulphate, etc...) and ferroelectrics (i.e., BaTiOs, LiTaO3, triglycine sulphate, etc...) for which it can be reversed [61].

A temperature change in time produces a correspondent variation in the induced charge. The pyroelectric modules are usually described as current sources. A general lumped-element in one dimension model of a pyroelectric transducer is shown in Figure 2.13(a) and Figure 2.13(b) shows a photograph of a pyroelectric cell.

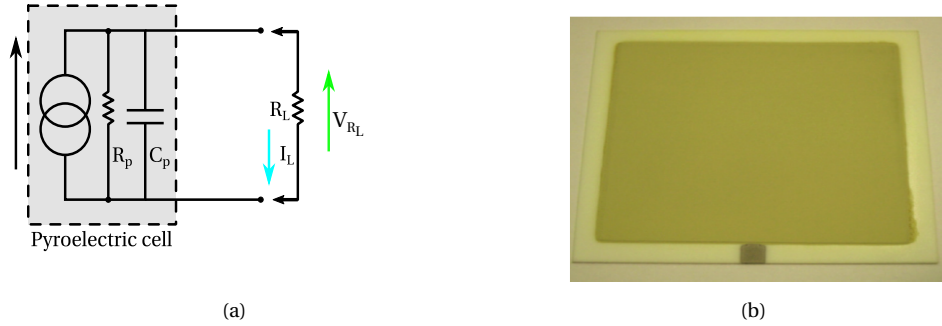


FIGURE 2.13: (a) Schematic model of electric energy harvesting process using pyroelectric cells directly driving a load resistance  $R_L$ . (b) Photograph of a pyroelectric cell [44].

In this kind of energy harvesters, the generated charge is found integrating equation 2.12 over time [44]:

$$Q = \int_{t_i}^{t_f} i_p dt = \int_{t_i}^{t_f} pA \frac{d\theta}{dt} dt = \int_{\theta_i}^{\theta_f} pA \frac{d\theta}{dt} = pA(\theta_f - \theta_i) \quad (2.27)$$

where  $\theta_i$  and  $\theta_f$  are, respectively, the temperatures at the considered final and initial times. From this expression is trivial to see that the generated charge does not depend on temperature change rate but in temperature difference. Moreover, increasing the surface of the sample,  $A$ , will produce an increase in the current at parity of incident thermal power density per unit area.

According to the voltage method [34], a general time-dependent pyroelectric voltage,  $V_{sp}$  can be expressed in terms of the time constant  $RC$ :

$$V_{sp}(t) = \frac{pA\Delta\theta}{C} \exp\left(-\frac{t}{RC}\right) \quad (2.28)$$

where  $C = C_p$  and  $R = \frac{R_p R_L}{R_p + R_L}$ .

Cuadras *et al.* [44] built pyroelectric cells based on fabricated screen-printed PZT films and commercial PVDF films as power sources in order to supply low-power autonomous sensors. Working with temperature fluctuations in the range of 300K to 360K within a time period of 100s, an output power density of  $1.56 \times 10^{-2} \mu\text{W cm}^{-2}$  is claimed. This generator exhibit a stored energy that can be as high as 0.5mJ. The generated current increases with

increasing thickness of the pyroelectric layer and poling electrical field during the fabrication process.

Numerous materials have been developed for pyroelectric energy harvesters. And ferroelectric materials have been found to show the highest pyroelectric figures of merit, for instance triglycine sulfate (TGS), polyvinylidene fluoride (PVDF), strontium barium niobate (SBN), perovskite structure, lead germanate. And pyroelectric nanogenerators using PZT thin films.

Siao *et al.* [62] have worked on PZT materials for pyroelectric generators as well. They presented simulated calculations and experiments to determine the relationships between the geometry of pyroelectric cells and the optimal period of temperature oscillations driving the optimal load resistance to improve the efficiency of pyroelectric harvesters. When designing pyroelectric harvesters using PZT materials, special attention must be paid on the geometrical parameters of the pyroelectric cells. The induced charge increases when the thickness of the pyroelectric cells decreases. Therefore, the designers of pyroelectric harvesters need to consider the coupling effect between the geometry of the pyroelectric cells and the optimal period of temperature fluctuations to drive the optimal load resistance.

Recently, Zabek *et al.* [50] have demonstrated that coupling pyroelectric elements with pulsating heat pipes is possible to harvest slow temperature fluctuations at low temperatures. They are the first to demonstrate that it is possible to exploit the rapid temperature oscillations of a heat pipe. and using a pyroelectric generator to charge a storage capacitor and to generate electrical energy while providing cooling. A continuously generated energy at  $95\text{pJ cm}^{-3}$  at  $0.45\text{Hz}$

In this section, the discussion centered on traditional direct methods of thermal energy conversion. The following section will discuss indirect conversion techniques of thermal energy into electricity.

### 2.3.2 Indirect conversion of thermal to electrical energy

When dealing with thermal energy conversion, most popular solutions for converting either temperature fluctuations (i.e., using pyroelectric converters) or thermal gradients (i.e., through thermoelectric generators) directly into electricity are highly dependent on the temperature rate of change ( $\frac{d\theta}{dt}$ ) or with large thermal gradients ( $\Delta\theta$ ) in order to have large output power. This is why, different conversion methods have been the focus of several works. Some of these indirect conversion methods of thermal energy into electricity are presented below.

#### 2.3.2.1 Thermo-acoustic generators

A thermoacoustic heat engine is an external heat engine that generates mechanical energy in the form of an oscillating acoustic wave within the engine's working fluid. They can operate in reverse to convert mechanical energy into a thermal difference for cryogenic coolers. The thermoacoustic engine involves the same cycles that occur in a standard heat engine,

such as compression, heating, expansion, and cooling. For the sake of classification, they can be divided into two categories: traveling wave devices that are governed by the Stirling cycle, and standing wave devices, which can be described by the Brayton cycle. Mechanical to electrical energy can be extracted from the acoustic energy using a diaphragm made of piezoelectric material at one end of the thermoacoustic tube.

Thermoacoustic standing wave heat engines follow the Stirling cycle. It has the following components; a compressor, heat exchanger, expander and regenerator. Using a tube and acoustic pressure, a thermal gradient is set up in the wall along the length of the heat engine. This is required for the thermoacoustic effect occurs. The cycle promotes the formation of the temperature gradient. When gas pressure increases towards the hot side, the following occurs. First, gas is compressed and an increase in temperature (i.e., compression), since the local temperature of the wall is higher than the gas. Heat then flows from the wall into the gas, forcing it to expand (i.e., heat addition). The high pressure gas expands, occupying a higher volume at a lower temperature. Due to the long thin design of the regenerator stack the volume of gas expands to the cold side, and as a result, reduces in temperature (i.e., expansion). The gas then cools down, due to the local temperature of the wall, which forces the gas to contract and reduce in pressure, completing the cycle (i.e., heat rejection). This process results in a node at the end of the thermal acoustic tube. Since this cycle sets up a standing wave in the tube, the acoustic wavelength is defined by the dimensions of the tube. Because the thermal gradient runs the length of the tube, conduction of heat into the outside environment causes an efficiency loss.

Figures 2.14(a) and 2.14(b) show, respectively, the schematic and photograph of a thermoacoustic standing wave heat engine coupled with piezoelectric transduction.

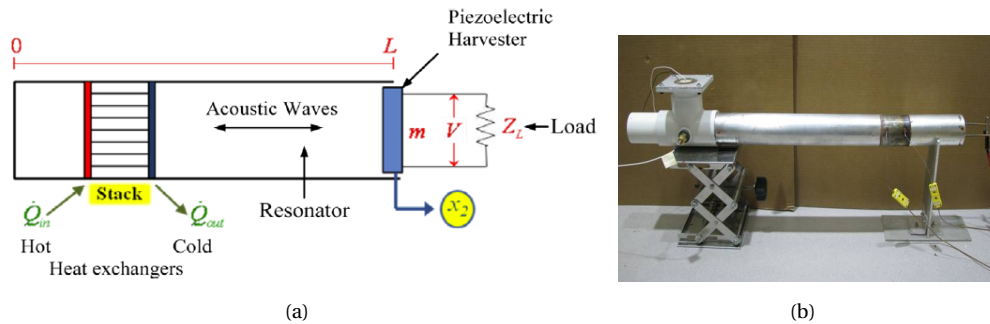


FIGURE 2.14: (a) Schematic of standing-wave thermoacoustic engine integrated with a piezoelectric element [63]. (b) Photograph of a thermoacoustic energy harvester [64].

Currently, conventional thermoacoustic engines have been integrated with piezoelectric membranes to harness the acoustic energy associated with this class of engines. Hernandez *et al*, [64] presented a mesoscale prototype of a thermoacoustic engine. In their work, tests were conducted in a simple setup consisting of a pipe with a pair of baffles and a piezoelement. Generated sound energy was partially converted into electrical energy by a piezoelement. About 0.55mW of electric power was produced on a resistive electric load at acoustic pressure amplitudes in the pipe about 170Pa and mean flow velocity  $2.6\text{m s}^{-1}$ .

### 2.3.2.2 Electrical generators based on shape memory alloys

Other indirect conversion of thermal energy into electricity is the well known shape memory alloy heat engines. Shape memory alloys (SMAs) are materials that recover their original shape after undergoing deformation by heating or cooling. This property was first observed in gold-cadmium and in copper-zinc alloys in the 1930s. The shape memory effect (SME) that these alloys undergo is achieved through a process called martensitic phase transformation. The alloys can be “trained” to remember a configuration through forming and constraining the SMA in a desired shape and annealing at a prescribed temperature. This rearranges the dislocations present in the SMA, and allows the material to take on a new shape without internal stresses.

Gueltig *et al.* [65] developed a generator using magnetic shape memory alloys. By using the thermally induced change of magnetization as well as the actuation capability of magnetic shape memory alloys, an energy harvester reaching average power densities of  $0.5\text{mW cm}^{-3}$  for a temperature change of 10K is presented. The device comprises the following basic components: magnetic shape memory alloy film, thermal interface to an external heat source, actuation or reset mechanism and power conversion unit. In this device, thermal interface is designed to adapt to the shape of the cantilever after out-of-plane deformation. A miniature permanent magnet is used to induce sufficient magnetization and to generate an actuation force.

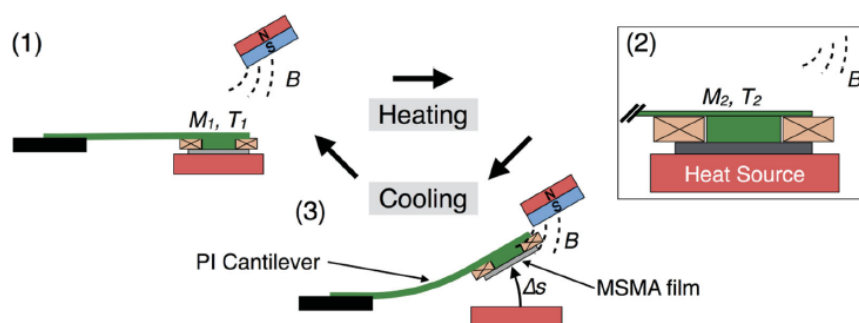


FIGURE 2.15: Concept of thermal energy harvesting using Shape Memory Alloy (SMA) film actuation [65]. (1) While in thermal contact to the heat source, the SMA film heats from temperature  $T_1$  to  $T_2$ , while corresponding magnetization  $M_1$  changes to  $M_2$ . (2) The change of magnetization causes a magnetic attraction force towards the external magnet. The magnetization change induces a current in the pick-up coil placed above the film. (3) The SMA film is cooled below the martensitic transformation temperature by heat conduction and convection. The magnetic attraction force vanishes and the elastic force of the polyimide (PI) cantilever restores the initial position.

Avirovik *et al.* [66] built a heat engine using SMA to first convert environmental heat into mechanical energy and then into electrical energy using a microturbine. Experimental results showed that 0.12g of SMA wire produced 2.6mW of mechanical power which was then used to drive a miniature electromagnetic generator that produced 1.7mW of electrical power. The generated electrical power was used to power a wireless sensor node. Figure 2.16 shows the schematic description of the generator.

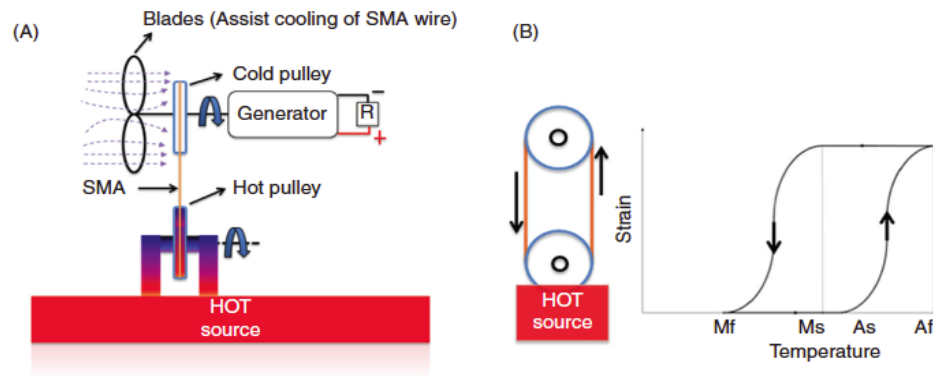


FIGURE 2.16: Schematic of the SMA based thermal energy harvesting [66], (a) illustrative diagram of the microturbine driven by a SMA wire, (b) representation of change of phase martensite to austenite.

### 2.3.2.3 Thermal buckling generators

Thermal buckling is another conversion technique to convert thermal energy into mechanical energy, which can then be converted into electricity by means of a simple piezoelectric transduction for instance.

Puscasu *et al.* [20] presented a set of energy harvesters based on this principle. A thermal bimetal is a double layer consisting of a material of high coefficient of thermal expansion, and the other one with a lower coefficient of thermal expansion. Resulting in a concave shape of the composite material in order to make it snap under the effect of rising or decreasing its temperature. This technique converts thermal gradients into mechanical energy and by attaching a piezoelectric layer to one of the materials, electrical power can be extracted. An electrical power of  $12\mu\text{W}$  has been reported on a hot plate at  $130^\circ\text{C}$ . Figures 2.17(a) and 2.17(b) outline, respectively, the schematic of a bimetal based thermal energy harvester and the photograph of a prototype.

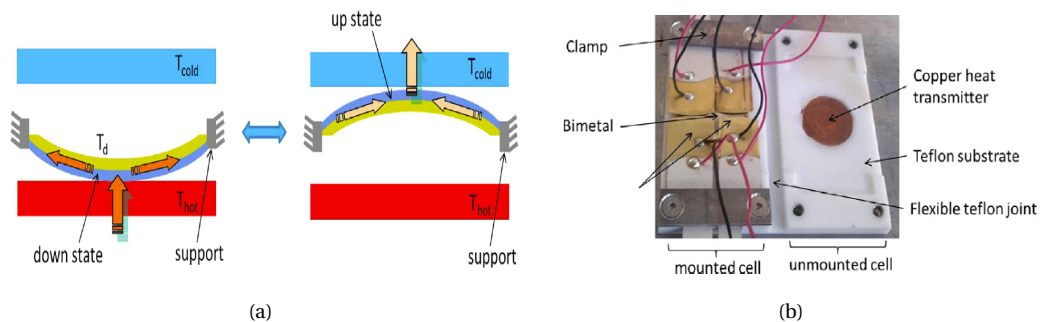


FIGURE 2.17: (a) Schematic of the bimetal based thermal energy harvester showing its two stable positions in a thermal gradient set up. (b) Photograph of the prototype of the array of thermal energy harvester based on thermal buckling energy conversion [20].

At MEMS scale, within our research group, Trioux *et al.* [67] have developed a thermal energy harvester. It implies double step transduction through thermal buckling of a bilayer

aluminium nitride and aluminium bridge for converting thermal energy into mechanical energy. Using piezoelectric transduction, electrical energy is then extracted. Advances in the geometry of the bilayer have been conducted in order to improve the output power of the generator. Implementing a butterfly shaped thermal buckling energy harvester an output energy density up to  $2450\text{pJ mm}^{-3}$  was reported. The buckling temperatures of the generator are  $63^\circ\text{C}$  and  $53^\circ\text{C}$  for the snap up and snap down transitions, respectively.

Despite the fact that the level of harvested energy is too low to be usable to power another device, one solution would be to put in parallel several devices with exactly the same buckling temperature, in order to add the energy produced by each harvester. A lot of effort has to be made in packaging to be able to maintain the thermal gradient on both sides of the plate.

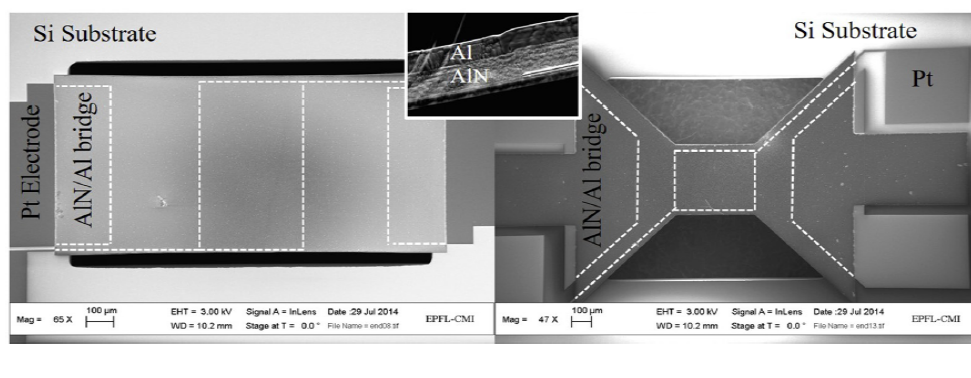


FIGURE 2.18: SEM images of thermal buckling MEMS energy harvester [67].

#### 2.3.2.4 Thermo-magnetic generators

Thermo-magnetic energy harvesting is another alternative to thermal energy conversion. This generation method of electricity relies on a change in magnetic properties that occurs with changing temperature for certain materials. If a material exhibiting thermally dependent magnetization is subject to a constant external magnetic field and cycled in temperature, its magnetization also cycles. This can interact with the external field to produce periodically cycling magnetic forces, as well as inducing its own periodically cycling magnetic field, both of which can be converted by simple means into usable electric power.

Ujihara *et al.* [68] reported a thermal energy harvesting device using ferromagnetic materials (see Figure 2.19). In this energy harvester, a thermomechanical actuator converts thermal energy into mechanical energy. The principle of the generator relies on a thermally induced second order phase transition producing mechanical energy. Although the device was not provided with a transducer to convert mechanical energy into electricity, experimental results shown a mechanical power density of  $3.6\text{mW cm}^{-2}$  with a temperature difference of  $\Delta\theta = 50\text{K}$ .

In the past, within our research group, Carlioz *et al.* [69] proposed a different approach for converting temperature fluctuations into electricity. A technique based on hybridization of a set of permanent magnets-soft magnetic materials and piezoelectric transduction. This system consists of a soft magnetic material, namely iron-nickel alloy, in contact with a

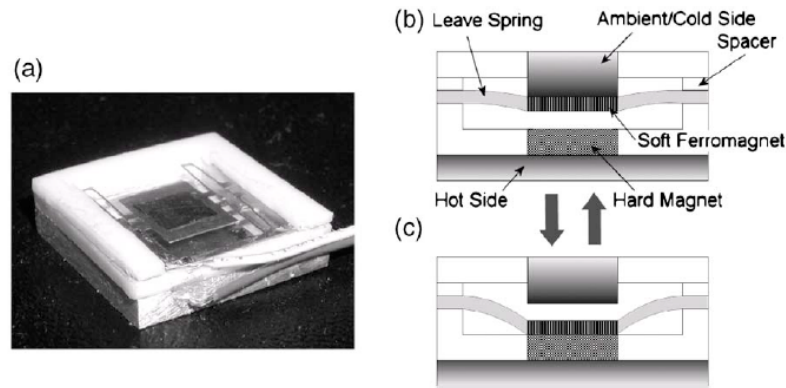


FIGURE 2.19: Heat engine device representation [68] (a) photograph of the heat engine, (b) cross section view when cooling stage, (c) cross section view when heating stage.

hot point and fixed at a gap distance below a permanent magnet, namely NdFeB, which is attached on a piezoelectric buzzer. The system actuates as a sort of thermal switch. When the temperature of the soft magnetic material is under its Curie temperature  $\theta_C$ , it has ferromagnetic properties. Therefore, it exhibits an attraction force between the movable magnets. Conversely, at temperatures above the Curie temperature, the soft magnetic material becomes paramagnetic. Hence, the permanent magnet is released. The piezoelectric material converts these mechanical movements into electricity. Figures 2.20(a) and 2.20(b) illustrate the schematic of this thermomagnetic generator and its low-cost prototype, respectively. This cycle is repeated as long as temperature fluctuates around the Curie temperature of the soft magnetic alloy. A study on tuning the temperature of operations was developed and demonstrated they can be tuned by modifying the gap distance on the triggering system. A maximum instantaneous power of  $324\mu\text{W}$  at the opening commutation of the generator was reported.

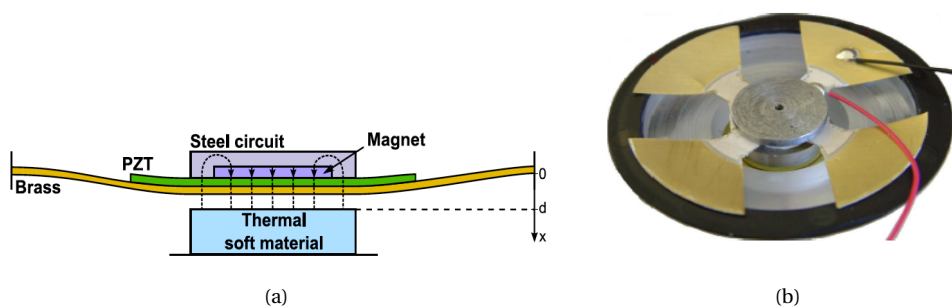


FIGURE 2.20: Representation of the low cost thermomagnetic generator [24] (a) side view of the generator showing the main parts, (b) photograph of the generator.

Thermomagnetic effect is used to convert thermal gradient into electricity as well. Bulgrin *et al.* [70] proposed a thermal switch that exploits the temperature dependence of the magnetization of a ferromagnetic material oscillating between a hot and a cold surface. As shown in figure 2.21(a). As previously determined by Carlioz, this study also proved that the operating temperatures of such devices can be tuned by adjusting physical parameters of

the device, such as the gap between the hot and cold surfaces and the spring constant of the structure. By changing the ferromagnetic element to a material other than gadolinium, it is possible to exploit different ranges of temperatures.

Post *et al.* [71] studied thermomagnetic generation. Their generator uses conventional ferromagnetic gadolinium material undergoing a first order phase transformation. In passive systems, the cycling magnetic force produced when a thermomagnetic material is cycled un temperature is used to actuate the magnet's movement between hot and cold thermal reservoirs, which in turn perpetuates the cycling temperature. This passive cycle is described as follows. A thermomagnetic material rests in a gap between a hot magnetic reservoir and a cold non-magnetic reservoir. A spring is providing restoring force onto the cold reservoir. If the magnet is initially below its Curie temperature, it experiences a large magnetic force and travels to the hot magnetic reservoir as indicated in figure 2.21(b) 1. The magnet then heats up (2 in figure 2.21(b)), losing magnetization and is pulled to the cold reservoir by the restoring spring (3 in figure 2.21(b)). The magnet cools down, regaining magnetization and is attracted back to the hot reservoir, completing the cycle (4 in figure 2.21(b)). Even if this work did not went to experimental stage, its simulations results suggest that through piezoelectric transduction, electrical energy can be obtained from the system using the motion of the magnet. This device operates in a temperature difference of  $0^{\circ}\text{C}$  and  $50^{\circ}\text{C}$  for the cold and hot surfaces, respectively.

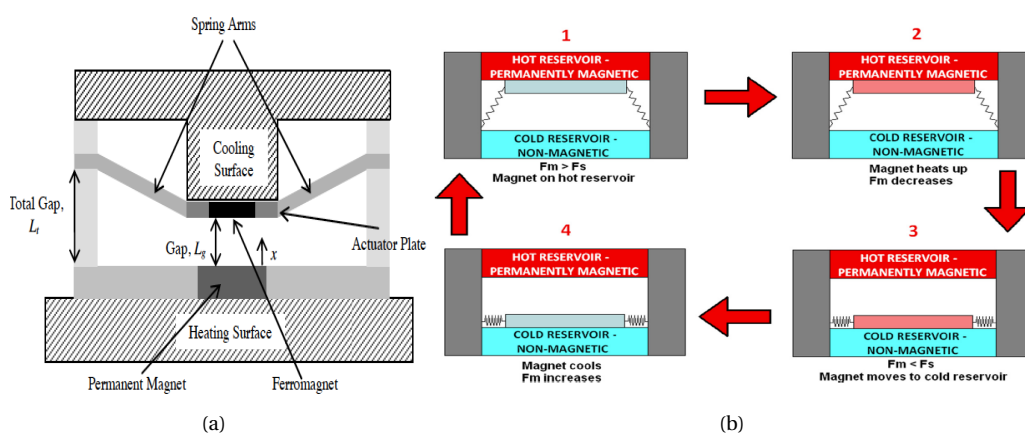


FIGURE 2.21: Representation of the thermomagnetic devices; (a) side view of a thermal switch using thermomagnetic effect [70], (b) schematic of a thermomagnetic generation due to fluctuating magnetic force and restoring spring forces [71].

### 2.3.3 Discussion

In summary, thermal energy conversion can be realized by either direct or indirect conversion techniques. Direct techniques of thermal energy conversion have major advantages as they not present moving parts. The most studied systems for converting thermal gradients are those based on the Seebeck effect (thermoelectric generators). Nevertheless, thermoelectric generators have major drawbacks, including:

- Low energy conversion rate (5%-10%).

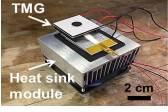
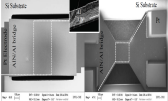
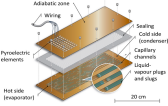
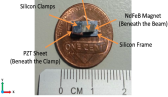
- Require high and constant thermal gradients.
- Require bulky heat sinks to maintain an efficient thermal gradient. Thermoelectric energy harvesting requires ensuring the maximum temperature gradient between the hot and cold surface.
- High cost of thermoelectric materials manufacturing.

And for temperature fluctuations, pyroelectric generators is the most used transduction conversion. However, they have major disadvantages, to name a few:

- Require rapid temperature fluctuations to get sufficiently amount of energy to power wireless sensor nodes. Natural temperature variations are quite unusual in the practical case whereas it is easy to find temperature space gradients.
- Difficulty to miniaturize without sacrificing the area of the electrodes.
- When implementing a thermal cycle for pyroelectric harvesting, practical requirements may be a limitation if this technology. For instance, in the Carnot cycle for pyroelectric energy harvesting needs adiabatic temperature changes (electro-caloric) and two isothermal paths [72].
- In resistive cycles using pyroelectric harvesting the major limitation is the Curie temperature of the material, pyroelectric behavior may disappears above this temperature and in the absence of an applied electric field [72].

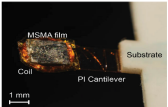
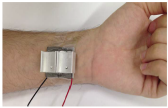
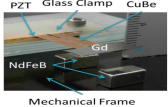
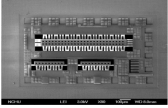
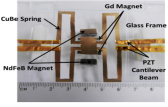
On the other hand, indirect conversion of thermal energy into electricity emerges as a promising alternative at micro scale. A detailed comparison of the thermal energy harvesters is listed in [Table 2.2](#).

TABLE 2.2: State of the art on thermal energy harvesting.

Publication		Actuation			Ambient source		Output	
Schematic	Ref., year	Principle <sup>a</sup>	Materials	Size	Form <sup>b</sup>	$\Delta\theta$ ( $\theta_{low}$ , $\theta_{high}$ )	Max. peak	Power- or Energy-density
	[25], 2017	TM, PE	Gd, Nd, PVDF	30cm <sup>3c</sup>	$\Delta\theta$	80°C (-10°C, 70°C)	2.6V	158μW
	[19], 2016	TB, PE	AlN, PZT	1.3 × 10 <sup>-6</sup> cm <sup>3</sup>	$\Delta\theta$	10°C (53°C, 63°C)	0.5mV	2.45μJ cm <sup>-3</sup>
	[50], 2016	PE	PMN-PT, PZT	96cm <sup>3c</sup>	$\frac{d\theta}{dt}$	30°C (25°C, 55°C)	0.8V	95pJ cm <sup>-3</sup>
	[73], 2015	TM, PE	Gd, PZT, NdFeB	6.3 × 10 <sup>-2</sup> cm <sup>3</sup>	$\Delta\theta$	20°C (6.7°C, 26.7°C)	37mV	6.29 × 10 <sup>-5</sup> μW cm <sup>-3</sup>
	[27], 2015	TEG	Bi-Te alloy, Al	32.03cm <sup>3</sup>	$\Delta\theta$	16°C (29°C, 45°C)	42mV	17.17μW cm <sup>-3c</sup>
	[74], 2014	TB, PE	INVAR, MC4, B72M	∅ = 8cm	$\Delta\theta$	36°C (64°C, 100°C)	31μJ	60μW cm <sup>-3</sup>

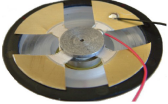
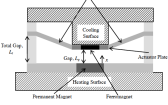
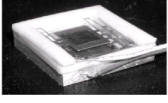
Continued on next page

**Table 2.2 – continued from previous page**

Publication		Actuation			Ambient source		Output	
Schematic	Ref., year	Principle <sup>a</sup>	Materials	Size	Form <sup>b</sup>	$\Delta\theta$ ( $\theta_{low}$ , $\theta_{high}$ )	Max. peak	Power- or Energy-density
	[65], 2014	TM, EM	Ni-Co-Mn-In alloy, NdFeB	$7.5 \times 10^{-2} \text{cm}^3$	$\Delta\theta$	10°C (120°C <sup>c</sup> , 130°C)	10μA	$1.6 \mu\text{W cm}^{-3}$
	[59], 2014	TEG	Commercial G2-30-0313 module	$3.87 \text{cm}^3$ <sup>e</sup>	$\Delta\theta$	NA <sup>d</sup> (22°C, NA <sup>d</sup> )	14mV	$2.2 \mu\text{W cm}^{-2}$
	[75], 2014	TM, PE	CuBe, Gd, NdFeB, PZT	$20 \text{cm}^3$	$\Delta\theta$	29°C (6°C, 35°C)	30.4mV	NA <sup>d</sup>
	[43], 2013	TEG	0.35μm CMOS	$0.3 \text{cm}^2$	$\Delta\theta$	15K (NA <sup>d</sup> , NA <sup>d</sup> )	0.55mV	$1.4 \mu\text{W cm}^{-2} \text{K}^{-2}$
	[76], 2013	TM, PE	CuBe, Gd, NdFeB, PZT, glass	$195 \text{cm}^3$	$\Delta\theta$	25°C (NA <sup>d</sup> , NA <sup>d</sup> )	16.6mV	NA <sup>d</sup>
	[77], 2010	LGPT	SiO <sub>2</sub> , Ordyll, HFE7100	$2.24 \text{cm}^2$	$\Delta\theta$	37K (NA <sup>d</sup> , NA <sup>d</sup> )	$1.29 \mu\text{W}^f$	$0.5 \mu\text{W cm}^{-2f}$

Continued on next page

Table 2.2 – continued from previous page

Publication		Actuation			Ambient source		Output	
Schematic	Ref., year	Principle <sup>a</sup>	Materials	Size	Form <sup>b</sup>	$\Delta\theta$ ( $\theta_{low}$ , $\theta_{high}$ )	Max. peak	Power- or Energy-density
	[44], 2010	PYR	PZT, PVDF, PdAg(Heraeus C1214),	16cm <sup>2</sup>	$\frac{d\theta}{dt}$	60K (300K, 360K) during 100s	21.5V	$1.56 \times 10^{-2} \mu\text{W cm}^{-2}$
	[23], 2009	TM, PE	Fe-Ni alloy, Piezo Buzzer, NdFeB	13.68cm <sup>3</sup>	$\Delta\theta$	10°C (40°C, 50°C)	30V	$19.4 \mu\text{W cm}^{-3}$
	[78], 2009	TM	CuBe, Gd, NdFeB	11cm <sup>3</sup>	$\Delta\theta$	50°C (0°C, 50°C)	NA <sup>d</sup>	$250 \mu\text{W cm}^{-3f}$
	[68], 2007	TM, PE	Gd, PZT, NdFeB	2.4cm <sup>3</sup>	$\Delta\theta$	50°C (0°C, 50°C)	NA <sup>d</sup>	$3.6 \text{mW cm}^{-2g}$

<sup>a</sup> **TB**:Thermal-Buckling, **TM**:Thermo-Magnetic, **PE**:Piezo-Electric, **TEG**:Thermo-Electric Generator, **EM**:Electro-Magnetic, **LGPT**:Liquid-Gas Phase-Transition, **PYR**:Pyro-Electric.

<sup>b</sup>  $\Delta\theta$ :Thermal gradient,  $\frac{d\theta}{dt}$ :Time-Dependent Temperature-Variations.

<sup>c</sup> Value estimated or extrapolated from data in reference.

<sup>d</sup> **NA**: Not available data in the reference.

<sup>e</sup> Heat sink not included because data not available in reference.

<sup>f</sup> Mechanical power because conversion to electricity was not realized.

<sup>g</sup> Predicted by modeling but not experimentally demonstrated.

## 2.4 Proposed solution review

The power generator has two main sections according to their respective functions: the energy transducer and the triggering system as shown in figure 2.22(a). The energy transducer is composed of a piezoelectric bimorph-type cantilever beam, namely PSI-5H4E from Piezo Systems, Inc with a series-type polarization. Concerning the triggering system, it consists of two permanent magnets (NdFeB), that is the magnetic volume  $V_{mag}$ , that are attached to the free end of the beam, and a soft magnetic material (FeNi), fixed under the free end of the beam, forming an air gap. As shown in figure 2.22(b)

The generator has two stable positions: the closed position and the open one. In the initial state, at a cold temperature, the soft magnetic material is magnetized so the cantilever beam is pulled-down due to magnetic force. After, when the environmental temperature increases, the magnetic properties of soft magnetic material change from ferromagnetic to paramagnetic, causing the magnetic force to decrease. The beam is pulled back to its initial state because of the spring-back force of the beam. This process of pulling down and pulling-back of the beam is periodically repeated as long as the energy harvester is placed in an environment with cycled variations in temperature.

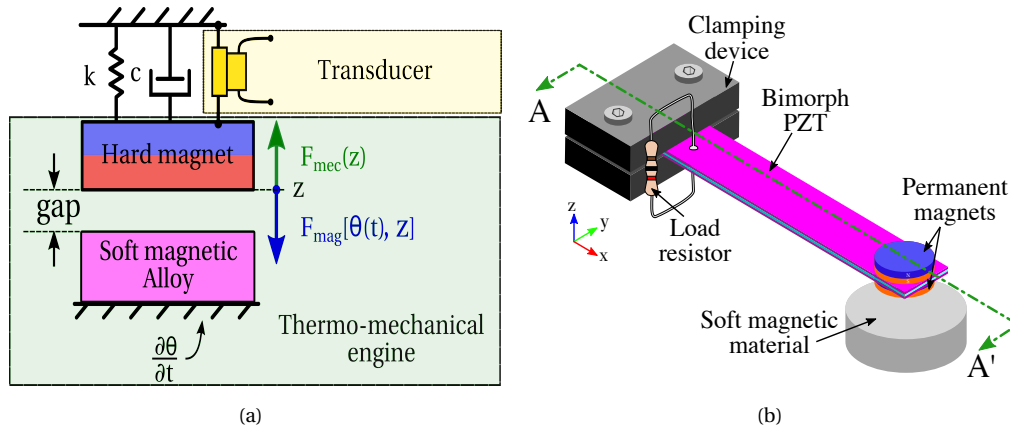


FIGURE 2.22: (a) 1D model of the generator, (b) Isometric view of the proposed solution of thermal energy harvesting using thermomagnetic effect and piezoelectric transduction.

On the following chapter, the working principle as well as the analytical description of the system is detailed. The device sketched on the figure above is only a possible architecture of the energy harvester device. As we will detail in following chapter, the piezoelectric layers of the bimorph cantilever beam can not be along the whole length of the structure in order to improve the dynamic behavior of the transducer. Also, it will be modeled several design parameters of the device in order to describe the behavior of the generator towards its miniaturization and maximization of its output energy.



## Chapter 3

# Design and modeling of the proposed generator

### Contents

---

<b>3.1 Thermal magnetization</b> .....	<b>46</b>
<b>3.2 Working principle</b> .....	<b>47</b>
<b>3.3 Analytical modeling</b> .....	<b>50</b>
3.3.1 Thermal model .....	51
3.3.2 Thermo-magnetic model .....	55
3.3.3 Magnetic force model .....	57
3.3.4 Mechanical model .....	61
3.3.4.1 Mechanical modeling of the static behavior .....	61
3.3.4.2 Mechanical modeling of the transient behavior .....	65
3.3.5 Electro-mechanical model .....	67
3.3.6 Dynamic behavior of the generator .....	72
<b>3.4 Design rules of the generator</b> .....	<b>77</b>
<b>3.5 Discussion</b> .....	<b>79</b>

---

*This chapter presents the working principle of the generator. A brief description of thermo-magnetic materials is reported. After, the analytical modeling of the multi-physic system is described. Finally, a set of design rules for such a generator is presented towards its miniaturization. Output energy maximization of the generator and having operating temperatures near to the human body temperature range are desirable for the final device.*

### 3.1 Temperature-dependent magnetization of FeNi alloy

In order to better understand the key parameter behind this approach of thermal energy harvesting, it is necessary to recall some general points about soft iron-nickel alloys. As this is the material used in our generator.

In the pure state, iron and nickel are ferromagnetic materials at room temperature. When they are combined to forming alloys, the product may also present this property. However, depending on the stoichiometry of this binary, the magnetic behavior may exhibit a vast diversity. Therefore, they are very attractive for industrial applications, such as electro-magnetic devices, transformers, induction motors, etcetera.

FeNi alloys are only used for their magnetic properties for nickel contents greater than 28%. And their structure is cubic with centered faces and they do not present phase transformation in the solid state. Therefore, these two properties give them a good ease of cool rolling (up to 10 $\mu$ m) and thermic treatment allowing to develop at the best their magnetic properties [79]

A key parameter of this alloys is the Curie temperature  $\theta_C$ , which corresponds to the temperature at which certain materials lose their magnetic properties. In other terms, it marks the limits of the ferromagnetism. Typically, a thermomagnetic curve of a material is a representation of its magnetic polarization as a function of temperature, as shown in Figure 3.1

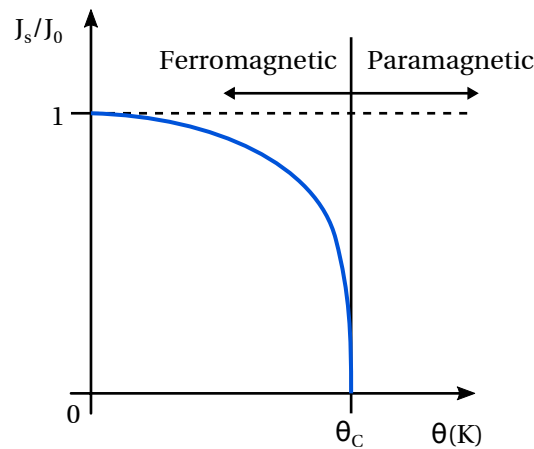


FIGURE 3.1: Representation of transition between ferromagnetism and paramagnetism as a function of temperature ( $J_0$  is the saturation magnetization at 0K)

In this application, we will focus on the saturation magnetization of iron-nickel alloy. Concretely at the variation of its magnetization with temperature. The behavior of a magnetic material is described by its magnetic response at an applied field strength  $\vec{H}$  in ( $\text{Am}^{-1}$ ). This response is represented by the magnetization  $\vec{M}$  in ( $\text{Am}^{-1}$ ) and the magnetic induction  $\vec{B}$  in (T). In this document, we are going to use either the magnetization  $\vec{M}$  in ( $\text{Am}^{-1}$ ) or the magnetic polarization  $\vec{J}$  in (T) with  $\vec{J} = \mu_0 \vec{M}$ . This variable is often used by experts in electromagnetism to characterize the materials.

$$\vec{B} = \mu_0 \vec{H} + \vec{J} \quad (3.1)$$

where  $\mu_0 = 4\pi \times 10^{-7}$  in ( $\text{H m}^{-1}$ ) is the permeability of the free space.

This equation has an important meaning. The induction  $\vec{B}$  has two contributions: the first term is the direct contribution of the magnetic field in the air and the second term is the contribution of the ferromagnetic material, spontaneously magnetized. The maximum magnetization  $\vec{M}$  is reached at the saturation, that is for high field strength  $\vec{H}$  its value depends on the stoichiometry of the alloy.

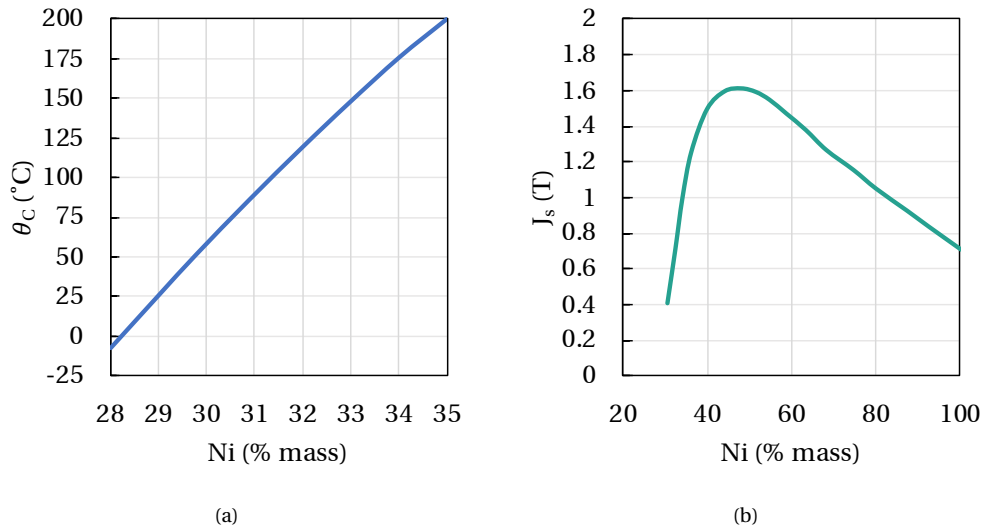


FIGURE 3.2: Representation of the principal electromagnetic characteristics of FeNi alloys, (a) variation of their Curie temperature as a function of their nickel content, (b) variation of the saturation magnetization of as a function their nickel content [80].

From figure 3.3(b), it is evident to see that iron-nickel alloys having a Ni content of 48% have the maximum saturation magnetization. The magnetization at saturation is reversible and can be made virtually linear. The value of the Curie temperature can be modified by adding other elements to the alloy. Also, other elements are used in this type of alloys such as Cr, or Mo to modify their magnetic properties. Figures 3.3(a) and 3.3(b) show the principal magnetic characteristics of ternary FeNiCr as a function of the content percentage of Ni for different chromium contents.

We have coupled an iron-nickel alloy with permanent magnet in order to activate a piezoelectric transducer in a unique system. The following section will describe the working principle of the generator.

## 3.2 Working principle

Figure 3.4 shows the schematic of a possible architecture of the proposed thermo-magnetically activated micro-generator. In this configuration, the generator can be divided into two main subsystems: the triggering system and the transduction one. The former is based

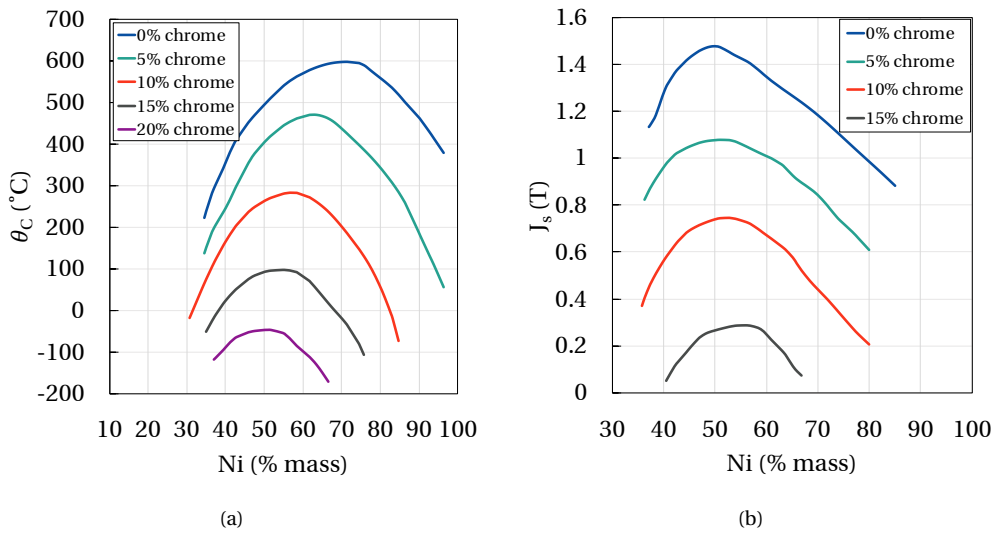


FIGURE 3.3: Representation of the principal magnetic characteristics of FeNiCr alloys, (a) variation of their Curie temperature as a function of their nickel content for different chromium content, (b) variation of the saturation magnetization of as a function their nickel content for different chromium content. [80].

on a thermo-magnetic circuit composed of a hard magnet and a soft magnetic alloy, for instance NdFeB and FeNi, respectively. Regarding the transducer system, it is composed of a cantilever beam made of a thin film of reinforcement material such as steel that is sandwiched between two thin films of piezoelectric layers, for instance PZT 5H.

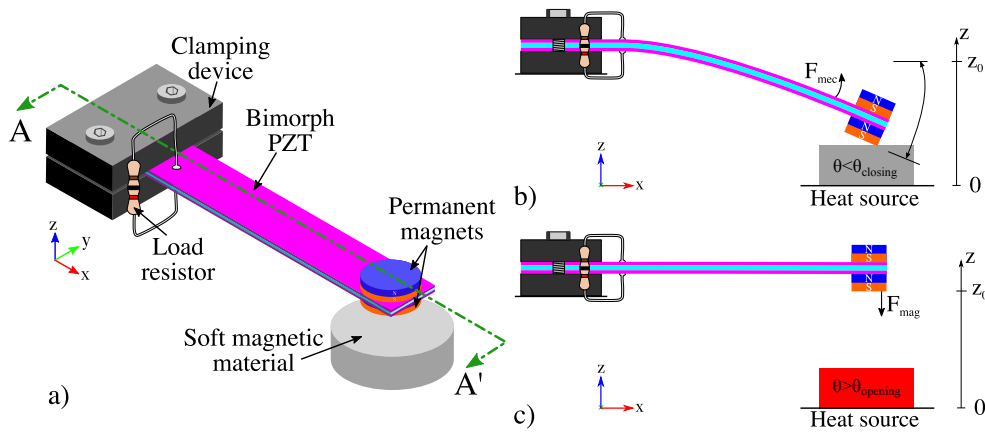


FIGURE 3.4: (a) Schematic view of the micro energy harvester and its stable operation position: b) the closed position and c) the open one.

The hard magnets were mounted on the free end of the cantilever beam whereas the soft magnetic alloy was centered and fixed below the permanent magnets at a certain initial gap distance  $z_0$  with reference to the horizontal plane of the cantilever beam. The soft magnetic material is assumed to be exposed to ambient temperature fluctuations.

The operating mechanism of the harvester shown in Figure 3.4 is as follows.

1. In the initial state, the soft magnetic alloy temperature is below its magnetic Curie temperature  $\theta_C$ ; hence an attraction magnetic force  $F_{mag}$  is exerted due to the permanent magnets. Thus, the permanent magnets are attracted towards the soft magnetic alloy and the free end of the beam travels towards the soft magnetic material surface making contact against each other under magnetic and inertial forces. At that instant, the generator is in the closed position (Figure 3.4b).
2. Once the ambient temperature increases; the soft magnetic material is now heated up by conduction and it loses its magnetism above its Curie temperature. At the time that the temperature of the soft magnetic alloy approaches its Curie temperature, the attraction magnetic force decreases drastically (i.e.  $F_{mag} \leq F_{mec}$ ). After that, the counter-reaction force  $F_{mec}$  of the cantilever beam pulls it away from the soft magnetic alloy. At that instant, the generator is in the open position (Figure 3.4c).
3. Next, when the ambient temperature decreases below the Curie temperature of the soft magnetic alloy, the soft magnetic alloy regains its spontaneous magnetization. After regaining magnetization, the permanent magnets are attracted towards the soft magnetic material and they travel towards the soft magnetic material surface making contact against each other. Temperature fluctuations on the soft magnetic alloy are driving the generator either its two stable operation positions.

Since the attraction magnetic force is nonlinear, and dependent on both temperature and initial gap distance, it is possible to create a thermal threshold as the temperature where the device shifts state. Actually, since the interaction between the hard-permanent magnets and the soft magnetic alloy drives the stable position of the generator, there are two thresholds, one for opening commutation  $\theta_{opening}$  and the other for closing commutation  $\theta_{closing}$ . The operation commutations can continue as long as the ambient temperature fluctuations are maintained between the two thermal thresholds. Finally, the transduction system is converting the kinetic mechanical energy on the cantilever beam during the two commutations.

The only assumption is that the ambient temperature fluctuations are maintained such that the thermal thresholds (i.e.  $\theta_{opening}$  and  $\theta_{closing}$ ) are reached. Further, the ambient temperature fluctuations can be done in several ways, like the waste thermal energy due to industrial machines or temperature fluctuations at the industrial pipes, which makes this model applicable to many scenarios. The contact surfaces also act as elastic members absorbing the impact energy of the permanent magnets attached to the free end of the cantilever beam and restoring its kinetic energy later. The mechanical stiffness of the cantilever beam is a very essential design parameter to determine the energy harvesting capabilities of the generator; it influence on strain energy due to the cantilever tip beam displacement and sets the restoring force required to overcome the magnetic attraction force to bring the cantilever beam back to its open position. The initial gap distance is also a crucial design parameter; it affects the attraction magnetic force exerted between the hard magnets and the soft magnetic alloy and it contributes to the initial elastic energy stored in the beam when the generator is at its closed position.

The chronograms of Figure 3.5 show the typical response of the system when a thermal cycle is achieved. It is evident to note that the hysteresis cycle created by this behavior corresponds to the minimum temperature span required for a complete operation of the generator. That is illustrated in Figure 3.6. It can be deduced that the opening commutation

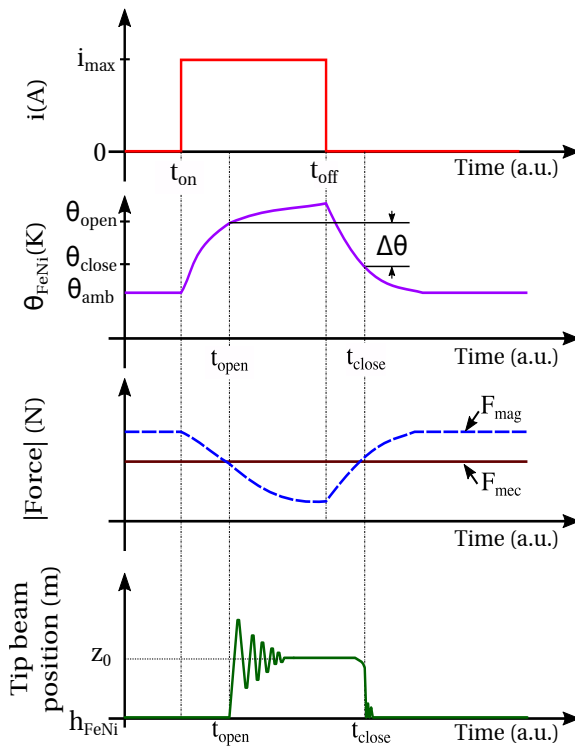


FIGURE 3.5: Schematic representation of the overall system operation during a thermal cycle. The reversible, and temperature dependent magnetization of soft magnetic alloy is driving the stable positions. Joule heating is used to make temperature variations on soft magnetic alloy. Magnetic and mechanical forces,  $F_{mag}$  and  $F_{mec}$ , respectively, are counterbalanced by temporal variations of temperature.

has an abruptly behavior, whereas the closing one is smooth. This is linked to the non-linearity of magnetic attraction force.

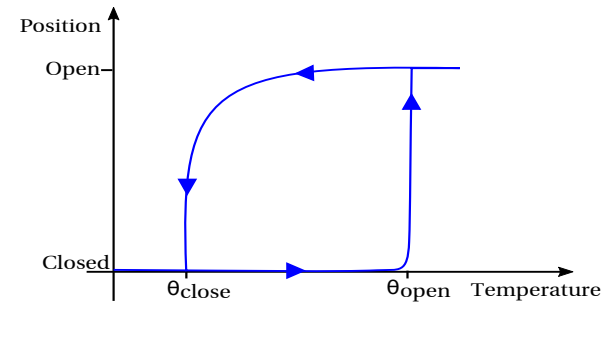


FIGURE 3.6: Schematic view of the micro energy harvester and its stable operation position: b) the closed position and c) the open one.

### 3.3 Analytical modeling

In this section, we present the analytical equations describing the operation of the generator. Modeling of the entire harvesting cycle can be divided into 3 distinct phases as follows:

- Phase I: the bottom permanent magnet is in contact with the surface of the soft magnetic alloy, thus the generator is in its closed position.

- Phase II: a temperature rising of the soft magnetic alloy makes it losing its spontaneous magnetization until reaching the opening threshold of the system, thus the opening commutation is reached resulting in an oscillatory motion of the beam.
- Phase III: the cantilever beam is now at its horizontal position and a temperature decreasing of the soft magnetic material makes it regaining its spontaneous magnetization up to reach the closing threshold of the system, therefore the closing commutation is achieved.

As mentioned earlier, Phase I corresponds to the base configuration, where the initial deflection of the cantilever beam is required to provide a unidirectional restoring force in the direction opposing the unidirectional magnetic force. At this stage, the attraction magnetic force is higher than the mechanical restoring force. Phase II, the soft magnetic material with time heats up and above its Curie temperature and it losses its spontaneous magnetization; hence the attraction magnetic force decreases drastically and it is no longer greater than the mechanical restoring force. Therefore, the cantilever beam is released and it starts to oscillating with a significant amplitude and velocity. Phase III corresponds to the state where a decreasing of temperature in the soft magnetic material makes it to regaining its magnetization: the cantilever beam tip is pressed against the surface of the soft magnetic material under a stronger magnetic force than the mechanical force. In this phase, a rebound due to the contact between the hard magnet and the soft magnetic material surface is significant as well as the velocity. Below we provide mathematical description of each of these phases.

### 3.3.1 Thermal model

Heat transfer occurs during heating up and cooling of the soft magnetic alloy. Initially, at the closed position of the generator, heating occurs at the heat source where the soft magnetic alloy and the cantilever beam tip are heated up by direct contact (i.e., conduction). Subsequently, at the open position of the generator, cooling of the system is achieved by either natural or forced convection through an oscillatory motion in air (i.e., convection). Equations for the time-dependent temperature at the upper face of the soft magnetic alloy, are formulated in order to describe heating and cooling processes. We started with an unsteady energy balance on the soft magnetic alloy of mass, and specific heat. In Phase I, the system is near its maximum displacement state. In this state, thermal contact conductance dominates the heat transfer physics. In Phase II; the role of thermal contact conductance is negligible and the temperature distribution changes only due to internal diffusion. Contact pressure is absent and thus the vibration is governed by the magnetic force and restoring spring force. Since the purpose of heat transfer modeling is to compute the temperature in soft magnetic alloy and the corresponding magnetic force, the heat transfer can be divided into two parts:

**Heating up:** increase of temperature of generator at its closed position, which implies a solid-solid interface present only where two surfaces are in contact. At this stage, the lateral surface  $S_L$  corresponds to that of the entire system (i.e., the soft magnetic volume and the piezoelectric transducer).

**Cooling down:** cooling down of the generator, at its open position through the interstitial fluid medium, which is always present or through a forced convection, like a fan for instance. For this stage, the lateral surface  $S_{L-FeNi}$  is that of the soft magnetic material as the transducer cantilever beam is not in contact.

Contact conductance causes conduction of heat through very small contact areas of the contacting surface that press against each other. The gap conductance is contributed by conduction through an interstitial fluid trapped between the contacting surface. It depends on the thermal conductivity, convection coefficient, of the interstitial fluid. In Phase I and Phase II, all the thermal contact conductance mechanisms are present, while in Phase III only the gap conductance due to the temperature.

To model the heat transfer on the system, first we consider the generator of a determined shape of mass  $m_i$ , (subscript  $i$  can be either “h” or “c” for the heating up and cooling down stages, respectively), volume  $V$ , surface area  $S_L$ , density  $\rho$ , and specific heat  $c_{pj}$  (subscript  $j$  can be either “h” or “c” for the heating up and cooling down stages, respectively) as an isothermal body (i.e., interior temperatures remain essentially uniform during a heat transfer process), so we can treat it as a “lump” system whose temperature is only a function of time,  $\theta(t)$ . Initially, the generator is at equilibrium with its environment  $\theta_{amb}$ , suddenly exposed to a heat source, that depending on the heat flow direction, it can be a conductive heat source: when increasing of temperature takes place (soft magnetic material heating up), or a convective heat source: when decrease of temperature occurs (soft magnetic material cooling up). To produce temperature variations on our soft magnetic material specimen, we assumed it is always in contact with a heat source. This heat source consists in electrical energy being converted into heat at a rate of  $Ri^2$  ( $R$  and  $i$  correspond to electrical resistance and current for Joule heating effect, respectively). This electrical current is flowing across a serpentine shaped printed circuit board, which is attached to the bottom surface of the soft magnetic alloy. From a steady-state energy balance we have that the time rate of change of the energy content of a given mass is equal to the rate at which energy is added to the mass plus rate of production of energy within the mass. An energy balance of the generator for a time interval  $dt$  can be expressed as:

$$m_h c_{ph} \frac{d\theta}{dt} = [Ri^2 - \lambda_c S_L (\theta - \theta_{amb})] \quad (3.2)$$

After a classical solution of the ordinary differential equation, and considering the initial condition  $\theta(0) = \theta_{amb}$ , we find the governing equation of the system during the heating up stage:

$$\theta(t) = \theta_{amb} + \frac{Ri^2}{\lambda_c S_L} \left( 1 - e^{-\frac{\lambda_c S_L}{m_h c_{ph}} t} \right) \quad (3.3)$$

where,  $\theta_{amb}$  is the ambient temperature,  $m_h$  the mass of the soft magnetic material including the transducer beam as they are in contact, and  $c_{ph}$  the specific heat of the system. During the heating process, the surface area is now composed of the whole system as the bottom magnet and the soft magnetic alloy are in contact. The heat transfer stops as soon as the electrical current is stopped. For the cooling up stage, the system changes as the soft magnetic alloy is no longer in contact with the bottom magnet, thus the transducer is not included into the cooling up volume. Therefore, the energy balance can be derived as

follows:

$$m_c c_{pc} \frac{d\theta}{dt} = (\theta - \theta_{amb}) (-\omega_{fan} \dot{m} c_{pc} - \lambda_c S_{L-FeNi}) \quad (3.4)$$

This equation describes the cooling process by forced convection of the soft magnetic alloy that is not in contact with the hard magnet (i.e., the surface area is only that one of the soft magnetic alloy). At this point, the surface area  $S_{L-FeNi}$  as well as the mass  $m_c$  are only those pertaining to the soft magnetic alloy, the reason is because the transducer beam is not in contact with it. The terms  $\omega_{fan}$  and  $\dot{m}$  are, respectively, the fan speed (revolutions per second) and its mass flow rate (kilogram per second). When natural convection is considered, this first term disappears. The second term represents the convection interaction of the system. After a classical solution of this ordinary differential equation considering the initial condition  $\theta(0) = \theta_i$  (i.e., the temperature of the iron nickel alloy at the beginning of the cool up stage) the governing expression for the cooling stage with forced convection can be written as

$$\theta(t) = \theta_{amb} + e^{\frac{(\omega_{fan} \dot{m} c_{pc} + \lambda_c S_{L-FeNi})t}{m_c c_{pc}}} (\theta_i - \theta_{amb}) \quad (3.5)$$

The single most remarkable observation to emerge from [Equation 3.3](#) and [Equation 3.5](#) was the time constants of the two heat transfer stages;  $\tau_{heating}$  and  $\tau_{cooling}$

$$\tau_{heating} = \frac{m_h c_{ph}}{\lambda_c S_L} \quad (3.6)$$

If natural convection is considered, the [Equation 3.7](#) describes the time constant for the cooling down phase of the generator

$$\tau_{cooling} = \frac{m_c c_{pc}}{\lambda_c S_{L-FeNi}} \quad (3.7)$$

As the surface area is lower when the generator is open compared with the closed generator, it suggests that size reduction can lead lower constant of time for both heating off and cooling off stages. Basically, these terms are strongly linked to the dimensions of the generator and they impact directly on the time needed to pass from one commutation to another. Therefore, the lower are the dimensions of the generator the lower are the time period between commutations. When considering forced convection, this constant of time is dramatically reduced because of the influence of the cooling down device (i.e., the fan). In order to explore this condition, we gave some initial parameters summarized in [Table 3.1](#).

It is useful to understand how time constants of both heating up and cooling down stages scale in the design of miniaturized generators. To explain the scaling effects on such a miniaturized generators, Trimmer's analysis of the scaling of micro-mechanical systems can be followed [\[81\]](#). The size of the system is represented by a single scale parameter  $\alpha$ , which describes the linear scaling of the system. The choice of  $\alpha$  is a bit arbitrary. It is assumed that all dimensions of the system are scaled down in size as  $\alpha$  is decreased. Nominally  $\alpha = 1$ ; if  $\alpha$  is then changed to 0.1, all the dimensions of the system are decreased by a factor of ten. As the mass of an object scales as  $\alpha^3$  (density is assumed to be constant with scale). And the lateral surface of an object scales as  $\alpha^2$ . Therefore, for the heat transfer on the present system, the time constants  $\tau_{heating}$  and  $\tau_{cooling}$  scale as  $\alpha$ .

Considering the aforementioned parameters, we evaluated the response in temperature of the model and results are depicted in [Figure 3.7](#). For this case, we considered a current being applied a half of the total simulation duration, then it is cut off and simultaneously

TABLE 3.1: General parameters for the temperature response of the generator.

Parameter	Symbol	Units	Value
Surface area of global device	$S_L$	$\text{m}^2$	$234 \times 10^{-6}$
Surface area of soft magnetic alloy	$S_{L-FeNi}$	$\text{m}^2$	$154 \times 10^{-6}$
Mass in heating up stage	$m_h$	kg	$4 \times 10^{-3}$
Mass in cooling down stage	$m_c$	kg	$3.7 \times 10^{-3}$
Specific heat in heating up stage	$c_{ph}$	$\text{J kg}^{-1} \text{K}^{-1}$	505
Specific heat in cooling down stage	$c_{pc}$	$\text{J kg}^{-1} \text{K}^{-1}$	350
Current	$i$	A	2
Resistance	$R$	$\Omega$	20
Heat transfer coefficient	$\lambda_c$	$\text{W m}^{-2} \text{K}^{-1}$	28
Fan speed	$\omega_{fan}$	<i>rps</i>	33.33
Mass flow rate	$\dot{m}$	$\text{kg s}^{-1}$	$5 \times 10^{-4}$

a fan is turned on to achieve the cooling stage of the system. The ambient temperature considered was 293K. The plot depicts the temperature of the soft magnetic alloy as function of time during temperature fluctuations controlled by heat flow rate sources as earlier mentioned.

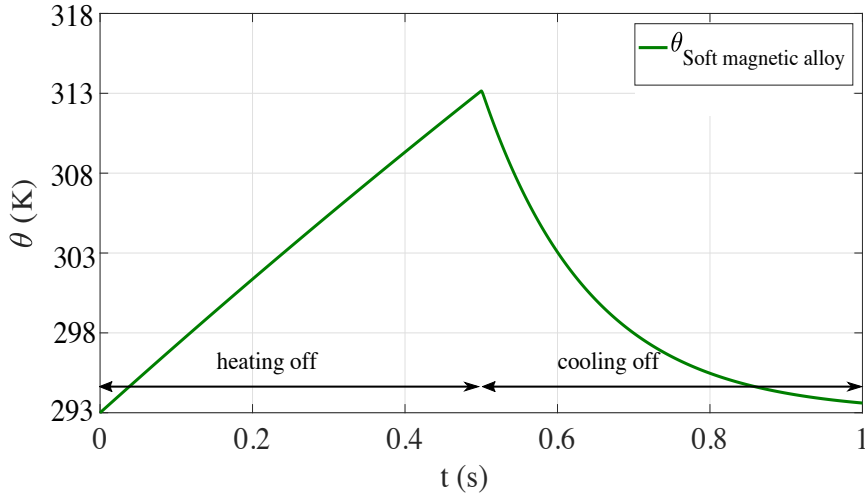


FIGURE 3.7: Temperature response of the generator during heating and cooling stages. It is clear that  $\tau_{heating} > \tau_{cooling}$  as for the heating up stage, there are considered bigger mass and lateral surface than for the cooling down stage.

### 3.3.2 Thermo-magnetic model

Triggering system is composed of the iron nickel alloy, which is a soft magnetic material with a Curie temperature near to room temperature, depending on its stoichiometry. It loses its magnetism if heated beyond its Curie temperature, thus making it very suitable for application near room temperature. On the other hand, the Neodymium Iron Boron permanent magnet, is a magnet available in various shapes and sizes. It has remanent flux density ( $B_r \cong 1.3\text{T}$  at room temperature) and a relatively high Curie temperature (583K) [82], also, it can retain its magnetization within the working range of ambient temperatures. The Neodymium Iron Boron magnet is of a cylindrical configuration as sketched in Figure 3.8, and its magnetic flux density can be expressed according to Equation 3.8 [83]:

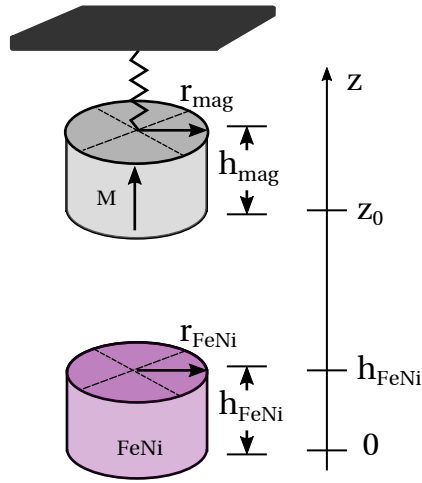


FIGURE 3.8: Schematic representation of a simplified model for the calculation of flux density along the axis of a cylindrical magnet, on the triggering system.

$$B_{mag}(z) = \frac{B_r}{2} \left[ \frac{z - z_0}{\left( (z - z_0)^2 + r_{mag}^2 \right)^{1/2}} - \frac{z - (z_0 + h_{mag})}{\left( (z - (z_0 + h_{mag}))^2 + r_{mag}^2 \right)^{1/2}} \right] \quad (3.8)$$

Here,  $B_r$ ,  $h_{mag}$ , and  $r_{mag}$  are, respectively, the remanent flux density, the thickness and the radius of the Neodymium Iron Boron magnet. It is magnetized in the thickness direction, which corresponds to the  $z$ -axis coordinate system,  $z$  is the distance away from the magnet surface, and  $B_{mag}(z)$  is the corresponding magnetic induction at location  $z$ . This induction subjects the soft magnetic alloy (FeNi) to an external field  $H_{mag}(z) = B_{mag}(z)/\mu_0$ , where  $\mu_0$  is the magnetic permeability of the vacuum.

Depending on the temperature within the material, soft magnetic alloy follows a corresponding magnetization distribution. Estimating the magnetization of such a soft magnetic material requires solving the equation given as [84]:

$$M_s(\theta) = M_s(0) \left(1 - \frac{\theta}{\theta_C}\right)^\beta \quad (3.9)$$

Here,  $M_s(0)$  is the value of magnetization at 0K,  $\theta_C$  is the Curie temperature, and  $\beta$  is the material-dependent critical exponent, a representative of mean field interactions. To bring out this temperature-dependent and reversible property of such a kind of alloy, Mavrudieva *et al*, [85] measured the saturation induction  $B_s$  versus temperature on a FeNi sample, that was elaborated by the Research Center of APERAM IMPHY ALLOYS (France) [86]. Considering that  $M = B_r \mu_0^{-1}$ , the measured saturation induction was used to identify  $M_s(0)$  and  $\beta$  by fitting as shown in Figure 3.9.

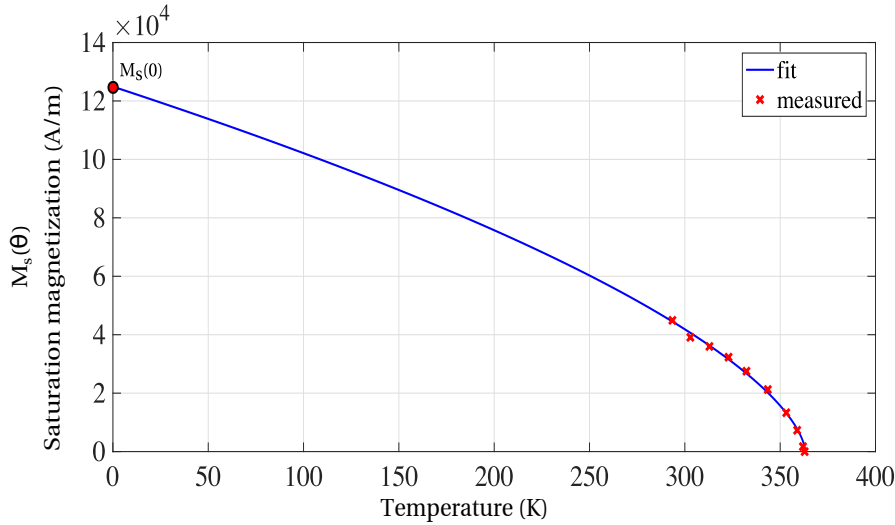


FIGURE 3.9: Measured saturation magnetization against temperature in FeNi material and its curve fitting from [85].

The change from the ferromagnetic to the paramagnetic state is perfectly sharp at the Curie temperature,  $\theta_C = 363.15\text{K}$ . The calculated values of parameters through fitting technique are summarized in Table 3.2.

TABLE 3.2: Identification results for saturation magnetization against temperature.

Parameter	Symbol	Units	Value
Saturation magnetization at 0K	$M_s(0)$	$\text{Am}^{-1}$	$1.25 \times 10^5$
Critical exponent	$\beta$	-	0.625
Curie temperature	$\theta_C$	K	363.15

Since the configuration of the triggering system is such as having an attraction magnetic force between the permanent magnet and the soft magnetic material, we have interest in calculating this actuation force.

### 3.3.3 Magnetic force model

In this device, the commutations are driven by the interaction of the restoring mechanical force, created by the cantilever piezoelectric beam, and the magnetic attraction force acting on the soft magnetic material, created by the applied magnetic field  $B_{ext} = B_{mag}(z)$  due to the Neodymium magnet. Therefore, it is important to understand what design parameters affect these forces and how to derive them. With regards the magnetic force, it may be apparent from Equation 3.8 that the remanent flux density  $B_r$  of the Neodymium magnet, its dimensions  $r_{mag}$  and  $h_{mag}$ , and the distance  $z$  away from it determine the external magnetic field at that location. Also, the magnetic attraction force is dependent on the volumetric and surface magnetic charge densities in the soft magnetic material, both of which are functions of the local magnetization and its dimensions. Magnetization of the soft magnetic material is a function of temperature, as shown in Figure 3.9. Hence, after solving the heat transfer model and getting the temperature of the generator, the magnetic force can be calculated.

In order to predict the behavior of triggering system of the form shown in Figure 3.4 we opted to chose a semi-analytical model developed by Soares *et al.* [87]. In this model, the surface current model was used [83] to discretize the magnet into a finite set of current loop elements. Then, the magnetic field of the magnet is obtained by superimposing the magnetic field distributions of the constituent current loops. The magnetic force between the hard magnet and the soft magnetic alloy as a function of their axial separation was computed by taking the derivative of their interaction energy with respect to the distance between them. The resulting equation to compute the axial force  $\vec{F}_{mag}(z)$  is as follows:

$$F_{mag}(z) = \Gamma \int_0^{\infty} J_1(\chi r_{FeNi}) J_1(\chi r_{mag}) \Psi \chi^{-1} d\chi \quad (3.10)$$

with

$$\begin{aligned} \Psi &= e^{-\chi z} + e^{-\chi(z-h_{FeNi}+h_{mag})} - e^{-\chi(z-h_{FeNi})} + e^{-\chi(z+h_{mag})} \\ \Gamma &= \mu_0 \pi r_{mag} r_{FeNi} M_{mag} M_{FeNi} \end{aligned}$$

here,  $M_{mag}$ ,  $r_{mag}$  and  $h_{mag}$  are, respectively, magnetization, radius and height of permanent magnet,  $M_{FeNi}$ ,  $r_{FeNi}$  and  $h_{FeNi}$  are, respectively, magnetization, radius and height of iron nickel alloy.  $\mu_0$  is the permeability of free-space,  $J_1$  is the first order Bessel function.

The approximation of the magnetic force is depicted in Figure 3.10 for a model architecture with the parameters listed in Table 3.3.

For this configuration of the triggering system, the iron-nickel alloy is considered to be fixed at the origin of the z-axis. The permanent magnet can be displaced along the z-axis in a range of  $z \in [h_{FeNi}, 14 \times 10^{-3} \text{m}]$ . It is clear that the maximum magnetic force between these two volumes is reached when they are in contact.

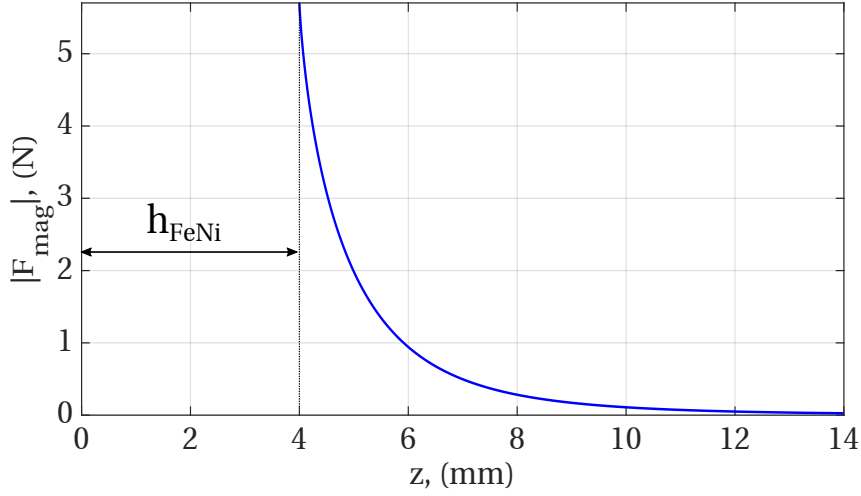


FIGURE 3.10: Absolute value of the attraction magnetic force on the triggering system as function of the separation distance  $z$  at a temperature of 293K.

TABLE 3.3: General parameters for the temperature response of the generator.

Parameter	Symbol	Units	Value
Magnetization of magnet	$M_{mag}$	$\text{Am}^{-1}$	$5 \times 10^6$
Magnetization of FeNi	$M_{FeNi}$	$\text{Am}^{-1}$	$200 \times 10^3$
Height of magnet	$h_{mag}$	m	$2 \times 10^{-3}$
Height of FeNi	$h_{FeNi}$	m	$4 \times 10^{-3}$
Radius of magnet	$r_{mag}$	m	$2 \times 10^{-3}$
Radius of FeNi	$r_{FeNi}$	m	$4 \times 10^{-3}$
Permeability of vacuum	$\mu_0$	$\text{H m}^{-1}$	$4\pi \times 10^{-7}$

From equation Equation 3.9, the saturation magnetization of the soft magnetic alloy,  $M_{FeNi}$  is dependent of temperature as shown in Figure 3.9. Thus, it is trivial from Equation 3.10 that the magnetic force is a function of: the separation between the magnets and the soft magnetic allow, the magnetization terms  $M_{mag}$ ,  $M_{FeNi}$  and the dimensions of the pair permanent magnet-iron nickel alloy. Combining Equation 3.9 ( $M_s = M_{FeNi}$ ) and Equation 3.10, we then obtained an expression of  $F_{mag}(z, \theta)$ , which was calculated numerically using MatLab.

$$F_{mag}(\theta, z) = \Gamma_2 \int_0^\infty J_1(\chi r_{FeNi}) J_1(\chi r_{mag}) \Psi \chi^{-1} d\chi \quad (3.11)$$

with

$$\Psi = e^{-\chi z} + e^{-\chi(z-h_{FeNi}+h_{mag})} - e^{-\chi(z-h_{FeNi})} + e^{-\chi(z+h_{mag})}$$

$$\Gamma_2 = \mu_0 \pi r_{mag} r_{FeNi} M_{mag} M_{FeNi}(0) \left(1 - \frac{\theta}{\theta_C}\right)^\beta$$

These results are shown in [Figure 3.11](#).

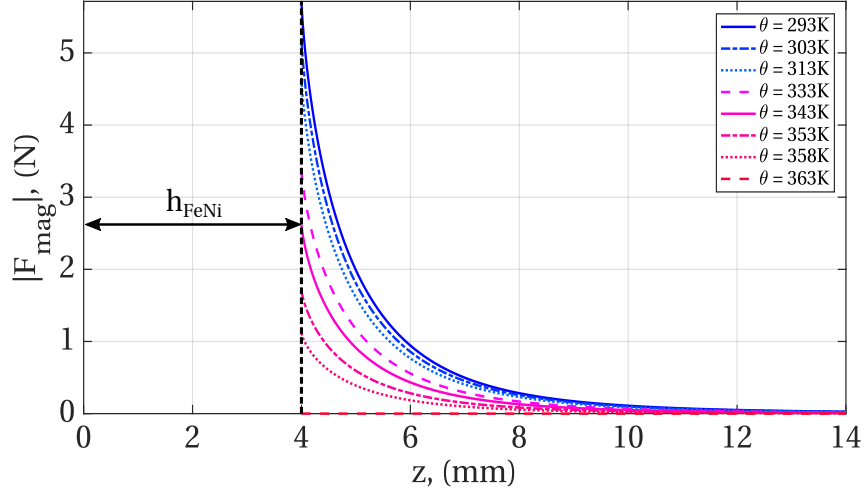


FIGURE 3.11: Evolution of magnetic force (absolute value) as a function of the temperature of soft magnetic material and the gap distance between the the permanent magnet. This model considers the following parameters:  $\theta_C = 363K$ ,  $h_{FeNi} = 4 \times 10^{-3}m$ ,  $h_{mag} = 2 \times 10^{-3}m$ ,  $r_{mag} = 2 \times 10^{-3}m$ ,  $r_{FeNi} = 4 \times 10^{-3}m$ .

These results revealed that the magnetic attraction force is not linearly dependent neither on the distance of separation between the magnet and FeNi, nor on the temperature of the FeNi alloy. Thus, this fact increase in complexity the system. However, we set out to investigate the influence of the dimensions of the volumes involved on the triggering system in order to establish the efficient direction in miniaturizing such a device.

As shown in [Figure 3.11](#), at the temperature of Curie of this soft magnetic volume, there exist a magnetic force but is no significant compared with that one of the restoring mechanical force. Thus, the generator can be driven to its two operation positions with the balance of these two forces. Moreover, from these results, it can be concluded that increasing the temperature of the soft magnetic alloy results in decreasing the magnetic force; similarly, for the dependence on the gap distance. With regards the dimensions of the permanent magnet, we decided to explore their influence on the magnetic force developed for a given volume and configuration of the soft magnetic alloy when a gap distance is constant as well as temperature. Because of the role of the permanent magnet is crucial (i.e., acting as seismic mass and providing the external magnetic field for actuation), we decided to do a parametric study in the dimensions of the magnet keeping constant the initial position of the transducer  $z_0$  as well as its temperature  $\theta$ . These results are depicted in [Figure 3.12](#)

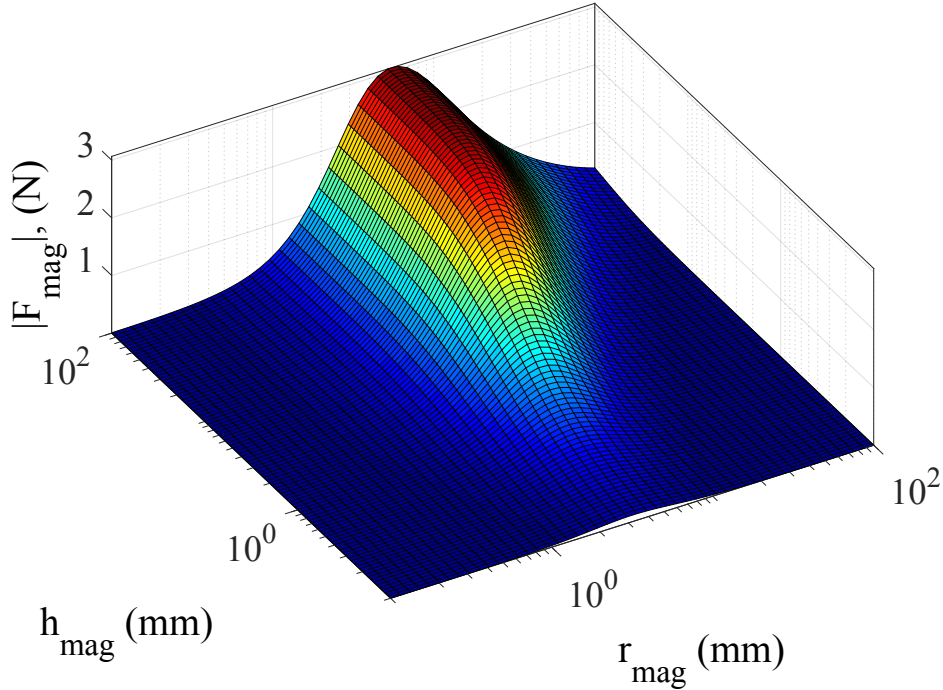


FIGURE 3.12: Influence of the magnet's dimensions on the attraction magnetic force for a given triggering system comprising a  $V_{FeNi} = 7 \times 10^{-7} \text{m}^3$ , a constant initial position  $z_0 = 6 \times 10^{-3} \text{m}$ , and room temperature  $\theta = 293 \text{K}$ .

From Figure 3.12 it is evident that maximum magnetic force can be reached when selecting the appropriate dimensions of the magnet. However, for this particular architecture of the generator; the permanent magnet is attached to the free end of the cantilever beam. Therefore, increasing the magnet dimensions results in increasing the effective mass of the cantilever beam, thus lower resonance frequencies. Regarding the soft magnetic alloy, an increase on its volume leads to greater magnetic force. However, this is increasing as well the constant of time for the temperature response of the generator. Miniaturization of this energy harvesting approach is the interest of deriving these design parameters, so decreasing the volume of the soft magnetic alloy has to be done at the same time of reducing the size of the permanent magnet so the ratio actuation forces and temperature response of the device is improved.

Following the scaling approach aforementioned, we can also explore the influence of the dimensions on this magnetic model section. Even if it is not trivial to see what could be the resulting contribution of the scale factor  $\alpha$  on the magnetic force, it scale at least as  $\alpha^2$  as can be deduced from Equation 3.11.

At this point, we have already derived the equations for one of the two actuation forces, calculation of the counter-reaction force is described below.

### 3.3.4 Mechanical model

Concerning the mechanical modeling of the generator, we decided to divided it into two main sections, the static behavior and the transient behavior. In the static behavior, it will be detailed the analytical expression for obtaining the operation temperatures of the device as a response of its design. While for the transient behavior, the main goal is to explore the performance of the generator for a given input scenario.

#### 3.3.4.1 Mechanical modeling of the static behavior

Before discussing the different effects governing the vibration, let us first understand the physics by just considering one complete thermal cycle. Firstly, given an initial design for the generator, its operation temperatures  $\theta_{opening}$  and  $\theta_{closing}$  have to be derived. The method we used to derive these parameters is in line with a variation of the same as that used by Korvink *et al.* [88] for an electrostatic parallel-plates actuator and its pull-in voltage and travel. First, we estimated the total balance force in the system. Since the actuation forces on the generator are  $F_{mag}$  and  $F_{mec}$ , we are interested in finding the stable position for this interaction. Thus, the resultant force can be described as:

$$F_{mec} = F_{mag} \quad (3.12)$$

Using Equation 3.10 and Equation 3.18 (neglecting the piezoelectric contribution), we can rewrite the force as follows:

$$k(z_0 - z) = \Gamma \int_0^{\infty} J_1(\chi r_{FeNi}) J_1(\chi r_{mag}) \Psi \chi^{-1} d\chi \quad (3.13)$$

with

$$\begin{aligned} \Psi &= e^{-\chi z} + e^{-\chi(z - h_{FeNi} + h_{mag})} - e^{-\chi(z - h_{FeNi})} + e^{-\chi(z + h_{mag})} \\ \Gamma &= \mu_0 \pi r_{mag} r_{FeNi} M_{mag} M_{FeNi} \end{aligned}$$

After arranging previous equation, it can be obtained the expression of the magnetization of the FeNi as a function of  $z$  as follows:

$$M_{FeNi}(z) = \frac{k(z - z_0)}{\Gamma_3 \int_0^{\infty} J_1(\chi r_{FeNi}) J_1(\chi r_{mag}) \Psi \chi^{-1} d\chi} \quad (3.14)$$

with

$$\begin{aligned} \Psi &= e^{-\chi z} + e^{-\chi(z - h_{FeNi} + h_{mag})} - e^{-\chi(z - h_{FeNi})} + e^{-\chi(z + h_{mag})} \\ \Gamma_3 &= \mu_0 \pi r_{mag} r_{FeNi} M_{mag} \end{aligned}$$

For a given transducer architecture (dimensions of piezoelectric bimorph and permanent magnet) it implies a mechanical stiffness  $k$ . For the purpose of simplicity we are going to assume a known value of stiffness (which can then be corroborated by finite element simulation or measurements of the transducers). A particular representation of this function  $M_{FeNi}(z)$ , for a given value of initial position of the transducer  $z_0$  is shown in Figure 3.13.

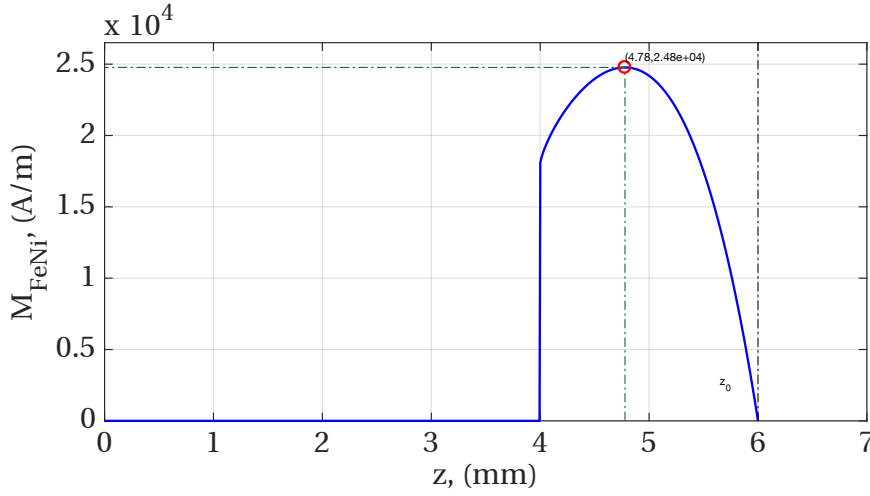


FIGURE 3.13: Representation of  $M_{FeNi}(z)$  for a given initial position  $z_0 = 6 \times 10^{-3}\text{m}$ ,  $h_{FeNi} = 4 \times 10^{-3}\text{m}$ ,  $r_{FeNi} = 7 \times 10^{-3}\text{m}$ ,  $h_{mag} = 2 \times 10^{-3}\text{m}$ ,  $r_{mag} = 2 \times 10^{-3}\text{m}$ ,  $k = 300\text{N m}^{-1}$  and when the entire system has a temperature of  $\theta = 293\text{K}$ .

Useful information can be extracted from the above figure. First, the FeNi alloy is located in such a way that from  $z = 0$  up to  $z = h_{FeNi}$  is occupied by this volume. Second, the movable magnet attached to the tip beam is initially positioned at  $z_0 = 6 \times 10^{-3}\text{m}$ . The latter can be displaced in the range  $[4 \times 10^{-3}\text{m}, 6 \times 10^{-3}\text{m}]$ . Second, a mechanical stiffness of  $k = 300\text{N m}^{-1}$  considered for this representation is assumed for a spring constant fixed at  $z_0$ . So the graph can be interpreted as follows: the magnetization of the FeNi alloy is considered only on the range where the movable magnet can be displaced. Below the height of the soft magnetic alloy, it is not a consideration for this magnetization. Furthermore, at the upper face of the FeNi alloy, it is seen that the magnetization increases abruptly from 0 until reaching a certain value, which can be considered as the value of magnetization of FeNi material required for maintaining the permanent magnet in contact (i.e., the closed position of the generator). Once the permanent magnet is away from the FeNi, the magnetization increases exhibiting a maximum point (i.e., it is also known as the critical point for which the system exhibits the threshold between the stable and unstable equilibriums). In this case, all values of  $z$  below the critical point are in the stable equilibrium zone, which means the magnetic contact of the triggering system. Conversely, all  $z$  values above the critical point correspond to the unstable equilibrium of the system, the open position and the oscillatory stage of the transducer beam.

Initially, we thought that finding this maximum point of the curve, we will be able to express the critical point of the system in a general form. However, we evaluated for different initial positions  $z_0$  of the magnet and what we found is that it does not follow a linear relationship. To put in evidence this behavior, we did a parametric study of the analytical expression as shown in [Figure 3.14](#).

It can be seen that the critical point of the system as a function of the initial position of the transducer  $z_0$  has a non linear behavior. This is why we decided to evaluate numerically the expression in order to find this critical point for every initial position value.

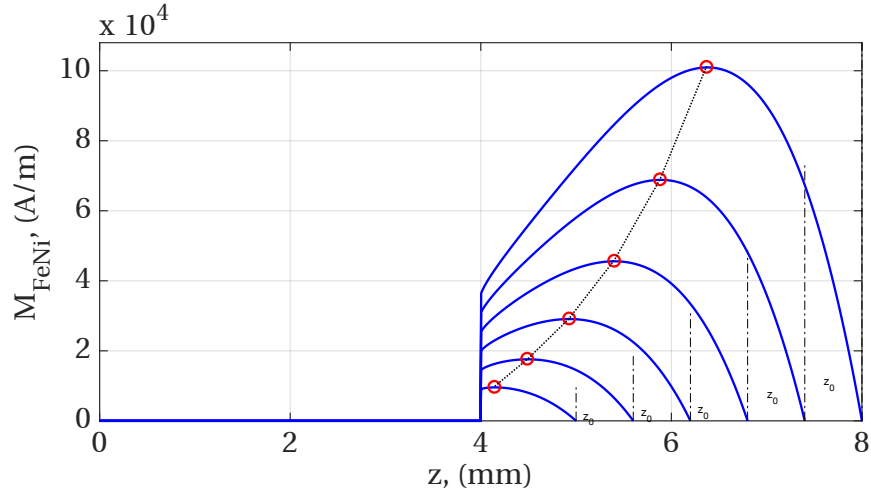


FIGURE 3.14: Parametric study of the Magnetization  $M_{FeNi}(z)$  for a constant spring magnet-mass system, the parameters are as listed in Table 3.1 and considering a spring constant  $k = 300\text{N m}^{-1}$  as the mechanical stiffness of the transducer beam.

From Figure 3.14 it is evident that for every initial position value, the critical point of equilibrium should be a fraction of it. So, let us assume that  $H$  is the fraction of the initial position of the transducer. Using this approach, we can obtain a general expression for the opening commutation of the generator as follows:

$$\theta_{open}(z_0) = \theta_C \left[ 1 - \left( \frac{k(Hz_0 - z_0)}{\Gamma_4 \int_0^\infty J_1(\chi r_{FeNi}) J_1(\chi r_{mag}) \Psi_2 \chi^{-1} d\chi} \right)^{\beta^{-1}} \right] \quad (3.15)$$

with

$$\begin{aligned} \Psi_2 &= e^{-\chi Hz} + e^{-\chi(Hz_0 - h_{FeNi} + h_{mag})} - e^{-\chi(Hz_0 - h_{FeNi})} + e^{-\chi(Hz_0 + h_{mag})} \\ \Gamma_4 &= \mu_0 \pi r_{mag} r_{FeNi} M_{mag} M_{FeNi}(0) \end{aligned}$$

Similarly, making the balance of actuation forces when the generator is at its open position. In other words, it is now required an attraction magnetic force greater than the maximal mechanical force to ensure the closing commutation. Thus, the temperature for closing commutation is given by:

$$\theta_{close}(z_0) = \theta_C \left[ 1 - \left( \frac{k(h_{FeNi} - z_0)}{\Gamma_4 \int_0^\infty J_1(\chi r_{FeNi}) J_1(\chi r_{mag}) \Psi_3 \chi^{-1} d\chi} \right)^{\beta^{-1}} \right] \quad (3.16)$$

with

$$\Psi_3 = e^{-\chi h_{FeNi}} + e^{-\chi h_{mag}} - 1 - e^{-\chi(h_{FeNi} + h_{mag})}$$

$$\Gamma_4 = \mu_0 \pi r_{mag} r_{FeNi} M_{mag} M_{FeNi}(0)$$

At this point, we are able to derive the thermal thresholds given for an initial design of the generator (i.e., initial position of transducer beam, mechanical stiffness and dimensions). To better understand the quasi-static behavior of the generator, we conducted experimental measurements on a prototype for which we fixed the parameters like the dimensions of soft magnetic material, transducer bimorph and permanent magnet. The only parameter we changed was the initial position of the transducer beam,  $z_0$ , consequently, the gap distance between the magnet and the soft magnetic material is also changed. We opted for three different values of this parameter  $z_0$ :  $5 \times 10^{-3}$ ,  $6 \times 10^{-3}$ , and  $7 \times 10^{-3}$  m, considering that the FeNi alloy is fixed at the origin of z-axis and it has a height of  $4 \times 10^{-3}$  m. For each initial position, the experiment was repeated under conditions in which the ambient temperature was about 295K and the maximum temperature at which the soft magnetic material was heated is 350K.

Through a triangulation technique using a laser sensor, we monitored the vertical displacement at the free end of the cantilever beam all the time during the experiment. These first set of experiments confirmed the impact of the initial gap distance on both the operation temperatures and the thermal hysteresis. The latter describes the separation between the commutation temperatures for a given design of the generator. Figure 3.15 shows these experiment results.

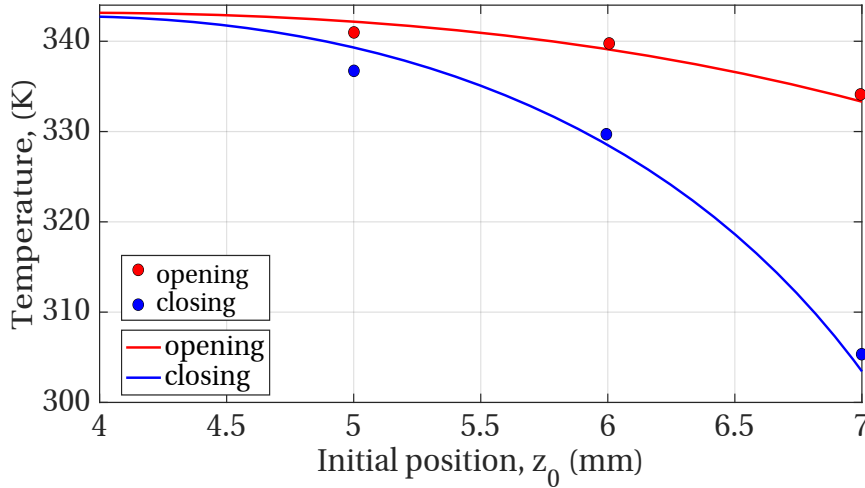


FIGURE 3.15: Comparison of analytical prediction of operating temperatures with experimental results showing the impact of the initial position of the transducer  $z_0$  for a constant design of transducer. The soft magnetic material sample having a Curie temperature around  $\theta_C = 343\text{K}$ , and the mechanical stiffness  $k = 300\text{N m}^{-1}$ .

The correlation between observed data and the model prediction was tested. Broadly speaking, we found values for opening and closing temperatures of a given generator design as function of the initial position of the transducer. Although our theoretically obtained

results differ slightly from those of experimentally obtained, it can nevertheless be argued that the prediction model is an approximation tool that allow engineers to get a first image of the possible operation temperatures range of the generator, without having to undertake a prototyping stage. This can be advantageous when designing to match with specific requirements for this kind of generators.

It is plausible that a number of limitations may have influenced the results obtained. First, the assumptions considered on characterizing the magnetic attraction force on the triggering system; supposing that the magnetic volume is perpendicular to the symmetry axis of the permanent magnet, which is not always true in practical experiences (i.e., the angle of flexion of the beam tends to be important when. large deflections are exhibit). Another possible source of error is the characterization of the soft magnetic material, which influences directly on the generator response. Unfortunately, we were unable to investigate the thermo-magnetic parameters of our iron-nickel sample directly from the fabricant. Further data collection would be needed to determine exactly the thermo-magnetic parameters of the soft magnetic alloy.

These data revealed that it is possible to tune the operation temperatures by adjusting the initial position of the transducer, thus modifying the traveling range of the beam. Moreover, to obtain commutation temperatures near to environment, higher traveling ranges must be considered. In contrast, by increasing the traveling of the beam, the thermal hysteresis is also increased, which may dramatically increase the period between commutations (i.e., the time needed for passing from one commutation to the other one).

We believe that reducing the volume of the soft magnetic material can dramatically reduce the thermal response response of the generator, in other terms the period time between commutations. Making an energy conversion balance of the system, it may be apparent that the initial deflection of the beam represents the maximum possible output energy that can be converted into electricity, thus greater initial gaps are desired. Added to this; lower thermal hysteresis is expected in order to reduce the transition period between commutations. This is the reason for believing that we found analytical model of such a system able to predict its quasi-static and dynamic behaviors as a response of its design.

In the next section; it will be detailed the electro-mechanical model of the thermo-magnetically triggered piezoelectric generator. This model takes into account the geometry design of the transducer bimorph, as well as the triggering system including the permanent magnets, hence, acting as a seismic mass for the transient response of the generator.

#### 3.3.4.2 Mechanical modeling of the transient behavior

The vibration of the piezoelectric cantilever beam under the attraction magnetic force can be described as a second order mass-spring-damper system, along with a piezoelectric element connected parallel to the damper. The electro-mechanical behavior of the micro generator, can be described with a good approximation by a one-dimension lumped parameter model. We assume that the system respects the Euler-Bernoulli theory for beams in flexion. The governing equation with the addition of suitable damping, can be written, as follows:

$$m\ddot{z} + C\dot{z} + kz = F_{mag} \quad (3.17)$$

Where  $m$ ,  $C$ , and  $k$  are, respectively, effective mass, total damping coefficient, and effective stiffness of the system. If the steady vibration is reached, we can safely state that the energy accumulated by the system due to the magnetic force equals the energy dissipated in damping. As mentioned earlier,  $F_{mag}$  is the magnetic attraction force, which depends on the beam's tip displacement and the temperature  $\theta$ . This force is countered by the mechanical force  $F_{mec}$  (i.e., the counter-reaction force exerted by the bimorph cantilever beam). This force is depending on the electro-mechanical coupling, which can be described as:

$$F_{mec}(z) = k(z_0 - z) + \alpha V_{piezo} \quad (3.18)$$

$$i(t) = \alpha_{piezo} \dot{z} - C_0 \frac{dV_{piezo}}{dt} \quad (3.19)$$

Where  $k$  is the mechanical equivalent stiffness of the cantilever beam,  $\alpha_{piezo}$  is the force factor of the piezoelectric material in  $\text{N m}^{-1}$ ,  $V_{piezo}$  is the piezoelectric generated voltage, and  $C_0$  is the capacitance of the piezoelectric elements. We further assume a series electrical configuration for the bimorph. The two piezoelectric layers of the cantilever beam are poled in opposite directions so that during bending, when one half is in tension and the other is in compression, the generated surface charges have additive effects. A load resistor is connected in parallel to the upper and bottom faces of the bimorph as shown in Figure 3.16

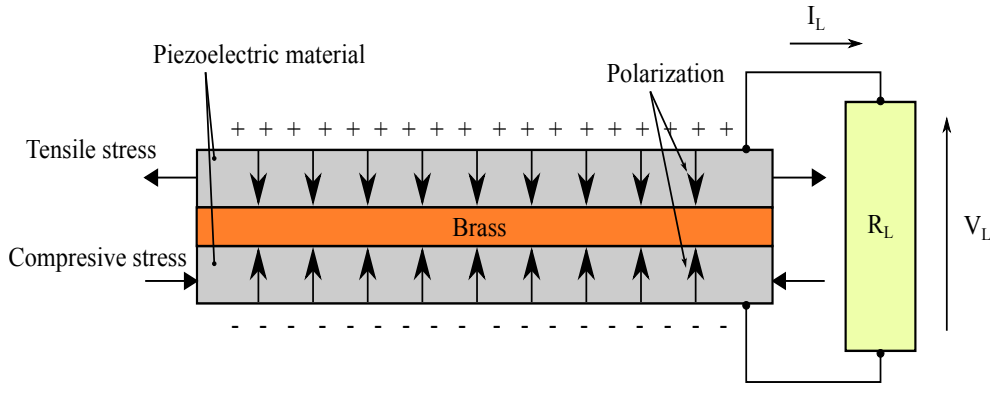


FIGURE 3.16: Schematic of the piezoelectric bimorph and the load resistance connected to the electrodes of the piezoelectric transducer.

When the commutations from closed to open positions of the generator are reached, the cantilever beam exhibits an oscillatory stage with an important velocity. Therefore, a piezoelectric tension is generated on the electrodes where the load resistor dissipates this power. At the open position of the generator, even if it reaches its stable position there is a mechanical strain in piezoelectric bimorph due to the presence of weak magnetic force in the system, however, the cantilever beam has not velocity and thus, no piezoelectric potential is generated. By cooling soft ferromagnetic material, it takes back its magnetization due to the external flux density of the permanent magnet. In this phase, the permanent

hard magnet is attracted towards soft magnetic material by magnetic force, and bending strain is applied to piezoelectric cantilever, resulting in piezoelectric potential.

The dynamic system is now a coupled system between the vibration and the electrical charge equation.

$$F_{mag}(z) = m\ddot{z} + C\dot{z} + k(z_0 - z) + \alpha_{piezo} V_{piezo} \quad (3.20)$$

$$i(t) = \alpha_{piezo} \dot{z} - C_0 \frac{dV_{piezo}}{dt} \quad (3.21)$$

The coupled system can be solved iteratively. More details including estimation of the equivalent stiffness and the effective mass are presented on the following sections.

### 3.3.5 Electro-mechanical model

As can be seen from the previous section, one of the design parameters that is not directly controlled is the equivalent stiffness of the transducer  $k$ . Approximating this parameter as a function of the dimensions of the generator can be advantageous in order to better designing such generators. It is important to remark that the presented architecture of the transducer beam (i.e., piezoelectric bimorph) is only one possibility of various possible. In order to explore the energy harvesting capabilities of different configurations of the piezoelectric transducer we chose to develop a mathematical model describing the behavior of the piezoelectric transducer for which the piezoelectric layers can be deposited all the length of the shim layer or only one portion, like a piezoelectric patch for instance. This is shown in Figure 3.17.

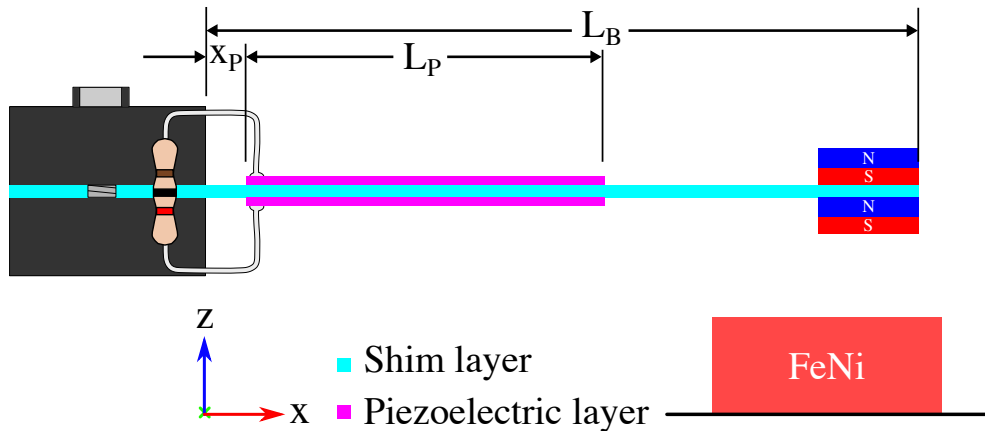


FIGURE 3.17: Schematic representation of possible architecture of piezoelectric transducer considered for the analytic model, the length of the piezoelectric layers can be shorter or the same of that of the shim layer.

For the sake of simplicity, we are considering the nomenclature of the mechanical motion as the same used of the mechanics experts. That is, for vertical displacement  $z \rightarrow w$ , horizontal displacement  $x \rightarrow u$ , and in-plane displacement  $y \rightarrow v$ .

We assume by hypothesis that the deformation at the free end of the beam is similar to that one produced when applying a static force  $F_s$  at the free end of the beam. In this case the equilibrium of the structure leads to the following equation

$$\ddot{w} = \begin{cases} \frac{F_s(L_B-x)}{c_B I_B} & \text{for } x \in [0, x_P \cup x_P + L_P, L_B] \\ \frac{F_s(L_B-x)}{c_B I_B + c_{PD} I_{PD}} & \text{for } x \in [x_P, x_P + L_P] \end{cases} \quad (3.22)$$

here,  $I_B$  and  $I_P$  are, respectively, the inertia moment the cantilever bimorph for the shim and the piezoelectric layers.  $c_{PD}$  represents the stiffness of the piezoelectric layer in open circuit under plane deformation and  $c_B$  the stiffness of the shim layer of the bimorph.  $x_P$  represents the separation length between the origin of the beam and the beginning of the piezoelectric layer. These parameters can be computed according with the following expressions [89].

$$c_B = \frac{Y_B}{1 - \nu_B^2} \quad (3.23)$$

$$I_B = \frac{1}{12} w_B h_B^3 \quad (3.24)$$

$$c_{PD} = \left[ S_{xx}^E - \frac{(S_{xy}^E)^2}{S_{xx}^E} - \frac{(d_{xz})^2 \left(1 - \frac{S_{xy}^E}{S_{xx}^E}\right)^2}{\epsilon_{zz}^T - \frac{(d_{xz})^2}{s_{xx}^E}} \right]^{-1} \quad (3.25)$$

$$I_P = 2 \left[ \frac{1}{12} w_B h_B^3 - w_B h_P \left( \frac{h_B + h_P}{2} \right)^2 \right] \quad (3.26)$$

The integration of Equation 3.22, and considering the boundary conditions of a fixed-free cantilever beam, give the following expression:

$$w = \begin{cases} \frac{F_s^2(3L_B-x)}{6c_B I_B} & \text{for } x \in [0, x_P[ \\ \frac{F_s^2(3L_B-x)}{6(c_B I_B + c_{PD} I_{PD})} + Gx + H & \text{for } x \in [x_P, x_P + L_P] \\ \frac{F_s^2(3L_B-x)}{6c_B I_B} + Ix + J & \text{for } x \in ]x_P + L_P, L_B] \end{cases} \quad (3.27)$$

where the constants  $G$ ,  $H$ ,  $I$ , and  $J$  are defined by

$$\begin{aligned}
G &= \left( \frac{1}{c_B I_B} - \frac{1}{c_B I_B + c_{PD} I_P} \right) \frac{F_s x_P (2L_B - x_P)}{2} \\
H &= \left( \frac{1}{c_B I_B} - \frac{1}{c_B I_B + c_{PD} I_P} \right) \frac{F_s x_P^2 (2x_P - 3L_B)}{6} \\
I &= \left( \frac{1}{c_B I_B} - \frac{1}{c_B I_B + c_{PD} I_P} \right) \frac{F_s x_P (2L_B - x_P) - F_s (L_P + x_P) (2L_B - x_P - L_P)}{2} \\
J &= \left( \frac{1}{c_B I_B} - \frac{1}{c_B I_B + c_{PD} I_P} \right) \frac{F_s x_P^2 (2x_P - 3L_B) - F_s (L_P + x_P)^2 (2x_P + 2L_P - 3L_B)}{6}
\end{aligned} \tag{3.28}$$

We suppose that the structure can be described by a lumped parameter model, so the parameters of the system respect energy considerations. The effective mass  $m$  of the system is determined by

$$m = m_{mag} + \frac{\int_0^{L_B} m_x w^2 dx}{w^2(L_B)} \begin{cases} m_x = w_B h_B \rho_B & \text{for } x \in [0, x_P \cup] x_P + L_P, L_B] \\ m_x = w_B (h_B \rho_B + 2h_P \rho_P) & \text{for } x \in [x_P, x_P + L_P] \end{cases} \tag{3.29}$$

where  $m_{mag}$  represents the mass of the magnet, and  $m_x$  the lineal mass of the structure. The equivalent stiffness of the structure  $k$ , depending on the section of the cantilever beam (i.e., section with only shim layer or with shim and piezoelectric layers, are computed by the following expression

$$k = \frac{1}{\frac{1}{k_1} + \frac{1}{k_{2PD}} + \frac{1}{k_3}} \tag{3.30}$$

where  $k_1$  represents the stiffness of the cantilever beam section from the fixed end to the beginning of the piezoelectric layer,  $k_{2PD}$  corresponds to the stiffness of the section with piezoelectric layers in open circuit, and  $k_3$  depicts the stiffness of the section of the cantilever beam without piezoelectric layer up to the free end of the beam.

$$\begin{aligned}
k_1 &= \frac{3c_B I_B}{x_P (3L_B^2 - 3L_B x_P + x_P^2)} \\
k_{2PD} &= \frac{3(c_B I_B + c_{PD} I_P)}{L_B (3L_B^2 - 3L_B L_P - 6L_B x_P + L_P^2 + 3L_P x_P + 3x_P^2)} \\
k_3 &= \frac{3c_B I_B}{(L_B - x_P - L_P)^3}
\end{aligned} \tag{3.31}$$

Now, we intend to conduct a dynamic simulation in order to explore the transient energy harvesting capabilities of the device. Exploiting [Equation 3.27](#), [Equation 3.28](#), [Equation 3.29](#), [Equation 3.30](#), and [Equation 3.31](#) the equivalent stiffness and the effective mass of the transducer can be obtained. The utility of calculating these parameters is demonstrated when developing a transient behavior study of the generator, which is described below.

Considering the material properties listed in [Table 3.4](#), we computed the equivalent stiffness of the system, after completion of this stage, the static and dynamic behavior of the generator can be explored. The presented architecture of the transducer beam (i.e., piezoelectric bimorph) is only one possibility of various possible. In order to explore the energy harvesting capabilities of different configurations of the piezoelectric transducer we chose to develop a mathematical model describing the behavior of the piezoelectric transducer for which the piezoelectric layers can be deposited all the length of the shim layer or only one portion, like a piezoelectric patch for instance.

The static behavior of the generator comprises the operation for which the system passes from the closed position to the open one and vice versa. This is critical for designing and giving a first estimation of the performance that can be achieved by the device under a specific scenario. By reducing the amount of soft magnetic material, the magnetic force is also reduced, however, it implies lower constants of time for the temperature transient response of the device. In addition, to compensate the weakness of this magnetic force due to reduction of the soft magnetic material volume, a lower equivalent stiffness of the generator has to be considered. This can be reached by means of different ways:

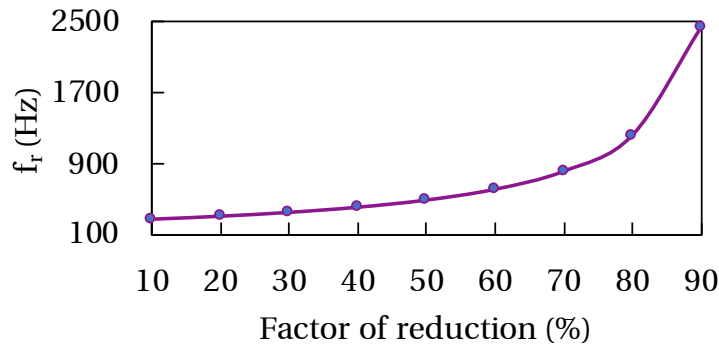
- Modifying the thickness of the piezoelectric layers; from [Equation 3.24](#) and [Equation 3.26](#), the equivalent stiffness  $k$  has a sensitivity to this parameter in a power of three.
- Adjusting the length of the piezoelectric layers; the mathematical model describing the electro-mechanical behavior of the generator able us to consider different lengths of the piezoelectric layers in order to adjust the equivalent stiffness of the system.
- Reducing the volume of permanent magnet, in this architecture of generator presented here considers the permanent magnet attached to the cantilever beam, by reducing the mass of the magnet, it reduces the effective stiffness of the transducer, which in turn implies a greater oscillation frequency of the transducer, thus higher amount of kinetic energy that can be converted into electricity during the open commutation.

Considering a dimension reduction factor for the whole system, we investigated the influence of the scale-reduction on the resonance frequency of the transducer during the opening commutation. These results are shown in [3.18\(a\)](#). Moreover, in order to bring out the influence of the scaling reduction on the energy harvesting capability of the generator, we opted for exploiting the theoretical model assuming that a reduction factor is considered for the whole generator dimensions. In order to compare these designs, we have taken into account a constant range of temperature for which the generator should be able to operate (i.e., open temperature and closing temperature); opening temperature always below the Curie temperature of the soft magnetic alloy which is 343K and closing temperature 283K. The reasons for selecting this criterion were to compare the generator commutations for its maximum possible initial gap; for the same closing temperature in all designs. These results are shown in [3.18\(b\)](#)

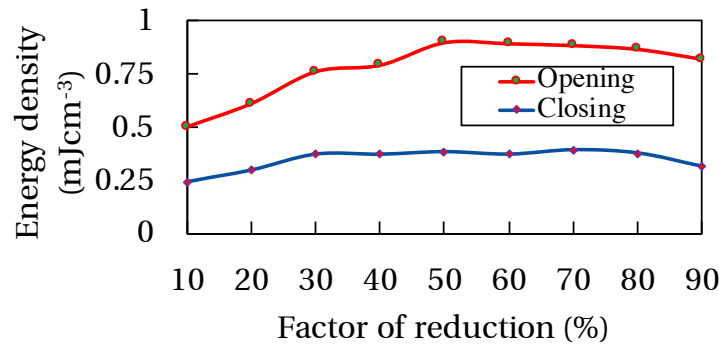
As mentioned above, a considerable improvement on the energy harvesting capabilities of the generator can be done by increasing the resonance frequency of the transducer. Also, this size reduction offers shorter time constants for the heat transfer stage. We believe

TABLE 3.4: General parameters of the initial design of the generator for calculating the operation temperatures.

System	Parameter	Symbol	Units	Value
Bimorph cantilever beam	Length of cantilever beam	$L_B$	m	$20 \times 10^{-3}$
	Width of cantilever beam	$w_B$	m	$4 \times 10^{-3}$
	Thickness of shim layer	$h_B$	m	$100 \times 10^{-6}$
	Young's modulus of shim layer	$Y_B$	Pa	$100 \times 10^6$
	Poisson's ratio	$\nu_B$	-	0.3
	Density of shum layer	$\rho_B$	$\text{kgm}^{-3}$	7500
Bimorph piezoelectric material	Length of piezoelectric layer	$L_P$	m	$20 \times 10^{-3}$
	Thickness of piezoelectric layer	$h_P$	m	$105 \times 10^{-6}$
	Compliance when closed circuit	$s_{xx}^E$	$\text{Pa}^{-1}$	$20.5 \times 10^{-12}$
		$s_{xz}^E$	$\text{Pa}^{-1}$	$-8.45 \times 10^{-12}$
		$s_{xy}^E$	$\text{Pa}^{-1}$	$-4.78 \times 10^{-12}$
		$s_{zz}^E$	$\text{Pa}^{-1}$	$13.45 \times 10^{-12}$
	Piezoelectric coefficient	$d_{xz}$	$\text{CN}^{-1}$	$-274 \times 10^{-12}$
	Permittivity at constant strain	$\epsilon_{zz}^S$	$\text{F m}^{-1}$	$30.1 \times 10^{-9}$
	Permittivity at constant stress	$\epsilon_{zz}^T$	$\text{F m}^{-1}$	$27.7 \times 10^{-9}$
	Triggering system soft magnetic alloy	Radius of soft magnetic alloy	$r_{FeNi}$	m
Thickness of soft magnetic alloy		$h_{FeNi}$	m	$4 \times 10^{-3}$
Density of soft magnetic alloy		$\rho_{FeNi}$	$\text{kgm}^{-3}$	6000
Curie temperature		$\theta_C$	K	343
Critical exponent		$\beta$	-	0.625
Specific heat		$c_{FeNi}$	$\text{J kg}^{-1} \text{K}^{-1}$	505
Saturation magnetization at 0K		$M_s(0)$	$\text{Am}^{-1}$	$1.25 \times 10^5$
Heat transfer coefficient		$\lambda_c$	$\text{W m}^{-2} \text{K}^{-1}$	28
Fan speed		$\omega_{fan}$	rps	33.33
Mass flow rate		$\dot{m}$	$\text{kg s}^{-1}$	$5 \times 10^{-4}$
Triggering system magnet	Radius of magnet	$r_{mag}$	m	$2 \times 10^{-3}$
	Thickness of magnet	$t_{mag}$	m	$2 \times 10^{-3}$
	Density of magnet	$\rho_{mag}$	$\text{kgm}^{-3}$	5000
	Initial position of transducer	$z_0$	m	$6 \times 10^{-3}$



(a)



(b)

FIGURE 3.18: Effect of the generator's dimension reduction on (a) its natural resonance frequency during the opening commutation, (b) its output energy density per commutations. The initial generator size is resulting from parameters listed on [Table 3.4](#).

this solution will aid to designing miniaturized thermo-magnetically triggered piezoelectric generators towards the MEMS scale. It can be also seen that the energy density per commutation of the generator has an optimal point. These results suggest that a design optimization study can aid to enhance the performance of the generator. The transient response of the system has been studied and most relevant outcomes are presented on the next section of this chapter.

### 3.3.6 Dynamic behavior of the generator

In order to investigate the dynamic performance of the initial design of generator, we conducted a transient simulation of the coupled system solving iteratively the equations aforementioned. We opted for implementing this mathematical model in Matlab for solving the coupled system iteratively. The simulation considers a time step of  $200\mu\text{s}$  to check the mechanical vibration of the beam during its commutations. First, the temperature response of the system was explored. At the initial time of simulation, an electrical current is applied and maintained constant up to the half of the time simulation end. The whole system is at ambient temperature of  $293\text{K}$ , therefore, it is in closed position. Once simulation reaches half of time, electrical current is turned off and simultaneously the fan is turned on to get a

forced convection on the generator system. This state continues until the end of the simulation.

We did monitor some important output variables of the generator over the simulation time, for instance: the temperature of the soft magnetic alloy, it confirms the quasi-static prediction of the generator, the operating temperatures of the system (which are expected to remain constant as the design is also constant), the tip cantilever beam displacement and its velocity, these values support the kinetic performance of the generator, and the output voltage on the terminals of the load resistor as well as the instantaneous power dissipated by the load resistor. Temperature response of this simulation is shown in Figure 3.19.

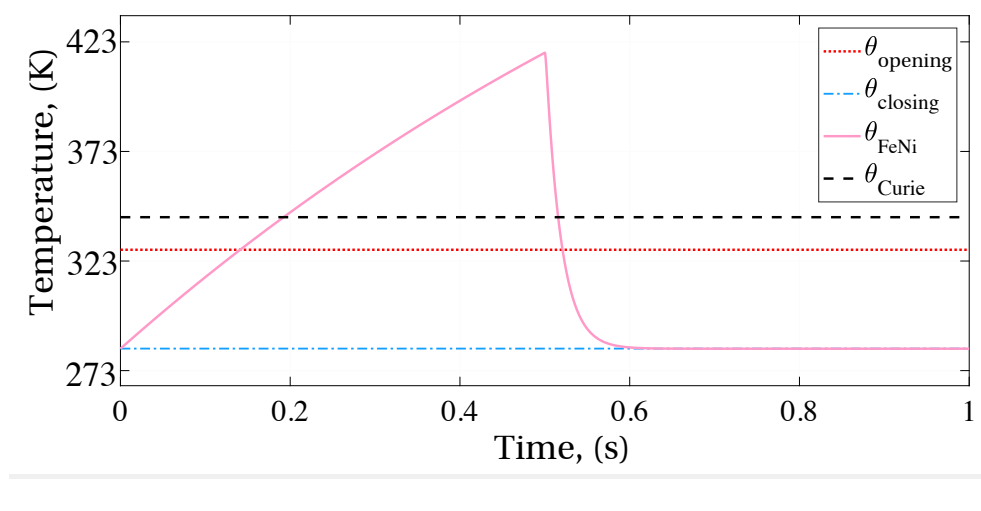


FIGURE 3.19: Temperature response of the generator, which has been reduced in a 50% of the size of the initial design listed in Table 3.4. The operating temperatures and the curie temperature are shown in the simulation transient behavior of the generator.

Based on the initial dimensions listed in Table 3.4, it has been theoretically demonstrated that if a reduction in size of the generator in 50%, it allows a faster temperature response. When compared with the temperature response of the design shown in Figure 3.7, it can be seen that the time constant for the heating off and cooling off stages are smaller when a miniature generator is considered. For this given design, let us consider a minimal closing temperature of 283K for which the maximal gap distance is 1.45mm. Then, to explore the transient response of the system the model has been solved iteratively over time. Figure 3.20 illustrates vertical displacement of the tip of the cantilever beam.

As expected, the initial position of the generator was at the closed position; thus, the contact between the soft magnetic material end the permanent magnet is done at the initial gap distance (i.e., -1.45mm with respect to the horizontal plane of the cantilever beam without deflection). This simulation result revealed that the frequency of the oscillations of the cantilever beam when the opening commutation is 475Hz. However, the value analytically estimated in a quasi-static behavior is 489Hz. The primary cause of this discrepancy is a result of the damping linked to the magnetic attraction force that is still present on the system even when the cantilever beam is released (at the opening commutation the magnetic attraction force is not strong enough to maintain the contact but to reduce the oscillations of the cantilever beam).

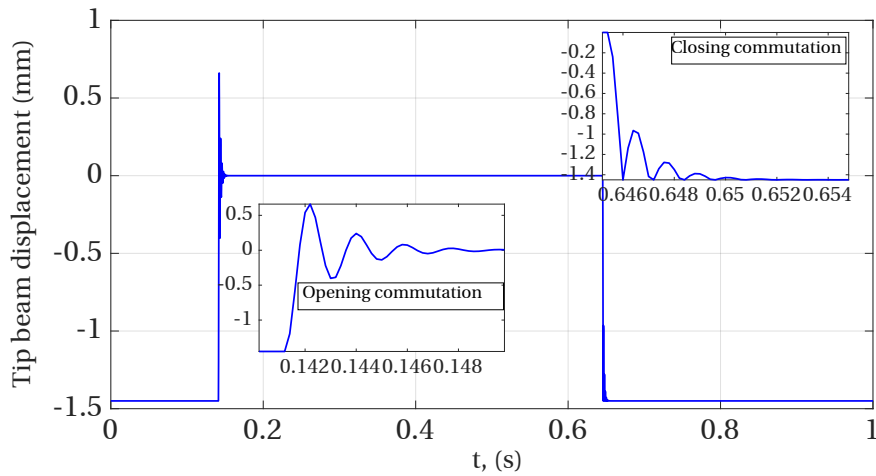


FIGURE 3.20: Simulation results of the tip beam displacement considering a reduced design of the generator in 50% with respect of its initial design listed in Table 3.4.

To describe the effect of the rebound when the closing commutation occurs, we adopted the approach of reinitialize the velocity of the tip cantilever beam to a new value at the instant the tip beam reaches the contact (i.e., the saturation limit, initial traveling distance  $z_0$ ). In our model, this method implies that when the magnet hits the soft magnetic alloy; its velocity can be set to a different value, i.e., to the velocity after the impact. Moreover, to capture the velocity of the tip cantilever beam just before the collision, a memory block is then used to calculate the velocity after the impact. The coefficient of restitution  $e$  is introduced as the ratio of the final to initial relative velocity between two objects after they collide. It normally ranges from 0 to 1 where 1 would be a perfectly elastic collision. For iron-nickel alloys, this coefficient oscillates between 0.15 and 0.7 [90], we have considered a value of 0.5.

The resulting vibration behavior of the cantilever beam can be validated as its velocity is zero for the phases where the generator is closed position and after it reaches steady state; it is after oscillations when releasing and impact due to contact. This is shown in Figure 3.21. In addition to the strain on the cantilever beam, these velocity responses would suggest that during the opening commutation another kind of transduction, electromagnetic for instance, could be implemented to extract electrical energy. It is desired to get greater deformations on the cantilever beam as this conduces to greater elastic energy initially stored on the generator. Furthermore, the influence of the equivalent stiffness on the natural frequency of the beam dictates that is suitable having higher frequencies as this increases the amount of energy during the opening commutation.

Solving for the electrical energy harvesting requires also solving a coupled system with an additional electrical boundary condition. The piezoelectric bimorph is considered to working linearly for the working range of the model; any internal resistance on the piezoelectric layers were ignored because of the lower value compared with the load resistance connected. The effect of the presence of the magnetic field on the electrical charge was neglected. A load resistor of  $15.8\text{k}\Omega$  was connected to the electrodes of the cantilever beam. This value of load resistor was selected to match with the value of the adapted resistance with a value described by the following expression

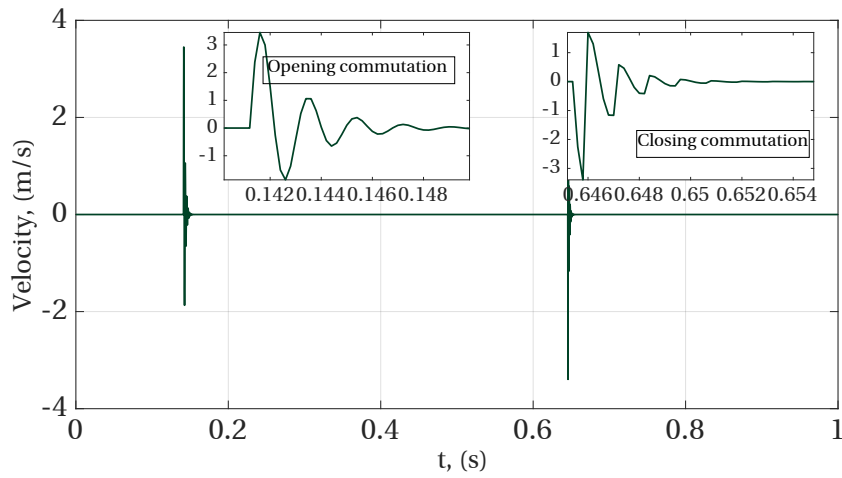


FIGURE 3.21: Simulation results of the tip beam velocity considering a reduced design of the generator in 50% with respect of its initial design listed in [Table 3.4](#).

$$R_L = \frac{1}{2\pi f_r C_0} \quad (3.32)$$

where  $f_r$  is the resonance frequency, of the transducer beam (including the permanent magnet attached to its free-end), and  $C_0$  is the piezoelectric capacitance. For this design, the resonance frequency of the transducer beam is  $f_r = 475\text{Hz}$  and its piezoelectric capacitance is  $C_0 = 21.1\text{nF}$ , resulting in a load resistance adapted  $R_L = 15.8\text{k}\Omega$ . The output voltage is shown in [Figure 3.22](#). The harvested power corresponds to the dissipated power on the load resistance. The instantaneous power is depicted in [Figure 3.23](#)

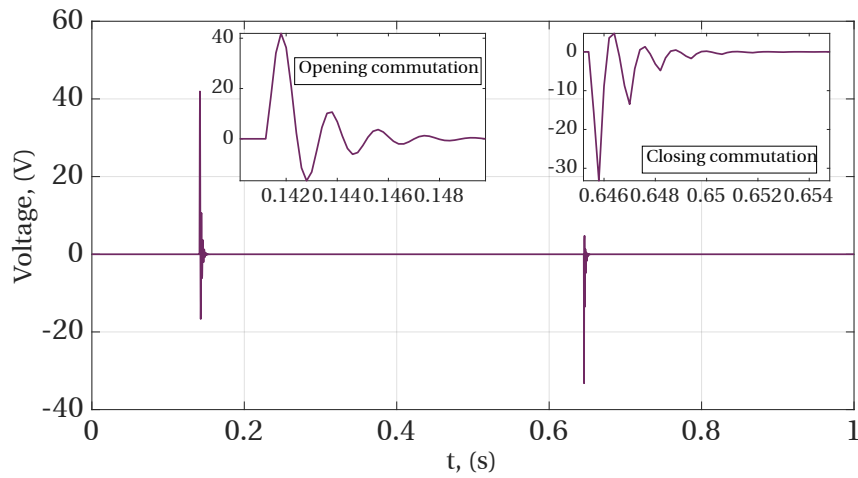


FIGURE 3.22: Output voltage response during a transient simulation of 1 thermal cycle of the generator when a load resistor  $R_L = 15.8\text{k}\Omega$  is connected to the electrodes of the transducer.

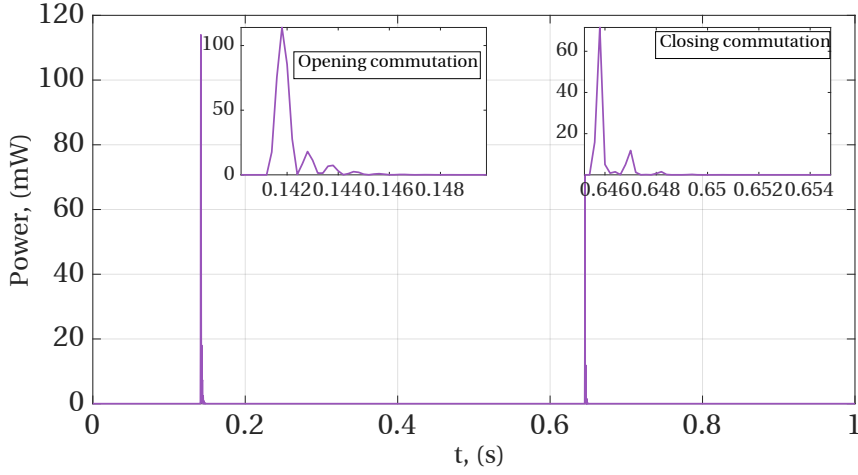


FIGURE 3.23: Instantaneous power response during transient simulation.

Since the input scenario where we planned to place this generator is uncertain and random, we decided to explore the performance of our generator in terms of energy density per commutation. In other words, for a worst case, when the temperature fluctuations allow the generator doing at least one thermal cycle of commutation (i.e., opening commutation and closing commutation). The effective volume considered is that generated when the cantilever beam reaches the maximum displacement towards the closed state and the opening one. Whereas for the average power per commutation it was estimated taking into account the duration time of 10 cycles of the fundamental oscillation of the cantilever beam, as shown in Equation 3.33. This approach is significant due to the possibility of comparing, based on the same criterion, different design generator's performance. The estimated energy densities per commutation of this initial design are listed in Table 3.5.

$$E = \int_0^{10T} p \, dt \quad (3.33)$$

here,  $T$  represents the period of the oscillations of the cantilever beam, and  $p$  the instantaneous power dissipated on the load resistor within a duration time of  $10T$  per commutation.

TABLE 3.5: Energy densities per commutation of the initial design of generator.

Energy density per commutations	Symbol	Units	Value
Opening commutation	$ED_{opening}$	$\mu\text{J cm}^{-3}$	900
Closing commutation	$ED_{closing}$	$\mu\text{J cm}^{-3}$	380

From Table 3.5 it can be seen that two different characterization indices have been employed; energy density at opening commutation and energy density at closing commutation. As the input scenario of for this kind of generator architecture will always drive the transition between the commutations, we have the interest in characterizing the performance of the generator based on each commutation. It is notable the difference in the amount of energy harvested between the two operation commutations of the generator.

### 3.4 Design rules of a thermo-magnetically activated piezoelectric generator

In conclusion, having an analytical model for this kind of generator is advantageous for doing some valuable predictions in terms of performance and efficiency. And having mathematical expression is useful in doing some scale factor analysis. As one of the goals of this dissertation is to investigate the feasibility of miniaturizing our presented generator, we decided first to present some design rules to take into account when designing such a kind of devices. After, a scale factor reduction analysis is presented and listed in Table 3.6 while an overall balance of the design parameters is listed in Table 3.7

TABLE 3.6: Scaling laws for a thermo-magnetically activated piezoelectric generator towards miniaturization.

Parameter	Symbol-Expression	Scaling factor	Effect
Stiffness	$k \propto E \frac{w_B h_B^3}{L_B^3}$	$\alpha$	$\searrow$
Mass	$m \propto w_B L_B h_B$	$\alpha^3$	$\searrow$
Resonance frequency	$f_r \propto \frac{1}{2\pi} \sqrt{\frac{k}{m}}$	$\alpha^{-1}$	$\nearrow$
Elastic force	$F_{mec} \propto E h_B h_B \frac{\Delta L_B}{L_B}$	$\alpha^2$	$\searrow$
Magnetic force	$F_{mag} \propto \frac{V}{4\pi\mu_0 r^3} \dot{j} \dot{i}$	$\alpha^3$	$\searrow$
Time constant heating	$\tau_{heating} \propto \frac{m_h c_{ph}}{\lambda_c S_L}$	$\alpha$	$\searrow$
Time constant cooling	$\tau_{cooling} \propto \frac{m_c c_{pc}}{\lambda_c S_{L-FeNi}}$	$\alpha$	$\searrow$
Piezoelectric capacitance	$C_0 \propto \frac{\epsilon A}{t}$	$\alpha$	$\searrow$
Thermal capacity	$c_p \propto \frac{\Delta E_{thermal}}{m \Delta \theta}$	$\alpha^3$	$\searrow$
Heat conduction rate	$Q \propto -\kappa S_L \frac{\Delta \theta}{\Delta z}$	$\alpha$	$\searrow$
Heat convection rate	$Q \propto \lambda S_L \Delta \theta$	$\alpha^2$	$\searrow$

As can be seen from these design guidelines, the reduction of the volumes of the generator device leads to better response in heat transfer. This reduction of the volume has to be done considering the rest of design rules listed in order to respect the operation restriction of the generator. The triggering system of the generator can be modified considering its two main parts: the soft magnetic alloy and the permanent magnet. The first can be reduced in volume without affecting the mechanical stiffness of the cantilever beam. In addition, reducing this part of the system, reduction on the time constants for heat up and cooling down processes is achieved. The strategy of reducing this soft magnetic volume has to be done always ensuring a strong enough magnetic force to ensure the closing commutation.

The reduction of size of the permanent magnet affects directly the oscillation frequency of the cantilever beam. But also it can be modified by moving the gravity center of the seismic mass (i.e., the permanent magnet at the tip of the cantilever beam). When placing the permanent magnet closer to the clamped section of the beam, actually the effective length (length from the clamped section and the contact zone of the beam) of the beam is reduced. This leads to higher frequencies on the oscillations. Thus higher amount of energy may be harvested during this commutation. Nevertheless, this action may be done with special

TABLE 3.7: Design guidelines of a thermo-magnetically activated piezoelectric generator.

Criterion	Design parameter	Operation	Design rule
Volume of soft magnetic material	$F_{mag}$	Drive thermal-dependent magnetization	It has to be strong enough to counter $F_{mec}$
	$\tau_{heating}$ $\tau_{cooling}$		As low as possible
Volume of magnet	$h_{mag}$ $r_{mag}$	Drive the external flux density $B_{mag}$ resulting in $F_{mag}$	Ensuring a functional $F_{mag}$ is a premise
	$m$	Acts as seismic mass	By reducing it, $\omega_n$ increases
	$k$	Stiffness of transducer	By increasing it, $\omega_n$ increases
Volume of piezoelectric transducer	$L_P$ $h_P$ $x_P$	Piezoelectric layers dimensions	They affect directly $F_{mec}$ , optimization needs to be conducted
	$L_B$ $h_B$ $w_B$	Shim layer dimensions	Thickness of layers have high impact on $k$
	$S_L$	Surface area of generator	As low as possible, so $\tau_{heating}$ decreases; thus, faster temperature response
Initial position of transducer $z_0$	$z_0$	Sets the generator operating temperatures: $\theta_{opening}$ and $\theta_{closing}$	Choice depending on the application (temperature fluctuations range)
	$F_{mec}$	Scales restoring force of the transducer	By increasing $z_0$ , $F_{mec}$ is increased; adjustment on $F_{mag}$ is then required to get both commutations

care as the vertical alignment with the FeNi alloy and the permanent magnet is important to ensure the best performance of the generator.

### 3.5 Discussion

Modeling of a thermo-magnetically activated micro-generator has been presented. The generator response for a particular scenario has been studied. This prediction method represents a viable alternative to rapid design of such as micro-generators. The multi-physic numerical model we presented here is capable of predicting a range of different scenarios of temperature fluctuations for which; the generator is supposed to work in. It also provides an opportunity to examine the interactions of several physic effects acting on each of the generator subsystems. Furthermore, it also provides an opportunity to study the influence of the device parameters on the dynamic performance of the generator. The theoretical framework of the generator has been formulated and a rapid design tool was developed using Matlab. **The main objective of this tool is to better understand the quasi-static (i.e., identification of the operating temperatures for a specific design of generator) and dynamic behavior of the generator.** It has been evidenced that the output power density of the generator can be increased when efficient miniaturization of the device is effectuated. A set of design rules was proposed considering the key design parameters and their effects on the generator operation.

Some of the conclusions are that **increasing the initial distance of separation of the triggering system may lead to greater elastic energy that is initially stored on the cantilever beam. Thus, resulting in greater energy harvesting capabilities.** However, having greater initial distances of separation, the counter-reaction force is increasing as well, therefore, the required attraction magnetic force to ensure the closed position is greater as well; which can easily exceed the magnetic properties of the triggering system. This finding suggests an optimal design for which the energy balance could be maximized. **Concerning the operation temperatures of the generator, they are depending on the design parameters, essentially on the triggering system including the initial position and the resulting effective stiffness of the cantilever beam. Hence, it is possible to tuning these thermal thresholds by modifying design parameters as the generator dimensions or the initial position of the transducer beam, which can be an advantage if the material selection is restricted.**

The thermo-magnetically activated piezoelectric micro-generator reported here shows a promising approach. It can operate through ambient temperature fluctuations or industrial environmental temperature variations depending on the tuning of their thermal thresholds. It could harvest small and slow temperature fluctuations present around us: walls of pipes carrying hot fluids, industrial machines, automobile radiators; to name but a few. **Moreover, it can play a second role; as a thermal switch. The rapid design tool we presented will be compared and validated with finite element simulations on the next chapter of this dissertation.**



## Chapter 4

# Finite element modeling of the generator

### Contents

---

<b>4.1 Three dimensional model of the generator</b> .....	<b>82</b>
4.1.1 Heat transfer simulation .....	83
4.1.2 Modeling of the temperature-dependent magnetization .....	89
4.1.3 Study of the piezoelectric energy conversion .....	96
4.1.3.1 Implementing piezoelectric effect .....	96
4.1.3.2 Mechanical contact .....	99
4.1.3.3 Harmonic simulation .....	102
4.1.3.4 Transient simulation .....	106
<b>4.2 Discussion</b> .....	<b>111</b>

---

*This chapter deals with a coupled multi-physics finite element modeling of our proposed generator. The model presented in this dissertation has been developed through software ANSYS. It promotes a better understanding of the generator response in several domains including static and transient. Special attention was put into the coupled multi-physic involved on the system, for instance, thermal-dependent magnetization of soft magnetic material, the piezoelectric transduction and the output power when a load resistor is connected to the electrodes of the transducer.*

## 4.1 Three dimensional model of the generator

In precedent chapters, an analytical model of our proposed generator was studied. In this chapter, a three dimensional model in finite element analysis is studied. The finite element method has become an essential solution technique in many areas of engineering and physics. The finite element method versatility lies in its ability to model arbitrary shaped structures, employing complex materials, and apply several types of loads as well as boundary conditions. The finite element method can also be adapted to different sets of constitutive equations, that is the main attractiveness for coupled physics simulation.

ANSYS finite element software has a large library of element types that support structural, thermal, electromagnetic analyses, as well as coupled field elements, including piezoelectric, electromagnetic-thermal, and thermal-structural, that simulate interactions between aforementioned fields. In our particular case, due to the multi-physic nature of the system of the indirect conversion of thermal energy we are interested in exploring the thermal behavior of the system in a first time.

We started by generating a computer based three-dimensional model of the energy generator. We used the finite element method to design and to predict the dynamic behavior of the device. This model takes into account different steps of the energy conversion: the temperature response of the energy harvester, the temperature-dependent magnetization of its triggering system, and the piezoelectric transduction until the output power dissipated across the load resistor (see Figure 3.16). This work has been performed. Figures 4.1(a) and 4.1(b) depict, respectively, the isometric and lateral views of the three-dimensional model for thermal analysis.

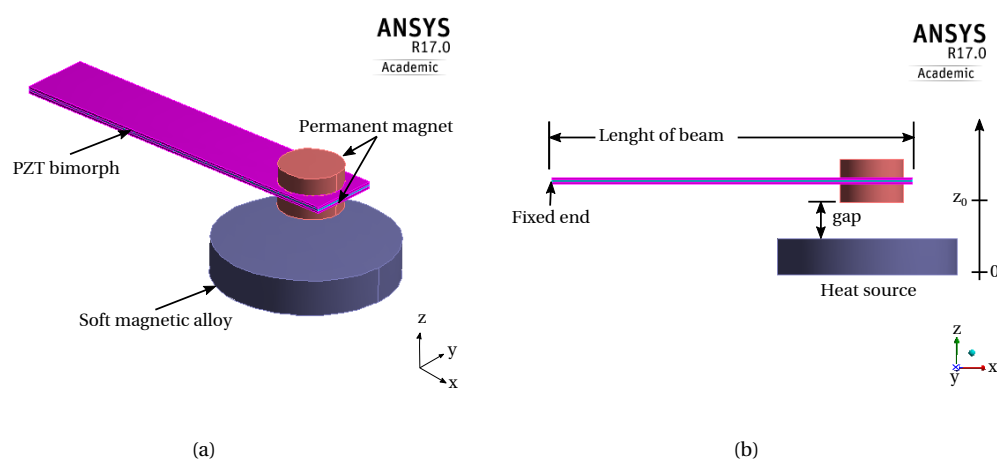


FIGURE 4.1: Schematic view of the three dimensional model of the generator, (a) isometric view of the generator and its main components, (b) lateral view of the generator showing the initial gap of separation in the triggering system.

On the next section, the thermal transient simulation is described.

### 4.1.1 Heat transfer simulation

In order to model the thermal response of the system, we opted by conducting a transient thermal simulation. The heat transfer takes place when heating up whole system, concretely at the soft magnetic material, which at the closed position is in contact with the hard magnets. Conversely, during the cooling down stage of the generator, either by natural or forced convection, there is not contact in the magnetic circuit. These conditions for sure impact on the temperature response of the system; because of the change in the dimensions (i.e., total volume considered for the generator) and in its thermal boundary conditions. The two stable positions are depicted in Figure 4.2.

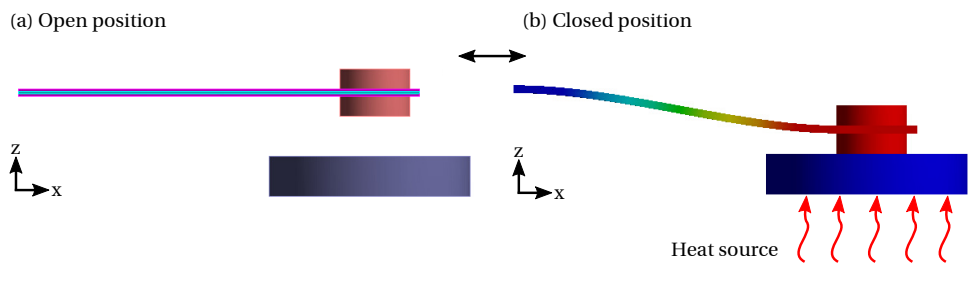


FIGURE 4.2: Three-dimensional model of the generator considering (a) open position of the generator and (b) closed position. The temperature of the FeNi alloy is driving the generator to at one of its stable position.

The initial conditions of the simulation are as follows: when the generator is in closed position, a heat load is applied to the bottom face of the soft magnetic material by using a heat element. Two scenarios were simulated to explore the temperature response of the entire structure (i.e., triggering system and transducer beam): considering a thermal contact between permanent magnet and the FeNi alloy for the closed position and without a thermal contact between permanent magnet and FeNi alloy for the open position. At the initial time of simulation, the entire system is at ambient temperature  $\theta_{amb} = 295\text{K}$  and the heat flux is applied. This condition is maintained until a certain time that we call  $t_{off}$  where the heat flux is deleted.

To consider the heat transfer between the soft magnetic material and its counterpart (i.e., bottom permanent magnet) we opted for using the pinball approach available in ANSYS workbench. The pinball region, also known as the pinball radius is involved with the distance from contact element to target element in a given contact region. Outside the pinball region, ANSYS does not bother to check to see if the elements on opposite sides of the contact region are touching or not. The software assumes they are far away from each other and does not worry about any additional calculations for the analysis.

In addition, it is possible to simulate many different type of contact in ANSYS, based on experimental data that will be detailed in Chapter 5, we decided to apply the bounded contact for the closed position of the generator. With this type of contact, the software's behavior when the contact and target elements are within the pinball radius is as follows: as long as the contact and target elements are close enough to be within the pinball region, the program considers the contact region to be closed. So, for bonded contact, our contact and target elements do not need to be touching in order for contact to be recognized. The

contact and target pairs just need to be inside the pinball region. There is a default value for the pinball radius. It can be modified is needed.

In ANSYS, one can use surface-to-surface contact elements and the node-to-surface contact element, in combination with thermal-structural coupled field solid elements or thermal elements, to model heat transfer that occurs in the contact surface. Figures 4.3(a) and 4.3(b), show, respectively, the boundary conditions for heat flux and convection.

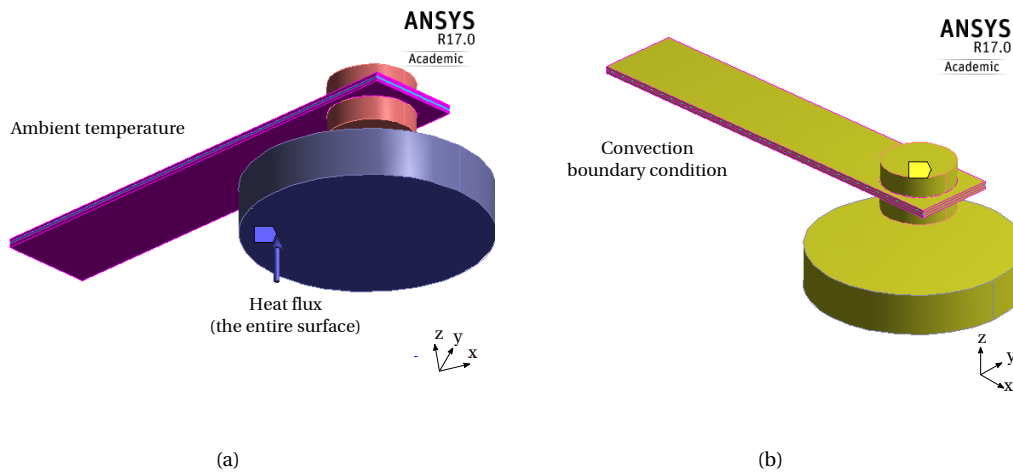


FIGURE 4.3: Representation of the boundary conditions of the three-dimensional model, (a) heat flux at the bottom surface of the FeNi alloy, (b) convection condition in all the surfaces of the generator.

The contact body is the bottom permanent magnet of the generator, as it is the volume which exhibit movement. While the other body, the FeNi alloy is selected as the target one. The target body is generally selected as the static body which receives the mechanical contact. Based on this assumption, the contact pair has been chosen for the model as shown in Figure 4.4.

In order to evaluate the temperature response of the system at its closed position, it is needed to set the radius pinball larger than the initial distance of separation. In this manner, the software considers the bounded contact on the pair FeNi-permanent magnet. The main parameters of the system are listed in Table 4.1.

The stepped heat flux is applied at the beginning of the simulation and it is maintained until  $t_{off}$ . The temperature at the upper face of the FeNi alloy is the target point. This is because at this surface is direct contact with the permanent magnet at closed position of the generator. Therefore, a temperature probe is set on the center of this surface in order to get its temperature over time. By the time simulation  $t = t_{off}$ , the input heat flux is turned off. Then, convection heat is then considered by the software. This behavior reproduces the experimental conditions for the measurements that were conducted in order to produce temperature evolutions on the FeNi alloy.

Thermal contact within the triggering system is considered at the beginning of simulation, once the temperature of FeNi alloy reaches the opening threshold, thermal contact is no longer considered. This behavior is depicted by the curve of temperature on the FeNi alloy and the permanent magnet. They are in line from the initial time until reaching the

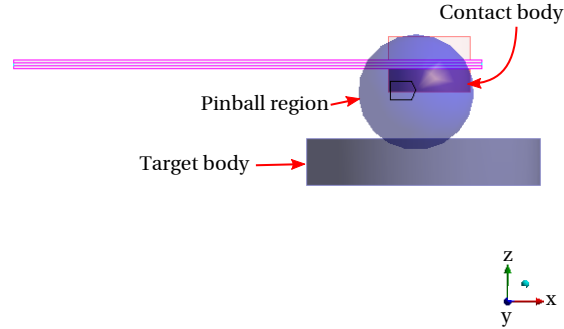


FIGURE 4.4: Schematic representation of the pinball region for thermal contact analysis, as well as target and contact bodies.

TABLE 4.1: General parameters of the 3D model of the generator for the transient thermal analysis.

System	Parameter	Symbol	Units	Value
Transducer beam	Length of cantilever beam	$L_B$	m	$20 \times 10^{-3}$
	Width of cantilever beam	$w_B$	m	$4 \times 10^{-3}$
	Thickness of shim layer	$h_B$	m	$100 \times 10^{-6}$
	Specific heat	$c_{pb}$	$\text{J kg}^{-1} \text{K}^{-1}$	430
	Thermal conductivity	$\kappa_b$	$\text{W m}^{-1} \text{K}^{-1}$	60
Permanent magnet	Height of magnet	$h_{mag}$	m	$1 \times 10^{-3}$
	Radius of magnet	$r_{mag}$	m	$2 \times 10^{-3}$
	Specific heat	$c_{pm}$	$\text{J kg}^{-1} \text{K}^{-1}$	480
	Thermal conductivity	$\kappa_{mag}$	$\text{W m}^{-1} \text{K}^{-1}$	45
FeNi specimen	Height of FeNi	$h_{FeNi}$	m	$4 \times 10^{-3}$
	Radius of FeNi	$r_{FeNi}$	m	$7 \times 10^{-3}$
	Specific heat of FeNi	$c_{pFeNi}$	$\text{J kg}^{-1} \text{K}^{-1}$	440
	Thermal conductivity	$\kappa_{FeNi}$	$\text{W m}^{-1} \text{K}^{-1}$	15
Environment and input conditions	Heat flux	$\dot{Q}$	$\text{W m}^{-2}$	$4 \times 10^3$
	Convection coefficient	$\lambda$	$\text{W m}^{-2} \text{K}^{-1}$	28
	Ambient temperature	$\theta_{amb}$	K	295
	Time in applying heat flux	$t_{on}$	s	0
	Time in turning off heat flux	$t_{off}$	s	140

opening commutation. After that, the temperature of the magnet is no longer increased because of convection boundary condition. However, the FeNi alloy is still in heating up stage as the heat flux input is still applied. Once the heat flux is turned off, the temperature of the FeNi is now decreasing and when it reaches the closing threshold, that is the generator reached its closing commutation. At this time, thermal contact is again considered until the system steady state. For the sake of comparison, figures 4.5(a) and 4.5(b) represent the temperature distribution, at an instant of the transient simulation, when thermal- contact and no-contact on the FeNi alloy is considered, respectively. It is evident that when thermal contact is considered, the contact between the permanent magnet and the FeNi alloy is changing the temperature distribution. Conversely, when no contact is considered, an uniform distribution on the surface of the FeNi alloy is noted.

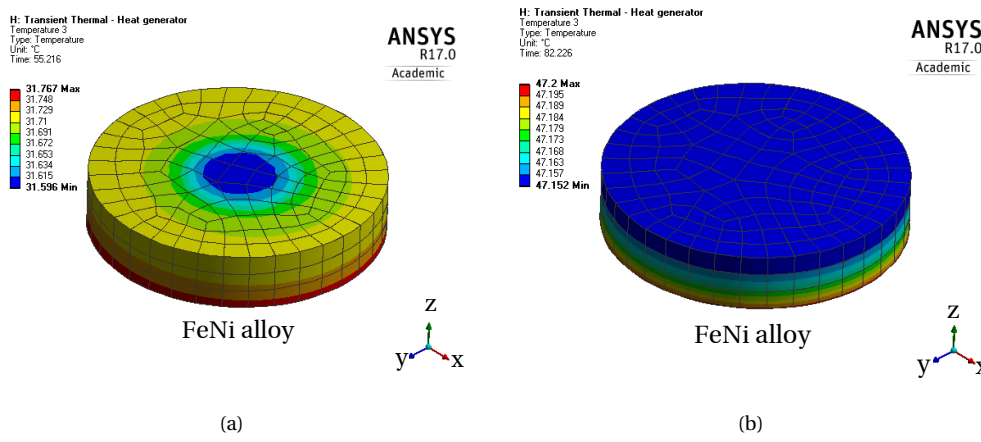


FIGURE 4.5: Representation of the temperature distribution on the FeNi alloy when: (a) thermal contact between permanent magnet and FeNi alloy is considered and (b) when no thermal-contact is considered.

The thermal contact within the generator is a crucial point to be considered. It impacts on the temperature response of the device. For the closed position of the generator, the total volume and characteristics of the generator are different to those pertaining to the generator at its open position. And once the generator is in the open position, the temperature response on the FeNi alloy should be different to the one of the transducer beam as the latter is no longer in direct contact with the heat flux input. To show this, we set another temperature probe on the permanent magnet in order to monitor the temperature once the generator has reached the open position.

Some results of this simulation are shown in Figure 4.6. From these simulation results, it can be seen that at initial time, the heat flux is applied. As a result, temperature on the FeNi is increased from ambient (i.e.,  $\theta_{amb} = 295K$ ). In order to explore the behavior of the generator in the closed and open position, we decided to establish opening temperature and closing temperature for this system. The main goal of this study is to see the temperature response of the device taking into account both operation conditions. For the opening temperature, we decided to put  $\theta_{opening} = 313K$ , while for closing temperature we opted for setting  $\theta_{closing} = 308K$ .

Experimental measurements were conducted in order to explore the real behavior of such a generator. A complete fixture for mounting the system was developed and built,

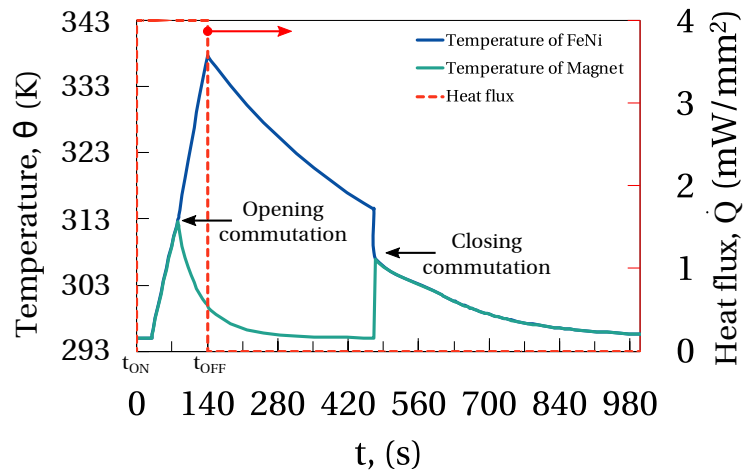


FIGURE 4.6: Temperature response of the generator considering thermal contact between the permanent magnet and the FeNi alloy,

more details of this clamping device are presented on next chapter. Concerning the temperature variations on the FeNi alloy, they are produced by means of Joule effect. By using an electrical current flowing across an electrical path, namely a PCB serpentine-shape located at the bottom face of the FeNi. Figure 4.7(a) shows the photograph of the PCB serpentine-shaped used as the support of the soft magnetic alloy. By means of an electrical current flowing across this path, temperature variations on the FeNi are achieved. Figure 4.7(b) depicts the mounted FeNi alloy on the PCB serpentine-shaped, it also shows the thermo-couple used to measure the temperature of the soft magnetic alloy.

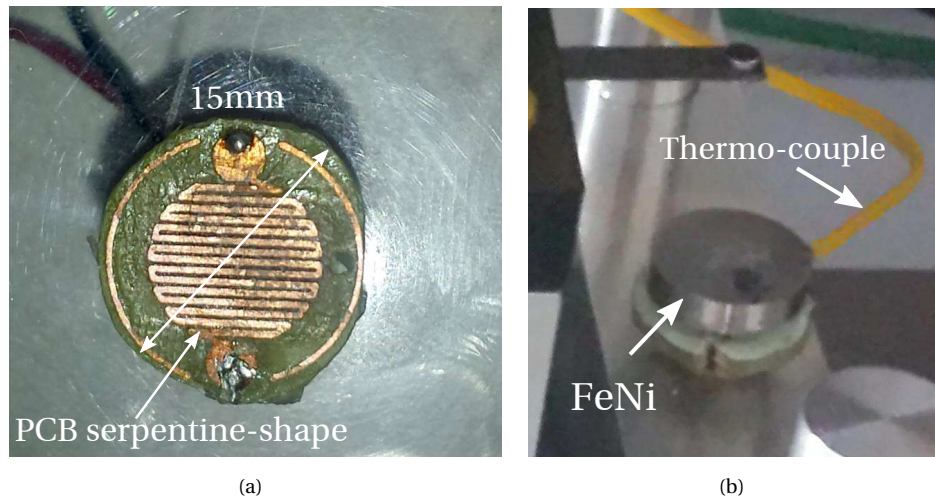


FIGURE 4.7: (a) Photograph of the top view of the PCB serpentine-shape used to put the FeNi in order to drive its temperature variations through an electrical current, (b) photograph of the mounted FeNi on the PCB support with the thermo-couple measuring the temperature of the soft magnetic alloy.

Now, considering experimental data, we adjusted the parameters of the finite element

model, including convection coefficient in order to get better agreement with real behavior of the generator. It is important to remember that at this stage, we are focused in knowing the thermal transient response of the generator. After, a magneto-static study will be undertaken in order to explore the key property of the system; the thermo-magnetization of the FeNi specimen. First simulation results are depicted in Figure 4.8.

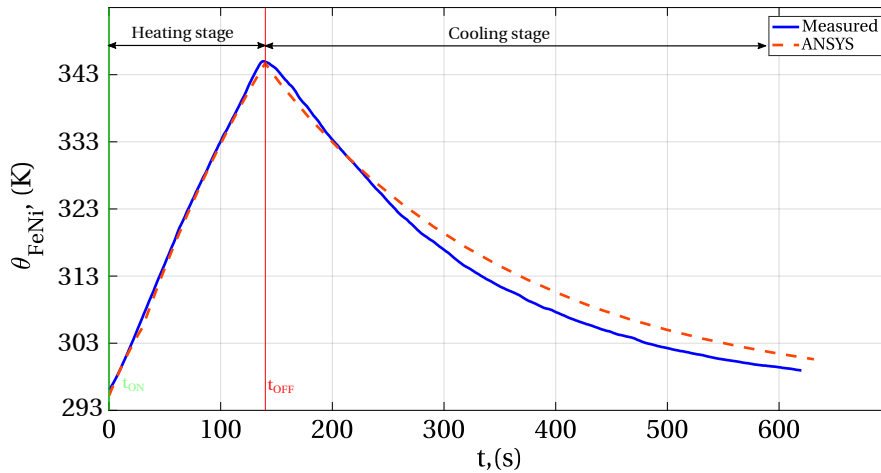


FIGURE 4.8: Results and comparison between measured data of a heating up stage and cooling down stage for the soft magnetic material specimen as well as the transducer beam (i.e., the two main parts of the generator).

From the above figure, it can be seen a good agreement with the measured data and the finite element method results. To do that, we have modified the convection coefficient of the model in order to fit the thermal response of the model. As the simulation time in finite element analysis takes more time than the single degree of freedom model we used the latter to approximate this parameter and then we come back to ANSYS in order to validate the value. We can make a finer tuning on the finite element model once we had a good approximation with measurements. Figure 4.9 illustrates the comparison between the ANSYS model, measured data and the analytical model presented on previous chapter.

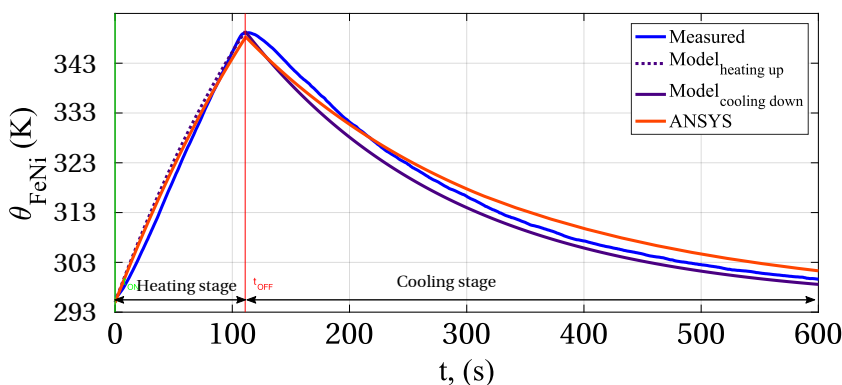


FIGURE 4.9: Comparison of the thermal response of the generator between finite element model, analytical model and measured data.

It is also crucial to remember that the input scenario is predominant on the performance of the generator. For scenarios where temperature variations are sporadic, the best design of this kind of generator may have not in priority the thermal response but the electromechanical energy conversion capabilities. Conversely, for scenarios where temperature variations are frequent, major attention on the thermal response of the device should be paid to ensure efficient thermal commutations (i.e., having thermal periods as short as possible).

On the next section, a study of the temperature-dependent magnetization, of the FeNi specimen is detailed. This study is also performed from a finite element point of view.

#### 4.1.2 Modeling of the temperature-dependent magnetization

The temperature-dependent magnetization of soft magnetic materials is the key property of the working principle of this kind of generators. This is a reversible property that is depending on the stoichiometry of the specimen. As detailed in Chapter 3, this property is present on some alloys, for instance the iron-nickel alloy. We opted for using ANSYS Maxwell software in order to investigate this property.

We started by creating a three-dimensional model of the generator, the triggering system and the transducer beam. Figure 4.10 shows the image of the model created.

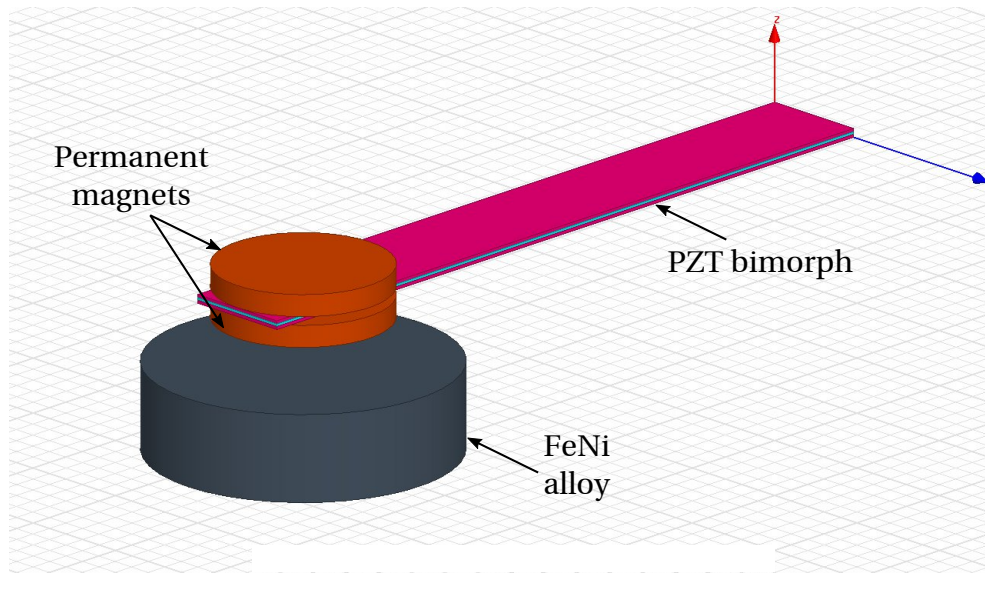


FIGURE 4.10: Isometric view of the three-dimensional model of the generator considered for the magneto-static analysis.

The magnetic analysis of the system aimed at exploring the magnetic force within the triggering circuit, namely, the couple permanent magnet and FeNi alloy. The magnetic polarization of a permanent magnet, in Maxwell software is considered to be along the x-axis, we have created a rotated coordinate system, whose x-axis is oriented to the vertical position (i.e., z-axis of the global coordinate system).

As we already mentioned, we are focused on modeling the magnetic force acting on the soft magnetic material, to do that in Maxwell software, a “virtual” force parameter has been set up on the model setup. And this parameter is aligned with the global coordinate system. Therefore, the stronger component of the force is expected to be along the z-axis, that is the vertical axis of the model. To confirm the validity of our model, we set an initial distance of separation between the permanent magnet and the FeNi alloy of 2mm and we performed a magneto-static simulation. In this type of study, only magnetic degree of freedom is considered. Concerning the material parameters of the model, we used the N45 type permanent magnet available on the library of the software. Figures 4.11(a) and 4.11(b) show the surface force density of the model, when not thermal magnetization is considered for the moment.

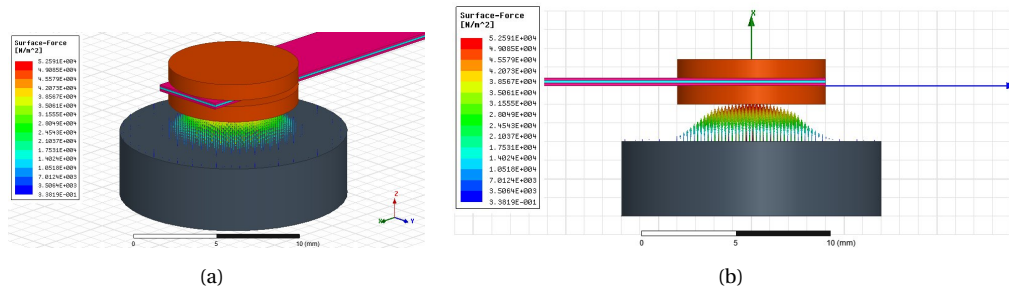


FIGURE 4.11: Representation of the surface force density acting over the FeNi alloy and the permanent magnet by finite element method, (a) isometric view and (b) lateral view of the model.

The vertical component of the magnetic force,  $F_{mag} = 1.64\text{N}$ . This result revealed that the magnetic force at room temperature is strong enough to close the generator, this can be seen on Figure 3.10. On this configuration of generator, it is noted that the magnetic force when an initial distance of separation of 2mm is about 1N.

We figured out, experimentally, that the vertical alignment between the permanent magnet and the soft magnetic specimen, is crucial to have an efficient magnetic attraction force. To explore the influence of this alignment on the resulting magnetic force, with initial distance of separation as a constant, we performed a parametric analysis. This study involves the alignment, along the x-axis, of the FeNi alloy, considering that the vertical center of both permanent magnet and FeNi alloy are located at  $\Delta x$ . This variable sweep study is illustrated in 4.12(a) and 4.12(b).

The goal of this variable sweep analysis is to explore in static regime, the influence on the attraction magnetic force. An optimal position of the FeNi alloy has to be considered after evaluating outcomes from this study. The position of the soft magnetic alloy along the x-axis was considered as follows: the position of the FeNi is in the range  $[-10\text{mm} \leq \Delta x \leq 10\text{mm}]$  with a step of 2.5mm. System temperature and distance of separation were kept constant at values  $\theta = 293\text{K}$  and 2mm, respectively. The vertical component of the attraction magnetic force as function of the horizontal position of the FeNi is depicted in figure 4.13(a) while the magnitude of the magnetic field strength is illustrated in 4.13(b).

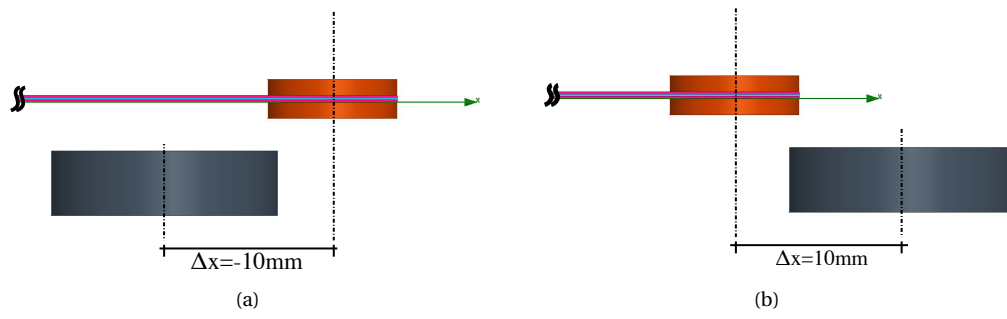


FIGURE 4.12: Schematic representation of the variable sweep analysis for the horizontal alignment of the FeNi with respect to the permanent magnet, (a) shows the FeNi alloy with a maximum misalignment while (b) depicts the maximum misalignment.

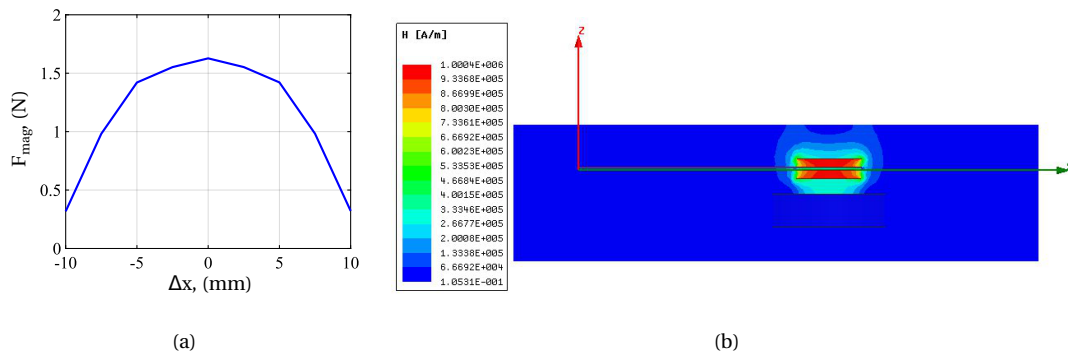


FIGURE 4.13: (a) Finite element results showing the influence of the horizontal alignment of the FeNi alloy on the magnetic attraction force within the triggering system, (b) lateral view of the system illustrating the magnetic field strength magnitude for the optimum position of the FeNi.

It is not surprising that the best position for the FeNi alloy in order to develop the maximum attraction component is aligned at the center of the permanent magnet, that is aligned with the center of the permanent magnet.

Now, it is important for us to explore the temperature-dependent magnetization of the FeNi alloy. Therefore, adapted to our model a thermally dependent magnetization to the soft magnetic material. It can be done by including temperature dependence under the menu *set object temperature* in Maxwell software. To consider the temperature dependence of the magnetization behavior, it is desirable to first describe the demagnetization curve by a function with a couple of temperature dependent parameters as variables. These parameters are generally associated with intrinsic flux density  $B_i$  versus  $H$  curve [79, 91, 92]. As we detailed in subsection 3.3.2, magnetization of soft magnetic materials can be expressed as a function of temperature.

We conducted a parametric analysis having as sweep variables the temperature of the

FeNi alloy and the distance of separation between the permanent magnet and the soft magnetic material. As in Maxwell software temperature is represented in  $^{\circ}\text{C}$ , from now on temperature will be expressed in  $^{\circ}\text{C}$ . The temperature range we have considered for this simulations is:  $[20^{\circ}\text{C} \leq \theta \leq 70^{\circ}\text{C}]$  with a step pass of  $1^{\circ}\text{C}$ . With regards the distance of separation ( $gap$ ) between the permanent magnet and the FeNi, it has been considered in the range  $[0\text{mm} \leq gap \leq 3\text{mm}]$  with a step of  $0.1\text{mm}$ . Therefore, it results in a matrix of 51 rows (temperature) and 31 columns ( $gap$ ). The reason of implementing such a matrix is to get finer representation of the magnetic force as function of the initial distance of separation and temperature of FeNi. We realized that the magnetic force has a non linear behavior, as function of the  $gap$  and the temperature, so we had the interest of exploring in a detailed way this parameter. Every element representing a point in the space temperature- $gap$  for which magnetic attraction force will be calculated. Figure 4.14 shows the representation of the magnetic force depending on the temperature of FeNi and the  $gap$  distance within the triggering system. This design is considering the parameters listed on Table 4.1.

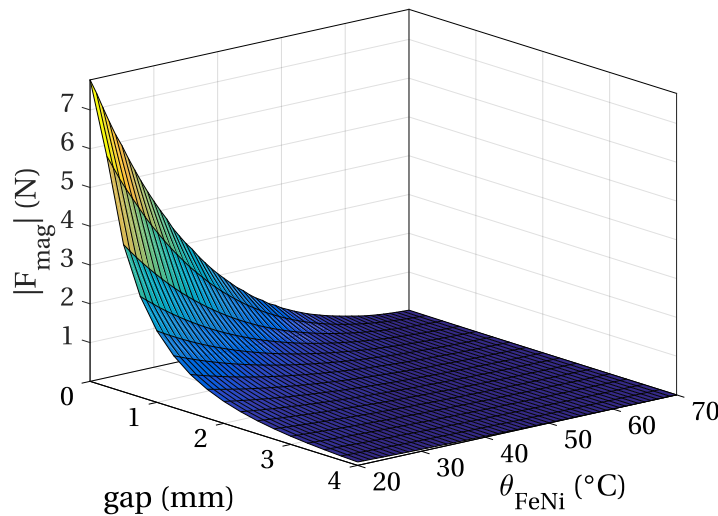


FIGURE 4.14: Magnetic force as a function of temperature of FeNi and distance of separation between the permanent magnet and soft magnetic material. The origin of the  $gap$  axis represents the upper surface of the FeNi alloy.

It is clear to see how the larger is the distance of separation, the lower is the magnetic attraction force. And similarly for temperature of the FeNi, the higher the temperature of FeNi the lower attraction magnetic force. It can be concluded that an operational zone on the temperature- $gap$  space should be taken into account for designing.

As we have highlighted before, one key design parameter for this generator is the distance of separation  $gap$  in the triggering system. Moreover, mechanical stiffness is also a crucial design parameter as it can impact the operation temperatures of the device. To better understand these points, we add, to the temperature- $gap$  space, a mechanical force representation for a given transducer beam design (i.e., dimensions and materials dependent). This mechanical force should be represented by a plane crossing the magnetic force

and gap axes. As the mechanical stiffness of the transducer depends only on the transducer beam elongation and its dimensions, temperature does not affect this property. We divided the next study into two main cases as listed below:

**Case 1**  $gap_1 = gap_2$  and  $k_1 < k_2$

**Case 2**  $gap_1 > gap_2$  and  $k_1 = k_2$

For **Case 1**, we decided to consider a transducer beam having a mechanical stiffness  $k_1 = 333\text{N m}^{-1}$  (the value of the mechanical stiffness has been obtained by the analytical model implemented on Matlab for a generator design as listed on Table 3.4) and an initial distance of separation of  $gap_1 = 3\text{mm}$ . Therefore, a maximum mechanical force is at the zero gap value (i.e., the generator is in closed position and the beam is in its maximum elongation). The minimum of the mechanical force is reached at the maximum gap distance (i.e., the generator is en open position and the beam is at its horizontal state). Afterwards, we increased by two times the mechanical stiffness, in such a way that  $k_1 < k_2$ . We have maintained the same initial distance of separation,  $gap_1 = gap_2$ . This is illustrated in figures 4.15(a) and 4.15(b), showing the representation of forces interaction for two different mechanical stiffness.

For **Case 2**, we opted for representing the mechanical force for a transducer beam having a mechanical stiffness  $k_1 = 333\text{N m}^{-1}$  and an initial distance of separation of  $gap_1 = 3\text{mm}$ . Then, we reduced in half the distance of separation, in such a way that  $g_1 > g_2$ . We have maintained the same initial distance of separation,  $k_1 = k_2$ . This second case is illustrated in figures 4.16(a) and 4.16(b), showing the representation of forces interaction for two different mechanical stiffness.

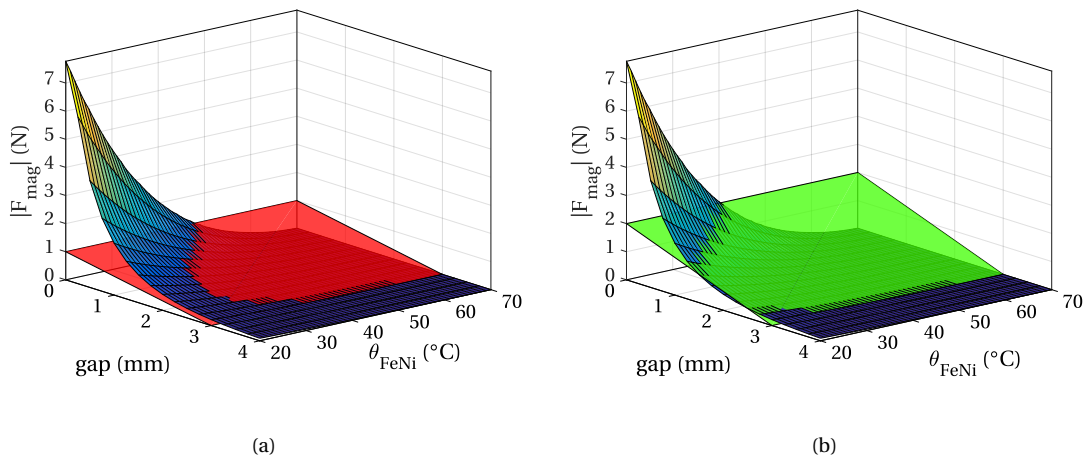


FIGURE 4.15: Representation of the interaction between mechanical and magnetic force as a function of temperature of FeNi and separation distance by finite element method. (a) The mechanical stiffness considered on this example is about  $k_1 = 333\text{N m}^{-1}$  and initial distance of separation  $gap_1 = 3\text{mm}$ , (b) The mechanical stiffness considered on this example is about  $k_2 = 666\text{N m}^{-1}$  and initial distance of separation  $gap_2 = 3\text{mm}$ .

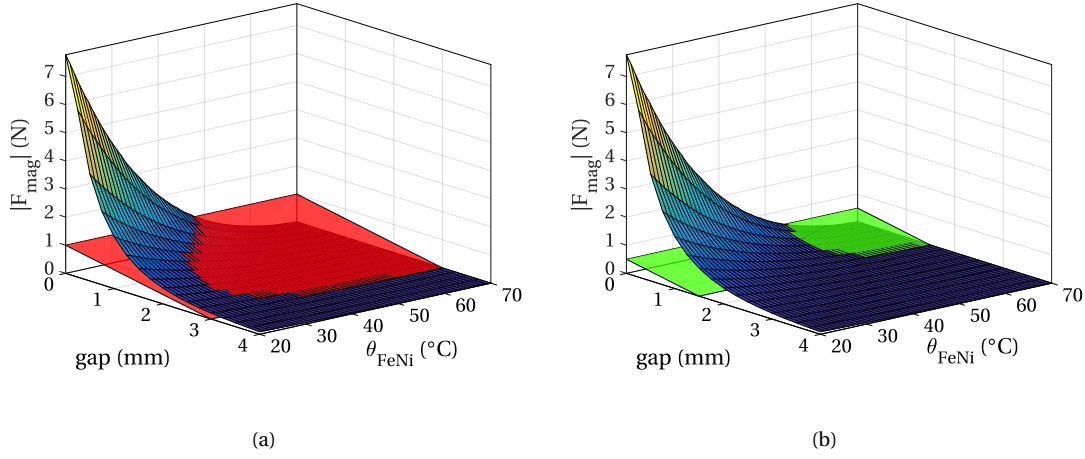


FIGURE 4.16: Representation of the interaction between mechanical and magnetic force as a function of temperature of FeNi and separation distance by finite element method. (a) The mechanical stiffness considered on this example is about  $k_1 = 333\text{N m}^{-1}$  and initial distance of separation  $gap_1 = 3\text{mm}$ , (b) The mechanical stiffness considered on this example is about  $k_1 = 333\text{N m}^{-1}$  and initial distance of separation  $gap_2 = 1.5\text{mm}$ .

Valuable conclusions can be outlined from these simulation results. Firstly, for both cases, operational zone can be remarked. That is, crossing points between forces correspond to the driving resulting force acting on the transducer and making it commutate. Secondly, it has been proved that tuning in temperatures of operation of the generator can be achieved by modifying these two parameters design, namely mechanical stiffness  $k$  and distance of separation  $gap$ . Design considerations are derived from these two cases:

**Case 1**  $gap_1 = gap_2$  and  $k_1 < k_2$ : For the same initial distance of separation, it can be seen that for lower mechanical stiffness, the operating temperatures tend to be higher than those ones corresponding to larger mechanical stiffness. By increasing  $k$ , higher elastic energy initially stored on the transducer beam can be converted into electricity after passing through thermal-to-mechanical energy conversion. In contrast, it requires lower temperatures to operate as the driving resultant force tends to be higher in such conditions. Changing the stiffness of the transducer without modifying the distance of separation may not be so easy as it implies to change materials or even the mass of magnets which also affects the resulting magnetic force. Therefore, **Case 2**, can be considered where changing the distance of separation in the triggering system may result in other advantages of the system.

**Case 2**  $gap_1 > gap_2$  and  $k_1 = k_2$ : When the same mechanical stiffness has to be constant, one can play with the initial distance of separation (i.e.,  $gap$ ). This cases can be the conditions where we can not play or change the transducer beam neither with the magnets attached to it, but the gap parameter can be easily modified. Finite element simulation results suggest that for larger initial distances of separation the initial elastic energy stored in the beam is higher as well. Nevertheless, lower temperatures are required in order to ensure the closing position of the generator. Contrarily, when smaller distances of separation, higher temperatures should be envisaged to efficiently operate the generator.

For the sake of validity, we conducted a comparison study among the analytical models and finite element simulation for the triggering system. In this study we did a benchmark case with the adhesive force calculator of [supermagnete calculator](#) in order to have an idea of what fabricants of permanent magnets provide for adhesive force between a permanent magnet and a magnetized material. The schematic of the model is shown in [Figure 4.17](#) and the results are shown in [Figure 4.18](#).

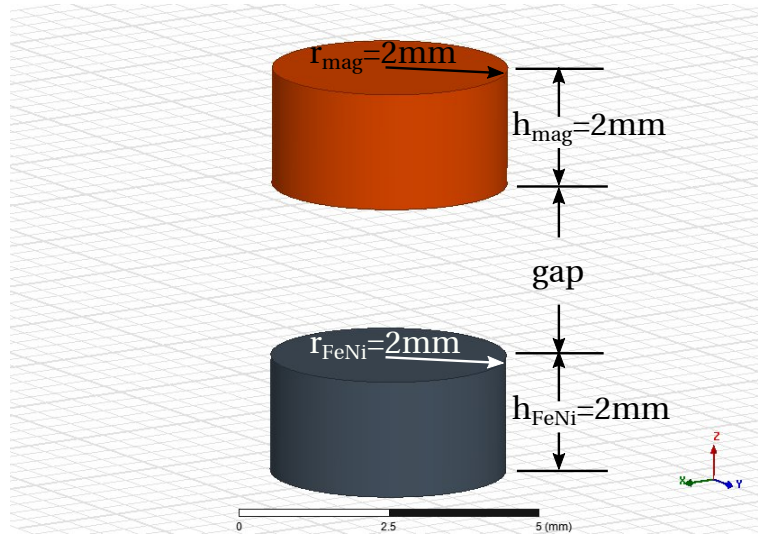


FIGURE 4.17: Representation of the benchmark study to validate the finite element model and the analytical model for the magnetic attraction force between a permanent magnet and a magnetized material.

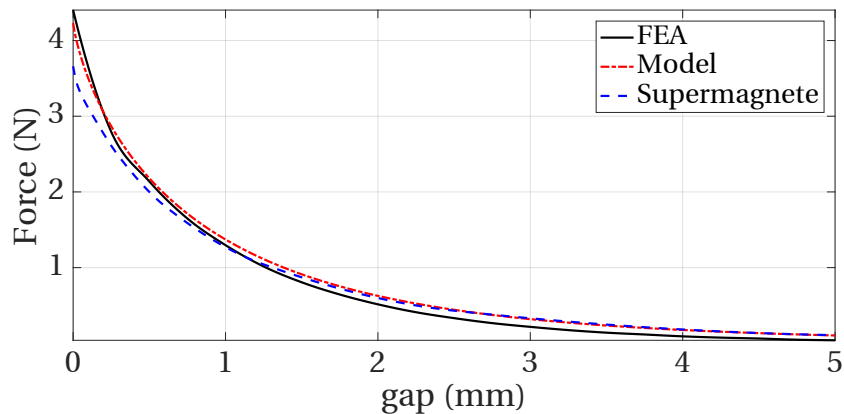


FIGURE 4.18: Comparison of the attraction force between a permanent magnet and a magnetized material.

Based on results of [Figure 4.18](#) we validated both our finite element model and the analytical simplified model of the attraction force between a permanent magnet and a magnetized material separated by a gap distance.

### 4.1.3 Study of the piezoelectric energy conversion

The reader is referred to the [Appendix A](#) for more details on piezoelectricity. After having outlined generalities of piezoelectric effect as our transduction technique, it is important to bring out some important points. The key parameter from piezoelectricity theory is that mechanical stresses inducing strains will be converted into voltage at the electrodes of piezoelectric material. It is trivial to tend to maximize these mechanical stresses in order to increase the output voltage. Piezoelectric cantilever beams modeling in finite element method are focused on this principle. As our goal is to extract the maximum electrical energy from the piezoelectric element, it is important to be in line with the vibration piezoelectric energy harvesting approach. This will be the base of our modeling.

#### 4.1.3.1 Implementing piezoelectric effect

In previous finite element analyses, we studied first thermal response of our generator when a specific heat input is applied. The output of that study was the temperature response of the generator. Afterwards, the thermo-magnetostatic analysis allowed us to realize how temperature changes affect the magnetic attraction force in the system. As temperature variations may be vary different from one scenario to other, the main interest in performing such a magnetic analysis is to know the operation range of the generator for a given input. Now, we know how temperature variations, as the main input of the system, produce magnetization variations and thus, they promotes a sort of bistable control on the transducer beam. In this section, we intend to study the piezoelectric transducer.

We decided to continue with a three-dimensional model for exploring piezoelectric effect. One of the reasons is because the complexity of the device. The more similar to the real model the better performance may be obtained in finite element model. We have considered three different architectures of the transducer beam as described below:

**Prototype 1 - Rectangular-shape wide beam:** The PZT bimorph has a rectangular shape as shown in figure [4.19\(a\)](#). The width of the beam is  $w_B = 5\text{mm}$ . A pair of permanent magnets of radius,  $r_{mag} = 2\text{mm}$  and height,  $h_{mag} = 1\text{mm}$ .

**Prototype 2 - Rectangular-shape narrow beam:** Similar shape as prototype 1, transducer beam consists in a rectangular shape piezoelectric bimorph. The width of the beam is  $w_B = 2\text{mm}$ . Maintaining the same permanent magnets as prototype 1. This is shown in figure [4.19\(c\)](#).

**Prototype 3 - Triangular-shape beam:** Unlike precedent prototypes, this prototype considers a triangular shape piezoelectric bimorph as the transducer element. Its maximum width is the same as prototype 1;  $w_B = 5\text{mm}$ . In all three prototypes, the same pair of magnets has been maintained constant. The model representation of this prototype is depicted in figure [4.19\(e\)](#).

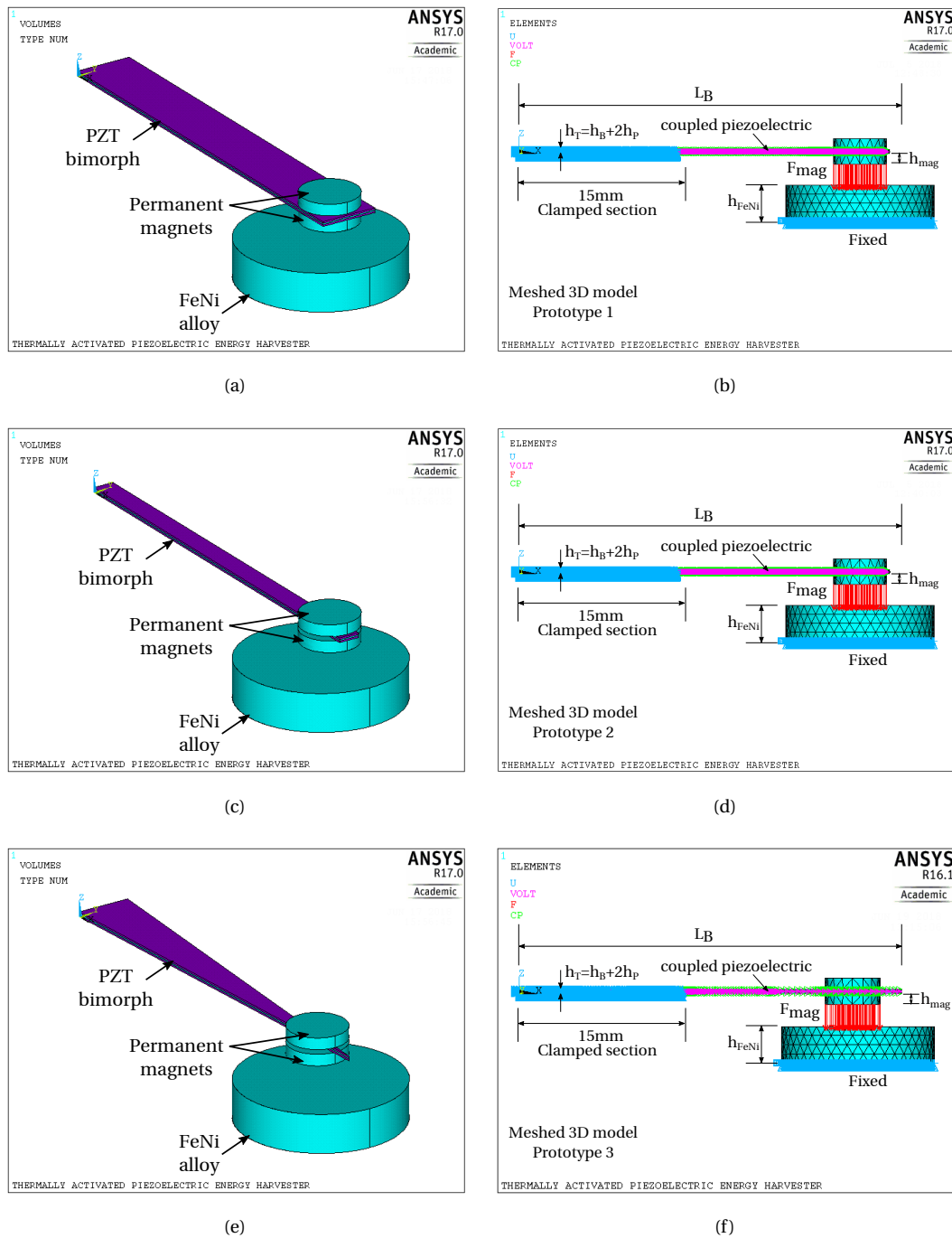


FIGURE 4.19: Schematic representation of three different configurations of transducer beam. (a) Isometric view of prototype 1 and (b) boundary conditions and meshed model representation in lateral view. (c) Isometric view of prototype 2 and (d) boundary conditions and meshed model representation in lateral view. (e) Isometric view of prototype 3 and (f) boundary conditions and meshed model representation in lateral view.

Some of main reasons for choosing these models are as follows: for the first case, we decided to model a real case of a transducer beam that we can easily fabricate. This is the initial reference case. In order to demonstrate that by reducing the size of the generator,

its performance may be enhanced. So, we opted by reducing the width of the transducer beam, as it can easily reproduced in a real prototype. This could reduce the temperature response of the generator as the lateral surface  $S_L$  is reduced. By reducing the width of the beam, the viscous damping can be reduced as a smaller area of the cantilever beam is being considered. And for the third case, we opted for a triangular shape cantilever beam to get a uniform stress distribution along the beam in flexion [93].

The general dimensions of these prototypes are listed in Table 4.2

TABLE 4.2: General parameters of three prototypes studied through finite element method.

Item	Parameter	Symbol	Units	Prototype		
				1	2	3
PZT bimorph beam	Beam length	$L_B$	m	$35 \times 10^{-3}$	$35 \times 10^{-3}$	$35 \times 10^{-3}$
	Width beam	$w_B$	m	$4.9 \times 10^{-3}$	$1.8 \times 10^{-3}$	$4.6 \times 10^{-3}$
	Thickness shim layer	$h_B$	m	$120 \times 10^{-6}$	$120 \times 10^{-6}$	$120 \times 10^{-6}$
	Thickness PZT layer	$h_p$	m	$140 \times 10^{-6}$	$140 \times 10^{-6}$	$140 \times 10^{-6}$
Permanent magnet	Radius	$r_{mag}$	m	$2.5 \times 10^{-3}$	$2.5 \times 10^{-3}$	$2.5 \times 10^{-3}$
	Thickness	$h_{mag}$	m	$1 \times 10^{-3}$	$1 \times 10^{-3}$	$1 \times 10^{-3}$
FeNi alloy	Radius	$r_{FeNi}$	m	$3.5 \times 10^{-3}$	$3.5 \times 10^{-3}$	$3.5 \times 10^{-3}$
	Thickness	$h_{FeNi}$	m	$7 \times 10^{-3}$	$7 \times 10^{-3}$	$7 \times 10^{-3}$
Design parameter	Initial distance of separation	$gap$	m	$2 \times 10^{-3}$	$2 \times 10^{-3}$	$2 \times 10^{-3}$

Table 4.3 lists the material parameters of the models.

The structural mechanical elements were modeled through SOLID186. While piezo-electric elements were modeled with SOLID226 element type. To illustrate the dissipated power due to piezoelectric conversion, a load resistor that has been modeled with CIRCU94 element type, is directly connected to the electrodes of the bimorph. Figures 4.19(b), 4.19(d), and 4.19(f) illustrate the boundary conditions, for prototypes 1, 2 and 3, respectively. The boundary conditions are similar for all the prototypes. First, we fixed the bottom face of the FeNi. Also, a section of 15mm of the transducer beam is fixed. This is because the fixture for mounting the cantilever beam has the same length so we wanted to reproduce similar conditions to the model. Second, the upper and bottom electrodes of piezoelectric beams are connected to an output load resistor (except for static simulations as it does not accept this kind of elements). The electrical connection between the piezoelectric layers is series, in such a way that flexion towards the FeNi will produce a negative tension, while positive output voltage is achieved by flexions towards the up direction. The magnetic force is acting over the bottom magnet towards the FeNi alloy.

TABLE 4.3: Material parameters of the finite element models.

System	Parameter	Symbol	Units	Value
Bimorph piezoelectric (shim)	Young's modulus of shim layer	$Y_B$	Pa	$1 \times 10^8$
	Poisson's ratio	$\nu_B$	-	0.3
	Density of shim layer	$\rho_B$	$\text{kg m}^{-3}$	8200
Bimorph piezoelectric material	Elastic compliance	$s_{11}^E$	$\text{Pa}^{-1}$	$20.5 \times 10^{-12}$
		$s_{12}^E$	$\text{Pa}^{-1}$	$-4.78 \times 10^{-12}$
		$s_{13}^E$	$\text{Pa}^{-1}$	$-7.21 \times 10^{-12}$
		$s_{33}^E$	$\text{Pa}^{-1}$	$20.45 \times 10^{-12}$
		$s_{44}^E$	$\text{Pa}^{-1}$	$43.55 \times 10^{-12}$
	Piezoelectric coefficient	$d_{31}$	$\text{m V}^{-1}$	$-274 \times 10^{-12}$
		$d_{33}$	$\text{m V}^{-1}$	$593 \times 10^{-12}$
		$d_{15}$	$\text{m V}^{-1}$	$741 \times 10^{-12}$
	Relative permittivity	$\epsilon_{11}^S$	$\text{F m}^{-1}$	$2.7 \times 10^{-8}$
		$\epsilon_{22}^S$	$\text{F m}^{-1}$	$2.7 \times 10^{-8}$
$\epsilon_{33}^S$		$\text{F m}^{-1}$	$3.1 \times 10^{-8}$	
Density of piezoelectric layer	$\rho_p$	$\text{kg m}^{-3}$	7500	
Permanent magnet	Density of magnet	$\rho_{mag}$	$\text{kg m}^{-3}$	5000
	Young's modulus of magnet	$Y_{mag}$	Pa	$1.6 \times 10^{11}$
FeNi alloy	Density of FeNi alloy	$\rho_{FeNi}$	$\text{kg m}^{-3}$	6200

#### 4.1.3.2 Mechanical contact

A very important aspect we realized during experimentations is the mechanical contact between the FeNi alloy and the permanent magnet attached to the transducer beam. Indeed, the closing position of the generator consists in the mechanical contact of these elements. Therefore, we had to take into account this contact on the model. Contact elements TARGE170 and CONTA174 were implemented on the surface implied in this stage. Target surface is the upper face of the FeNi alloy. Since this volume is fixed and it will receive the impact of the moving transducer beam, it is decided to assign it as target surface. The bottom face of the permanent magnet attached to the beam is selected as the contact surface. Even is in ANSYS is hard to model mechanical contact, we opted for using a contact pair to better understand this topic. The contact surfaces for the prototype 1 are illustrated in figures 4.20(a) and 4.20(b).

We conducted a static simulation in order to obtain a general representation of the closed position for each prototype generator. The magnetic force has been applied as a static force over the bottom face of permanent magnet and we studied the deflection of the

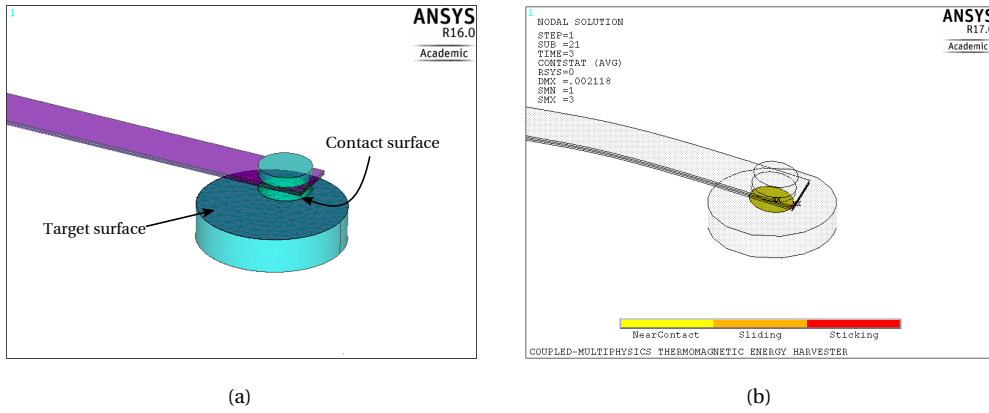


FIGURE 4.20: (a) Representation of the contact surface (CONTA174) and target surface (TARGE170) of the 3D model of prototype 1, (b) status of mechanical contact at the closed position of the generator.

beam as well as its contact with the FeNi alloy. These results are illustrated in figures 4.21(a) to 4.21(f).

From this static study of the generators, it can be highlighted some important aspects: all of them presenting an efficient close position. However, the contact is not achieved in all the surface of the set permanent magnet-FeNi. This can be explained because of the stiffness of the transducer beam. Reducing the width of the transducer beam, for example from prototype 1 to prototype 2, piezoelectric material is also reduced. This can be seen on the maximum output voltage of these cases. For the prototype 1 it exhibits a maximum around  $\pm 70V$  (depending on the direction of the deflection of the beam), while for prototype 2 a maximum voltage of  $\pm 65V$ . It was also founded the minimal magnetic force required to get the closed position of the generator. The mechanical stiffness of each architecture generator was obtained. By using a transducer beam with a triangular shape, a more uniformly distributed mechanical stress due to deflection of the beam is achieved. This may imply better piezoelectric conversion capabilities. In addition, modal simulations were conducted to explore the performance of these three architectures. Main features of prototypes are listed in Table 4.4.

TABLE 4.4: Summary of the main static and modal characteristics of the prototypes.

Item	Prototype 1	Prototype 2	Prototype 3
Resonance frequency $f_r$	93Hz	83Hz	119Hz
Mechanical stiffness $k$	895N m <sup>-1</sup>	319N m <sup>-1</sup>	413N m <sup>-1</sup>
Minimum $F_{mag}$ to ensure contact in closed position	1.8N	0.68N	0.86N

These results revealed valuable insights in improving designs of these generators. The first conclusion we can highlight is that by reducing the width of the cantilever beam, mechanical stiffness is also reduced. However, lower magnetic force is required to ensure the

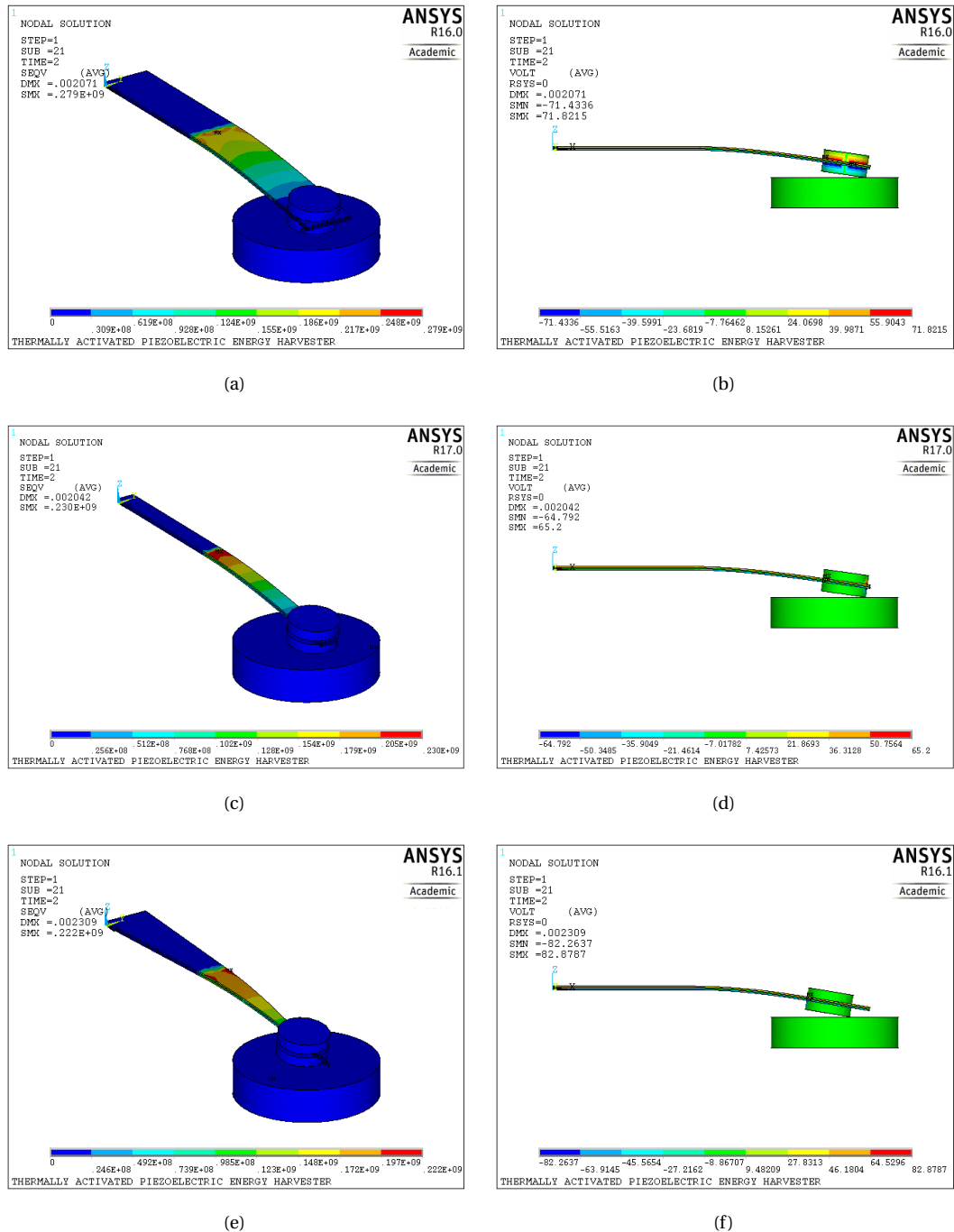


FIGURE 4.21: Results comparisons of the three different prototypes in static domain showing. Prototype 1 (a) equivalent von misses stress and (b) piezoelectric output voltage at closed position. Prototype 2 (c) equivalent von misses stress and (d) piezoelectric output voltage at closed position. Prototype 3 (e) equivalent von misses stress and (f) piezoelectric output voltage at closed position.

closed position of a narrow width transducer beam. The second outcome is that by making use of a triangular-shape transducer beam, the mechanical stiffness can be increased as well as the resonance frequency. Both enhancements can be achieved without needing higher magnetic force to ensure efficient closed position. In summary, the triangular-shaped cantilever beam emerges as the best candidate of these three architectures from a static characterization.

One main outcome of static and modal studies is knowing the frequency of the resonance of the system. When complexes architectures are considered for the generator, using finite element analysis simplifies this task.

On next section, harmonic analyses of these three prototypes architectures will be detailed. **The reason for doing harmonic analysis is because the generator can also be designed to work in environments where vibrations are present. That is, not only temperature variations are present but also it is common to find in industrial applications, like machines that are wasting heat and generating vibrations when operate.** It is desired to know the performance of the system under harmonic input like vibrations. It is evident that the vibrations should be exploited by the generator once it is in its open position.

#### 4.1.3.3 Harmonic simulation

Harmonic analysis is generally used to determine the steady-state response of a linear structure to loads that vary sinusoidally (i.e., harmonically) with time. The idea is to calculate the structure's response at several frequencies and obtain a graph of some response quantity (usually displacements) versus frequency. "Peak" responses are then identified on the graph and stresses reviewed at those peak frequencies. We opted for using the full method harmonic analysis available in ANSYS. The load applied to the system is an acceleration of amplitude  $A = 9.8\text{ms}^{-2}$  in the z direction applied at the origin of the global coordinate system (see Figure 4.22).

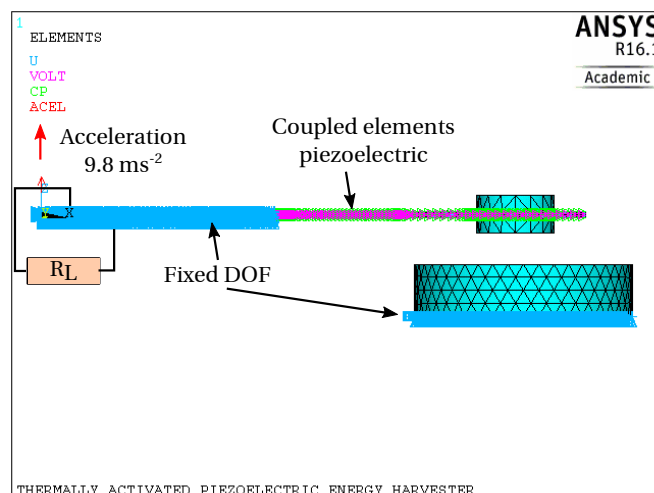


FIGURE 4.22: Schematic representation of boundary conditions for harmonic analysis when applying an acceleration of  $9.8\text{ms}^{-2}$  in z- direction

As we already know, from modal simulation, the eigenfrequency of the system, we can refine the frequency range near to this resonance frequency of the system. Damping term is crucial to be identified in this study. We opted for doing a parametric study, exploiting the finite element model in order to explore the influence of the damping coefficient  $C$ , to the power output of the generator. In ANSYS, it is possible to introduce a variety of damping terms, including Rayleigh damping, coefficient damping ratio, material-dependent damping, global damping ratio, etc. We decided to use the Rayleigh damping coefficient as it can be used in harmonic and transient analyses. Harmonic study we conducted is described as follows: for three architecture prototypes the acceleration was applied at the origin of the coordinate system. In order to explore the output power and vertical displacement of the tip of the beam, as function of load resistor and frequency, we performed a parametric analysis. With regards the prototype 1, simulation results of this harmonic study are shown in figures 4.23(a) and 4.23(b) for output power and vertical displacement of the tip of the beam as function of frequency and load resistor, respectively, considering a Rayleigh damping coefficient,  $C = 0.5 \times 10^{-4}$ . While figures 4.23(c) and 4.23(d), depict output power and vertical displacement of the tip of the beam when  $C = 2 \times 10^{-4}$ .

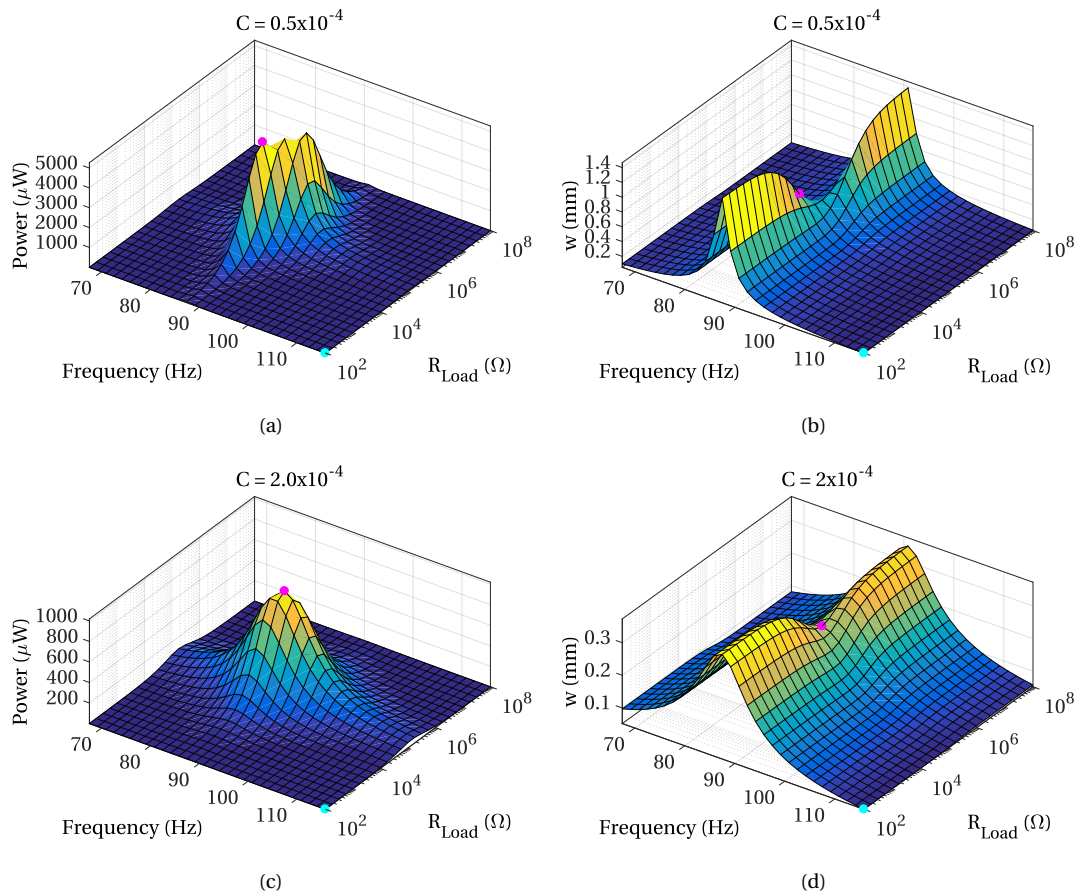


FIGURE 4.23: Harmonic results of prototype 1. (a) Output power as function of frequency and load resistor when for a Rayleigh damping value  $C = 0.5 \times 10^{-4}$  (b) vertical displacement of the tip of the beam. (c) Output power as function of frequency and load resistor when for a Rayleigh damping value  $C = 2.0 \times 10^{-4}$  (d) vertical displacement of the tip of the beam.

From these results of prototype 1, it can be remarked that the frequency of resonance of the system;  $f_r = 88\text{Hz}$  is in good agreement with modal analysis previously performed. Also, it can be noted an optimal load resistance for which the output power is maximum;  $R_{Load} = 56\text{k}\Omega$ . As resonance and antiresonance frequencies are close each, it can be deduced that electromechanical coupling is not so strong. When damping coefficient is increased, as expected, the peaks corresponding to the output power and the vertical displacement of the system are decreased.

Now, to explore the harmonic response of the prototype 2 we have conducted the same analysis (i.e., same acceleration load and load resistor values). Output power and vertical displacement of the tip beam as function of load resistor and frequency are depicted in figures 4.24(a) and 4.24(b) for a damping term  $C = 0.5 \times 10^{-4}$ , respectively. Whereas figures 4.24(c) and 4.24(d), represent the output power and vertical displacement as function of frequency and load resistor, respectively, when  $C = 2 \times 10^{-4}$ .

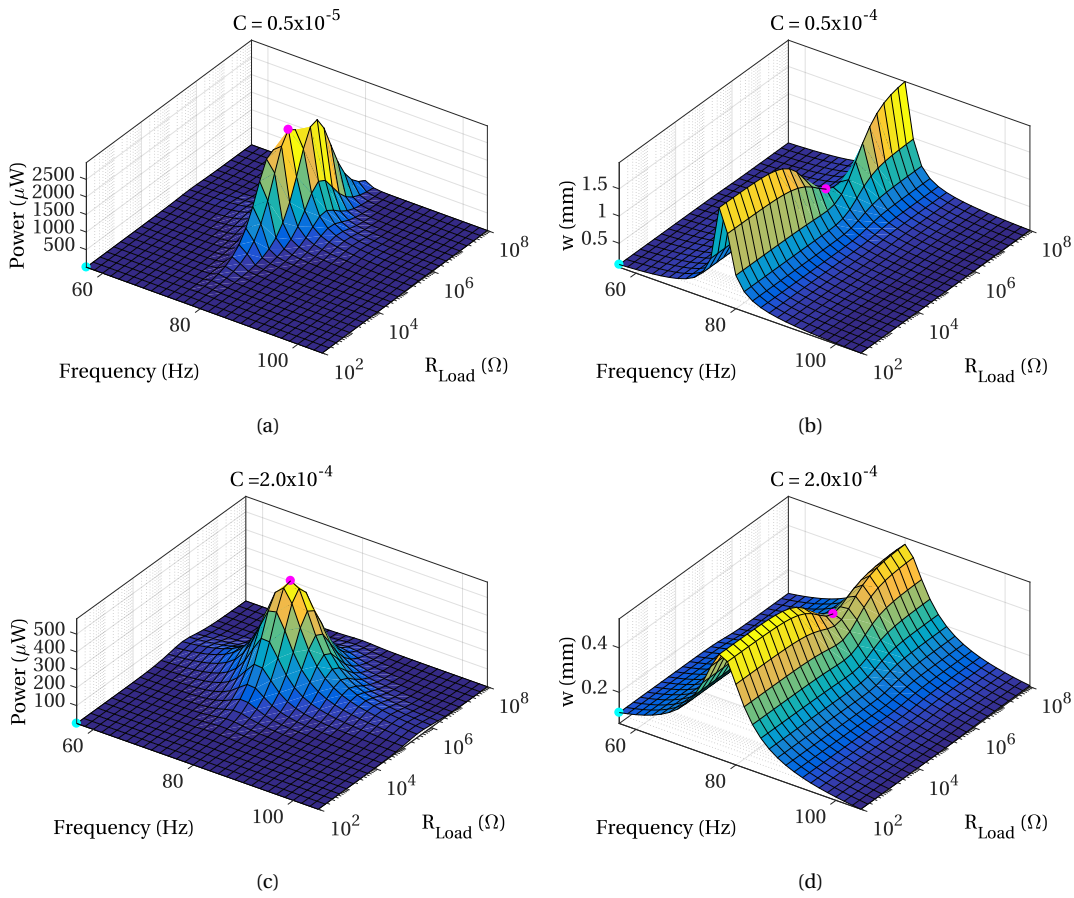


FIGURE 4.24: Harmonic results of prototype 2. (a) Output power as function of frequency and load resistor when for a Rayleigh damping value  $C = 0.5 \times 10^{-4}$  (b) vertical displacement of the tip of the beam. (c) Output power as function of frequency and load resistor when for a Rayleigh damping value  $C = 2.0 \times 10^{-4}$  (d) vertical displacement of the tip of the beam.

And finally, to conclude with harmonic study, the prototype 3 was studied also under the same conditions aforementioned. Its output power and vertical displacement of the tip beam as function of load resistor and frequency are depicted in figures 4.25(a) and 4.25(b)

for a damping term  $C = 0.5 \times 10^{-4}$ , respectively. Whereas figures 4.25(c) and 4.25(d), represent the output power and vertical displacement as function of frequency and load resistor, respectively, when  $C = 2 \times 10^{-4}$ .

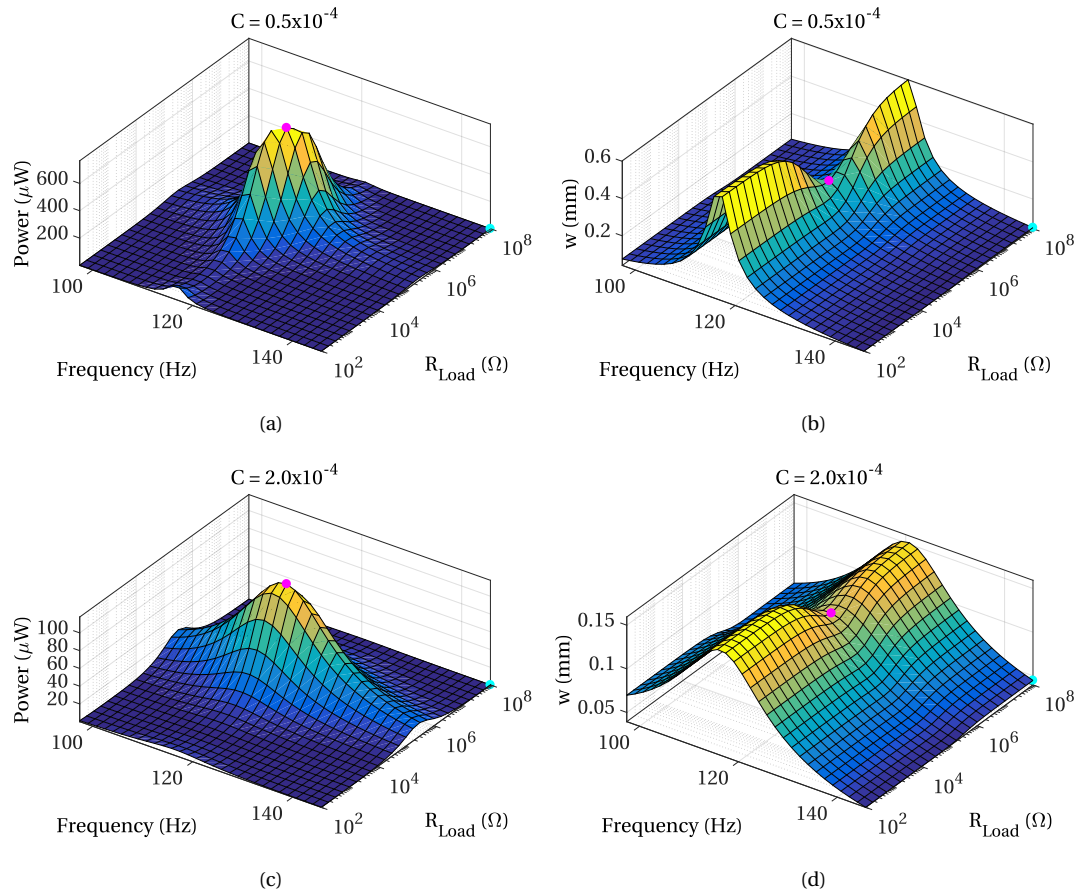


FIGURE 4.25: Harmonic results of prototype 3. (a) Output power as function of frequency and load resistor when for a Rayleigh damping value  $C = 0.5 \times 10^{-4}$  (b) vertical displacement of the tip of the beam. (c) Output power as function of frequency and load resistor when for a Rayleigh damping value  $C = 2.0 \times 10^{-4}$  (d) vertical displacement of the tip of the transducer cantilever beam.

Harmonic analysis can be advantageous when inertial based energy harvesters are targeted. Even if our generator is not supposed to work in vibrational environments, it is not forbidden to be designed with such capabilities. This is why designers can take advantage of this coupled model to undertaking harmonic analysis. Results have revealed that damping can be a challenge to overcome in order to ensure long oscillations of the transducer beam. As it is based to working by events (opening and closing commutations), the more oscillations the more mechanical energy can be converted into electricity.

**The versatility of this kind of generators relies on the fact that they can also convert vibration energy, once in open position, until a decrease of temperature closes it. In other words, let us suppose the generator is placed in an industrial environment where a machine is operating several times during a short period of time (i.e., some minutes of operation over a day). And, this machine also produces vibrations, such as the case of a drill,**

a die casting machine or even a protection contactor block of a three-phases motor control panel. Once the temperature leads the generator to its opening commutation; the generator can vibrate as a response of the environment excitation. Thus, a great interest in designing both, good temperature response and vibration energy conversion capabilities should be an optimal design.

The main finding of this harmonic analysis is to know an optimal load resistor. This resistor has to be considered for the opening commutation. Even if the original operation of the device is based by events, as we mentioned, a plus can be whether the temperature variations are accompanied with some vibrations. So, designers should pay attention on the impact of the structural damping of the device when considering such a kind of input excitation.

In order to explore the transient performance of these architectures, we have conducted transient analysis that are detailed and presented on the following section.

#### 4.1.3.4 Transient simulation

Transient dynamic analysis can be performed in ANSYS under different methods, including full transient or modal superposition method. We decided to perform full transient simulations in all the cases because of the precision of the response even if calculation time can be sacrificed. A transient dynamic analysis is used to determine the response of a structure subjected to a time-dependent loading considering inertia and damping effects. It is often referred to as a time-history analysis. The main load we considered in transient dynamic analysis is the magnetic force within the triggering system. A general representation of a transient response of the generator is illustrated in Figure 4.26.

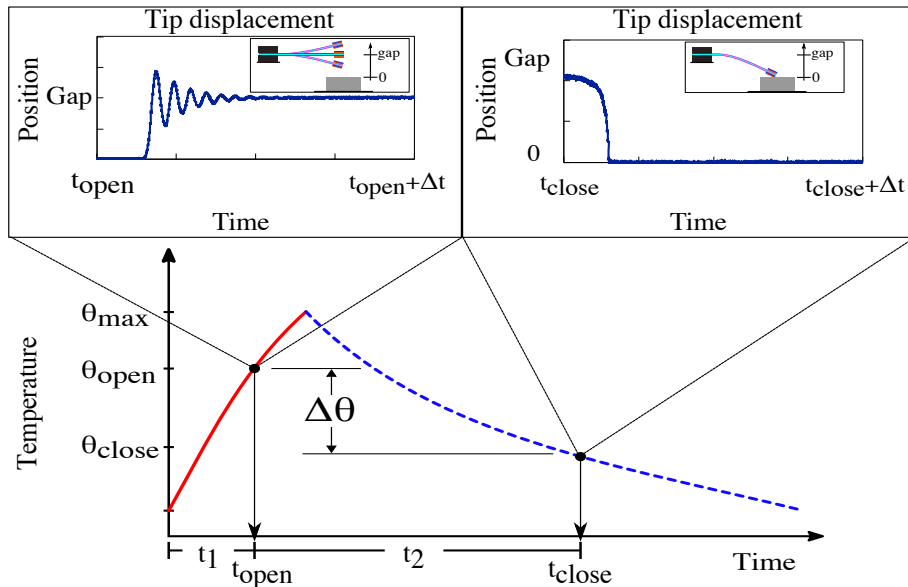


FIGURE 4.26: Schematic representation of the response of the generator during one thermal cycle, showing the opening and closing commutation along the overall time of temperature fluctuation of the FeNi alloy.

As we are interested in exploring the dynamic vibration of the beam when it is released (from the closed position to the open one), we have considered that at the beginning of the simulation time, the generator is in open position. Then, we suppose that the temperature of the FeNi-alloy is increased in such a manner that the magnetic force is reduced being lower than the mechanical force of the deflected beam. Considering initial conditions as follows: the system is at thermal equilibrium with the environment, that is at room temperature (below to open and close thresholds). Later, an increase in temperature will lead the FeNi temperature until a maximum value. Passing through the opening threshold  $\theta_{open}$  at time  $t_{open}$ . At this moment; a close up on the oscillations of the transducer beam can be noted. Once the transducer beam reached its steady state after oscillations, temperature may be high.

The input scenario will drive the operation frequency of the generator. It means that if temperature does not decreases, the generator may stay open. Nevertheless, in this condition; as we mentioned on the previous section, if the environment exhibit some vibration that can be transmitted to the device. It can convert them into electricity making use of piezoelectricity transduction. On the other hand, when temperature decreases, FeNi alloy will cool down crossing the temperature of closing,  $\theta_{close}$  at a time  $t_{close}$ . Finally, the closing commutation is reached. Unlike, to the opening commutation where the beam exhibits oscillations, for the closing commutation, energy conversion is done through an abrupt impact magnetic contact between the set permanent magnet-FeNi specimen.

The integration time step of the transient simulation is selected according to:

$$ITS = \frac{1}{80f_r} \quad (4.1)$$

where,  $f_r$  is the resonance frequency of the transducer beam. This allowed us to perfectly monitor the oscillations of the beam at the opening commutation. The eigenfrequency of the transducer is obtained through a modal analysis. For the sake of simplicity, we decided to start the transient simulation with a particular condition, the generator is in open position and it is static (i.e., no oscillations). The transient simulation setup and previous preparation is described below:

- QRDAMP modal simulation: a modal study is performed to know the damped frequency of resonance of the system.
- Full transient simulation: after having obtained the damped frequency of resonance of the system, Software can calculate  $ITS$ .
  1. Load step 1: at time  $t = 0$ , the generator is in static condition and in open position.
  2. Load step 2: at time  $t = 150ITS$ , the magnetic force is activated in a step way (ANSYS command KBC=1).
  3. Load step 3: at time  $t = 500ITS$ , the magnetic force is deactivated, releasing the transducer beam.
  4. Load step 4: at time  $t = 2000ITS$ , the end of the simulation.

In order to explore the dynamic performance, in displacement and output voltage, master nodes were declared at the tip of the beam and at the output load resistor, respectively.

Considering the case of the prototype 2, we conducted a transient simulation, the eigenfrequency is found to be  $f_r = 85\text{Hz}$ . Therefore,  $ITS = 1.4 \times 10^{-4}\text{s}$ . First, the free oscillation of the cantilever beam is investigated, as shown in Figure 4.27.

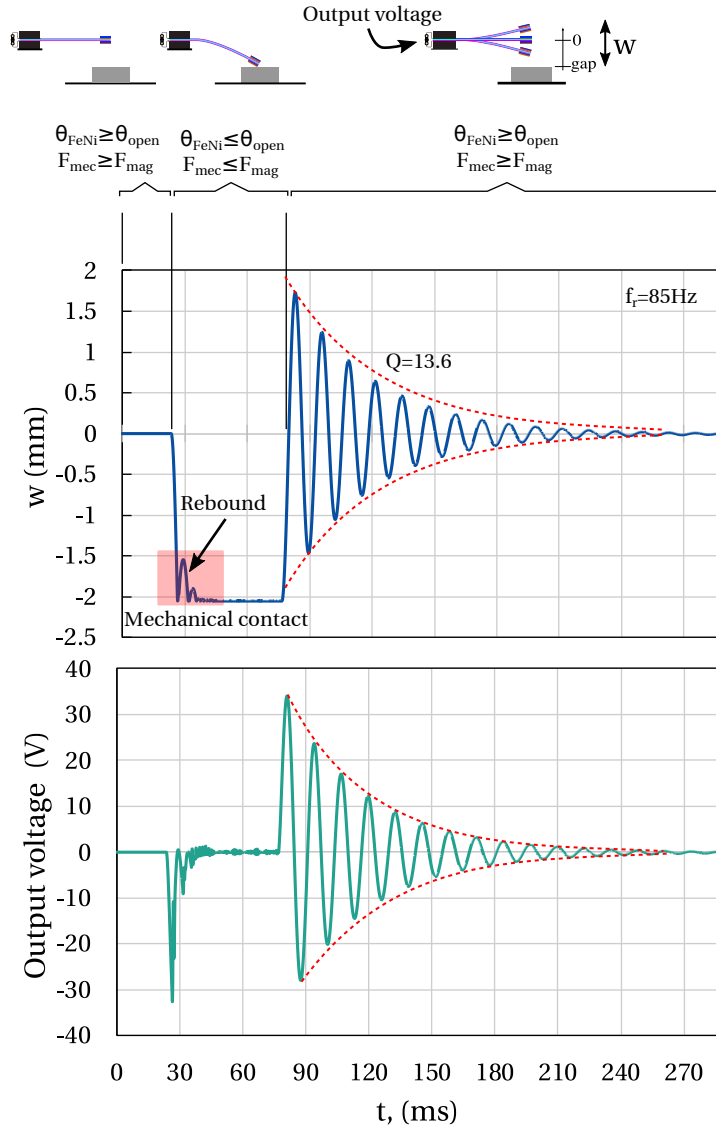


FIGURE 4.27: Simulation results of a transient analysis of the prototype 2. Vertical displacement of the tip of transducer,  $w$  and its output voltage when a load resistor of  $R_{\text{Load}} = 350\text{k}\Omega$  (optimal value from harmonic analysis).

These results demonstrate the dynamic performance of the generator. These data can be read as follows: the generator is in static condition in open position; thus no vertical displacement neither electric voltage at the load resistor. By the time the tip of the transducer travels towards the FeNi alloy, which is away at a distance of separation of 2mm, output voltage is then produced because of the deflection of the beam. It is perfectly reproduced

the mechanical contact between the permanent magnet and the soft magnetic alloy. It produces a rebound that in turn produces output voltage oscillations during the closing commutations. We believe that when the mechanical contact is done, the configuration of cantilever beam is no longer present. Indeed, the structure boundary conditions have changed for a very short time. Now, it can be seen as a clamped-supported beam. Hence, very quick oscillations (compared with those during the opening commutation) are present during the closing commutation. As the magnetic force is predominant in the system, the cantilever beam is in contact and in static condition. So no more output energy is produced. This is the first event for which the generator can operate. By the time the magnetic force decreases as a function of temperature; the mechanical force of the cantilever beam becomes predominant. In consequence, the beam is released. The oscillations of the beam are now present with a frequency near to the resonance (it can be present a contribution of magnetic force that affects the free oscillations).

For the decaying oscillation, a strong damping can be identified. The quality factor can be determined by:

$$Q = 2\pi \frac{E_{cycle}}{E_{loss}} \quad (4.2)$$

whereas  $E_{cycle}$  is the energy stored at a certain amplitude, and  $E_{loss}$  is the energy loss, calculated from the amplitude decrease. In addition a simplest way to quickly obtain the Q-factor is by making use of the ring-down method [94]. It is extremely simple. Once having the structure at its natural frequency oscillations, we observe the amplitude of the oscillations decrease, counting how many cycles  $N$ , it takes to halve the amplitude and then we multiply this number by 4.53 to find  $Q$ . In other terms,  $Q$  can be deduced as:

$$Q = \frac{\pi N}{\ln(2)} \cong 4.53N \quad (4.3)$$

Figure 4.28 illustrates the instantaneous output power.

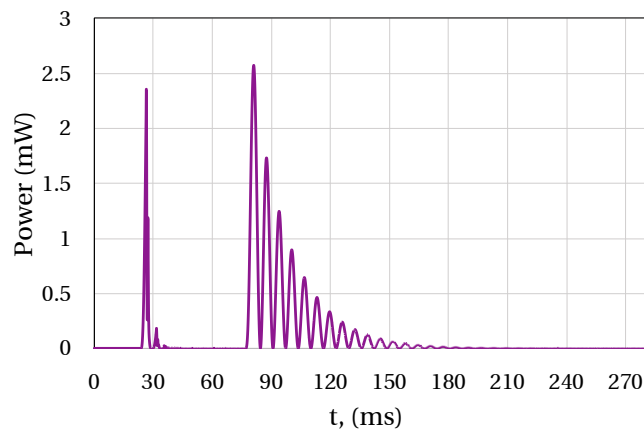


FIGURE 4.28: Instantaneous power representation of the prototype 2 when a load resistor,  $R_{Load} = 350\text{k}\Omega$  (this value has been obtained as the optimal value for opening commutation.)

Peaks up to 2.5mW are achieved during opening commutations of the prototype 2. Although, instantaneous power is a relative measure to characterize this kind of device (i.e., energy conversion based on events), the overall performance of the model has been demonstrated. As we did for the heat transfer model and for the magnetic force model, we compared the transient response of the generator in finite element model with measured data and analytical simplified model. Figure 4.29 illustrates the vertical displacement of the tip beam during a thermal cycle of operation and Figure 4.30 the output voltage generated during these two commutations.

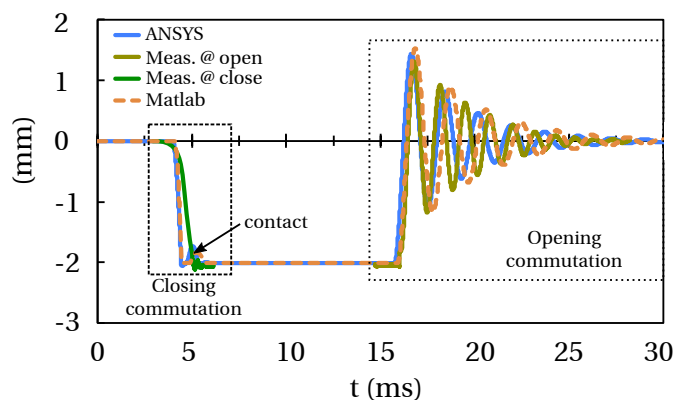


FIGURE 4.29: Validation of the finite element model and analytical simplified model in transient simulation with measured data of a generator. Vertical displacement of the tip beam (the measured data has been superposed on the graph for comparison purposes).

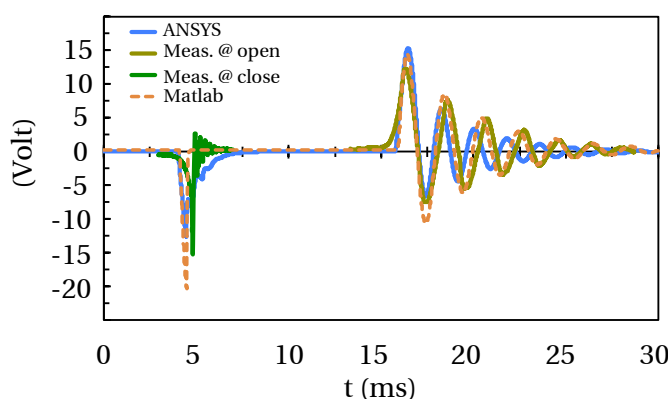


FIGURE 4.30: Validation of the finite element model and analytical simplified model in transient simulation with measured data of a generator, output voltage generated.

More transient simulation can be performed, however, it is important to remark that time of simulation is considerable (several weeks). This is due to the difference between the dynamics of the system; in one hand, thermal response of the generator is in the range of minutes while the operating commutations do not take more than several tens of ms. This is why a simplified model such as the one presented in Chapter 3 is advantageous.

## 4.2 Discussion

This chapter has treated the finite element modeling of our generator. The 3D model has been built using ANSYS software. **The main reason for using finite element simulation is to validate our analytical model.** The “disadvantage” of using finite element model versus the simplified model is the time of calculation that it needs. However, it is evident that for exploring complex architecture of the generator, the simplified model is no longer useful.

The process of simulation has been as follows:

**Thermal simulation.** It has revealed the temperature response of the generator when it is in closed and open positions. The main output of this simulation is a temperature vector depending on time. The finite element model corroborates the hypothesis of having different behaviors in terms of heat transfer when thermal contact on triggering system of the generator.

**Magneto-static simulation.** This study has been performed to explore the temperature dependent magnetization of the soft magnetic material, namely, FeNi alloy. The results of this study demonstrated the key principle of the generator operation. As temperature of the FeNi increases, its magnetization is decreased. The 3D model has been implemented on Maxwell and the input was the temperature variation that we obtained from previous thermal simulation. The finite element model has validated the simplified model we developed on Matlab for a simple architecture of permanent magnet and FeNi separated by a gap.

**Piezoelectric simulation.** The goal of this simulation can be divided into four principal domains. The first is on modal analysis. No loads are considered for this study, but the output is the mode of vibration of the structure. Damping coefficients can be introduced in this study in order to understand the damped frequency of resonance. Second, static study is carried out to investigate the mechanical contact on the triggering system. The open circuit voltage of the cantilever beam is studied here. Third, harmonic analysis is conducted aiming at knowing the optimal load resistor when the generator is subjected to accelerations. Although this approach is generally used for inertial energy harvesters, the bonus of this generator is that it can also harvest energy when it is open position if the environment provides vibrations. Lastly, transient behavior of the generator completes the characterization stage. It couples the mechanical vibrations with piezoelectric effect and the output voltage across a load resistor is the main output of this study.

Finally, we have contributed to energy harvester designs in proposing a finite element model that couples the physics involved on the operation system. To exploit all the advantages of this 3D model, complex architecture of generator should be a starting point. Miniaturized architectures can be easily implemented using the finite element model. Exploration of other materials are also one crucial advantage of using finite element simulation.

Several prototypes of the generator are described on the next chapter. These prototypes will be characterized and compared in order to corroborate design guidelines and some hypothesis about the operation of the system.



## Chapter 5

# Generator prototypes and experimental evaluation

### Contents

---

<b>5.1 First generation prototypes</b> . . . . .	<b>114</b>
5.1.1 Mounting fixture . . . . .	114
5.1.2 Transducer system assembly . . . . .	114
5.1.3 Soft magnetic material . . . . .	116
5.1.4 Permanent hard magnets . . . . .	117
5.1.5 Characterization of first generation prototypes . . . . .	117
5.1.6 Discussion . . . . .	127
<b>5.2 Second generation energy harvester</b> . . . . .	<b>128</b>
5.2.1 Portable test prototype 1 . . . . .	128
5.2.2 Optimal load resistor per commutation . . . . .	133
5.2.3 Output voltage rectification . . . . .	135
<b>5.3 Second portable test prototype</b> . . . . .	<b>139</b>
<b>5.4 Equivalent electrical model</b> . . . . .	<b>144</b>
5.4.1 Electrical representation of the generator . . . . .	144
5.4.2 Curve fitting and parameters estimation . . . . .	147
5.4.3 Influence of magnetic breaking on the generator performance . . . . .	150
<b>5.5 Power management module</b> . . . . .	<b>151</b>
<b>5.6 Discussion</b> . . . . .	<b>154</b>

---

*This chapter introduces the experimental prototypes that we built as proof of concept. Moreover, it presents all characterizations conducted to put in evidence the feasibility of this thermomagnetic energy harvesting with piezoelectric transduction. A fixture for clamping different piezoelectric transducer beams has been designed and fabricated in order to test first mesoscale prototypes. Last generation of reduced-size energy harvesters were produced to put in practice some design rules in miniaturizing the generator.*

## 5.1 Fabrication of the proof of concept

In this section, the main goal is to present the proof of concept of this generator. The purpose of this first generator was to validate the possibility of manufacturing an autonomous generator capable of detecting temperature thresholds. Moreover, it was desired that the prototype is quickly and easily achievable. Finally, one should not lose sight of the possibility of industrializing the product if it was satisfactory. Therefore, it had to be inexpensive to make, although it is still possible to reduce costs by simplifying manufacturing processes or by producing large quantities. This roadmap is therefore presided over our realization. It explains in part the size of the prototype or why the materials used are not always optimal.

### 5.1.1 Mounting fixture

For repeatability reasons of the prototypes we envisaged, we decided to design a fixture that allow us to play with some parameters of the generator's design such as the initial distance of separation between the FeNi alloy and the permanent magnet. The clamping configuration of the beam is also a sensitive aspect to be considered. We have designed through SolidWorks software the mounting fixture as shown in figures 5.1(a) and 5.1(b).

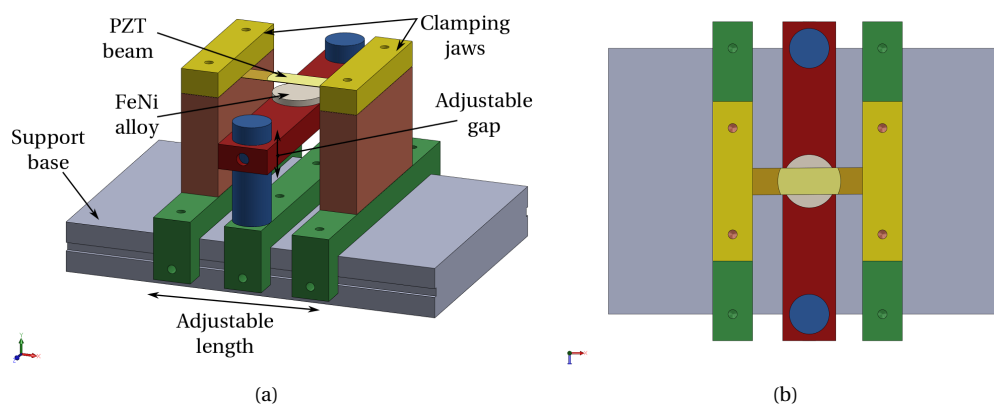


FIGURE 5.1: Fixture for mounting test prototypes (a) dimetric view of the 3D-CAD mode and its (b) top view representation.

The model has been fabricated entirely in aluminum excluding the clamping jaws; which are made of an isolating material. With this, an electrical isolation can be ensured for the electrodes of the piezoelectric beams. More details of this mounting fixture are presented in [Appendix B](#).

### 5.1.2 Transducer system assembly

We will make a brief inventory of possible piezoelectric materials, keeping in mind that it would be desirable that they can be used in thin layers to be able to reduce the size of the generator later. The use of aluminum nitride AlN or zinc oxide ZnO can be envisaged as piezoelectric candidates. There are several methods for their integration: epitaxy by vapor

deposition or sputtering. The structure of these materials makes it piezoelectric, so no polarization is necessary. In addition, since the deposition can be done at low temperature (200 to 300°C), their manufacture is compatible with the rest of the microelectronics steps. For this reason, they are widely used in applications such as Bulk Acoustic Wave Filters.

Thin layers of PZT are becoming more widespread since the problem of diffusion of Pb in the substrate is mastered. The properties of thin layers are now approaching those of massive ceramics. Two manufacturing methods are mainly used: sputtering and the sol-gel method which requires a high-temperature annealing (sometimes hardly compatible with the electronic part). It should not be forgotten that the PZT also requires a polarization step to align the dipole moments. Finally, with regard to polymers and piezo-composites, although their thickness is more question of downscaling, we admit to lack of hindsight and experience to judge their interest or not.

We propose a summary table of the different materials thus discussed and their properties. The goal this sort of table generally is to putting forward the key parameters in order to choose the most suitable material. In the case of piezoelectric materials, this choice is not easy because there is not a single parameter allowing to decide with certainty in all cases. The application intended usually eliminates some of them. For example, in our case, we have an approach that could be described as quasi-static or event-based. And, stiffer materials can offer better conditions for elastic energy conversion.

In general, however, it can be estimated that the coupling factors  $k_{33}$  or  $k_{31}$  and the piezoelectric coefficients  $d_{33}$  or  $d_{31}$  must be high. This reasoning seems to refer to the PZT family as the best choice. However, the permittivity of the material also plays an important role as it influences the voltage generated, which is advantageous for materials such as AlN for example. Finally, the mechanical quality factor of the material is also very important.

TABLE 5.1: Comparison of different piezoelectric materials and their characteristics.

<b>Material</b>	$\rho$ kgm <sup>-3</sup>	$\epsilon_r$ -	$d_{33}$ pCN <sup>-1</sup>	$d_{31}$ pCN <sup>-1</sup>	$k_{33}$ -	$k_{31}$ -	<b>Q</b> -	$\theta_C$ °C
Soft PZT	7600	3400	600	-276	0.75	0.4	60	200
Hard PZT	7600	1350	300	-108	0.68	0.33	1200	320
PZT 5H	7800	3800	650	-320	0.75	0.44	30	230
PVDF	1780	14	-30	20	0.2	0.1	10	180
AlN	3200	9	6.7	2.65	0.3			

Among the numerous prototypes we fabricated we can first present first generator prototypes we have modeled in finite elements method. The prototypes 1, 2 and 3, shown in figures 4.19(a), 4.19(c), and 4.19(e), respectively.

The photograph of these three architectures of transducer beams is shown in Figure 5.2.

For all these three architectures, we used as the piezoelectric bimorph material; PZT5H from piezo systems inc [95]. The clamping zone for all is marked in magenta color. Over this zone, the clamping jaws of the clamping fixture are exerting mechanical pressure against the block support ensuring a quite rigid mounting.

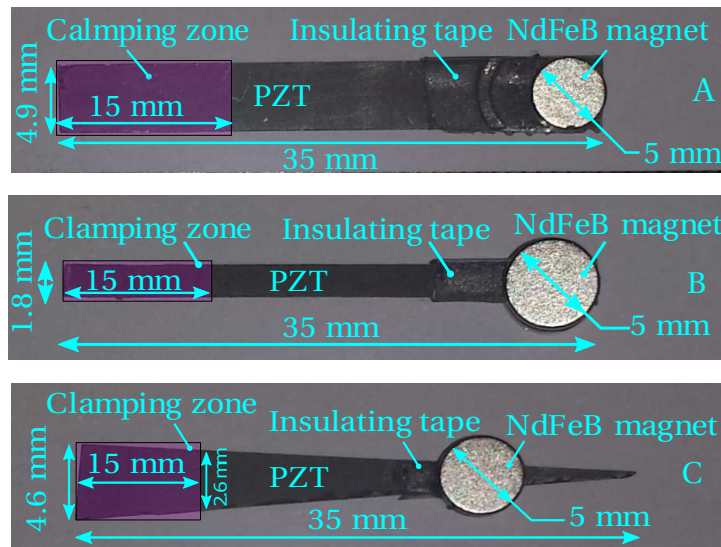


FIGURE 5.2: Photograph of the three different architectures of transducer beams. (A) Prototype1 wide beam, (B) narrow beam, (C) triangular-shape beam.

### 5.1.3 Soft magnetic material

The most important, since it will control the triggering of the generator depending on the temperature. It consists of a cylinder of soft magnetic material. The soft materials themselves do not have any magnetization, but they are sensitive to external magnetic sources. This results in a weak coercive field. Once this limit is crossed, the soft material quickly reaches saturation. The saturation magnetization varies with the temperature (the closer we get to the Curie temperature, the lower it tends to 0), which makes it possible to obtain a reversible system. Indeed, the magnetic field strength produced by the magnet remains constant, only the magnetization of the soft material varies. The soft material demagnetizes above the Curie temperature but becomes re-magnetized by cooling up in the field of the magnet.

In our case, we chose a FeNi alloy of a particular composition. Regarding this family of materials, it is possible to easily adjust their Curie temperature using the composition. Thus, with only a simple FeNi binary alloy,  $\theta_C$  can easily be passed from 0 to 200°C for Ni ranging from 28 to 35% of the total mass (see figure 3.2(a)). Adding other elements like Cr, Mo or Si also allows this kind of adjustment. For example, adding Cr increases this effect by obtaining a  $\theta_C$  of -150 to 600°C (see figure 3.2(b)).

This characteristic makes it easy to obtain a material with a transition temperature close to the area in which we would like to operate the generator (industrial environment or human body temperatures). In our case, the pre-requisites of the material were a  $\theta_C$  temperature close to the ambient (i.e., between 20 and 50°C approximately) and a saturation magnetization as large as possible in order to ensure sufficient magnetic force to close the generator.

Unfortunately, in despite many attempts and efforts in trying to procure more samples of these material family we could not obtain more samples of these materials. Therefore,

we had to re-use the cylinder sample provided to our research group back in 2009 by the research center Imphy Alloys, in the person of Thierry Waeckerle. The characteristics provided with the material were a Curie point,  $\theta_C$  at  $35 \pm 5^\circ\text{C}$  and a saturation magnetization of 0.39T at  $20^\circ\text{C}$ .

#### 5.1.4 Permanent hard magnets

Permanent magnets used consist in a pair of disc shaped NdFeB hard magnet as they can easily procurable. Moreover, their remanent magnetization is between 1.2 and 1.5 T which makes it possible to easily magnetize to saturation the soft magnetic material that will be placed against. In addition, it is recommended to use them at a temperature below  $80^\circ\text{C}$  which makes them suitable for most uses in the human environment. These  $80^\circ\text{C}$  are not the Curie temperature of the magnets, but rather mark the threshold at from which the magnetization begins to decrease sharply when the temperature increases. It will therefore be assumed that we will work sufficiently below this temperature and over a temperature range sufficiently reduced so that we can consider that their magnetization remains constant.

If it is necessary to work at higher temperatures, it is always possible to use magnets with a higher Curie temperature, such as SmCo. Their remanent magnetization is lower, but it remains sufficient to saturate many soft materials. So there should not be any trouble generating enough magnetic force. The magnet is fixed in the free end of the piezoelectric beam.

Figure 5.3 shows the photograph of a pair of hard permanent magnet in NdFeB and its main parameters are listed in Table 5.2.



---

FIGURE 5.3: Photograph of the pair of magnets used for the triggering system of the test prototype of the generator.

#### 5.1.5 Characterization of first generation prototypes

The characterization of the first prototypes is described as follows: Making use of a testbed we developed, as shown in 5.4(a), we conducted characterizations.

TABLE 5.2: General parameters of permanent hard magnets.

Item	Description
Material	NdFeB
Shape	Disc
Diameter	5mm
Height	1mm
Magnetization direction	Axial (parallel to height)
Finishing	Nickel-plated
Magnetization	N52
Adhesion strength	6.7N
Weight	$3 \times 10^{-4}$ kg
$\theta_C$	310°C
Remanence $B_r$	1.42 - 1.48 T
Coercive field strength $bH_c$	880 - 995 kAm <sup>-1</sup>
Energetic product $B \times H$ (max)	390 - 420 kJ m <sup>-3</sup>

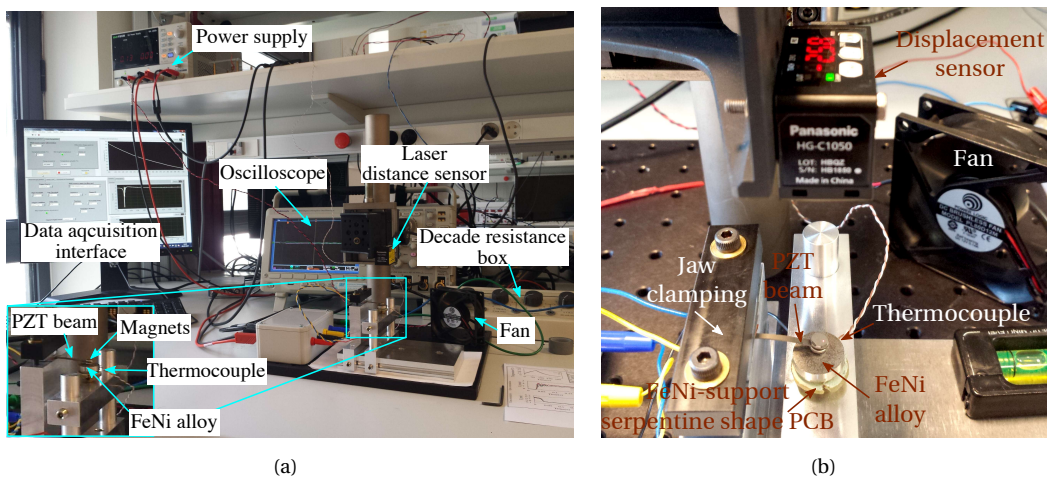


FIGURE 5.4: (a) Photograph of the testbed developed for first generation energy harvesters, showing the clamping fixture with a generator mounted and the data acquisition interface and the measurement equipments (c) close up view to the mounting fixture with the prototype.

The testbed consists in the mounting fixture already described. This support holds the cantilever beam. By adjusting the distance of separation of the FeNi alloy, we can tune the operating temperatures of the generator. The temperature evolutions of the FeNi alloy are produced by making flow an electrical current through a PCB serpentine-shaped attached to the FeNi alloy. We observe a peak of tension followed by some oscillations when the generator opens and a single peak when it closes. The tensions are of opposite signs. It

is easy to visualize the results on the oscilloscope. However, to record longer sequences (for example when you also want to acquire a slowly evolving temperature), this solution is no longer suitable. In this case, we developed a LabView interface in order to control the triggering of the oscilloscope and then record the output voltage at the commutation. The interface is also able to acquire temperature measurements through a thermocouple inserted into the FeNi sample. High impedance oscilloscope probes were used to allow us to use load resistor near to  $10M\Omega$ . Figure 5.5 presents such a recording over a time of 480s of the temperature of the FeNi.

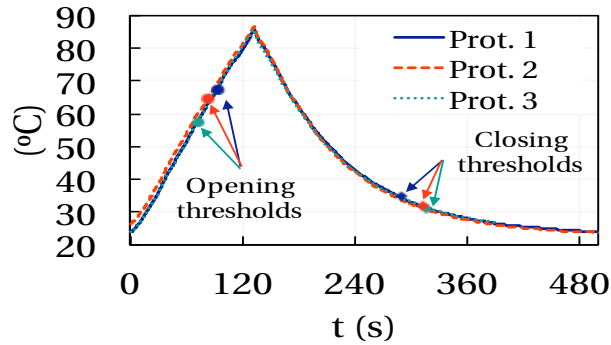


FIGURE 5.5: Experimental measurements of temperature response of first generation prototype architectures (Prototype.1 in blue solid line, Prototype 2 in red dashed line, and Prototype 3 in green dotted line). Opening and closing thresholds are marked over the graph for each device.

It can be seen that the thermal response is quite similar for all three prototypes. In part, this is due to the same volume of the FeNi alloy, as we only have changed the transducer beam dimension (i.e., width), therefore the influence is not significant to change the temperature response of the generator.

Thermal characterization of these prototypes is summarized on Table 5.3.

TABLE 5.3: Thermal characterization of the test prototypes.

Item	Units	Prototype 1 (wide beam)	Prototype 2 (narrow beam)	Prototype 3 (Triangular beam)
$\theta_{start}$	°C	25	26	24
$\theta_{open}$	°C	67	64	57
$\theta_{close}$	°C	34	32	31
$\Delta\theta$	°C	33	32	26
$t_{open}$	s	94	84	73
$t_{close}$	s	289	316	312

Then we sought to gather information about the power and the energy produced by our generator. We have therefore copied the protocol used generally for the characterization

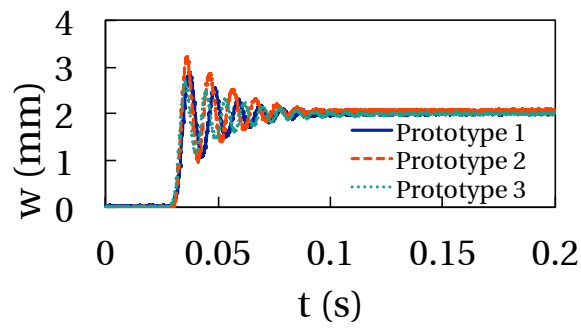
of piezoelectric generators extracting energy from vibrations. Thus, we connected a set of load resistances across the piezoelectric bimorph to determine its optimal value, a very important parameter to maximize harvested energy. The measurement was then performed using an oscilloscope connected to a measurement probe. However, we very quickly encountered a difficulty due to the differences between our source of excitation and those of vibratory generators. Indeed, the latter are generally subjected to sinusoidal excitation, generating a voltage also sinusoidal. It is therefore easy to extract data such as power and energy. As our temperature variations were cyclical at best, we had to use different order of magnitude.

We have opted for measuring the output voltage produced during commutations of the generator. Making use of the oscilloscope in trigger mode, we measured the differential voltage across the load resistor. We set the oscilloscope for capturing 10000 points in a window of 200ms. A delay of 3ms is considered in order to capture the totality of the signal. Moreover, by using a laser sensor connected to the oscilloscope, we monitored the vertical displacement at the tip of the beam during the commutations. In addition; temperature measurements were obtained through a thermocouple inserted into the FeNi alloy and connected directly to a NI data acquisition card. The temperature measurements are obtained every second. Therefore, we were able to get the temperature evolution of the FeNi at the moment we started to heat up the generator, the output voltage during commutations and displacements of the beam are presented as events from the overall experimentation.

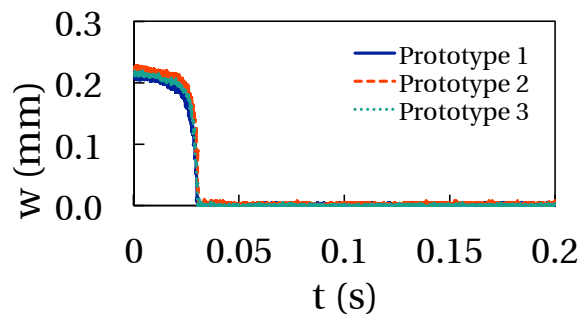
In order to compare all three responses, we decided to extract these two commutations from the overall elapsed time of experimentation. Indeed, these commutations do not happen at the same (i.e.,  $t_{open}$  and  $t_{close}$ ). Figures 5.6(a) and 5.6(b) present the vertical displacement of the tip of the beam during the opening and closing commutations, respectively. The interpretation of these result is as follows: we have superposed the measurement capture of 200ms regarding the output voltage and the vertical displacement  $w$ . Figures 5.6(c) and 5.6(d) depict the output voltage response for the opening and closing commutations, respectively.

After examining these results, it can be remarked that for all the prototypes, an initial distance of separation between the FeNi alloy and the horizontal position of the transducer beam (at open position) is  $z_0 = 2\text{mm}$ . Therefore, for the first 3ms, there is no vertical displacement. For this measurements,  $w = 0$  means a closed position of the generator. By the time opening commutations, transducer beam oscillates for a moment then resting in open position (i.e.,  $w = 2\text{mm}$ ). At closing commutation, it can be seen that vertical displacement does not corresponds to the initial distance of separation. This is due to the way the FeNi re-gains its magnetization and the magnetic force increases slowly. At a certain moment, when the magnetic force becomes predominant, the permanent mass is attracted towards the soft magnetic alloy.

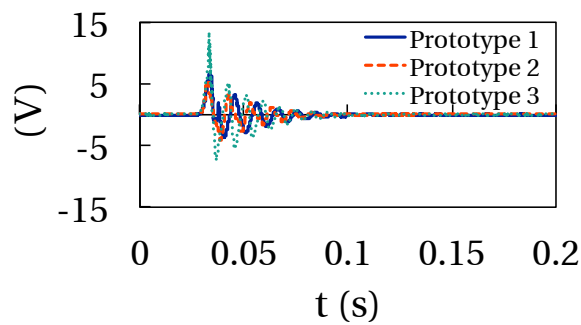
As expected, the output voltage during the opening commutations has oscillating form. Whereas the closing commutation produces a kind of peaks in voltage with amplitudes even larger than opening commutation. These voltages are almost always high enough to start any electronics. Nevertheless, these curves are not very meaningful, therefore we will instead calculate the instantaneous power produced during thresholds. To do this, we used the voltage that we squared before dividing them by the value of the corresponding load



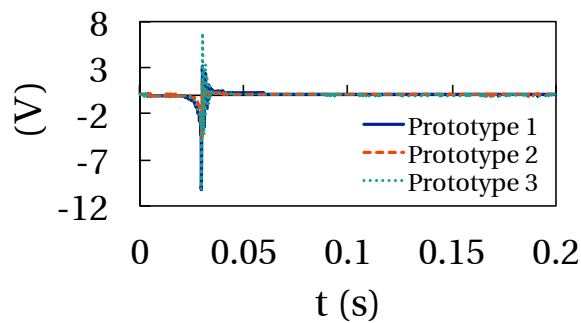
(a)



(b)



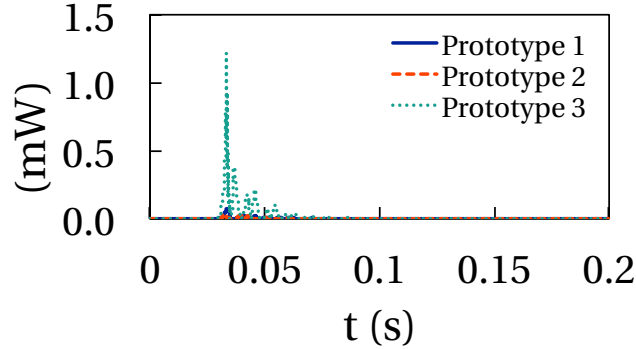
(c)



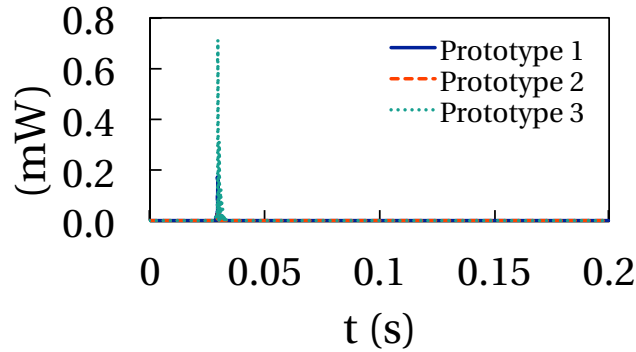
(d)

FIGURE 5.6: Experimental results comparison. (a) Vertical displacement of the tip of the beam during the opening commutation (b) and the closing commutation. (c) Generated voltage during the opening commutation and (d) during the closing commutation.

resistance. The instantaneous power makes it possible to better highlight the optimum resistance of the generator. Whether opening or closing as shown in figures 5.7(a) and 5.7(b), respectively.



(a)



(b)

FIGURE 5.7: Comparison of instantaneous power output of three first test prototypes of first generation energy harvester. (a) During opening commutation and (b) closing commutation of the generator.

In a first time, concerning the load resistor for each prototype, we opted to use a value that matches with the electrical impedance at resonance for each device. This resonance has been measured through impedance analyzer. After evaluating these results, [Table 5.4](#) compares their results.

Our experiments corroborate the finite element results regarding the resonance frequency of the transducer beam. For all three architectures, we considered an identical same initial gap, as well as a same magnetic volume. For calculating the average power,  $P_{ave}$ , at opening and closing, we considered 40ms and 7ms, respectively. The prototype 3 shows the highest output power per commutation. It also has the highest frequency of resonance.

In a second stage of experimentations, we decided to reduce the permanent magnetic volume by using smallest permanent magnets. We have used two permanent magnet discs of 1mm height and 2mm diameter. Now, the new magnetic volume is of  $6.28\text{mm}^3$ . With this new magnetic volume, the magnetic attraction force exerted in the triggering system was not strong enough to close the prototype 1. Only prototypes 2 and 3 were able to close with

TABLE 5.4: General characterization of the test prototypes.

Item	Units	Prototype 1 (wide beam)	Prototype 2 (narrow beam)	Prototype 3 (Triangular beam)
Initial gap	mm	2	2	2
Magnetic volume	mm <sup>3</sup>	39.2	39.2	39.2
Resonance frequency	Hz	90	85	120
Load resistor <sup>a</sup>	kΩ	610	720	150
Generator's volume <sup>b</sup>	cm <sup>3</sup>	0.140	0.038	0.024
$P_{ave}$ at opening <sup>c</sup>	μW	8.2	4.6	77.8
$P_{ave}$ at closing <sup>d</sup>	μW	9.5	1.9	43.3
Energy at opening	μJ	0.328	0.184	3.112
Energy at closing	μJ	0.066	0.013	0.303
Energy density at open	μJ cm <sup>-3</sup>	2.34	4.84	129.66
Energy density at close	μJ cm <sup>-3</sup>	0.47	0.34	12.625

<sup>a</sup>Value corresponding to device's electrical impedance in resonance

<sup>b</sup>Considering the transducer's oscillation maximal amplitude

<sup>c</sup>Considering a time duration of 40ms from the opening commutation

<sup>d</sup>Considering a time duration of 7ms from the closing commutation

this new magnetic volume. Therefore, we will call these two new prototypes as “Prototype 2b” and “Prototype 3b”. However, these new prototypes were not able to operate at a same initial gap we tested before, instead we opted for investigating the new maximum initial gap.

Figure 5.8 shows the temperature evolution of the generator as well as the opening and closing temperatures for these two prototypes. It can be seen a quite similar response for both prototypes. As we only modified the permanent magnet volume, and the FeNi volume keeps constant, thermal response of the generator seems to not be influenced.

Opening and closing thresholds are represented on the graph. From Figure 5.8 it can be seen that **for prototype 2b, these thresholds are higher than those of prototype 3b. However, thermal hysteresis  $\Delta\theta$  is higher for prototype 3b.**

This can be attributed to the difference in mechanical stiffness of these prototypes; that is, **prototype 3b being stiffer than prototype 2b, hence, its mechanical force to be overcome is higher than the one of prototype 2b. Thus, lower temperatures are required to decrease magnetization to overcome forces.**

Unlike, the first experimentation we conducted, on this second stage of experimentation we extracted the two events (i.e., opening and closing commutations) and we put them over the overall temperature evolution. Figures 5.9(a) and 5.9(b) show the vertical displacement of the tip of the transducer beam for the opening and closing commutation, respectively.

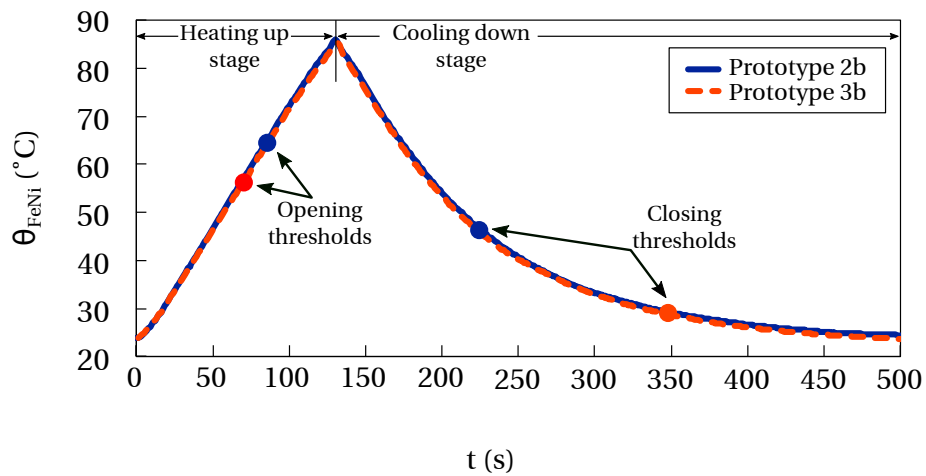


FIGURE 5.8: Experimental results of the temperature evolution of prototypes 2b and 3b. Opening and closing thresholds are represented over the graph.

Interpretation of these results proceeds as follows: **zero vertical displacement ( $w = 0$ ) means that the generator is in closed position; thus permanent magnets attached to the free end of the beam are in contact with the FeNi alloy.**

By the time the transducer beam is released, the oscillations of the device are captured and the final horizontal position corresponds to the initial distance of separation of the system. In this case, the prototype 2b starts its opening commutation at  $t_{open} = 86\text{s}$  and  $t_{open} = 71\text{s}$  for prototype 2b and 3b, respectively.

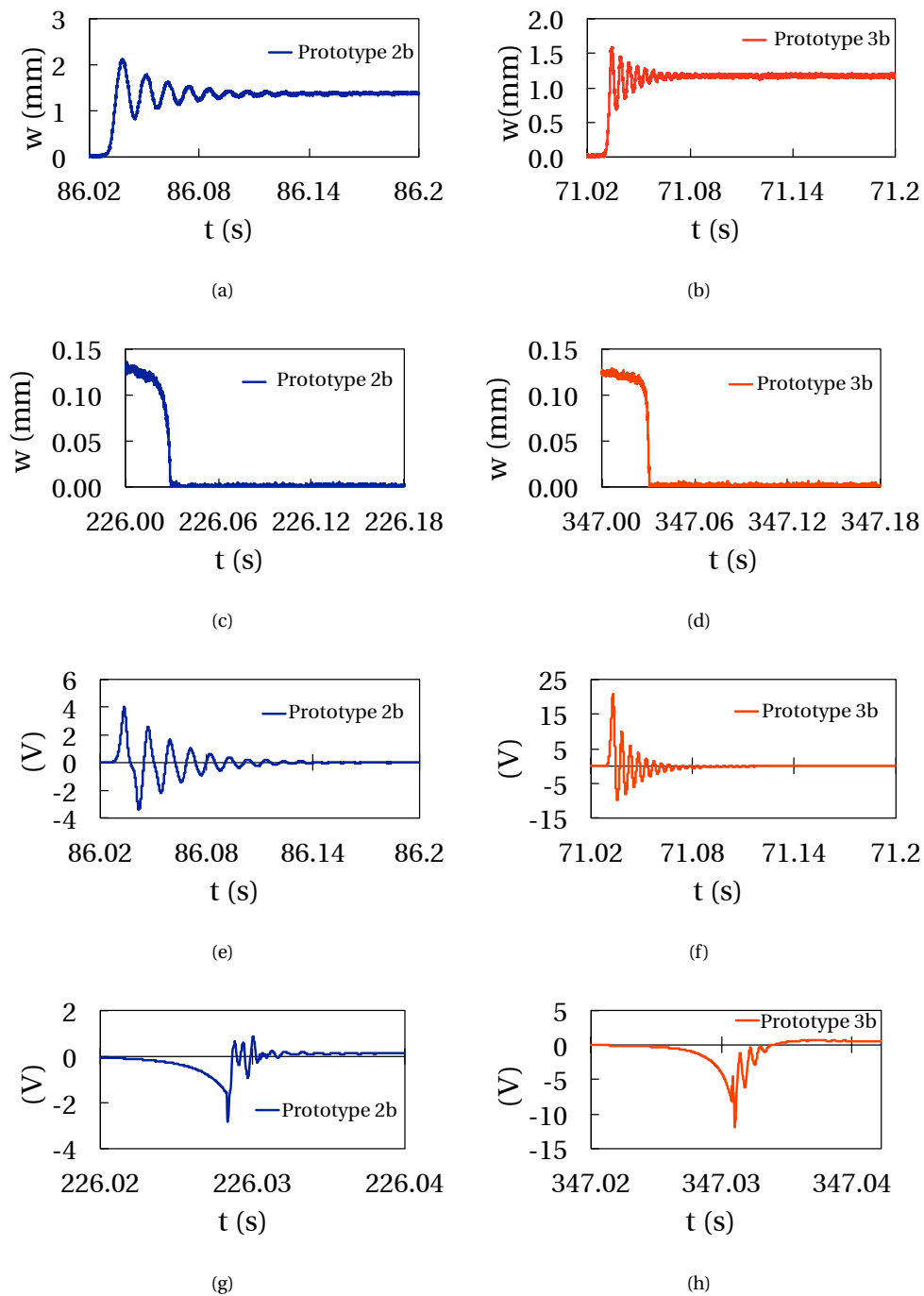


FIGURE 5.9: Experimental behavior of test prototypes of generator when a smaller magnetic volume for prototype 2 and 3 is considered (i.e., Prototype 2b and 3b). (a) Vertical displacement of the tip of the beam during the opening commutation for prototype 2b and (b) prototype 3b. (c) Vertical displacement of the tip of the beam during the closing commutation of prototype 2b and (d) prototype 3b. (e) Output voltage of prototype 2b and (f) prototype 3b during their opening commutations. (g) Output voltage of prototype 2b and (h) prototype 3b during their closing commutations.

Figures 5.9(c) and 5.9(d) illustrate the response of the generators during their corresponding closing commutation. It is clear that the initial distance of separation is not the total stroke of the permanent magnet at this commutation. As explained before, the “avalanche effect” when the FeNi sample is regaining its magnetization produces this behavior, first smooth and then abruptly.

Regarding output voltage of the generators during commutations; during both opening and closing transitions oscillations are present on the output voltage. This corroborate the hypothesis of the structure changes its boundary condition. That is, it passes from fixed-free during the opening commutation, to fixed-pinned during the closing transition. The effect of the rebound between the permanent magnet and the FeNi alloy is evident on the output voltage signal as shown in figures 5.9(e), 5.9(f), 5.9(g), and 5.9(h).

These results corroborate the hypothesis of reducing the volume of the permanent magnetic volume, two main modifications are obtained: resonance frequency of the transducer is increased as the seismic mass (permanent magnet attached to the beam) has been reduced. And the attraction magnetic force has been also reduced, this is why the initial distance of separation could not be the same as the first stage of experimentation. This time, these initial distance of separation are, 1.17 and 1.15mm, for prototype 2b and prototype 3b, respectively.

We also estimated the instantaneous power during opening commutation of these two prototypes as shown in figures 5.10(a), and 5.10(b). While figures 5.10(c), and 5.10(d) show the instantaneous power during the closing transition.

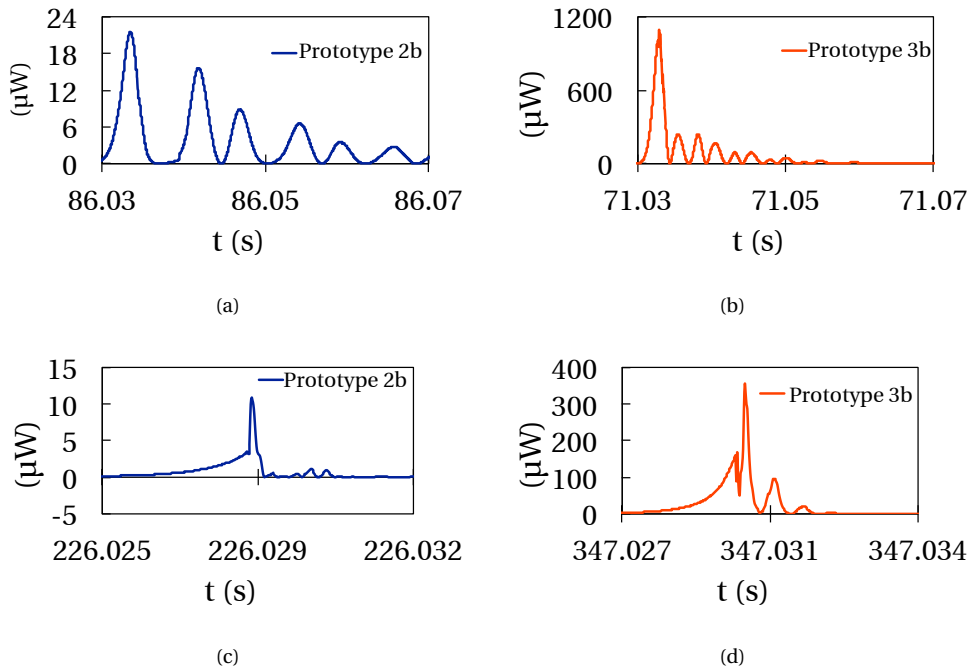


FIGURE 5.10: Instantaneous power per commutation of test prototypes of generator using smaller permanent magnets. (a) and (b) Instantaneous power during opening commutations of prototypes 2b and 3b, respectively. (c) and (d) Instantaneous power during closing transitions of prototypes 2b and 3b, respectively.

Table 5.5 summarizes the main features of these two prototypes with smaller magnets.

TABLE 5.5: General characterization of the test prototypes when smaller magnets are considered.

Item	Units	Prototype 2b	Prototype 3b
		(narrow beam and smaller magnets)	(Triangular beam and smaller magnets)
$\theta_{open}$	°C	64	56
$\theta_{close}$	°C	46	28
$\Delta\theta$	°C	18	28
$t_{open}$	s	86	71
$t_{close}$	s	226	347
Initial gap	mm	1.17	1.15
Magnetic volume	mm <sup>3</sup>	6.28	6.28
Resonance frequency	Hz	100	205
Load resistor <sup>a</sup>	k $\Omega$	740	400
Generator's volume <sup>b</sup>	mm <sup>3</sup>	58	14
$P_{ave}$ at opening <sup>c</sup>	$\mu$ W	3.77	72.58
$P_{ave}$ at closing <sup>d</sup>	$\mu$ W	0.78	27.42

<sup>a</sup>Value corresponding to device's electrical impedance in resonance

<sup>b</sup>Considering the transducer's oscillation maximal amplitude

<sup>c</sup>Considering a time duration of 40ms from the opening commutation

<sup>d</sup>Considering a time duration of 7ms from the closing commutation

Analyzing these results, we can note an increase on the frequency of resonance of the devices. Also, a tuning in the temperatures for opening and closing is obtained by modifying the mechanical stiffness of the transducer through the seismic mass reduction. By reducing the volume of the permanent magnet, total volume of the generator is logically reduced as well, thus output power density can also be improved. And, this improvement is more evident on results for prototype 3b.

### 5.1.6 Discussion

These two experimentation stages, allowed us to put in evidence the proof of the concept. Coupling thermo-magnetization of soft magnetic alloys, such as FeNi binary, and piezo-electric transduction, it is possible to convert temperature fluctuations into electricity.

The architecture of the generator offers a wide range of possibilities in order to adjust the temperature range for the operation of the generator. Two key design parameters have been identified as the main points to be taken into account for efficient operation of the device; initial distance of separation and equivalent stiffness of the transducer beam. By increasing

the initial distance of separation, it is possible to obtain larger oscillations amplitudes of the transducer beam.

By reducing the volume of the permanent magnet, it is possible to increase the frequency of resonance of the transducer beam, thus better energy conversion capabilities. As our general intention is to miniaturize this type of generator, we have undertaken a second stage of test prototype fabrication. This time, we focused in having a portable prototype and we intended to better improve temperature variations as the input excitation of the system.

## 5.2 Second generation energy harvester

A second generation test prototypes is detailed in this section. The main goals of this experiments are:

1. To produce a portable test prototype,
2. To check repeatability of the opening and closing temperatures given a generator design,
3. To explore, experimentally, optimal load resistor for both, opening and closing transitions.

The main change we had to do is the fixture for mounting the prototype. As we saw, the fixture we developed in a first experimentation stage being bulky, it has to be modified. Secondly, the cantilever beam should be reduced in length as it might increase the frequency of resonance of the device. Since, we could not procure different thickness piezoelectric materials, we decided to explore reduction in length and width of the transducer beam as well as the permanent magnet size.

### 5.2.1 Portable test prototype 1

Having in mind these main goals, we decided to build different frames for mounting the generator. In a first attempt, we realized a prototype as shown in figures [Figure 5.11](#). It consists in a clamping frame made on acrylic. The main advantage of this material is its lightness compared with precedent aluminium mounting fixture. Other positive point of using such a material is its ease in manufacturing and machining as drilling and cutting. There are two rectangular pieces of acrylic with a main hole at the center. This hole is allowing the fixation of the FeNi alloy making use of a lateral inserted screw to fix it. These two rectangular pieces are holding the PZT bimorph.

For this second generation of energy harvesters, we also enhanced the method of producing temperature fluctuations. Indeed, instead of using heat Joule, we procured a Peltier module which is placed in contact with the FeNi alloy. The intention of using the Peltier module is to explore repeatability of temperature thresholds. Accelerating the heating up and cooling down stages, we believe that in a same period of time where we could have 1 thermal cycle, we will have several thermal cycles (i.e., opening and closing transitions).

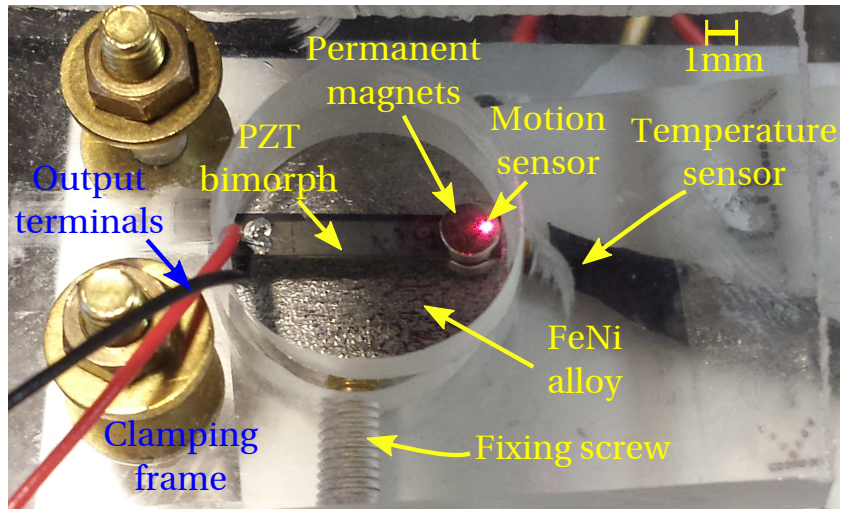


FIGURE 5.11: Photograph of the first portable test prototype of a second generation energy harvester.

The main characteristics of the first portable prototype of the second generation energy harvester are listed in [Table 5.6](#)

TABLE 5.6: General dimensions of the main parts of the first portable test prototype of the second generation energy harvester.

System part	Parameter	Symbol	Units	Value
Transducer beam	Length of cantilever beam	$L_B$	m	$10 \times 10^{-3}$
	Width of cantilever beam	$w_B$	m	$2 \times 10^{-3}$
	Thickness of shim layer	$h_B$	m	$100 \times 10^{-6}$
	Thickness of PZT layer	$h_p$	m	$130 \times 10^{-6}$
Permanent magnet	Height of magnet	$h_{mag}$	m	$1 \times 10^{-3}$
	Radius of magnet	$r_{mag}$	m	$1 \times 10^{-3}$
FeNi specimen	Height of FeNi	$h_{FeNi}$	m	$4 \times 10^{-3}$
	Radius of FeNi	$r_{FeNi}$	m	$7 \times 10^{-3}$

We produced temperature fluctuations on the FeNi alloy by using the Peltier module. Starting at ambient temperature, we performed at least two thermal cycles and we captured the opening and closing thresholds for this prototype. The evolution of the temperature of the portable prototype is shown in [Figure 5.12](#)

The evolution of temperature of the FeNi alloy is better controlled with respect to the first generation energy harvesters. Now, it can be seen that in a period time of 170s, two thermal cycles can be completed. This experimentation was carried out considering the

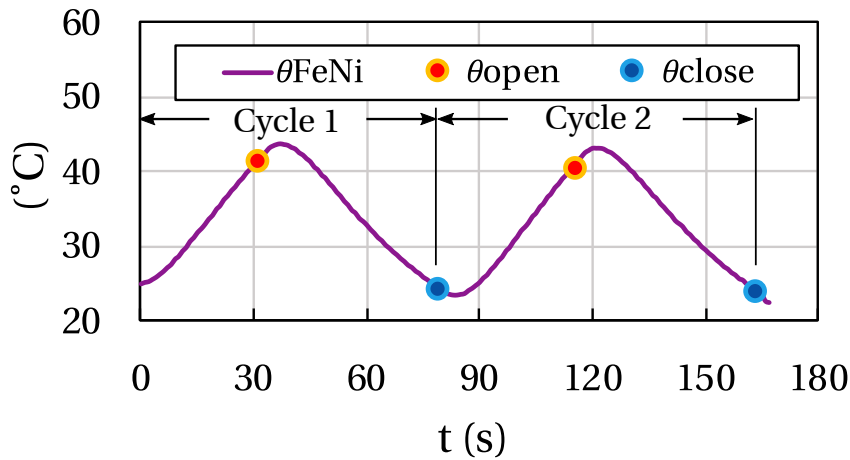


FIGURE 5.12: Evolution of the temperature of the first portable test prototype of energy harvester. Operation of two thermal cycles are represented.

initial position of the generator is closed. The temperature of the FeNi alloy at the beginning is about 25°C. We have built an automatized control for the Peltier module so that when opening commutation is reached, the heating up stage ends and the cooling down process starts. We also added a control to the interface in order to repeat  $N$  cycles this experimentation.

From these results, it can be seen how the temperature of the FeNi can be lead up to the opening temperature at  $\theta_{open} = 41^\circ\text{C}$ , next the closing threshold is reached when temperature decreases to  $\theta_{close} = 24^\circ\text{C}$ . The entire cycle was completed in 80s. Afterwards, the second thermal cycle is completed at  $t = 167\text{s}$ . The opening and closing temperatures are constant for the two thermal cycles. Considering this input excitation as the best case for this generator design; the thermal cycle is then 80s. We have just corroborated the repeatability of thermal thresholds experimentally.

Now, we are going to investigate the transient behavior of the generator in terms of energy converted. Figures 5.13(a) and 5.13(b) depict the vertical displacement of the tip of the beam during the opening and closing transitions of the first thermal cycle, respectively. It can be deduced that, the opening transition is reached at  $t_{opening1} = 31\text{s}$ . Once the transducer is released, it oscillates with strongly damped amplitudes up to 0.75mm. The horizontal position of the transducer beam is about 0.65mm. This corresponds to the initial distance of separation for this design.

The closing transition of the first cycle is reached at time  $t_{closing1} = 79\text{s}$ . As expected, the “avalanche effect” at the closing transition is also evident as the initial distance of separation is not represented in the closing commutation. For this design, the captured closing transition show a gap of 0.3mm. However, this transition show also the contact when the generator closes.

Figures 5.13(c) and 5.13(d) depict the output voltage during the opening and closing transitions of the first thermal cycle, respectively. The opening transition shows an alternate signal because of the free oscillations of the beam. While the closing transition shows a

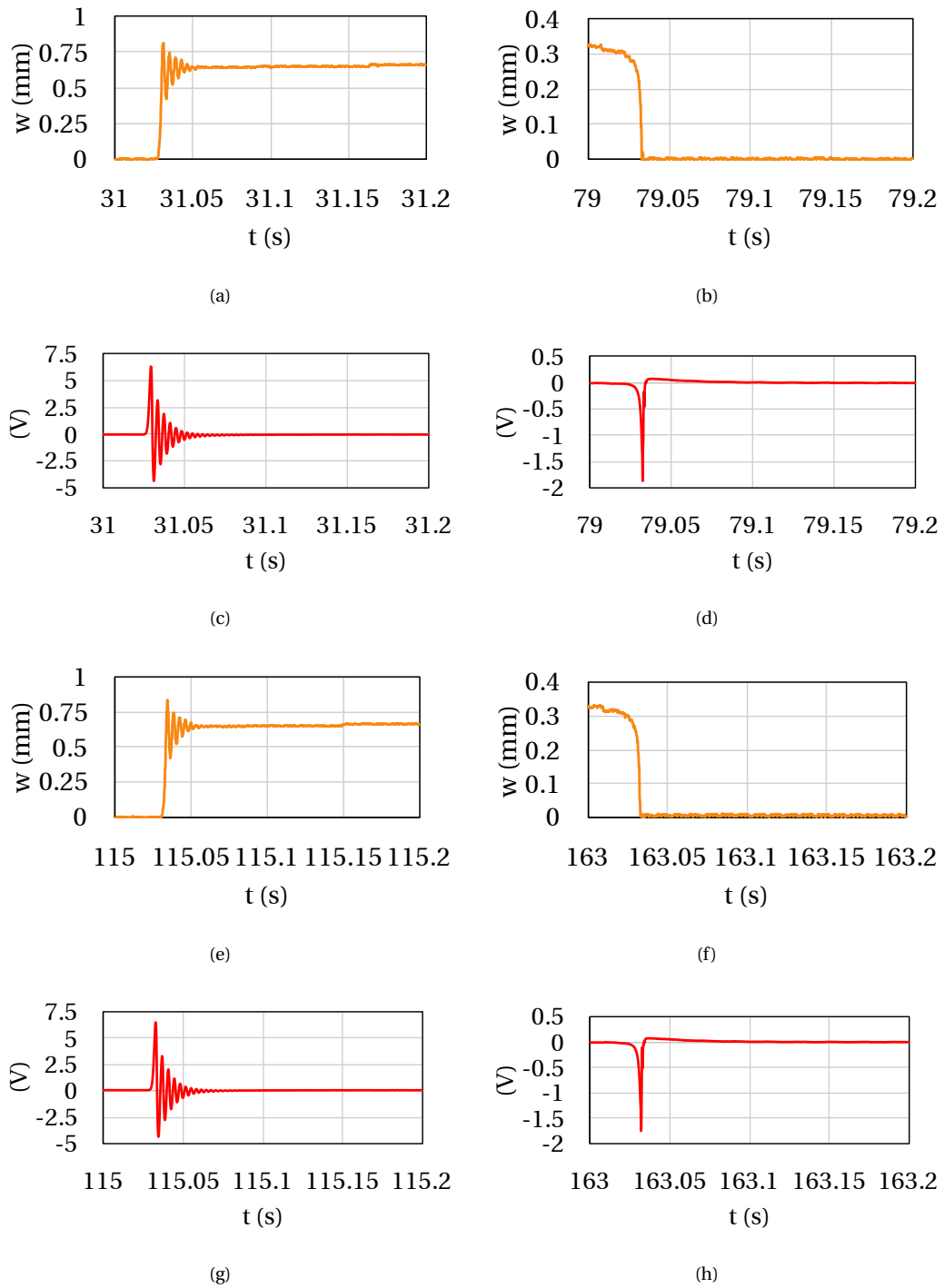


FIGURE 5.13: Experimental results of the first portable test prototype of second generation energy harvester, dynamic behavior characterization. (a) Vertical displacement of the tip of the beam during the opening and (b) closing commutations of the first thermal cycle. (c) Output voltage generated during the opening and (d) closing commutations of the first thermal cycle. (e) Vertical displacement of the tip of the beam during the opening and (f) closing commutations of the second thermal cycle. (g) Output voltage generated during the opening and (h) closing commutations of the second thermal cycle.  $R_{Load} = 390k\Omega$ .

negative peak of voltage; this is concordant with our expectations from previous prototypes and simulations, in despite the small initial gap of separation, this peak is reaching almost -2V. A load resistor,  $R_{Load} = 390k\Omega$  is connected to the electrodes of the PZT bimorph. This value has been selected after performing a set of measures making a variable sweep for this parameter. This experiment will be presented later on this section.

By making a direct FFT of the output voltage signal, during the oscillation period, we can find the natural frequency of these oscillations. A frequency of resonance of  $f_r = 255\text{Hz}$  is found. For opening commutations, maximum peaks of 7V and -4.7V are reached. These values are repeated during the second opening commutation (represented in figure 5.13(g)). Second thermal cycle of this experiment revealed a good repeatability on the behavior of the generator.

In order to get better information about the energy harvesting capabilities of this prototype we decided to extract the power generated during a determined period of time within a commutation. To do this, we considered 10 oscillations during the opening transition. In this way, if the resonance of frequency changes for a different design, we will also consider  $N = 10$  oscillations of that new period of time. Figures 5.14(a) and 5.14(b) show the instantaneous power during opening and closing transitions of the generator during its first operation cycle, respectively.

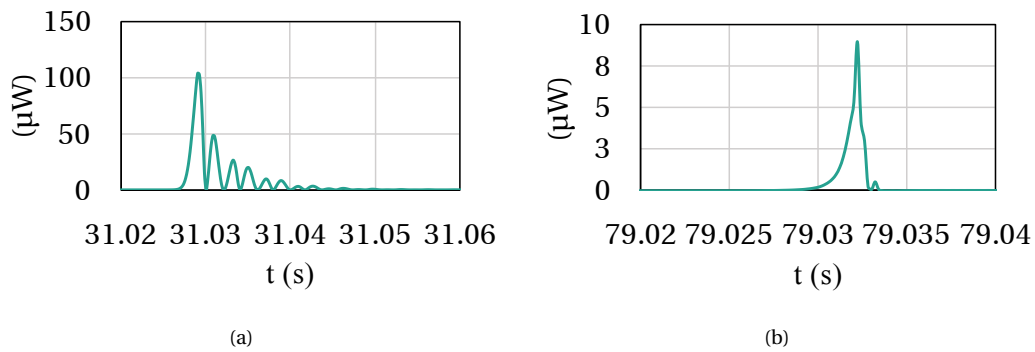


FIGURE 5.14: Instantaneous power of the portable test prototype of second generation energy harvester when a load resistor  $R_{Load} = 390k\Omega$  is connected to the electrodes of the PZT bimorph. (a) Instantaneous power during the opening commutation and (b) closing commutation.

We realized again that during the opening commutation of the generator more energy is converted than during the closing commutation. It can also be a critical point into design considerations. Because of the difference in the output signals for both commutations, an optimal load resistor may be different for each transition. In order to have most valuable information about the performance of the generator, we presents the main features of this first portable prototype of second generation energy harvester listed on Table 5.7.

TABLE 5.7: Characterization values of the first portable prototype of second generation energy harvester.

Item	Units	Cycle 1		Cycle 2	
		Opening	Closing	Opening	Closing
Resonance $f_r$	Hz	255	-	255	-
Average power <sup>a</sup>	$\mu\text{W}$	$1.29 \times 10^1$	$4.9 \times 10^{-1}$	$1.3 \times 10^1$	$4.85 \times 10^{-1}$
Energy	$\mu\text{J}$	$5.16 \times 10^{-1}$	$1.96 \times 10^{-2}$	$5.19 \times 10^{-1}$	$1.94 \times 10^{-2}$
Generator's volume <sup>b</sup>	$\text{cm}^3$	$5.87 \times 10^{-1}$	$5.87 \times 10^{-1}$	$5.92 \times 10^{-1}$	$5.92 \times 10^{-1}$
Energy density	$\mu\text{J cm}^{-3}$	$8.79 \times 10^{-1}$	$3.34 \times 10^{-2}$	$8.77 \times 10^{-1}$	$3.28 \times 10^{-2}$
Temperature $\theta$	$^\circ\text{C}$	41.4	24.4	40.7	24.2
Time at commutation $t$	s	31	79	115	163

<sup>a</sup>Within a period time of  $10T$  ( $T$  is the fundamental period of oscillations).

<sup>b</sup>Considering the volume of transducer's maximum deflection.

Compared with previous test prototypes, frequency of resonance of the transducer has been increased. The average power has been calculated within a time period of  $10T$ ; where  $T$  is the fundamental period of the transducer beam. Taking the values of this prototype,  $T \approx 4\text{ms}$ , hence,  $40\text{ms}$  is the resulting time period. By making use of Equation 3.33, we obtained the energy per commutation. As we demonstrated, the output signal during the commutations of the generator are different; so we decided to explore the behavior of the generator under different values of load resistor. This experimentation is presented in the next section.

### 5.2.2 Optimal load resistor per commutation

This part of the chapter deals with the experimentation of the first portable test prototype under different values of load resistor. Besides of exploring the response of the generator as a function of load resistor, we checked also for repeatability and we conducted, for each load resistor value, measurements of two thermal cycles to have two opening and two closing commutations. To carry out these measurements, the generator was connected to various load resistances (which made it possible to verify at the same time that the value of the resistance does not affect the thresholds, a normal conclusion since the load resistance does not modify the magnetic properties of FeNi). We then made recordings simultaneous piezoelectric voltage and temperature in the core of FeNi. The voltage produced at each threshold allowed us to determine the moment of position transition; we only had to note the corresponding temperature. Figure 5.15 shows the operating temperatures of the prototype as function of load resistor.

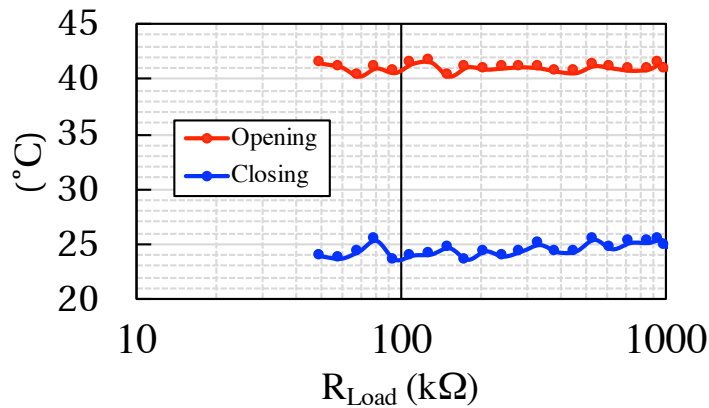


FIGURE 5.15: Operating temperatures of the first portable prototype as a function of load resistor, in red line opening temperature and in blue line closing temperature.

It is not surprising that thermal thresholds keep quite constant. As magnetic properties of the FeNi alloy do not depend on load resistor connected to the generator. The opening temperature for this architecture is about  $\theta_{opening} = 41^\circ\text{C}$ , while closing temperature is about  $\theta_{closing} = 24^\circ\text{C}$ . The range of load resistor values is from  $50\text{k}\Omega$  to  $1\text{M}\Omega$ . Using an oscilloscope probe of  $10\text{M}\Omega$  we have taken the output voltage directly at the load resistor.

Figures 5.16(a) and 5.16(b) show the average power per commutation as well as the energy density, respectively, of this first portable test prototype of second generation energy harvester.

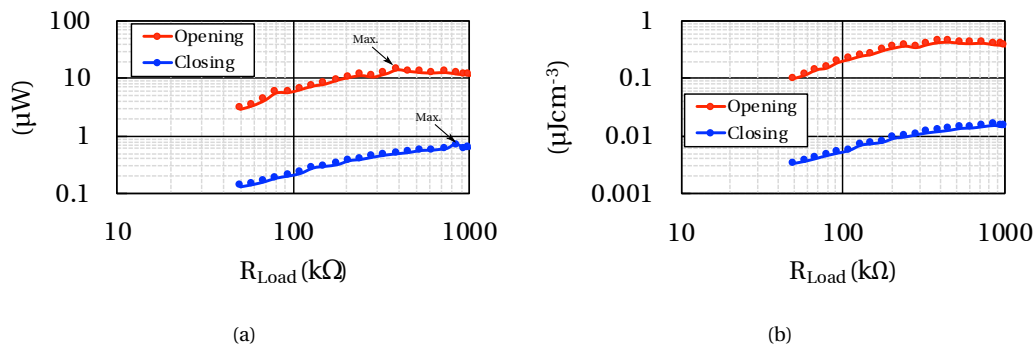


FIGURE 5.16: Output average power and energy density as function of load resistor of the first portable teste prototype of second generation energy harvester. (a) Output average power per commutation as function of load resistor, (b) Energy density per commutation as function of load resistor.

These results corroborate the hypothesis of having different optimal load resistance for each commutation. As can be deduced from these measurements, for the opening commutation, the maximum power output is  $13.2\mu\text{W}$  when  $R_{Load} = 390\text{k}\Omega$ . For the closing commutation, a maximum output power of  $0.63\mu\text{W}$  is reached when a load resistor

$R_{Load} = 855k\Omega$  is connected. These results are rather good since the variation of the thresholds is practically negligible. This means that the generator can be efficiently incorporated in a node or system that requires the monitoring of certain temperatures with a precision of the order of the degree (such as an air conditioning circuit). Furthermore, these data suggest that different adapted load resistor to each generator commutation should be considered. Indeed, as we have initially thought, the quasi-static behavior of this device leads to two completely different output signals. Unlike vibration based energy harvesters, where the input excitation produces a single output signal type, the approach to extract the maximum of the converted energy should be different. And, the use of a rectifier to convert the AC output signal from piezoelectric transduction could be another important aspect to be considered.

### 5.2.3 Output voltage rectification

In practical applications, adapting a load resistor to opening commutation should be the first attempt in order to maximize the energy transfer stage. However, in most of practical applications, a rectification stage is required to power any electronic device such as wireless sensors. To go beyond the energy harvester design and implementation, we have decided to implement a full wave rectifier instead of the load resistor in order to explore the behavior of the test prototype under such a condition. Figure 5.17 shows the schematic representation of the full wave rectifier bridge we connected directly to the output of the generator.

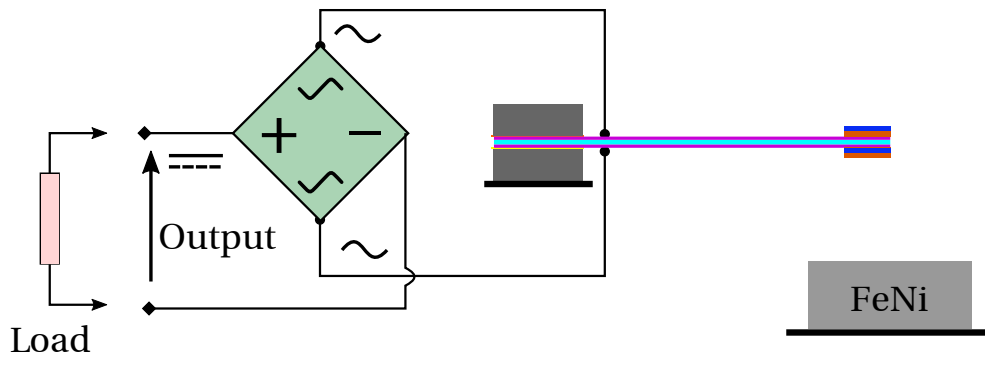


FIGURE 5.17: Schematic representation of the energy harvester with a full wave rectifier bridge.

On the schematic, the load element can be either a simple load resistor, a storage capacitance or even another circuitry to be powered. In a first time, we used the oscilloscope probes, which were directly connected at the rectifier bridge. Figure 5.18 shows the evolution of the temperature and the operating thresholds of first portable test prototype of energy harvester when a full wave rectifier bridge is connected to the output. The rectifier bridge has been implemented using Small Signal Fast Switching Diodes, namely, 1N4148.

We performed experimentations by producing temperature fluctuations on the FeNi alloy in order to open the generator and then to close it. Once the generator changes its stable position, we captured the temperature and the output voltage generated.

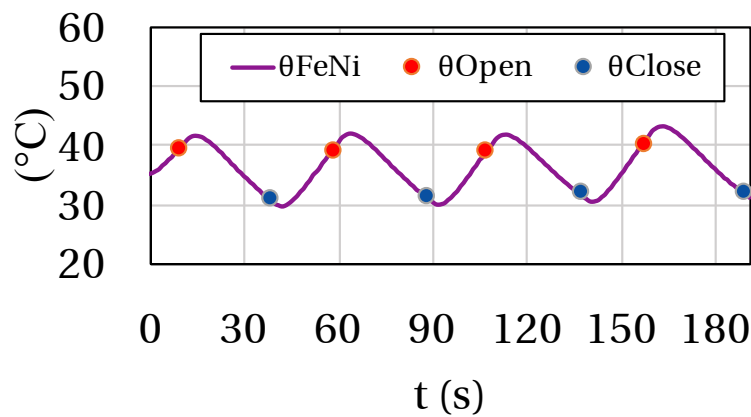


FIGURE 5.18: Evolution of temperature during 4 thermal cycles of operation of first portable test prototype with a full wave rectifier bridge connected to the output.

From these results we can corroborate a good precision on the opening and closing thresholds for this test prototype. It is clear that input excitations of the system affect the performance of the generator, we have recreated the best case of the input scenarios, where the temperature variations are ranging the thermal thresholds of the device.

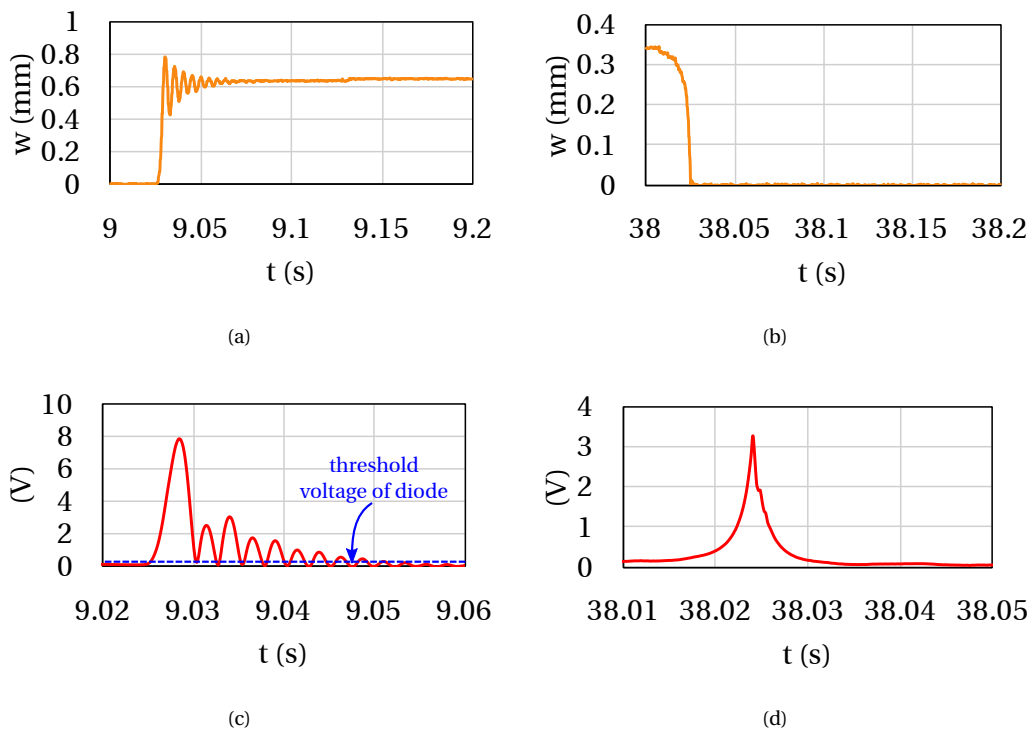


FIGURE 5.19: Measurements, for the first thermal cycle, of: the vertical displacement of the tip beam during (a) opening and (b) closing commutations, the output voltage during (c) opening and (d) closing commutations. A full wave rectifier bridge is connected to the generator.

It can be seen that the initial distance of separation for this architecture was 0.6mm. For the opening transition, we can see the first peak is reaching values of 8V. However, it is strongly damped as the second and third oscillation peak decrease below the half of this maximum amplitude.

As expected, for the closing commutation, the output peak of voltage is now positive. However, the amplitude of this peak is considerably lower than the ones of the opening transition.

Table 5.8 summarizes the main features of the generator response considering its first two thermal cycles of this experimentation.

TABLE 5.8: Main features of the first portable prototype of second generation energy harvester with a full wave rectifier bridge connected as a load.

Item	Units	Cycle 1		Cycle 2	
		Opening	Closing	Opening	Closing
Resonance $f_r$	Hz	250	-	250	-
Average power <sup>a</sup>	$\mu\text{W}$	$6.94 \times 10^{-1}$	$1.26 \times 10^{-2}$	$7.87 \times 10^{-1}$	$5.87 \times 10^{-3}$
Energy	$\mu\text{J}$	$2.78 \times 10^{-2}$	$5.04 \times 10^{-4}$	$3.15 \times 10^{-2}$	$2.35 \times 10^{-4}$
Generator's volume <sup>b</sup>	$\text{cm}^3$	$5.87 \times 10^{-1}$	$5.87 \times 10^{-1}$	$5.91 \times 10^{-1}$	$5.91 \times 10^{-1}$
Energy density	$\mu\text{J cm}^{-3}$	$4.74 \times 10^{-2}$	$8.59 \times 10^{-4}$	$5.33 \times 10^{-2}$	$3.98 \times 10^{-4}$
Temperature $\theta$	$^{\circ}\text{C}$	39.4	31.2	39.2	31.5
Time at commutation $t$	s	9	38	58	88

<sup>a</sup>Within a period time of  $10T$  ( $T$  is the fundamental period of oscillations).

<sup>b</sup>Considering the volume of transducer's maximum deflection.

The most important finding is that operating temperatures of this test prototype are near to human body temperature (see Figure 1.2). This opens dramatically potential applications for such a generators. As opening temperature is below  $40^{\circ}\text{C}$ , it suggests that this device may be opened by the heat of human body being near to  $37^{\circ}\text{C}$ . Concerning the closing temperature, it can easily provided by ambient temperature. In other terms, let us imagine we put this portable generator in a watch frame in such a manner that the FeNi alloy is exposed to be touched by hand. At that moment, the temperature of the FeNi is increased by means of the human body heat. The generator opens and converts this temperature fluctuation into electricity. Afterwards, by releasing the hand from the generator, it cools down through convection heat transfer (supposing ambient temperature is below closing threshold). At that moment, the generator converts this temperature variation into electricity through the closing commutation.

In another vein, the rectified output voltage can be stored in a capacitor connected to the rectification stage. It could help to store the energy of this first peak and those later. We opted for exploring this approach and we connected to the output of the rectifier bridge a capacitor,  $C_{Load} = 2\text{nF}$  and we repeated the experiments. This value has been selected in order to have a constant time in the order of some tens of ms (with the oscilloscope probe of  $10\text{M}\Omega$ ).

The evolution of the temperature of the FeNi alloy showing opening and closing thresholds are shown in Figure 5.20. Figures 5.21(a) to 5.21(d) show dynamic performance of the generator during the first thermal cycle of this experimentation.

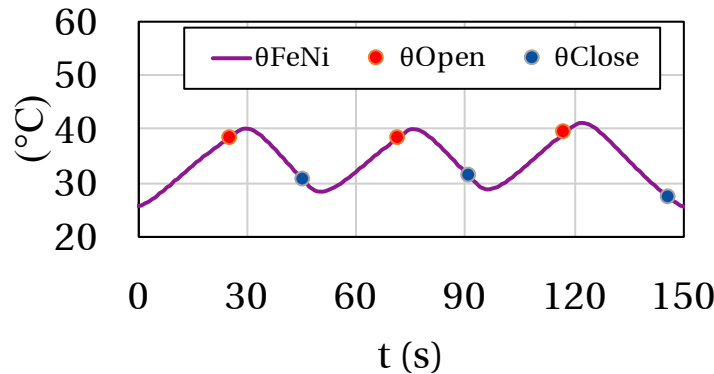


FIGURE 5.20: Evolution of temperature of the FeNi alloy during 3 thermal cycles of operation with a full wave rectifier bridge and a load capacitor,  $C_{Load} = 2\text{nF}$  connected to the output of generator.

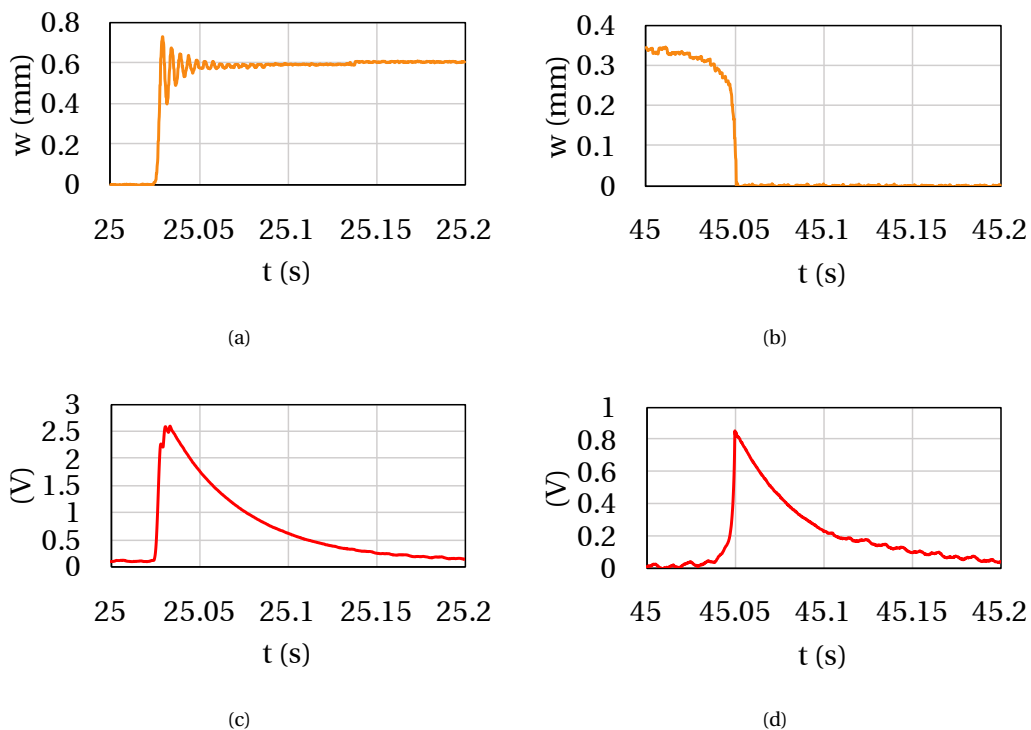


FIGURE 5.21: Experimental results of the first portable test prototype of second generation energy harvester, when full wave rectifier bridge and a capacitance  $C_{Load} = 2\text{nF}$  is connected to output. (a) Vertical displacement of the tip of the beam during the opening and (b) closing commutations of the first thermal cycle. (c) Output voltage generated during the opening and (d) closing commutations of the first thermal cycle.

It can be noted that the vertical displacement is the same as the previous experimentation, that is the initial distance of separation within triggering system 0.6mm. Thermal thresholds are quite similar to previous setup, as expected. Main difference is observed on the output voltage during both, opening and closing commutations. As for opening commutation, the maximum voltage level reaches 2.5V. So, the maximum stored energy as function of the voltage reached on the capacitor electrodes can be calculated as follows:

$$E_{C_{Load}} = \frac{1}{2} C_{Load} V^2 \quad (5.1)$$

where,  $C_{Load}$  is the load capacitor connected to the output of the rectifier bridge and  $V$  the output voltage. For this case, the maximum energy stored in the capacitor is 6.28nJ and 0.72nJ during opening and closing commutation. The discharge of the capacitor is done because of the oscilloscope probes used to measure these signals.

On the next section, a second portable prototype is described. The main objective of having this second portable prototype is to reduce as much as possible the general size of the device and to prove that scaling down the generator, operating temperatures near to human body can be obtained.

### 5.3 Second portable test prototype

The main goal is to reduce as much as possible the size of the transducer beam and to increase the energy harvesting capabilities of the device. As we reduced the width of the beam up to 1mm as well as the length to 8mm, we were able to ensure closing commutation of this architecture device by using only one magnet. Until now, this is our smallest portable prototype produced and tested. We also used the Peltier module in order to create temperature fluctuations on the FeNi alloy. This allowed us to better characterize the device under best cases of input scenarios. The materials are the same as previous demonstrators as listed in [Table 5.9](#).

TABLE 5.9: General dimensions of the main parts of the second portable test prototype of the second generation energy harvester.

System part	Parameter	Symbol	Units	Value
Transducer beam	Length of cantilever beam	$L_B$	m	$8 \times 10^{-3}$
	Width of cantilever beam	$w_B$	m	$1 \times 10^{-3}$
	Thickness of shim layer	$h_B$	m	$100 \times 10^{-6}$
	Thickness of PZT layer	$h_p$	m	$130 \times 10^{-6}$
Permanent magnet	Height of magnet	$h_{mag}$	m	$1 \times 10^{-3}$
	Radius of magnet	$r_{mag}$	m	$1 \times 10^{-3}$
FeNi specimen	Height of FeNi	$h_{FeNi}$	m	$4 \times 10^{-3}$
	Radius of FeNi	$r_{FeNi}$	m	$7 \times 10^{-3}$

The photographs of the second portable test prototype of second generation energy harvester are shown in figures 5.22(a) and 5.22(b).

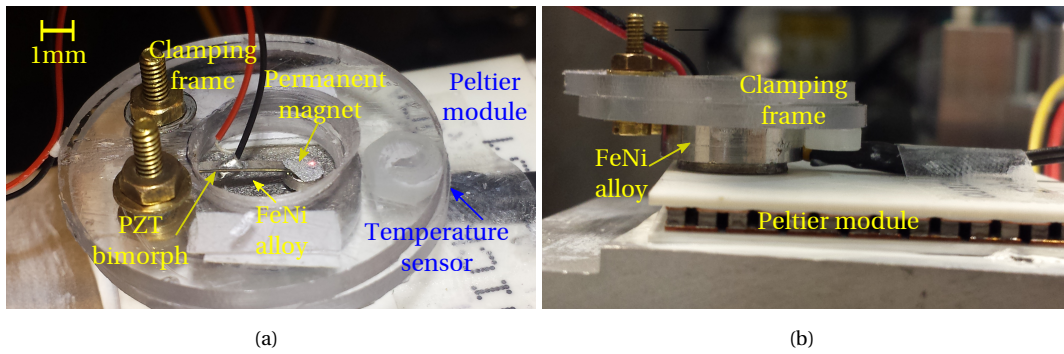


FIGURE 5.22: Photographs of the second portable test prototype of second generation energy harvester. (a) Photograph of the second portable test prototype and (b) photograph of the lateral view of the test prototype.

It can be noted that, this portable generator has only one permanent magnet attached to the bottom face of the PZT bimorph. We believe that this can increase the frequency of resonance of the transducer beam, as we reduced the volume, hence, the mass of the permanent magnet. In addition, by reducing the thermal operating thresholds, we believe that thermal periods can be shorter. In other words, it may imply that in shorter time periods, thermal cycles can be obtained, compared with previous prototypes.

We conducted several experimentations for different load resistor values, this is with the intention of validating the hypothesis of the load does not affect the thermal thresholds of the device. These results will be presented later on this section. Before that, we will take a look to the evolution of the temperature of this device and its operating commutations as shown in Figure 5.23.

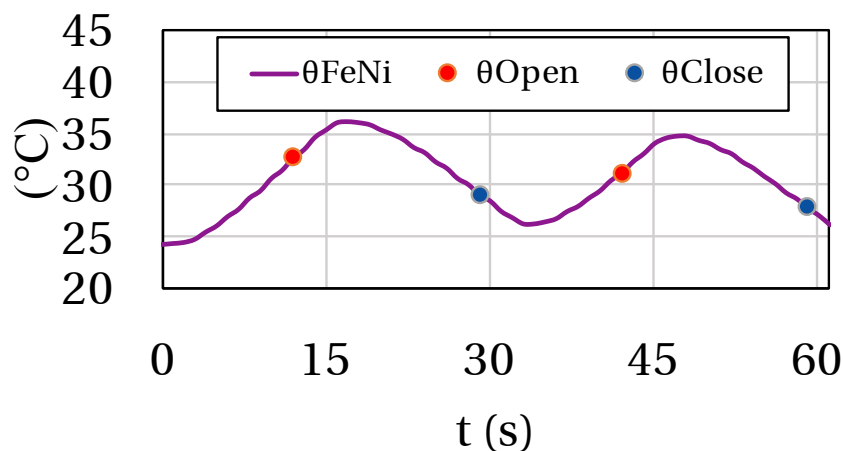


FIGURE 5.23: Thermal response of second portable test prototype of second generation energy harvester. Two thermal cycles are depicted on the graph.

These experiment reveals that for our smallest test prototype, temperature operations even under  $30^{\circ}\text{C}$  are possible. This corroborate our hypothesis of operating this type of generators with human body temperature fluctuations. For instance, to power wearable devices with the heat transfer of the human body and the ambient temperature. Other finding is that the thermal period was significantly reduced. For this test prototype, the thermal cycle, in the best case, can be of 30s. Unfortunately, we were not able to reduce the size of the FeNi alloy, which could even improve the thermal period by reducing it dramatically.

Measurements of transient response in vertical displacement and output voltage of second portable test prototype are illustrated in figures 5.24(a) to 5.24(d).

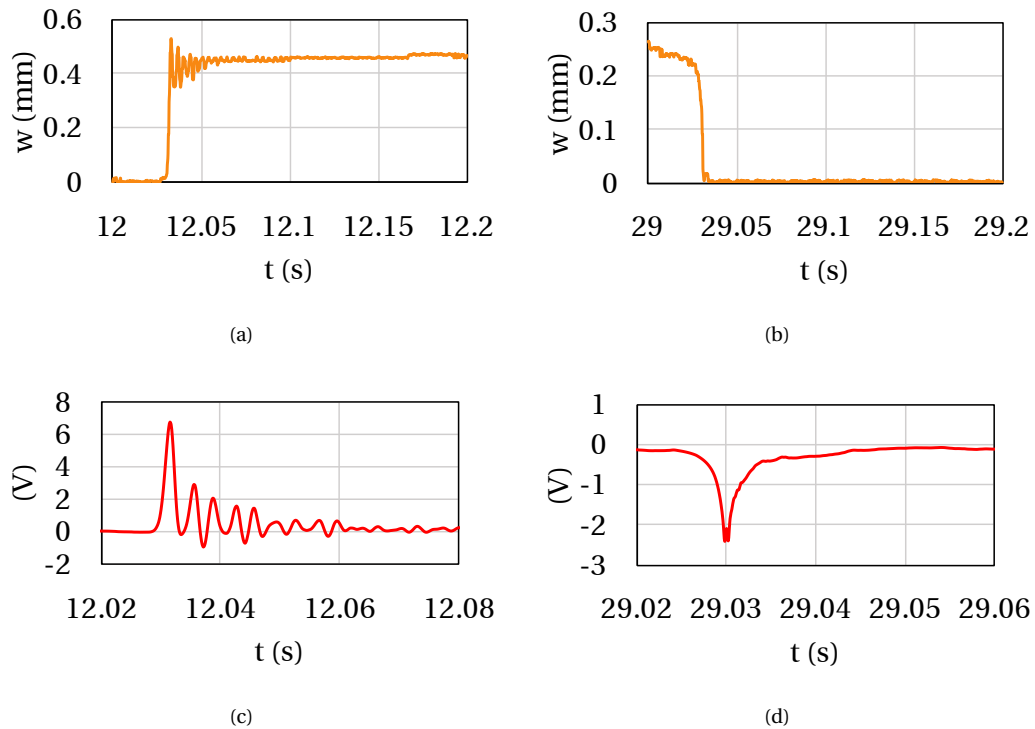


FIGURE 5.24: Experimental results of the second portable test prototype of second generation energy harvester, dynamic behavior characterization. For the first thermal cycle: (a) vertical displacement of the tip of the beam during the opening and (b) closing commutations. (c) Output voltage during the opening and (d) closing commutations. (e) Vertical displacement of the tip of the beam during the opening and (f) closing commutations of the second thermal cycle. (g) Output voltage generated during the opening and (h) closing commutations of the second thermal cycle.  $R_{Load} = 2.6\text{M}\Omega$ .

As can be noted, the initial distance of separation for this prototype is the smallest we have until now tested; 0.42mm. We have tested with higher values for this parameter, however, the generator was not able to close. So we can determine that this architecture corresponds to the maximal effective initial distance of separation. Moreover, it can be noted that the frequency of resonance has been increased. Quantitative characteristics of this new portable prototype are listed in Table 5.10.

TABLE 5.10: Main features of the second portable prototype of second generation energy harvester.

Item	Units	Cycle 1		Cycle 2	
		Opening	Closing	Opening	Closing
Resonance $f_r$	Hz	290	-	290	-
Average power <sup>a</sup>	$\mu\text{W}$	1.39	$2.13 \times 10^{-2}$	1.45	$2.4 \times 10^{-1}$
Energy	$\mu\text{J}$	$4.18 \times 10^{-2}$	$6.39 \times 10^{-3}$	$4.34 \times 10^{-2}$	$7.2 \times 10^{-3}$
Generator's volume <sup>b</sup>	$\text{cm}^3$	$5.83 \times 10^{-1}$	$5.83 \times 10^{-1}$	$5.87 \times 10^{-1}$	$5.87 \times 10^{-1}$
Energy density	$\mu\text{J cm}^{-3}$	$7.17 \times 10^{-2}$	$1.1 \times 10^{-2}$	$7.4 \times 10^{-2}$	$1.23 \times 10^{-2}$
Temperature $\theta$	$^\circ\text{C}$	32.6	29	31.1	27.7
Time at commutation $t$	s	12	29	42	59

<sup>a</sup>Within a period time of  $10T$  ( $T$  is the fundamental period of oscillations).

<sup>b</sup>Considering the volume of transducer's maximum deflection.

It can be corroborated that reducing the dimensions of the generator, even if the FeNi alloy still constant compared with previous devices, thermal thresholds can be tuned towards ambient range temperatures. It also has been demonstrated that the frequency of resonance of this new prototype has been increased up to 290Hz. Which could be explained by reducing the mass attached at the free end of the transducer (i.e., permanent magnet).

As we did for the first portable test prototype, we conducted a set of experimentations changing the load resistor connected to the electrodes of the transducer. Figure 5.25 shows the operating temperatures of this prototype as function of load resistor.

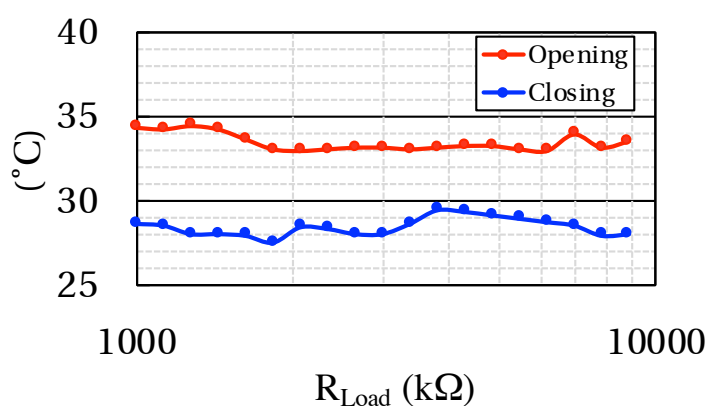
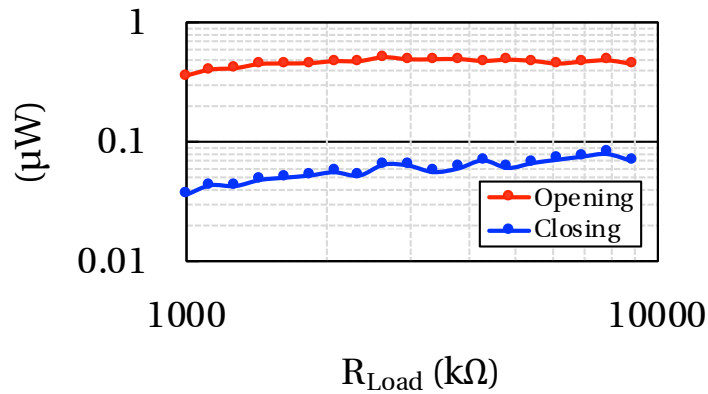


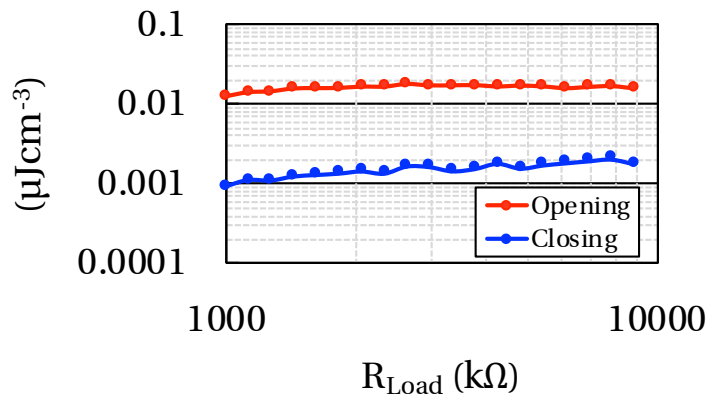
FIGURE 5.25: Operating temperatures of the second portable prototype as a function of load resistor, in red line opening temperature and in blue line closing temperature.

These result suggest that operating temperatures have been decreased and a thermal hysteresis has also been decreased as we reduced the initial distance of separation of this

prototype. Figures 5.26(a) and 5.26(b) the power and energy density of this generator for each commutation as a function of load resistor, respectively.



(a)



(b)

FIGURE 5.26: Output average power and energy density as function of load resistor of the second portable teste prototype of second generation energy harvester. (a) Output average power per commutation as function of load resistor, (b) Energy density per commutation as function of load resistor.

From these results, it can be corroborated that the behavior of the generator at the opening and at the closing commutation is different. The approach of characterizing our energy generator by connecting a resistor as electrical load is in part because of its linear and passive behavior. Therefore, its power dissipation is straightforward. Nevertheless, all electronic devices for which, this generator is intended to be power source, are not linearly and have not a passive behavior. Thus, the need of designing a power management module to be the intermediate between the generator and the final electronic device to be powered.

## 5.4 Electrical equivalent model on PSpice

This section deals with an equivalent electric circuit model of our thermo-magnetically activated piezoelectric generator along with its PSpice implementation. The model, which is developed of lumped circuit elements, is valid under both parallel and series wired thermo-magnetically activated piezoelectric generator operation modes. It also takes into account the effect of mechanical losses due to damping as well as dielectric and mechanical losses linked to the materials. A curve fitting and a parameter estimation processes are presented in order to determine the losses elements values from experimental measurements of the electrical admittance of the thermo-magnetically activated piezoelectric generator.

One of the reasons of having an electric equivalent model is to overcome the problematic of implementing losses linked to materials, for instance dielectric and mechanical losses. We opted by developing an electric equivalent model, instead of using the previous model implemented on Matlab. Another main advantage of using an electric equivalent model is that we can go beyond the design of the generator. That is, we can also design the power management module to be connected to the generator. Having this implementation in a same software accelerates dramatically the design process of such a system.

### 5.4.1 Electrical representation of the generator

When designing piezoelectric energy harvesters, an equivalent model of the system is very helpful in estimating its main features, including the achievable energy output before manufacturing prototypes, assessing the performance of the generator, and the effects of design changes. And efficient design of energy harvesters is particularly advantageous if the theoretical model of the whole energy harvester system (i.e., energy harvester and power management electronics) is implemented using a common software tool, such as PSpice. Therefore, we have adapted the equivalent electric model, presented by Roundy *et al.*, [96] to describe the system we are proposing. By making use of PSpice, we implemented the model, that is extremely convenient to analyze the complete system (i.e., thermo-magnetic, mechanical, and electrical parts).

Figure 5.27 shows the circuit representation of piezoelectric generator.

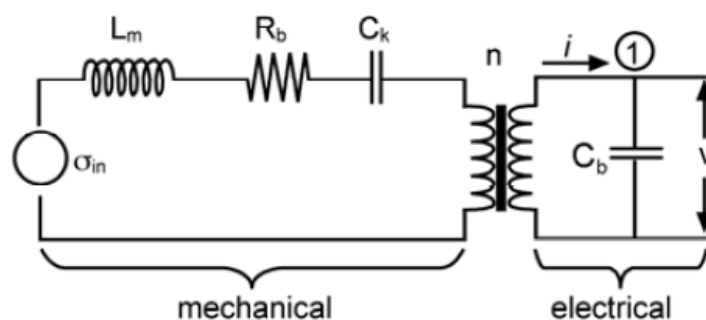


FIGURE 5.27: Circuit representation of a piezoelectric vibration energy harvester. Taken from [96].

The mechanical elements such as mass, spring and damper are represented by their electrical analogous items, i.e., equivalent inductance  $L_m$ , resistance  $R_b$ , and capacitance  $C_k$ , respectively. The equations governing a piezoelectric element are generally obtained by introducing an equivalent circuit for the mechanical and electrical parts of the piezoelectric system. In the case of the hypothesis of a piezoelectric force comparable to a viscous damping, the piezoelectric effect (i.e., electromechanical) is then described by using voltage controlled voltage sources. The electromechanical conversion block, relating input stress on mechanical side to the voltage on electric domain, is represented by means of controlled sources (i.e., piezoelectric mechanical-electrical conversion is modeled using *Voltage Controlled Voltage Source* and the electrical-mechanical conversion is modeled using *Current Controlled Current Source*). The dielectric losses in piezoelectric materials can be described using a complex dielectric constant. This behavior can be modeled with a frequency-dependent resistance in parallel with the piezoelectric capacitance  $C_b$ .

$$C_b = \frac{\varepsilon w_B L_p}{2h_p} \quad (5.2)$$

Dielectric losses in piezoelectric materials can be explained using a complex dielectric constant [97]. The complex Young's modulus of the shim layer can be expressed as:

$$Y_{eff} = Y(1 + i \tan \delta_{ms}) \quad (5.3)$$

where  $\tan \delta_{ms}$  is the tangent loss related to the shim material.

The complex compliance constant of the piezoelectric layer is expressed as:

$$s_{11} = s_{11}(1 - i \tan \delta_{mp}) \quad (5.4)$$

where  $\tan \delta_{mp}$  is the tangent loss related to the piezoelectric material.

The complex inertia moment of the bimorph cantilever beam shown in Figure 3.4 is expressed as:

$$I = \frac{1}{12} w_b h_b^3 Y(1 + i \tan \delta_{ms}) s_{11}(1 - i \tan \delta_{mp}) + 2w_b \left( \frac{1}{12} h_p^3 + h_0^2 h_p \right) \quad (5.5)$$

where  $w_b$  is the width of the beam and the seismic mass (i.e., the permanent magnet),  $h_0$  is the distance between the center of the piezoelectric layers and the neutral axis of the beam (i.e.,  $h_0 = (h_p + h_b)/2$ ) and  $h_p$  is the thickness of piezoelectric layer.

The stresses in the layers of the beam result from the force applied on the permanent magnets due to the attraction force. And the average stress in the piezoelectric layer is proportional to the force applied at the end of the beam. Therefore, we define the proportionality factor  $k^*$  as:

$$k^* = \frac{h_0(2L_B + L_m - L_p)}{2I} \quad (5.6)$$

where  $L_B$ ,  $L_m$ , and  $L_p$ , are the length of shim, permanent magnets and piezoelectric materials, respectively.

The vertical displacement at the tip of the beam and the strain are related by a proportionality factor  $k^{**}$  (a complex number as  $I$  is a complex number as well):

$$k^{**} = \frac{L_B^2 (4L_B + 3L_m)}{6h_0 (2L_b + L_m - L_p)} \quad (5.7)$$

Stress and force are related to through the geometrical constant  $k^*$ .

The equivalent complex element,  $R_b$ , which relates stress to strain rate, considers the mechanical losses due to damping coefficient  $C$ , it is expressed by:

$$R_b = k^* k^{**} C$$

$$= \frac{L_B^2 (4L_B + 3L_m) C}{6 \left( \frac{1}{6} w_b h_b^3 Y (1 + i \tan \delta_{ms}) s_{11}^E (1 - i \tan \delta_{mp}) + 4 w_b \left( \frac{1}{12} h_p^3 + h_0^2 h_p \right) \right)} \quad (5.8)$$

The complex equivalent capacitance,  $C_k$ , which represents the compliance, relates stress and strain, and it is simply equal to the inverse of the Young's modulus of the piezoelectric material.

$$C_k = s_{11} (1 - i \tan \delta_{mp}) \quad (5.9)$$

The equivalent inductance,  $L_m = k^* k^{**} m$  which relates the second derivative of strain to stress, represents the inertia of the permanent magnet (proof mass). And the complex equivalent inductance,  $L_m$ , which represents the mass or inertia of the generator is expressed as:

$$L_m = k^* k^{**} m$$

$$= \frac{L_B^2 (4L_B + 3L_m) m}{6 \left( \frac{1}{6} w_b h_b^3 Y (1 + i \tan \delta_{ms}) s_{11}^E (1 - i \tan \delta_{mp}) + 4 w_b \left( \frac{1}{12} h_p^3 + h_0^2 h_p \right) \right)} \quad (5.10)$$

Having derived the complex elements of the model, we built it on PSpice. This model takes into account the vibration-based generator geometrical, mechanical, electromechanical coupling parameters, and losses elements linked to materials as shown in [Figure 5.28](#).

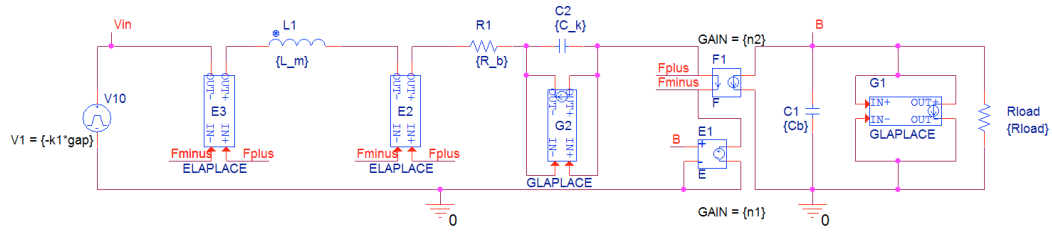


FIGURE 5.28: Schematic representation of the electric equivalent model of our generator in mode generation actuation.

Regarding the coefficient of controlled voltage and current sources (i.e., E1 and F1),  $n_1$  and  $n_2$ ; they are expressed as:

$$n_1 = -\frac{d_{31}}{2h_p s_{11}} \quad (5.11)$$

$$n_2 = \frac{\omega_B L_p d_{31}}{s_{11}} \quad (5.12)$$

The reader is referred to [Appendix C](#) for the implementation of losses elements in PSpice. The equivalent input stress is a result of the input force,  $F_{in}$ , which is exerted by the permanent magnet as a direct result of the predominant balance of forces  $F_{mec}$  and  $F_{mag}$ . The input excitation we consider is described as a pulse voltage source. Thus, the input excitation,  $F_{in} = k(gap)$ , where,  $k$  is the equivalent stiffness of the transducer, and  $gap$ , the initial distance of separation between magnet and soft magnetic alloy (i.e.,  $gap = z_0 - z$ ).

### 5.4.2 Curve fitting and parameters estimation

To obtain the values of these complex elements, we decided to extract experimental data of the electrical admittance and then making a parameter estimation stage. Therefore, we decided to build a test prototype (details of this prototype will be presented on [Chapter 5](#)). [Figure 5.29](#) depicts the photograph of the test prototype.

First, by making use of HIOKI im3570 impedance analyzer, we measured the admittance of the generator when it is in open position. This data revealed a resonance frequency along with its rotation of phase. These measurements of the electrical admittance were carried out under the conditions described as follows: we produce an increase of temperature of the soft magnetic alloy to produce its opening commutation. Then, electrical admittance is measured. Second, these data have been introduced on the optimizer tool of PSpice to estimate the loss parameter values. The electric circuit model is presented in actuator mode, in such a manner that the admittance can be computed at the input of the electrical block.

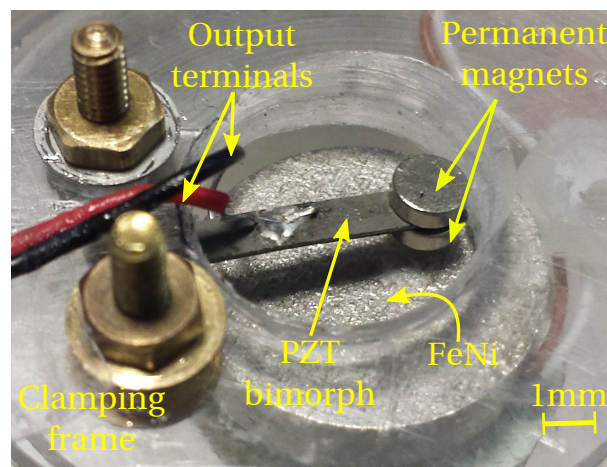


FIGURE 5.29: Photograph of the test prototype of generator using to validate equivalent electrical circuit of the generator.

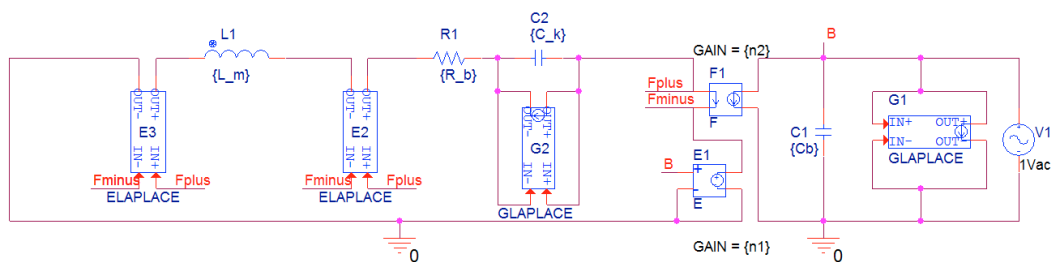


FIGURE 5.30: PSpice schematic of the thermo-magnetically triggered piezoelectric generator in actuator mode to conduct the curve-fitting study and to finding the losses elements values.

After 12 iterations of the curve fitting process, using the LSQ solver available in PSpice, the losses elements were estimated and they are listed in [Table 5.11](#).

TABLE 5.11: Material parameters of the electric equivalent model.

Symbol	Description	Units	Real part	Imag. part
C	Damping ratio	-	10.5%	-
$\tan \delta_d$	Dielectric loss tangent	-	2.9%	-
$\tan \delta_m$	Mechanical loss tangent	-	3.7%	-
$d_{31}$	Piezoelectric coefficient	$\text{CN}^{-1}$	$-98.8 \times 10^{-12}$	$3.02 \times 10^{-12}$
$\epsilon_{33}^T$	Dielectric permittivity	$\text{F m}^{-1}$	$1.35 \times 10^{-3}$	$-3.169 \times 10^2$
$s_{11}^E$	Elastic compliance	$\text{Pa}^{-1}$	$25.7 \times 10^{-12}$	$-1.3 \times 10^{-12}$

Once obtained the parameters of the model, we validated the model in actuator mode. Figure 5.31 illustrates the results of the curve fitting and parameter estimation process of the electrical admittance of the generator.

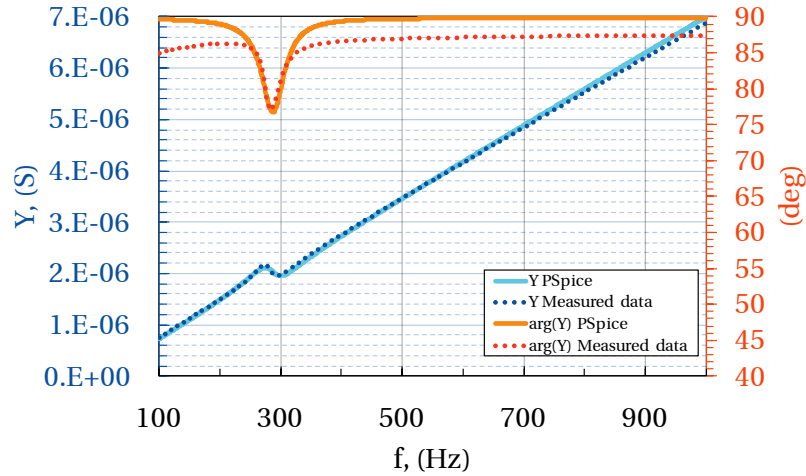


FIGURE 5.31: The curve fitting on the admittance showing a good agreement with the equivalent model.

However, it is important to say that besides the losses linked to materials, there is another factor on the system that affects the oscillations of the transducer; that is the damping due to the magnetic force at the opening commutation of the generator. Indeed, when the opening commutation is reached, the FeNi alloy has not lost all its magnetization. And a contribution of magnetic force is still present. Therefore, the transducer oscillates not at its natural frequency of resonance but with a damped frequency. To show this, we measured, for the same prototype but in at different moment during the opening position, its electrical admittance and we performed again a parameter estimation and curve fitting process with this new data. In other terms, the generator was heated up to produce its opening commutation. The measurements of electrical admittance was taken when the FeNi alloy reached 80°C. A second parameter estimation and curve fitting process was realized. Table 5.12 lists the parameter estimated for the model under the described condition. Figure 5.32 shows the results of the second curve fitting a parameter estimation process.

TABLE 5.12: Material parameters of the electric equivalent model, when FeNi is heated up to 80°C.

Symbol	Description	Units	Real part	Imag. part
C	Damping ratio	-	0.8%	-
$\tan \delta_d$	Dielectric loss tangent	-	1.9%	-
$\tan \delta_m$	Mechanical loss tangent	-	3.2%	-
$d_{31}$	Piezoelectric coefficient	C N <sup>-1</sup>	$-97.8 \times 10^{-12}$	$3.12 \times 10^{-12}$
$\epsilon_{33}^T$	Dielectric permittivity	F m <sup>-1</sup>	$1.25 \times 10^{-3}$	$-3.469 \times 10^2$
$s_{11}^E$	Elastic compliance	Pa <sup>-1</sup>	$24.7 \times 10^{-12}$	$-1.12 \times 10^{-12}$

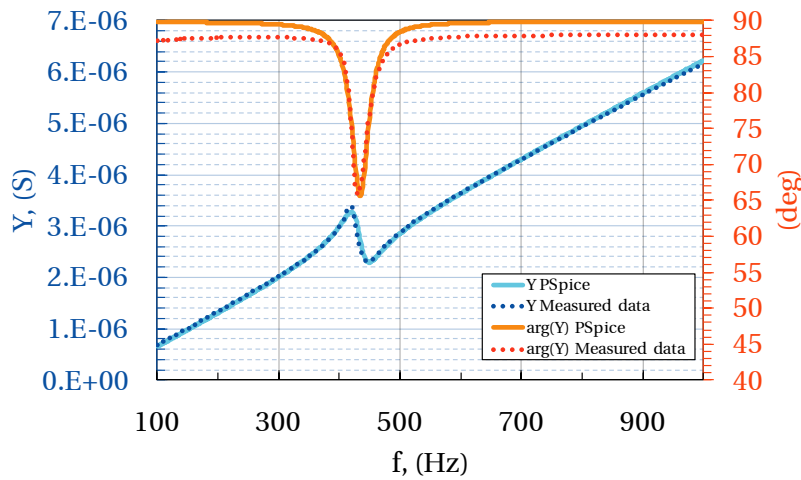


FIGURE 5.32: The curve fitting on the admittance of a test prototype. Measurements of admittance being taken when the generator is heated up to 80°C.

As can be seen from this second validation of the model, the parameter that changed the most was the damping ratio  $C$ . Initially we thought that the losses linked to materials changed so much as the damping ratio. However, we had to explore the curve fitting tool of PSpice by fixing the terms of losses linked to materials and letting damping ratio to change with the fitting algorithm.

From the first validation of the model, it can be noted a frequency of resonance around 300Hz. While for the second measurements, the frequency of resonance is noted around 400Hz. This shift in frequency can be explained because of the influence of the magnetic force on the oscillations of the beam. Depending on the temperature of the FeNi, even if the the beam has been released, magnetic contribution may affect the efficient performance of the device. This point, highlights the need of having larger initial distance of separation for triggering system, in order to reduce this damping.

These results also suggest that other element considering this damping factor would improve the model. In addition, it demonstrates the complexity of such a system to be modeled. However, we opted for use this model for designing as it responds quickly to our needs in designing the next stage, power management module.

The next section will present a rapid experimentation we performed to a test prototype in order to demonstrate the influence of the magnetic force on the oscillations, once the generator has reached its opening commutation.

### 5.4.3 Influence of magnetic breaking on the generator performance

Experimental measurements revealed an unexpected behavior on the generator. In particular, during the opening commutation of the generator. Once the opening threshold is achieved and the mechanical force becomes predominant, the transducer beam is released exhibiting oscillations. Nevertheless, just at the moment when opening commutation is reached, the FeNi alloy has not completely lost its magnetization (i.e.,  $F_{mag}$  is still in a small

contribution). Therefore, oscillations of the beam are affected by a kind of damping due to this contribution of the magnetic force. To put in evidence this hypothesis, we performed a set of measurements of the electrical impedance. The prototype we use to conduct this experimentation, having a frequency of resonance around 120Hz (i.e., the triangular shape transducer beam).

The generator is first heated up to produce its opening commutation. Once it is open, temperature is leaded until 80°C. At this moment, the first measurement of electrical impedance is performed by using HIOKI impedance analyzer. The duration of this measurement is in average of 10s and it depends on the range of frequency and the number of points. All measurements were conducted with the same frequency range from 95Hz to 140Hz. The total number of points was 800. The second measurement was taken just after the first one and similarly for the third and fourth measurement. It is surprising how the frequency of resonance is so sensitive to the magnetic force still present on the system (even at the open position). Figure 5.33 shows the rotation of phase of the impedance measured.

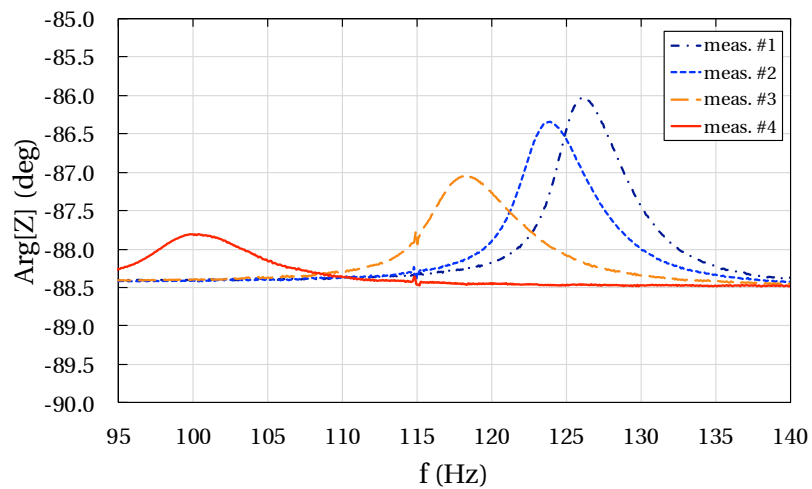


FIGURE 5.33: Experimental measurements of the rotation of phase of electrical impedance of a test prototype, showing the shift in the resonance frequency of a test prototype.

These results proved our hypothesis: **the damping ratio of the system is linked to the magnetic force, hence to temperature**. As long as the FeNi is cooled down, it is re-gaining magnetization. Hence, the magnetic force  $F_{mag}$  affects the dynamic of the transducer. In other terms, we can conclude that the damping ratio of the generator depends on temperature,  $C = f(\theta)$  as the magnetic force is a function of temperature,  $F_{mag} = f(\theta)$ .

## 5.5 Power management module

This section presents some simulation results making use of the electric equivalent model we developed for our energy generator.

These sets of simulation are intended to be the beginning of a more deeply study that is part of perspectives and future work on this research line. In order to optimize the output

power as a function of load resistance, two circuits were tested: a full-wave bridge voltage rectifier and the LTC3108 circuit.

In a first time, we are going to test our equivalent electric circuit model connected with a full wave rectifier bridge as long as a load resistor and capacitor in parallel as shown in [Figure 5.34](#). The full-wave bridge voltage rectifier circuit is widely used in energy harvesting systems that converts AC voltage to DC voltage [98, 99]. It consists in four small signal diodes that convert an AC voltage into a DC voltage using the two half cycles (positive and negative) from the piezoelectric generator. In the positive half cycle of the AC wave, diodes D1 and D2 are forward biased. In the negative half cycle, diodes D3 and D4 are forward biased, converting all negative components into positive ones. In this way, the voltage of the two half-cycles at the end of the bridge are positive and the rectified signal completes a period twice as fast as the input frequency, thus the period is halved and the frequency is doubled.

Even if our electrical equivalent circuit model has only the opening commutation part, (closing commutation modeling being part of the perspectives and future work of this research), it can give fundamental insights about the behavior of the generator under different active or passive power management modules.

The output of the generator is directly connected to the full wave bridge rectifier. Then, a RC circuit is connected to the output of the rectifier bridge. The values of this circuit have been selected after doing a parametric analysis in order to maintain at the maximum the charge stored on the capacitor. The value of  $C_{Load} = 200\mu\text{F}$  and for  $R_{Load} = 800\text{k}\Omega$ .

The input conditions to the equivalent circuit are: opening commutations are reached every 60s. This period time has been selected according to the experimental results obtained from test prototypes showing thermal periods of the same order of magnitude.

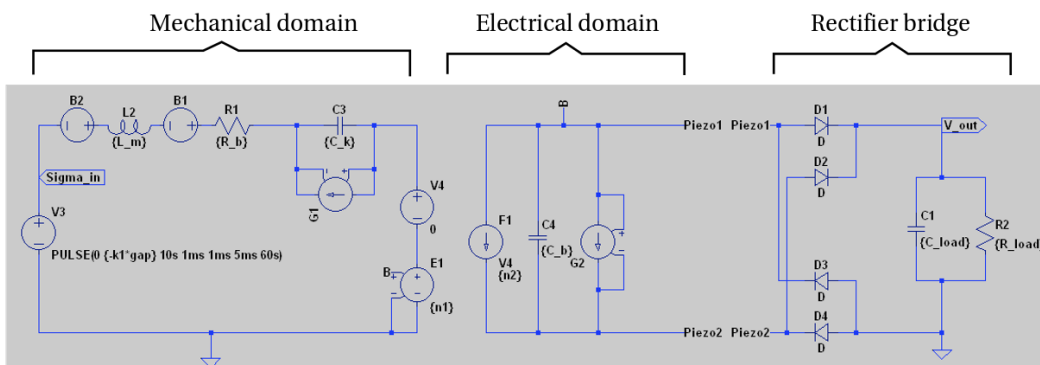


FIGURE 5.34: Schematic representation of electric equivalent circuit of the generator with a full wave rectifier bridge.

From [Figure 5.34](#) it can be seen that the equivalent electric circuit of the generator is directly connected to a full wave rectifier bridge. At the output terminals of the bridge, a RC circuit is connected. The intention of this simulation is to explore the behavior of the model when a charge different of resistor is connected.

Output voltage, measured at the load capacitor electrodes is shown in [Figure 5.35](#).

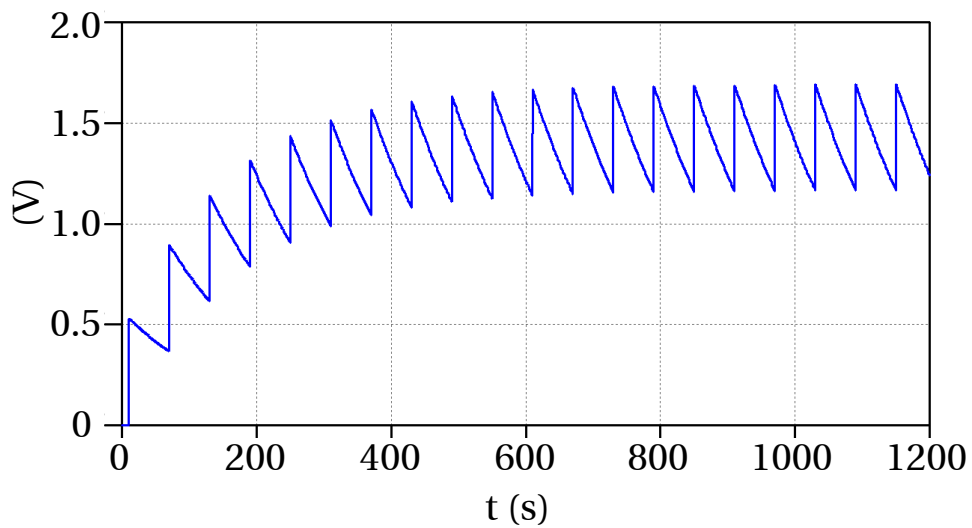


FIGURE 5.35: Output voltage of the electrical equivalent model of the generator when a full wave rectifier bridge is connected along with a parallel RC circuit.

From Figure 5.35 it can be noted that every 60s (i.e., for each commutation of the generator) the output circuit is charging showing voltage peaks. Since the discharging behavior of the circuit, the output voltage has a ripple. After 500s of simulation time, the output voltage reaches a “stable” value around 1.2 and 1.6 V.

One advantage of having an electric equivalent model of the generator, is that we can also use commercial circuits such as LTC3108. The integration of this circuit has been conducted under the same initial conditions as the previous attempt.

Figure 5.36 shows the equivalent electric model implemented on LTspice software. The schematic shows the generator as well as the LTC3108 circuit. This circuit has been designed to work with thermoelectric generators. The reason we decided to use it is to put in evidence the advantage of having an equivalent model of our device implemented on benchmark software.

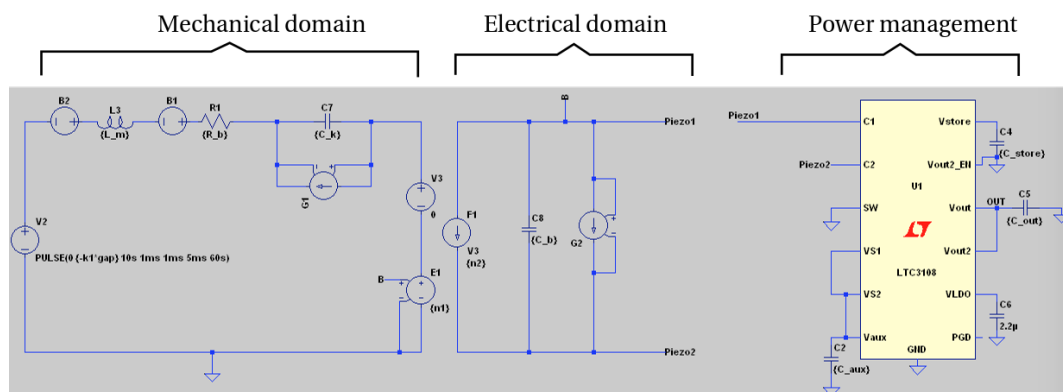


FIGURE 5.36: Schematic representation of electric equivalent circuit of the generator with a power management module LTC3108.

The output voltage signal is represented by [Figure 5.37](#)

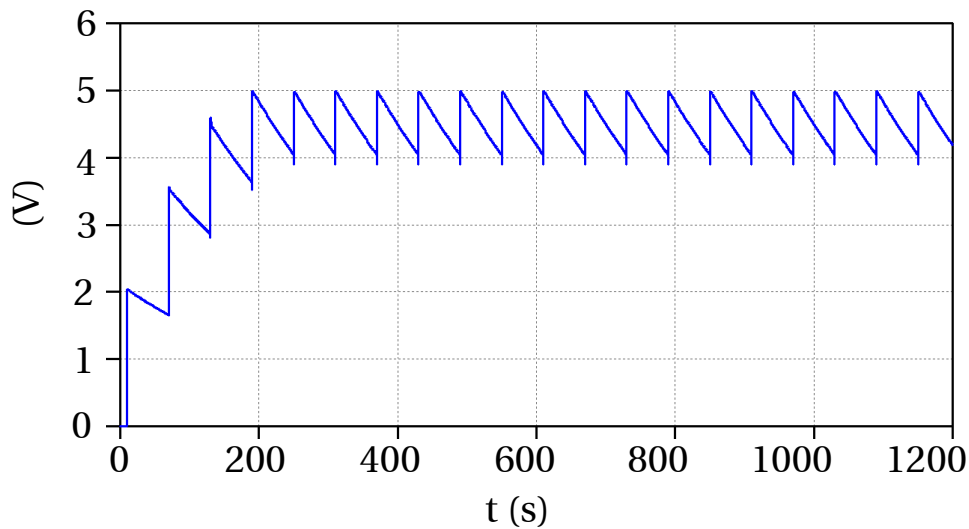


FIGURE 5.37: Output voltage of the electric equivalent circuit using the LTC3108 chip.

The output voltage is quite similar in form than the previous circuit. Nevertheless, the final amplitude of the signal is on the range of 4 and 5 V. This is due to the integrated DC/DC converter LTC3108.

After 200s of simulation, the output voltage is reaching the steady state. When connecting this circuit, higher output voltage can be reached compared to the full wave rectifier bridge. The main advantage of this circuit is that it provides an output for a storage capacitor. This capacitor provides power when the input voltage source is unavailable.

## 5.6 Discussion

The test prototypes of generators we built have demonstrated the feasibility of harvesting thermal energy in the form of temperature variations into electricity. Several hypothesis have been corroborated:

1. First generation generator prototypes. These prototypes have revealed that the transducer beam design can be optimized by different ways: by reducing the width of the beam, the viscous damping can be also reduced (i.e., narrow beams have less lateral surface area that is affected when oscillations). During these prototypes characterization, it has been demonstrated that using triangular cantilever beam, improvements on the output energy is achieved. This is due to the uniform distributed stress of the cantilever beam.

2. First generation prototypes with smaller permanent magnets. By reducing the volume of the permanent magnets attached to the free end of the cantilever beam, improvements on the output energy is obtained. This is due to the increase in the frequency of resonance of the structure. Nevertheless, it was also corroborated that when reducing the permanent magnetic volume, the maximum magnetic force is lower than the one for the prototype using a couple of permanent magnets.
3. Second generation of portable prototypes. These prototypes are characterized by portability, as the frame holding the cantilever beam as well as the FeNi is a single piece made of acrylic. Despite the fact that the FeNi sample was not reduced in size, the thermal thresholds for these prototypes were reduced. Also, the initial gap could be reduced when a simple permanent magnet is used on the triggering system. With these improvements on the thermal thresholds, applications like powering wearable devices can be addressed.
4. Electrical equivalent model. By using this equivalent model, losses linked to materials can be implemented. The versatility of introducing these losses is reflected on the influence of magnetic breaking on the generator performance. By using an equivalent model, the implementation of a power management module can be addressed.



## Chapter 6

# Design optimization and variability analysis

### Contents

---

<b>6.1 Design optimization</b> .....	<b>158</b>
6.1.1 Second optimization design attempt .....	166
6.1.2 Discussion .....	172
<b>6.2 Variability analysis</b> .....	<b>173</b>
<b>6.3 Discussion</b> .....	<b>178</b>

---

*This chapter introduces the design optimization stage we conducted for our generator. In this work, the model was implemented and solved using a time step model in Simulink. This tool has the main advantage of speed in transient simulation. In addition, a variability analysis has been conducted. The main goal is to determine the robustness of the generator's design towards a production stage. Using techniques like Monte Carlo simulation and Design of Experiments, we could explore our optimized design space and calculate parameter influence on model behavior.*

## 6.1 Design optimization

We developed a simplified model of our generator. This model is able to predict the dynamic behavior of the generator. The input of the model is a heat flux that generates temperature fluctuations on the FeNi alloy. The output of this model are parameters allowing characterization of the device performance, including the voltage generated by the piezoelectric transducer, the tip beam displacement of the transducer. Parameters of characterization of the generator, including the opening and closing temperatures, the vertical displacement of the tip of the beam and its corresponding velocity, as well as the dissipated power per commutation can also be obtained through this time step model.

Design optimization is the process of finding the best design parameters that satisfy project requirements. Engineers typically use design of experiments, statistics and optimization techniques to evaluate the effects that design parameters have across interrelated physical domains. In Simulink, the general process for doing design optimization can be divided into 5 main steps:

**Specify Design Variables:** Definition of the model parameters being optimized, like the dimensions of the transducer beam, length, width, thickness, etc...

**Specify Design Requirements:** Definition of the design requirements. The generator design must ensure the two operation positions of the device: open and closed. It implies that thermal thresholds of the generator have to be within the input temperature fluctuations range.

**Create Optimization Objective Function:** Creation of an anonymous function that calls a “sub-function”, which evaluates the optimized parameter of the model. The Simulink model calls the anonymous function at each iteration. In our case, the objective function is the output energy per commutation.

**Evaluate custom parameter requirement functions:** Evaluates the custom requirement, “maximize” or “minimize”, that uses the custom objective function. In our particular case, a custom parameter requirement has to be the response of the tip beam displacement. Since this parameter reflects the operation position of the device for all designs. That is, when the generator is in closed position, there a vertical displacement equal to the initial gap, and conversely, when it is in open position, vertical displacement is zero (after oscillations of the beam).

**Optimize the Design:** Optimization design using optimization methods like gradient descent, simplex search or pattern search.

In a first attempt, we opted for exploring the design optimization of the transducer beam on the basis of having the same input excitation on the triggering system, that is, the same magnetic force countering a design dependent mechanical force. Then, a sensitivity study is performed to this optimized design. In a second attempt, we added, to the design variables, the generator’s operating temperatures and we set the model takes the decision of a valid or invalid design according on the magnetic force developed by the design in turn.

For this first design optimization attempt, we focused on the piezoelectric layers as well as on its position along the length of the shim of the transducer beam. Therefore, we decided to establish the design variables as listed in Table 6.1.

TABLE 6.1: Design variables of the first design optimization attempt.

Variable	Symbol	Unit	Design space
Length of piezoelectric layers	$L_p$	mm	$[5 \leq L_p \leq 15]$
Thickness of piezoelectric layers	$h_p$	$\mu\text{m}$	$[1 \leq h_p \leq 300]$
Position of piezoelectric layers	$x_p$	mm	$[0 \leq x_p \leq 5]$
Thickness of shim	$h_B$	$\mu\text{m}$	$[100 \leq x_p \leq 300]$
Load resistor	$R_{Load}$	$\text{k}\Omega$	$[1 \leq R_{Load} \leq 1000]$

Working with these design variables modifications on the mechanical stiffness can be achieved, resulting in changes on the frequency of resonance of the beam. It is also trivial to see that magnetic attraction force will not be modified for these designs. Therefore, we can define a constant attraction magnetic force which will be exciting the model. Based on the model we developed (see Figure 3.10) to describe the magnetic force on the triggering system, we take the value of 1N as the constant magnetic force acting on triggering system.

The schematic representation of the architecture of the generator is illustrated on Figure 6.1.

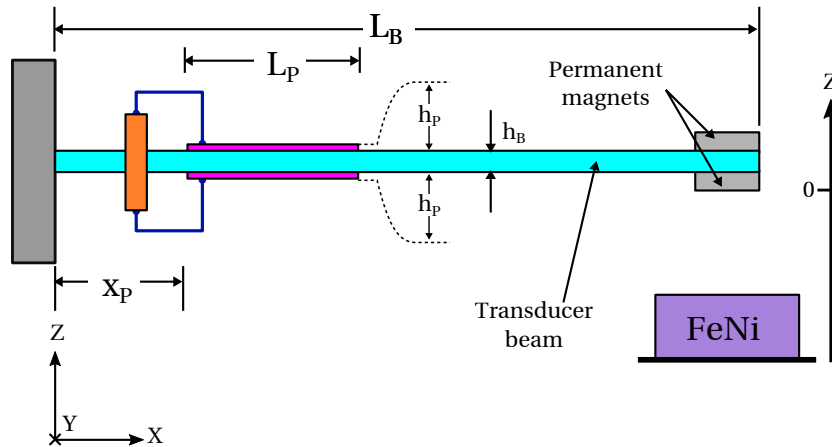


FIGURE 6.1: Schematic representation of the architecture of the generator to be optimized through Simulink.

The step time model implemented on Simulink is illustrated in Figure 6.2. The model can be divided into two sections, the magnetic force as the input of the model and the transducer system. In this first attempt of design optimization we decided to describe the input excitation as a stepped applied force at the tip of the beam.

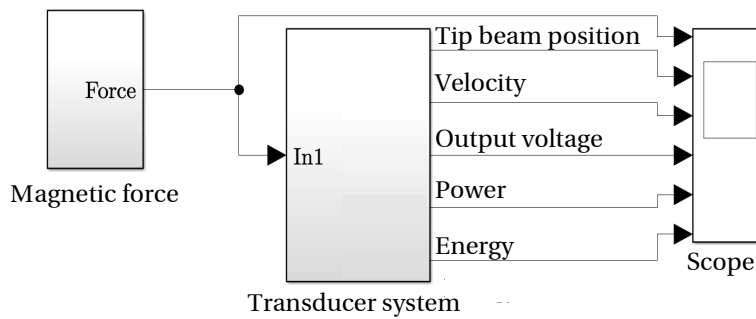


FIGURE 6.2: Implementation of the first step time model of the energy harvester in Simulink. The input of the model is a stepped force (magnetic force) applied on the tip of the beam.

The transducer system block of the Simulink model is shown in Figure 6.3. This block describes the dynamic of the generator implementing Equation 3.20 and Equation 3.21.

One of the main advantages of using this kind of models is the easy in implementing equations. The model relies on a integrator of second order. The output of this block are the position of the tip beam and the velocity. The input of this block is the magnetic force.

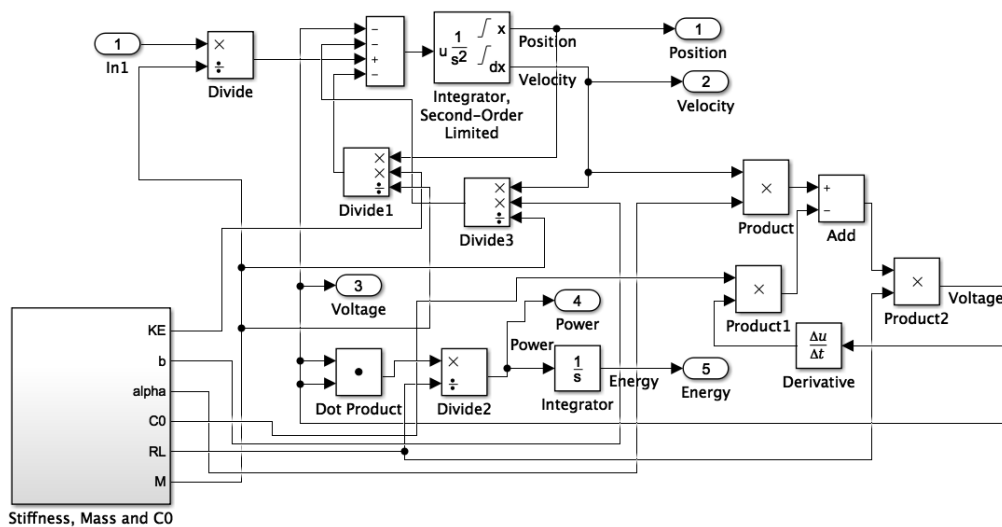


FIGURE 6.3: Schematic representation of the transducer system.

In order to ensure that every design will meet the requirements; we can set up a bound signal condition as a requirement response of the device. As shown in Figure 6.4.

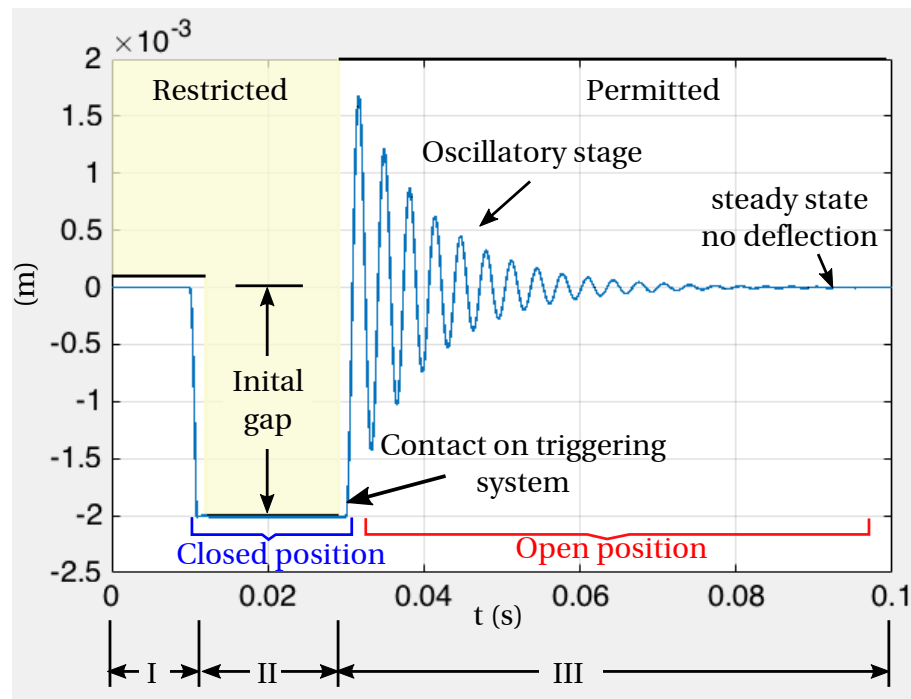


FIGURE 6.4: Schematic representation of signal bound as a requirement on first design optimization of generator.

The schematic representation of the bound signal can be interpreted as constraining the displacement of the tip of the beam.

**Phase I** The generator is in open position and it is static. We consider that temperature is above the closing threshold.

**Phase II** During the stage II, the magnetic attraction force is applied to the tip of the beam, and if the generator exhibits its closing transition, mechanical contact is achieved on triggering system. By the time the contact between permanent magnet and the FeNi alloy is reached, the generator produces an output voltage peak of negative sign and the beam's tip travels from its horizontal position ( $w = 0\text{mm}$ ) to the initial gap ( $w = -2\text{mm}$ ).

**Phase III** For the phase III, the magnetic attraction force becomes lower than the mechanical force, hence the beam is released and the oscillatory stage is present. During this oscillatory stage, the tip beam displacement is within the permitted area, thus the output voltage has the same signal form. Any design that does not meet these requirements is rejected by the algorithm. At the end of each iteration, the dissipated power is obtained and by doing integration of these power, the electrical energy generated is compared to the previous iteration. Maximization of this objective function is the main objective of this process.

The initial design parameters have been selected arbitrary. Mostly with the intention of testing the optimization process to the model. The initial design is considering the values listed in [Table 6.2](#).

TABLE 6.2: Initial design of the generator for the first design optimization attempt.

Variable	Symbol	Unit	Value
Length of piezoelectric layers	$L_P$	mm	5
Thickness of piezoelectric layers	$h_P$	$\mu\text{m}$	130
Position of piezoelectric layers	$x_P$	mm	5
Thickness of shim	$h_B$	$\mu\text{m}$	300
Load resistor	$R_{Load}$	$\text{k}\Omega$	1

The initial design output is shown in Figure 6.5 and Figure 6.6. For the sake of simplicity, we defined a step input of the magnetic force. The initial value of this force, during the Phase I is zero, then when the Phase II starts, the force is applied and maintained. This describes a decrease in temperature thus a magnetic force predominant on the triggering system. The tip beam position of the generator is consistent with the requirements. That is, when the generator is in open position, the beam is at its horizontal state, thus, zero displacement. At the time when the beam is under the magnetic force, the mechanical contact is ensured, it is represented by the limit of the tip beam displacement at the initial distance of separation; 2mm. The negative sign is only a representation of the direction motion of the tip of the beam.

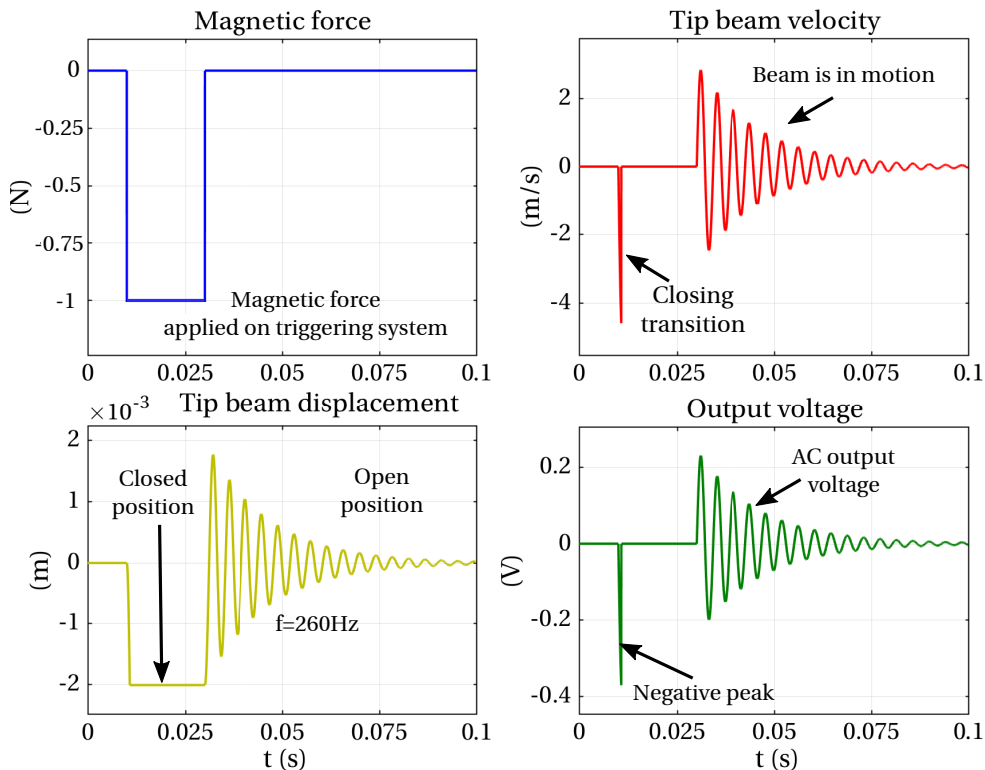


FIGURE 6.5: Typical response of the generator during a thermal cycle (closing and opening commutations) of operation of the simplified step time model implemented on Simulink. Input force, tip beam velocity, vertical displacement of tip beam and voltage.

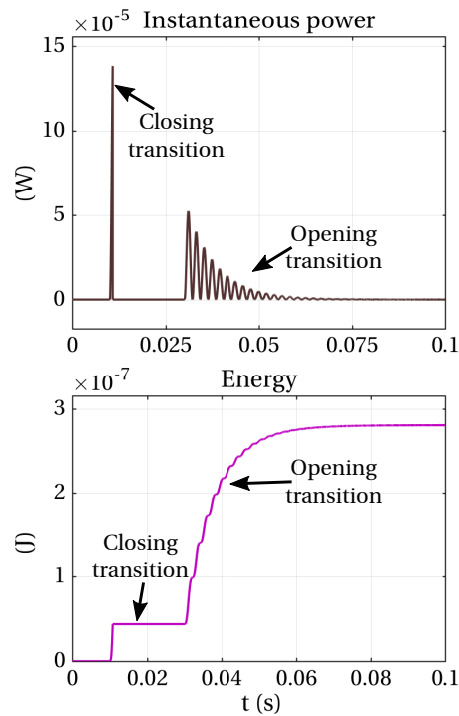


FIGURE 6.6: Typical response of the generator during a thermal cycle (closing and opening commutations) of operation of the simplified model implemented on Simulink, (instantaneous power and output energy).

The curve of the velocity can confirm the validity of the model. When the beam is in static state, it has no motion thus a null velocity. When the contact of the magnet and the FeNi allot is achieved, the velocity corresponding this motion is of a negative peak form. This can describe the “avalanche” effect on the closing transition. Next, when the transducer beam is released at the opening transition, the velocity has an oscillatory form like the output voltage. The output voltage is considered at the terminals of the load resistor connected to the electrodes of the piezoelectric layers. It can be seen that the negative peak of voltage during the closing transition can reach even higher absolute amplitudes than the opening commutation. However, the oscillations are significantly more important during the opening transitions. The instantaneous power can illustrate this behavior. For this design architecture, peaks up to 12mW are reached at the closing commutations, while amplitudes up to 5mW when the opening commutation. Finally, a most significant parameter to characterize our generator is the electrical energy converted during this simulation time. We have considered the instantaneous power and by integrating it, we obtained the evolution of the energy, which is represented as an output of the model. It is evident that for the opening transition, a higher amount of energy is converted than during the closing commutation. The final amount of energy is the objective function to be maximized on this design optimization process.

By using the pattern search method and after 43 iterations the algorithm has converged. The evolution of the energy over these iterations is illustrated in [Figure 6.7](#).

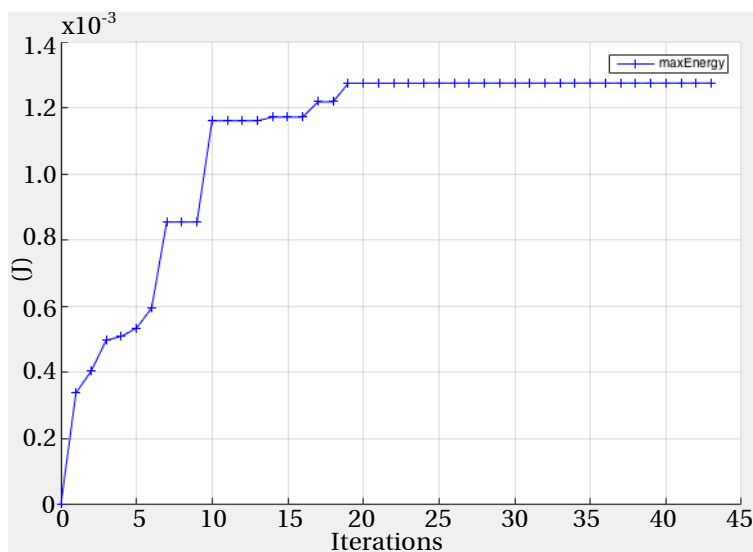


FIGURE 6.7: Evolution of the energy over iterations on design optimization process.

From the initial design of the generator, a total energy of  $0.28\mu\text{J}$  is generated. These results suggest that this energy can be maximized up to  $1.26\text{mJ}$ . The optimal design resulting from this process is listed in [Table 6.3](#).

TABLE 6.3: Optimum design of the generator for the first design optimization attempt.

Variable	Symbol	Unit	Value
Length of piezoelectric layers	$L_p$	mm	14.3
Thickness of piezoelectric layers	$h_p$	$\mu\text{m}$	98.85
Position of piezoelectric layers	$x_p$	$\mu\text{m}$	364
Thickness of shim	$h_B$	$\mu\text{m}$	247.31
Load resistor	$R_{Load}$	$\text{k}\Omega$	72.15

These results reveal interesting conclusions. The position of the piezoelectric layer may not be along the whole length of the beam. It can be explained as the transducer beam does not exhibit a strain along all its dimension. That is, the points along the length of the beam where the stress is more significant are near to the clamping zone, that is  $x_p$  tends to zero. By reducing the thickness of the piezoelectric layers, the mechanical stiffness is dramatically increased. These improvements on the dynamic behavior of the generator design are illustrated on [Figure 6.8](#) and [Figure 6.9](#).

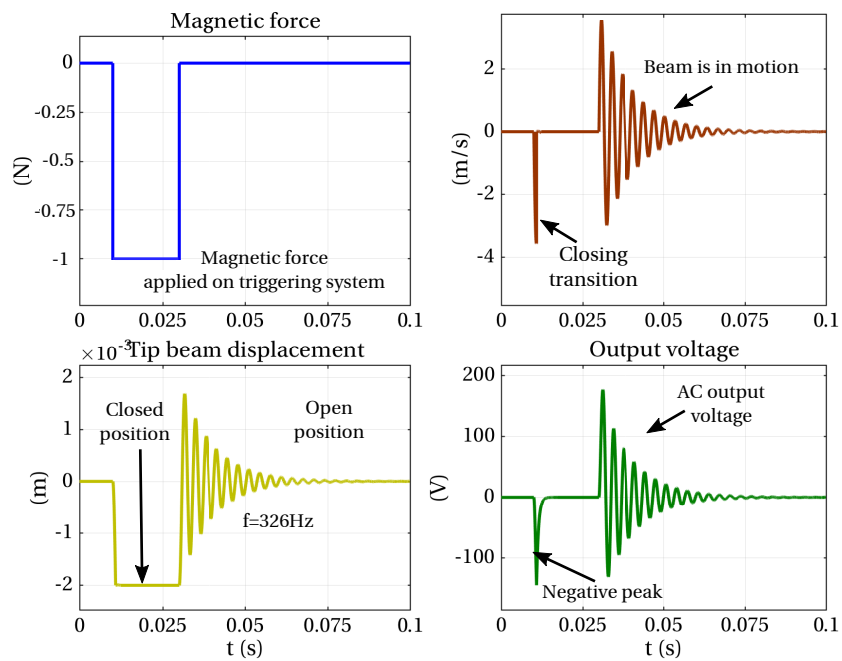


FIGURE 6.8: Typical response of the optimum design of the generator during a thermal cycle (closing and opening commutations) for input force, velocity, tip beam displacement and output voltage.

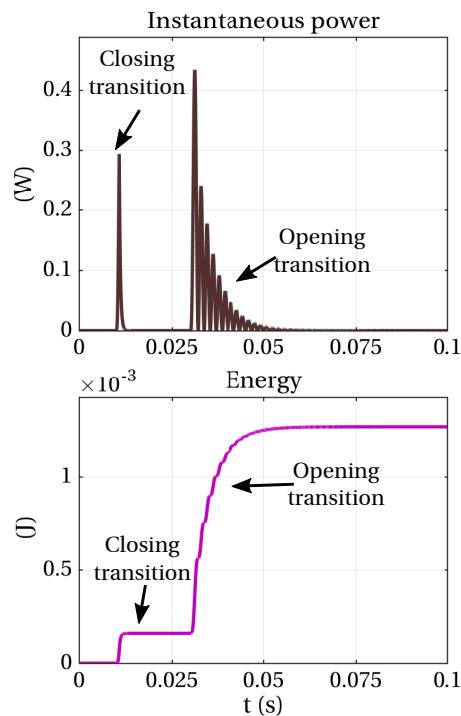


FIGURE 6.9: Typical response of the optimum design of the generator during a thermal cycle (closing and opening commutations) for power and output energy.

The optimum design response shows some interesting improvements that we have been predicted from our analytical model. First, the frequency of resonance has been significantly increased, from 260Hz to 326Hz. It is consistent with the hypothesis of having higher oscillations frequency, higher amount of mechanical vibration can be converted into electricity. Second, the optimum thickness of piezoelectric layers are lower than the initial design. It is evident that higher amplitudes of output voltage are reached with this optimized design. Optimal load resistor is near to 72k $\Omega$ . Finally, the harvested energy level is increased as well.

This design optimization attempt has been corroborated some guidelines in improvements of the transducer beam. Nevertheless, the inclusion of the triggering system has to be considered in order to optimize the whole design of generator. Therefore, we added to the step time model a block describing the triggering system. In addition, we believe that design optimization should be considered upon thermal requirements besides considering the signal bound response.

### 6.1.1 Second optimization design attempt

In this section, a second attempt on design optimization is presented. The main difference with respect to the previous design optimization attempt is the inclusion of the triggering system on the step time model. As we experimentally corroborated, the magnetic force is not stepped applied, so we opted for modeling this behavior.

Figure 6.10 and Figure 6.11 shows the implementation of the improved model of the energy harvester in Simulink and its triggering system. The magnetic model is described by Equation 3.10 as we already detailed.

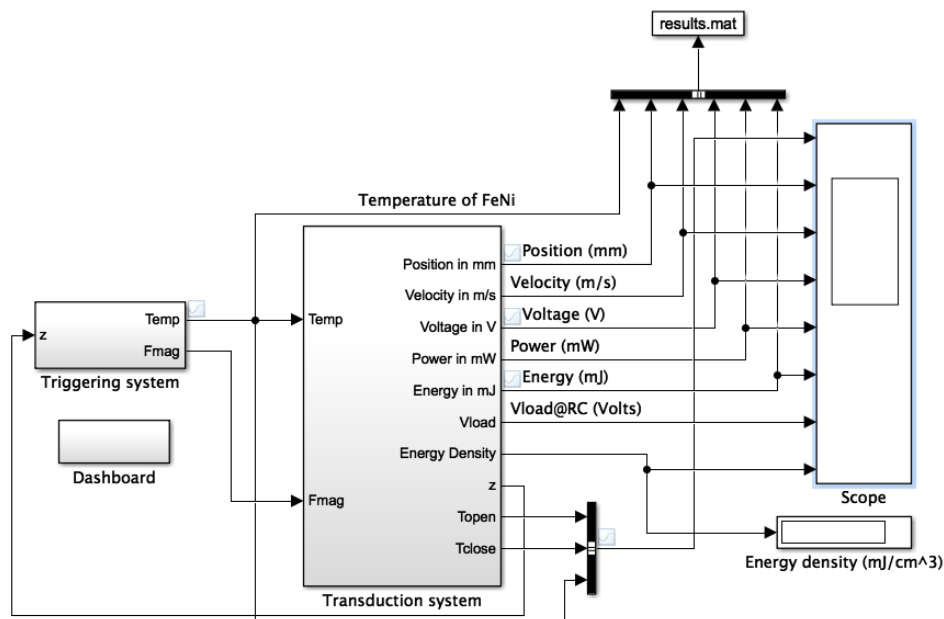


FIGURE 6.10: Implementation of thermo-magnetically activated piezoelectric energy harvester model in Simulink.

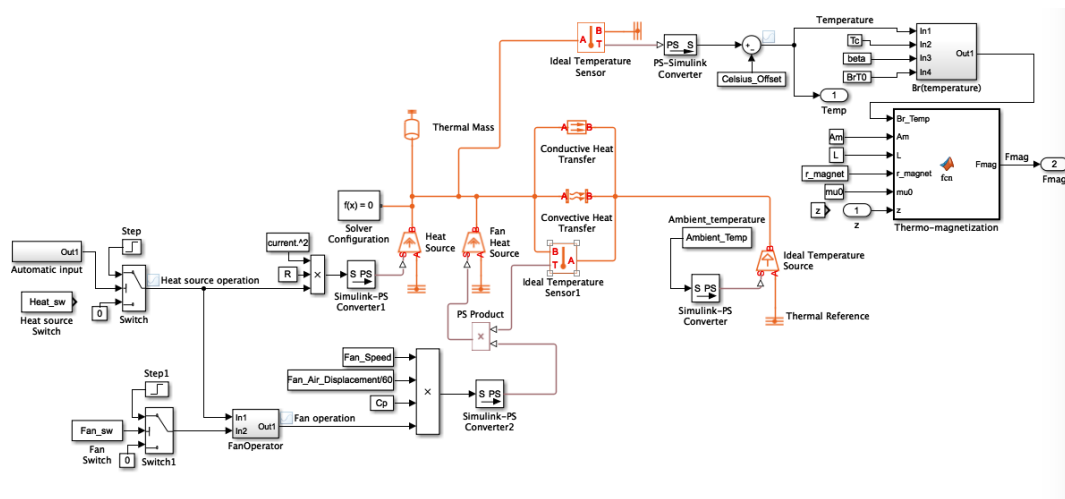


FIGURE 6.11: Implementation of the triggering system.

The model can be divided into two main sections: the triggering system and the transduction system. The first is aimed to describe thermo-magnetic behavior of the device as a response from an input temperature variation. It takes into account the materials and dimensions of the device in order to estimate the thermal response and the output is the magnetic force which in turns depends on the temperature and time. This output is then injected on the transduction block.

The transduction block calculates the mechanical force as a result of the architecture of the transducer beam as well as the initial distance of separation. At every step time, the model solves these forces that are counterbalancing and drive the position of the device. A general equation of motion is describing the behavior of the generator and thus parameters including position of the tip beam, velocity, voltage, instantaneous power, and energy are the output of these general model.

In addition, we have also added a dashboard interface that allow us to interact with the simulation at any moment on the simulation. This also allowed us to extract the energy per commutation in order to extract a better representative parameter of characterization. Figure 6.12 illustrates the dashboard interface implemented on the step time model on Simulink.

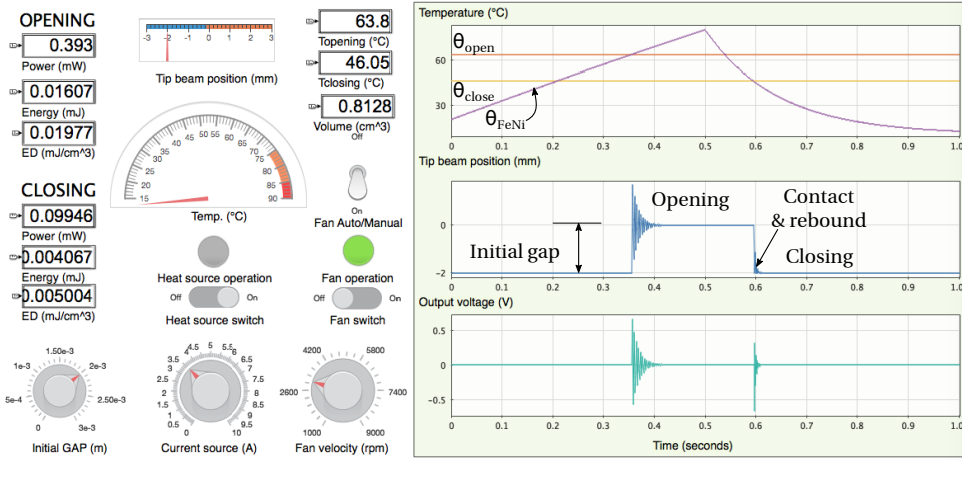


FIGURE 6.12: Representation of the dashboard implemented on the step time model of the energy harvester.

The interface presented is able to show at any time during simulation the transient behavior of the generator on its tip beam displacement, its output voltage and the thermal response (i.e., the temperature of the FeNi alloy as well as the thermal thresholds). The main advantage of this model is the possibility of tuning some design parameters such as the initial gap of the generator. Besides this parameter, temperature fluctuations of the FeNi alloy can be produced by using a heat joule effect (i.e., an electrical current flowing across a resistor attached to the FeNi alloy) and the cool down stage can be controlled by using a fan (i.e., with a determined velocity).

An important feature of this second design optimization attempt is the fact of including, in the custom requirements the temperature response. On the temperature response, we can establish a permitted zone on the temperature spectrum, where the opening and closing temperatures should be inside. For example, let us suppose that temperature fluctuations are in a range from a minimum temperature  $\theta_{min}$  to a maximum temperature  $\theta_{max}$ . Thus, the closing temperature,  $\theta_{close}$  and the opening temperature,  $\theta_{open}$  have to be designed to be inside the range of temperature fluctuations. As illustrated on Figure 6.13. The design variables considered for the second attempt of design optimization are summarized in Table 6.4.

TABLE 6.4: Design variables of the second design optimization attempt.

Variable	Symbol	Unit	Design space
Length of transducer beam	$L_B$	mm	$[17 \leq L_B \leq 23]$
Thickness of piezoelectric layers	$h_p$	$\mu\text{m}$	$[110 \leq h_p \leq 130]$
Thickness of shim	$h_B$	$\mu\text{m}$	$[90 \leq h_p \leq 120]$
Width of beam	$w_B$	mm	$[3 \leq w_B \leq 5]$
Initial distance of separation	$z_0$	mm	$[1 \leq z_0 \leq 2.25]$
Load resistor	$R_{Load}$	$\Omega$	$[10 \leq R_{Load} \leq 5000]$

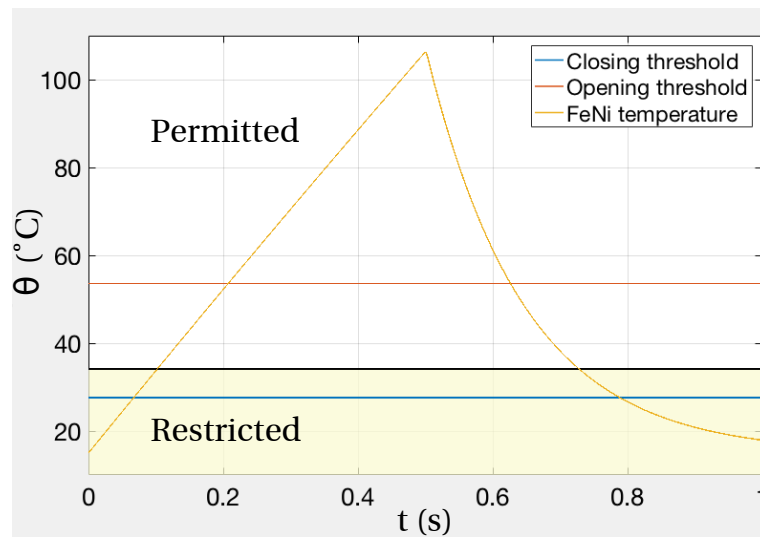


FIGURE 6.13: Custom requirement representation for second attempt of design optimization of energy harvester model implemented on Simulink.

In this particular case, the opening threshold is  $\theta_{open} = 53^{\circ}\text{C}$ , and the closing threshold is  $\theta_{close} = 27^{\circ}\text{C}$ .

The requirement on this particular case has been established as the closing temperature to be no lower than  $35^{\circ}\text{C}$ . That means that any generator design should ensure that the closing temperature is equal or higher than  $35^{\circ}\text{C}$ .

In this conditions, the design considered for this example does not meet the custom requirements. Therefore, we need to find an optimum design that maximizes the generator's energy per commutation and that also meets with this requirements.

This example may be the design of a generator destined to operate in a scenario where the temperature fluctuations are in such a temperature range. So in this way, the generator proposed will have closing and opening commutations.

The transient behavior of the initial design generator is illustrated on [Figure 6.14](#) and [Figure 6.15](#).

The transient behavior of the optimized design generator is illustrated on [Figure 6.16](#) and [Figure 6.17](#).

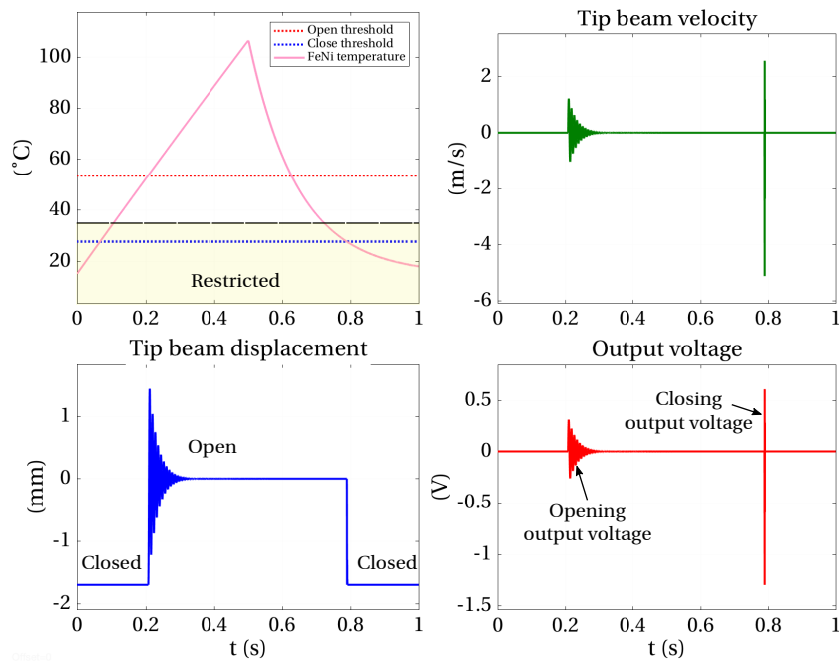


FIGURE 6.14: Typical response of the initial design generator for the second attempt of design optimization (temperature response, vertical displacement, velocity and output voltage of the cantilever beam).

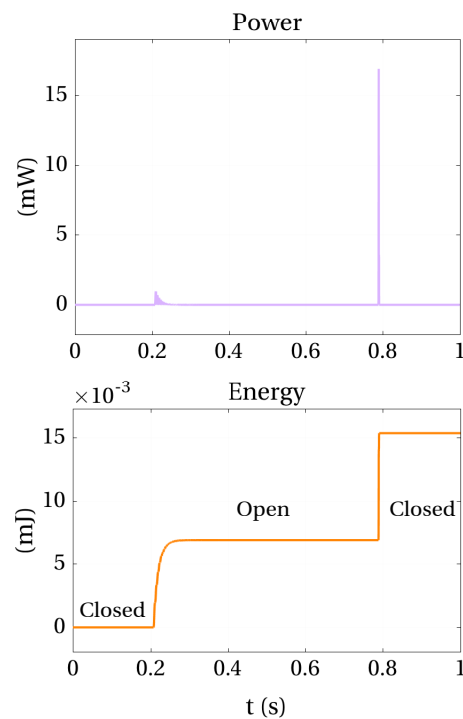


FIGURE 6.15: Typical response of the initial design generator for the second attempt of design optimization (power and energy output).

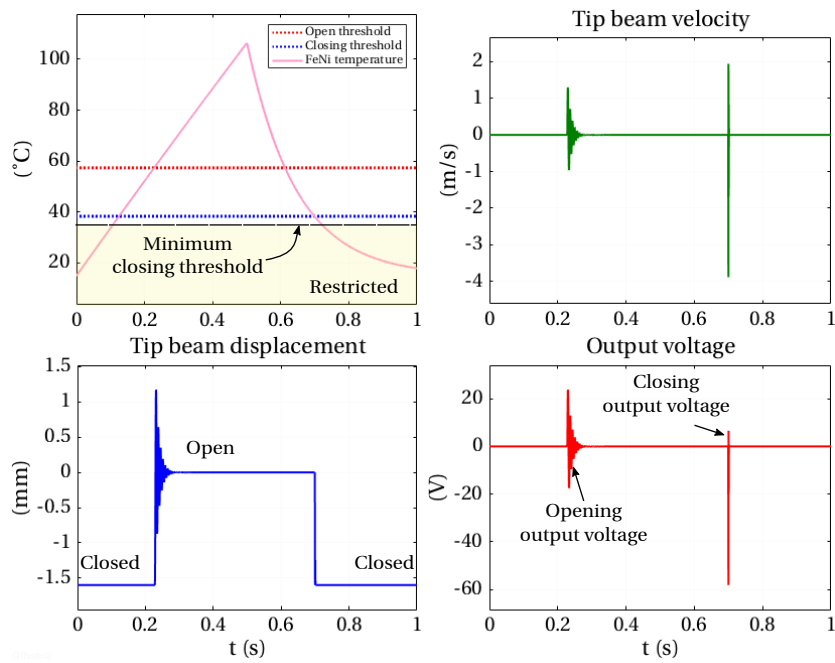


FIGURE 6.16: Typical response of the optimum design generator for the second attempt of design optimization (temperature response, velocity, vertical displacement and output voltage).

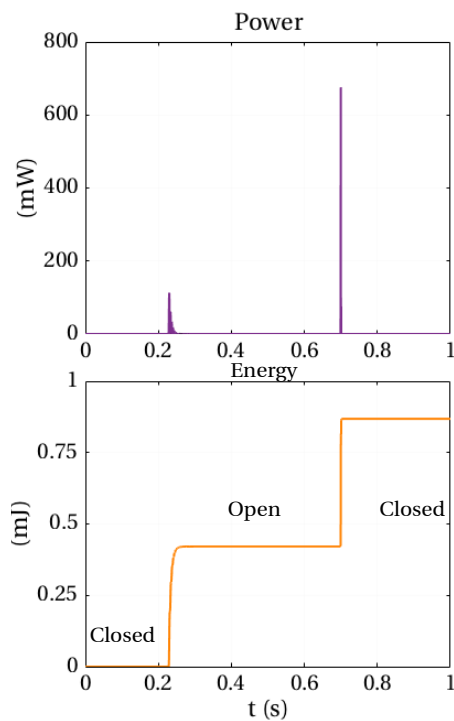


FIGURE 6.17: Typical response of the optimum design generator for the second attempt of design optimization (power and output energy).

Table 6.5 presents the initial and final values of design variables.

TABLE 6.5: Summary of the design variables of the initial design and the optimum design of the second attempt of design optimization process.

Variable	Symbol	Unit	Initial value	Final value
Length of transducer beam	$L_B$	mm	20	17
Thickness of piezoelectric layers	$h_P$	$\mu\text{m}$	120	130
Thickness of shim	$h_B$	$\mu\text{m}$	100	90
Width of beam	$w_B$	mm	4	5
Initial distance of separation	$z_0$	mm	1.7	1.55
Load resistor	$R_{Load}$	$\Omega$	10	5000
Opening temperature	$\theta_{open}$	$^{\circ}\text{C}$	53	57
Closing temperature	$\theta_{close}$	$^{\circ}\text{C}$	27	38
Energy	$E$	mJ	0.14	0.86

These results reveal a slightly reduction in length of the cantilever beam. It is not trivial to see the size reduction of the generator when a specific requirement such as the closing temperature is a design condition. In despite the size of the new generator design; an important increase in energy output is achieved. Another expected modification that can be seen from the dynamic behavior of these designs is the frequency of oscillations in the opening transition. The initial frequency of oscillations being 100Hz, it has been increased to 145Hz.

In addition, it is notable that the calculation time of these design optimization processes are no higher than 1 hour. Which is much shorter than the simulation time for a transient analysis that can reach up to 24 hours of simulation.

### 6.1.2 Discussion

In this section, design optimization processes have been conducted to two cases. These design optimization studies were conducted through Simulink by using time step models. Main findings can be listed as follows:

**First design optimization attempt:** when considering magnetic attraction force and the initial distance of separation on triggering system as constant parameters of the design optimization process, the dynamic performance of the transducer system can be improved by modifying the mechanical stiffness of the cantilever beam. Despite that these conditions of design variables constrain the design to the magnetic force needed to counter the mechanical force, optimization design on the transducer beam is possible. Under these design conditions, it is necessary to know the temperatures for which this magnetic force can be reached. The main requirement that ensures the two operation positions of the generator is the response of the cantilever beam

at its commutations. Improvements on the device are mainly reflected on the transducer beam dynamic response. Increase on the energy output during a thermal cycle of operation is theoretically possible.

**Second design optimization attempt:** by including the block of triggering system to the time step model, it is possible to design for a specific range of temperatures. Design requirements are now the operating temperatures of the generator. That is, knowing the temperature range of the environment where the final device will be placed, it is possible to design for specific temperature variations. We can design generators that will work in different temperature ranges. We demonstrated that output energy can be improved when designing generators for a specific temperature range. By using the simplified time step model of the generator, optimum designs of such generators are possible.

After defining the optimum design of this generator, and before passing to the production or fabrication stage, it is desirable to conduct a variability analysis of this design. Next section will present a study case of this kind of analysis.

## 6.2 Variability analysis

We all know that in production, there is always tolerances in design to be considered. Therefore, there is also a variability between parameter values that will not make possible to get the same results for each generator fabricated. Even if we can build thousands or billions of each of these parts of the generator, there is always a variability between these parts. So, as a designer what we need to do is to make sure that our design parameters are robust and we have to take in consideration the variability of production as well as the model variability. Before passing to a production stage, we can save time and money by doing simulations that consider variabilities of the model and the design parameters.

From the previous design optimization cases, we opted by selecting the optimum design of the first attempt of design optimization case to perform variability analysis. Based on the simulation results, the optimum design of the generator can reach an output energy of 1.26mJ in during one thermal cycle.

We can verify the design of the generator using Monte Carlo simulations. The variability design study we conducted can be divided into 5 main steps:

**Generating the design parts:** use Monte Carlo simulation to study variance in the output energy of the generator. We generated 10000 simulation points for each of the design variables with a normal distribution considering a tolerance.

**Gather performance results:** calculate the energy output of each of these 10000 combinations of generator.

**Variance evaluation:** evaluate the variation in the predicted model's energy output through histogram plot. We estimated the mean and standard deviation.

**Probability of pass:** based on a target output energy of 1mJ, we estimated the probability of having a device with an energy output of at least this target energy. The probability of fail is also estimated.

**Estimating process capability:** use these simulation results to explore the process capability. The process capability compares the process output with the customer's specification. Assuming an upper specification limit of 1.4mJ and a lower specification limit of 0.95mJ, the process capability  $c_p$  is estimated.

And assuming that manufacturing uncertainty of the generators parts is listed in [Table 6.6](#), we need to verify that these variations in the design parameters will enable the generator to maintain a robustness around the output energy.

TABLE 6.6: Design parameter values and uncertainty.

Design variable	Unit	Value $\pm$ 5%
Shim layer length, $L_B$	mm	$20 \pm 1$
Shim layer width, $w_B$	mm	$5 \pm 0.25$
Shim layer thickness, $h_B$	$\mu\text{m}$	$247.3 \pm 12.36$
Piezoelectric layer thickness, $h_P$	$\mu\text{m}$	$98.8 \pm 4.94$
Piezoelectric layer length, $L_P$	mm	$14.3 \pm 0.715$
Piezoelectric layer width, $w_P$	mm	$5 \pm 0.25$
Piezoelectric layer position, $x_P$	$\mu\text{m}$	$364 \pm 18.2$
Load resistor, $R_{Load}$	k $\Omega$	$72.15 \pm 3.6$

The first step is to produce 10000 random generator parts according to the tolerance and a normal distribution. [Figure 6.18](#) shows the histograms for the 10000 generator parts. All of them are centered at the design value for each part.

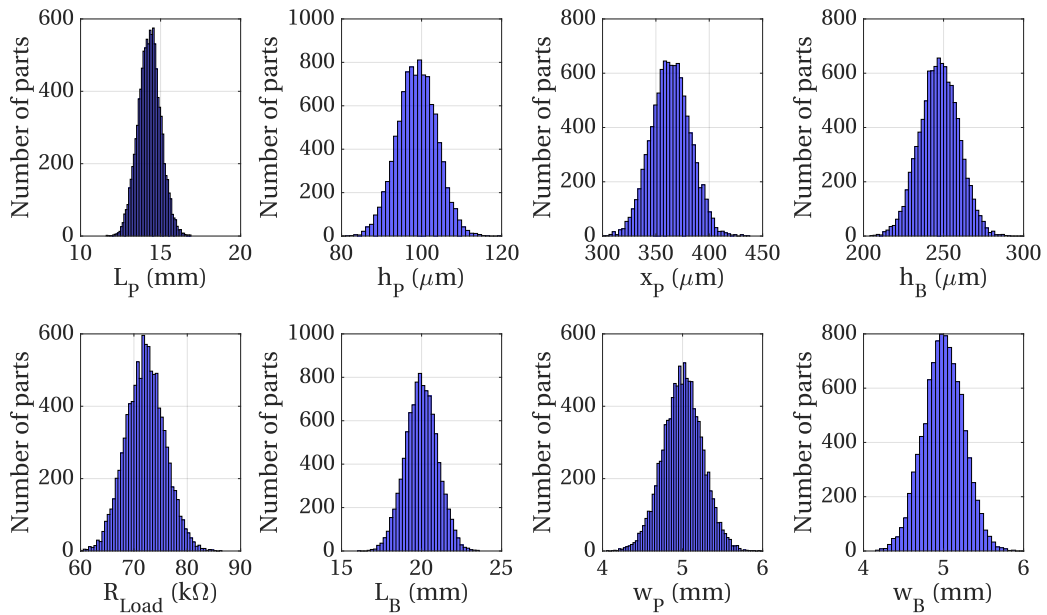


FIGURE 6.18: Histograms of the generator parts obtained by Monte Carlo simulation, when a tolerance of  $\pm 5\%$  is considered.

The 10000 different parts of the generator are now available to be integrated each of them in a single generator device. The next step is to simulate for all generator (i.e., the simulation points) a thermal cycle of operation and to calculate its output energy. Figure 6.19 illustrates this simulation result.

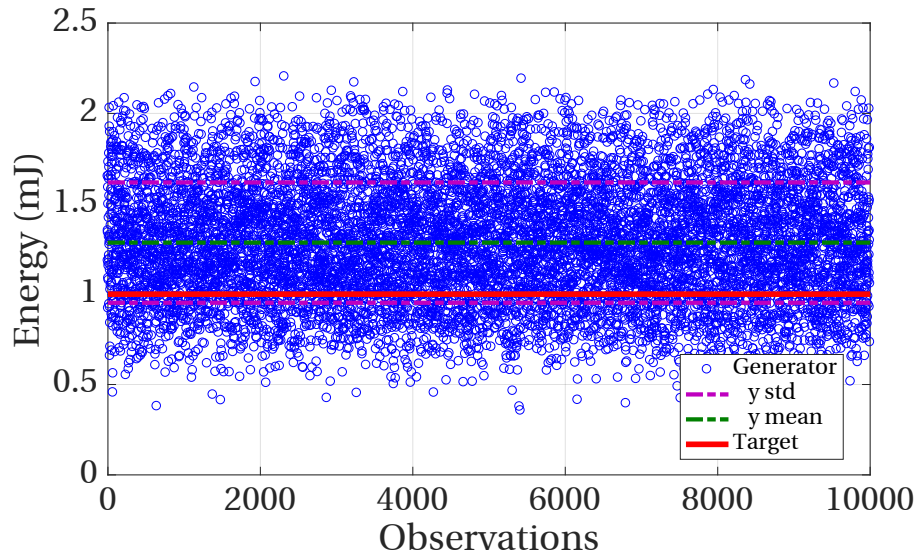


FIGURE 6.19: Simulation results of the output energy for the 10000 generators sample.

It can be seen that the performance of the generator has a significant robustness to the variability. And we can compute the probability of fail,  $P_{fail}$ . We can take the cumulative distribution function (cdf). And the probability of pass,  $P_{pass}$  which is the probability of having a generator with an output energy of at least 1mJ.

$$P_{pass} = cdf(fitdist, target) \quad (6.1)$$

$$P_{fail} = (1 - P_{pass}) * 100 \quad (6.2)$$

Where *fitdist* represents the distribution family, for instance a normal distribution or Poisson distribution. *target* is the value at which the distribution is evaluated. In Matlab, the function “*cdf(pd,x)*”, returns the cumulative distribution function of the probability distribution object “pd”, evaluated at the values in vector *x*. And the function “*fitdist(x,distname)*” creates a probability distribution object by fitting the distribution specified by “*distname*” to the data in column vector *x*.

We decided to go beyond on this variability study and we opted by calculating the process capability. The process capability compares the process output with customers’s specifications. The purpose of a process capability study is to compare the process specification to the process output and determine statistically if the process can meet the customer’s specifications.

The indicator  $c_p$  estimates what the process is capable of producing if the process mean were to be centered between the specification limits. Assumes process output is approximately normally distributed. Finally, we can also extract the indicator  $C_{pk}$ , Estimates what the process is capable of producing, considering that the process mean may not be centered between the specification limits. That is, the capability measure preferred in most industries because it indicates whether it is capable and how well-centered the process is.

In Matlab, the function *capability(data,specs)* estimates capability indices for measurements in data given the specifications in *specs*. *data* can be either a vector or a matrix of measurements. *specs* can be either a two-element vector of the form [LSL,USL] containing lower and upper specification limits. We assume an upper and lower specification on the output energy of the generator as follows:

**Upper specification limit (USL):** 1.4mJ

**Lower specification limit (LSL):** 0.95mJ

In order to explore how the tolerances of these design variables affect the process capabilities, we also considered a tolerance of  $\pm 2\%$  of the design parameters values. We then repeated the process of the variability study as illustrated in [Figure 6.20](#) and [Figure 6.21](#) for the histograms of the generator parts and the simulation results of the output energy, respectively.

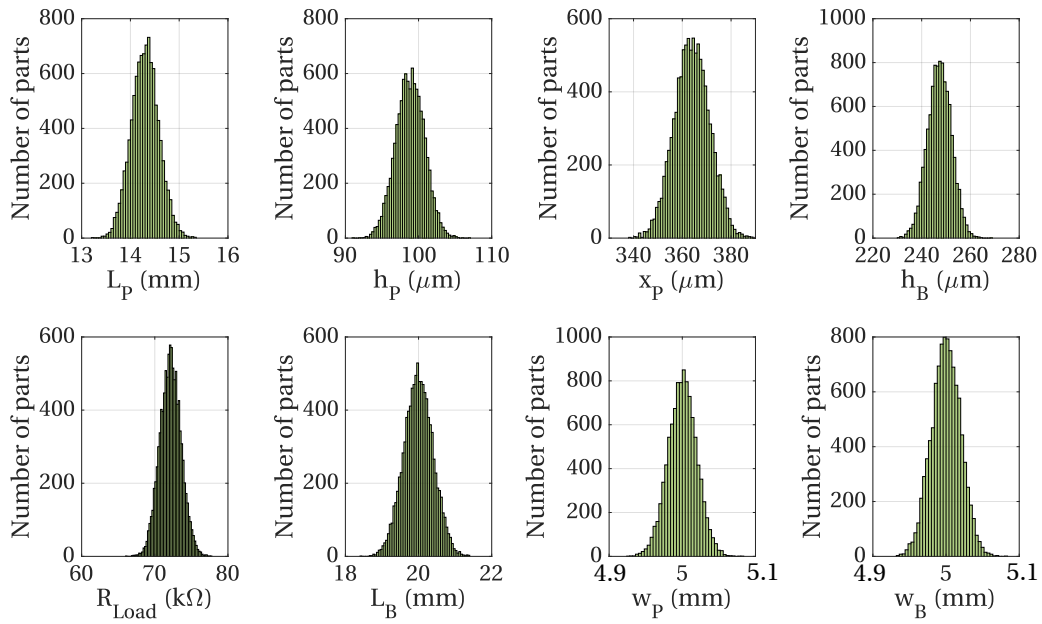


FIGURE 6.20: Histograms of the generator parts obtained by Monte Carlo simulation, when a tolerance of  $\pm 2\%$  is considered.

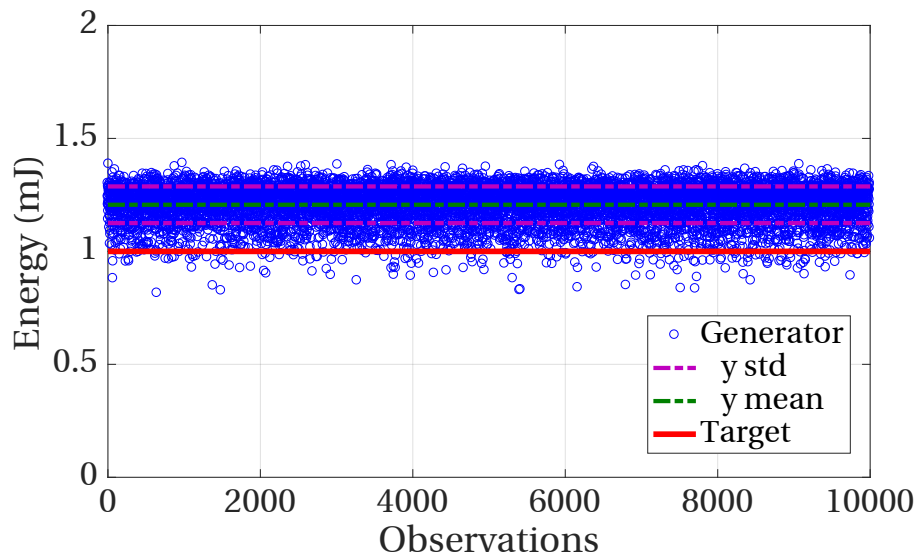


FIGURE 6.21: Simulation results of the output energy for the 10000 generators sample when a tolerance of  $\pm 2\%$  is considered on the design variables.

Table 6.7 summarizes the probabilities of fail and passing (with a target energy of 1mJ) and the process capabilities for the optimum design for two different dimension tolerances and variability of the production.

TABLE 6.7: Probability of fail and process capability of optimum design of generator depending on tolerances.

Item	Symbol	$\pm 5\%$ tolerance	$\pm 2\%$ tolerance
Probability of fail	$P_{fail}$	19.57%	0.54%
Probability of passing	$P_{pass}$	80.42%	99.45%
Probability of being within limits	$P$	47.7%	99%
Probability of being below LSL	$P_L$	15.69%	0.07%
Probability of being above USL	$P_U$	36.5%	0.84%
Process capability	$c_p$	0.22	0.92
Process capability index	$c_{pkm}$	0.087	0.29
Adjusted sigma level	$\sigma$	1	3

The index  $c_{pkm}$  estimates process capability around a target, and accounts for an off-center process mean. Assumes process output is approximately normally distributed.

### 6.3 Discussion

Design optimization of the generator precesses were conducted by using the simplified model of the generator. Using Simulink and Matlab, two stages of design optimization were presented. The main conclusions of these analyses can be discussed as follows:

1. Design optimization of the energy generator model can be realized in Simulink.
2. The single-degree-of-freedom model describes the dynamic behavior of the generator and it can easily studied under a variability analysis in Simulink.
3. The main advantage of doing a variability analysis is to explore robustness of the generator design.
4. When designing for variability, a production process of a device can be considered in order to explore the capabilities of such a process.
5. We have demonstrated a basic application of tolerance analysis of our generator by using a simplified model of the generator.
6. Speed on optimization design can be obtained by using simplified models, when giving rapid response to potential customers is crucial as commercial product developer.

# Chapter 7

## Conclusions and future work

### Contents

---

<b>7.1 Conclusions</b> .....	<b>179</b>
7.1.1 Thesis contributions .....	181
<b>7.2 Future work</b> .....	<b>182</b>

---

### 7.1 Conclusions

This thesis was originally intended to focus on energy harvesting and, in particular, the conversion of temporal variations of temperature into electricity. Combining thermal-to-mechanical energy transduction, in a first step, by way of the thermal magnetization of a soft magnetic alloy having a Curie temperature close to the ambient temperature and piezoelectric transduction in a second step. The aim of this project is to downscale a mesoscale prototype.

A thermo-magnetically triggered piezoelectric generator has been presented in this thesis. We designed test prototypes and have demonstrated the feasibility of converting temperature fluctuations into electricity through indirect conversion method. The goal was, from this generated energy, to be able to feed a sensor node so that it transmits information. Since the system had to be able to operate in a “human” environment, the specifications required that the temperature evolve slowly, with a low amplitude and around the ambient temperature.

From these requirements, we have reviewed several direct principles of thermal energy conversion and the materials implementing them. Depending on the cases considered, we encountered two major locks. The first concerned the availability of materials (expensive, difficult to obtain or to achieve). The second, even more problematic, was that most of the solutions proposed had a temporal dependence of their properties. In other words, when the temperature exhibits slow variations, the generated electrical energy becomes very low and unrecoverable.

We have therefore developed an innovative solution by coupling soft magnetic material, namely a specific FeNi alloy with a Curie temperature close to the ambient temperature,

permanent hard magnets, and piezoelectric materials. In order to overcome this temporal dependence, it was necessary to leave aside the idea of a continuous electrical generation with the variation of temperature and to approach a sudden trigger, allowing to concentrate the energy during thresholds of temperature. Thermo-magnetization and piezoelectric coupling has made this possible by creating forces that do not evolve in the same way and thus creating a system that shifts abruptly from one position to another. During these transitions, energy is generated that can be recovered.

Assuming that the initial temperature is a “cold” temperature, the system has its equilibrium position in the closed position. Indeed, the soft material behaves like a ferromagnetic and the resulting magnetic force between the magnets and FeNi closes the circuit. When the temperature becomes hot, the FeNi loses its magnetic properties and the mechanical force of the cantilever beam becomes predominant, thus it opens the system. The transitions are abrupt because the two opposing forces have very different characters: the mechanical one is linear while the magnetic is not at all. The piezoelectric layers then translate these brutal deformations into electricity.

A mathematical model was developed to describe the generator’s characteristics as a function of design parameters. This model has been divided into four parts. First, we studied the thermal response of the generator as a function of its dimensions, equilibrium position, and its material properties. Second, we investigated the magnetic force between a permanent magnet and a magnetized volume of soft magnetic material. Then we investigated thermo-magnetization of the triggering system, that is, how temperature change modifies the magnetic force. Third, we coupled thermo-magnetization with mechanical behavior of a cantilever beam in large deflection in order to predict the operating temperatures of the generator as a function of its design. Fourth, coupled the entire system to obtain transient behavior of the system. Coupling piezoelectricity to mechanical energy produced by the generator’s commutations, we were able to explore the two output signals of the generator. We concluded that our analytical model was valid for quickly sizing a generator.

By using finite element method, 3D models of the generator were developed to explore the multi-physic system in static, modal, harmonic and transient domains. Thermal loads applied to finite element models describe the response of the generator in targeted temperature fluctuations environments. Magneto-static simulation showed the response of thermo-magnetization within triggering system. Piezoelectric transduction applied to the finite element model demonstrated the energy harvesting capabilities of the device.

Afterwards, we implemented this energy harvester principle by building different test prototypes of generators. These generators were based on a piezoelectric cantilever beam, cut in several forms, which allowed to obtain generators easy to build and inexpensive. The subsequent characterization of the generator made it possible to determine its constituent parameters and also the energy levels generated. We opted by characterizing the performance of these prototypes by measuring the energy density per commutation. We made a second generation prototype, which is portable and capable of working with such a source and can generate electricity when certain thresholds are exceeded. Finally, we have put in place theoretical bases in order to simulate the generator in a global way. This simulation can both be used to predict the behavior of the structure but also to think about its optimization. We then verified that the experimental results were consistent with those obtained by simulation. The piezoelectric voltage exhibited the same characteristic shape during opening and closing, and its amplitude was also similar. But the most important

thing was that the energies generated were almost identical. In conclusion, this thesis work fulfilled the objectives initially set. We have validated the exploitation of slow temperature variations as a “new” source that can be used for energy recovery. Table 7.1 summarizes the test prototypes performance.

TABLE 7.1: Test prototypes performance comparison.

Test prototype	Gap mm	Commutation			
		Opening		Closing	
		Energy density $\mu\text{W cm}^{-3}$	$\theta_{open}$ $^{\circ}\text{C}$	Energy density $\mu\text{W cm}^{-3}$	$\theta_{close}$ $^{\circ}\text{C}$
<b>Prototype 1 (wide beam)</b>	2	2.34	67	0.475	34
<b>Prototype 2 (narrow beam)</b>	2	4.84	64	0.35	32
<b>Prototype 3 (triangular beam)</b>	2	130	57	12.7	26
<b>Prototype 2b (narrow beam and smaller magnets)</b>	1.17	2.6	64	0.094	46
<b>Prototype 3b (triangular beam and smaller magnets)</b>	1.15	223	56	14.8	28
<b>Portable prototype 1 (second generation)</b>	0.7	0.88	41	0.033	24
<b>Portable prototype 2 (second generation)</b>	0.42	0.074	32	0.012	29

### 7.1.1 Thesis contributions

1. A termo-magnetically activated piezoelectric generator as well as its power energy management module. There is a meso-scale prototype showing the feasibility of this approach on thermal energy harvesting developed in this thesis.
2. The development of new prototypes to promote the miniaturization of such a double-step thermal energy conversion. Experiments on those prototypes demonstrate that thermo-magnetic effect can be used in combination with piezoelectric material to generate electricity. This approach could be used in the design of future thermo-magnetically activated piezoelectric generators in micro scale.

3. A mathematical model is developed to describe the generator's characteristics as a function of the materials, dimensions and temperature variations and verified by finite element analysis and experimental testing.
4. A design tool implementing the mathematical model developed to promote a rapid design of thermo-magnetically activated piezoelectric generators depending on the materials selection and its parameters' design space. Moreover, the dynamic performance of such a generator can be predicted and enhanced by means of optimization design methods and variability analysis.
5. By incorporating a Peltier module to the generator in order to create temperature variations, it is possible to characterize the generator response according to the input scenario. The recently developed prototype consists of a piezoelectric transducer of 8mm length and 1mm width along with a iron nickel alloy of a disc shape of 4mm height and 14mm of diameter
6. An electrical equivalent model of the generator. This model is intended to provide useful data to promote designing of its energy management module using a unique software, namely LTspice.

## 7.2 Future work

There are several items that need to be addressed before the micro-fabrication of the generator. Having shown that recovery of temporal variations of temperature was possible, we hope that new principles, new structures will be explored to enrich this field of applications. In particular, the thermal magnetization seems to us a promising way. We have never managed to get the other soft magnetic alloys, in reduced sizes, but the design rules for miniaturization results shown suggest interesting results. A critical requirement is the perpetually thermal oscillator, that can be obtained by inverting the place of the soft magnetic alloy and permanent magnets. That is, putting the permanent magnet fixed and in contact with the heat source, and the soft magnetic material attached to the cantilever beam.

Returning to the concepts that we have developed and applied in this thesis, many points can be improved. One of the issues we struggled against was the quality of the soft magnetic material we had at our disposition. We have tried contacting several fabricants to obtain these kind of materials, unfortunately, we have never obtained a response. Due to time remaining to this thesis, comparisons with Ansys and Matlab/Simulink have been reduced at the simple minimum. It seems obvious to us that there are still many things to explore at this level. This data would also benefit from being compared to a more complex architecture of such a generator, which would definitively decide who is the most accurate. In the same way, the global simulation can be exploited much more deeply, we only scratched the surface of the possibilities offered.

Finally, the whole part about energy conversion electronics was quickly discussed at the end of this thesis. Other techniques can extract more efficiently energy. In particular, we think of synchronized switching, which usually leads to better results. This part remains to explore whether it is experimentally or numerically by integrating it with our global simulation under LTspice.

## Appendix A

# Piezoelectricity generalities

Piezoelectricity couples mechanical properties and electrical properties in a same material. Both are linked across a tensorial representation. The local macroscopic quantities chosen to illustrate this coupling are, respectively, strain tensors  $S$  and stress  $T$ , and induction vectors  $D$  and electric field  $E$  [100]. Table A.1 illustrates these variables.

TABLE A.1: Variables involved on piezoelectric equations.

Domain	Symbol	Description	Units
Electric	D	Electric displacement	$\text{C m}^{-2}$
	E	Electric field	$\text{V m}^{-1}$
Mechanic	S	Strain	no units
	T	Stress	$\text{N m}^{-2}$

In order to express the constitutive equations of piezoelectricity, a reference system is required. Since the piezoelectric materials are anisotropic, the axis 3 of the marker is generally chosen to be collinear with the direction of polarization. The other two axes (1 and 2) are chosen so that the trihedron formed by 1, 2 and 3 is direct (see A.1(a)). In this frame, 6 different movements can take place: a translation movement along each of the three axes and three rotational movements around these same three axes (denoted 4, 5 and 6 respectively).

Among the piezoelectric materials, some of them are also ferroelectric, this is the case of many materials having a perovskite crystal structure. An exciter electric field  $E$  implies the appearance of a polarization  $P$ , which makes it possible to define a remanent polarization  $P_r$  and a saturation polarization  $P_s$  as well as a coercive field  $E_c$  (see figure A.1(b)).

Also, the Voigt notation is often used to simplify the representation of symmetric tensors as those of strain or stress. This nomenclature allows passing from a  $3 \times 3$  matrix, whose coefficients  $i j$  are from 1 to 3 each to a set of 6 coefficients. These coefficients can be also ranged as in Table A.2.

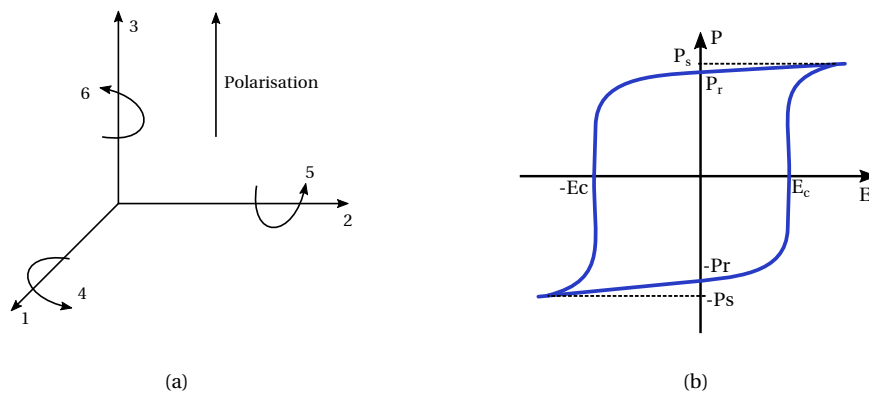


FIGURE A.1: (a) schematic of the reference system representing the piezoelectric polarization along z-axis. (b) Hysteresis cycle of the polarization  $P$  as a function of electric field  $E$  of a ferroelectric material.

TABLE A.2: Relation between tensor subscript and Voigt representation.

Tensor	$ij = 11$	$ij = 22$	$ij = 33$	$ij = 32$ or $23$	$ij = 13$ or $31$	$ij = 12$ or $21$
Voigt	$I = 1$	$I = 2$	$I = 3$	$I = 4$	$I = 5$	$I = 6$

The coefficients relating the variables of mechanics, electrics and piezoelectric domains are as follows:  $\epsilon$  is the dielectric permittivity (its inverse is the dielectric impermeability  $\epsilon = \iota^{-1}$ ),  $s$  is the compliance material (its inverse is the stiffness of material  $s = c^{-1}$ ). As the terms  $d$ ,  $e$ ,  $h$  and  $g$  are the piezoelectric coefficients, 3-order tensor that links mechanic and electric variables:

$$d = \epsilon^T g = e s^E \quad (\text{A.1})$$

$$e = \epsilon^S h = d c^E \quad (\text{A.2})$$

$$g = \iota^T d = h s^D \quad (\text{A.3})$$

$$h = \iota^S e = g c^D \quad (\text{A.4})$$

These coefficients are listed in [Table A.3](#)

Having presented the coefficients involved on piezoelectric effect, it remains is to write the constitutive equations connecting the components of the electric field and induction to the components of the mechanical tensors of strain and stress thanks to the different coefficients mentioned above. Variables can be chosen arbitrarily, as long as they are independent. This means that four pairs of fundamental equations can be used depending on whether one chooses to use  $(S, D)$ ,  $(T, E)$ ,  $(T, D)$  or  $(S, E)$  (see [Table A.4](#)): The exponents  $E$ ,  $D$ ,  $S$ , and  $T$  mean that these quantities are assumed to be null or constant. The exponent  $Tr$  means the transpose of the matrix considered.

TABLE A.3: Summary of mechanical, electrical and piezoelectrical coefficients.

Domain	Expression	Description	Units
Mechanical	$s = \frac{\partial S}{\partial T}$	Compliance	$\text{m}^2 \text{N}^{-1}$
	$c = \frac{\partial T}{\partial S}$	Stiffness	$\text{N m}^{-2}$
Electrical	$\epsilon = \frac{\partial D}{\partial E}$	Dielectric permittivity	$\text{F m}^{-1}$
	$\iota = \frac{\partial E}{\partial D}$	Dielectric impermeability	$\text{m N}^{-1}$
Piezoelectrical	$d = \left(\frac{\partial D}{\partial T}\right)^E = \left(\frac{\partial S}{\partial E}\right)^T$	Piezoelectric constant	$\text{C N}^{-1}$
	$h = -\left(\frac{\partial T}{\partial D}\right)^S = -\left(\frac{\partial E}{\partial S}\right)^D$	Piezoelectric constant	$\text{N C}^{-1}$
	$e = -\left(\frac{\partial T}{\partial E}\right)^S = \left(\frac{\partial D}{\partial S}\right)^E$	Piezoelectric constant	$\text{N V}^{-1} \text{m}^{-1}$
	$g = \left(\frac{\partial S}{\partial D}\right)^T = -\left(\frac{\partial E}{\partial T}\right)^D$	Piezoelectric constant	$\text{V m N}^{-1}$

TABLE A.4: Constitutive equations of piezoelectric effect.

	<b>T</b>	<b>S</b>
<b>E</b>	$S = s^E T + d^{Tr} E$	$T = c^E S - e^{Tr} E$
	$D = d T + \epsilon^T E$	$D = e S + \epsilon^S E$
<b>D</b>	$S = s^D T + g^{Tr} D$	$T = c^D S - h^{Tr} D$
	$E = -g T + \iota^T D$	$E = -h S + \iota^S D$

The reason why piezoelectricity manifests itself in a material is related to the non-symmetry of its crystallographic mesh [55]. However, depending on the materials, this lack of symmetry is not marked identically. Piezoelectric ceramics with perovskite structure are more symmetrical and the number of coefficients decreases. We know that the PZT element is made up of transversely isotropic material. Let us assume the PZT element is polarized along the 3 axis. Some of the items in compliance matrix become zero. We know that the PZT element is made up of transversely isotropic material. Let's assume the PZT element is polarized along the 3 axis. Some of the items in compliance matrix become zero. Those left non-zero items are:

$$S_{11} = S_{22}$$

$$S_{13} = S_{31} = S_{23} = S_{32}$$

$$S_{12} = S_{21}$$

$$S_{44} = S_{55}$$

$$S_{66} = 2(S_{11} - S_{12})$$

$$d_{31} = d_{32}$$

$$d_{15} = d_{24}$$

$$\varepsilon_{11}^T = \varepsilon_{22}^T = \varepsilon_{33}^T$$

and they can be expressed in the piezoelectric, dielectric, and compliance matrix as follows:

$$d = \begin{bmatrix} 0 & 0 & 0 & 0 & d_{15} & 0 \\ 0 & 0 & 0 & d_{15} & 0 & 0 \\ d_{31} & d_{31} & d_{33} & 0 & 0 & 0 \end{bmatrix} \quad (\text{A.5})$$

$$\varepsilon = \begin{bmatrix} \varepsilon_{11} & 0 & 0 \\ 0 & \varepsilon_{11} & 0 \\ 0 & 0 & \varepsilon_{33} \end{bmatrix} \quad (\text{A.6})$$

$$s = \begin{bmatrix} s_{11} & s_{12} & s_{13} & 0 & 0 & 0 \\ 0 & s_{11} & s_{13} & 0 & 0 & 0 \\ 0 & 0 & s_{33} & 0 & 0 & 0 \\ 0 & 0 & 0 & s_{44} & 0 & 0 \\ 0 & 0 & 0 & 0 & s_{44} & 0 \\ 0 & 0 & 0 & 0 & 0 & s_{66} \end{bmatrix} \quad (\text{A.7})$$

It is trivial to see that matrixes  $\varepsilon$  and  $s$  are symmetrical. In addition, from Equation A.5, it can be remarked that the following elements  $d_{31}$ ,  $d_{33}$ , and  $d_{15}$  correspond to first three operation modes on piezoelectric ceramic materials: longitudinal mode, transversal mode and shear mode, respectively. Polarization direction is along the axis 3. These three principal modes of operation are illustrated in figures A.2(a), A.2(b), and A.2(c).

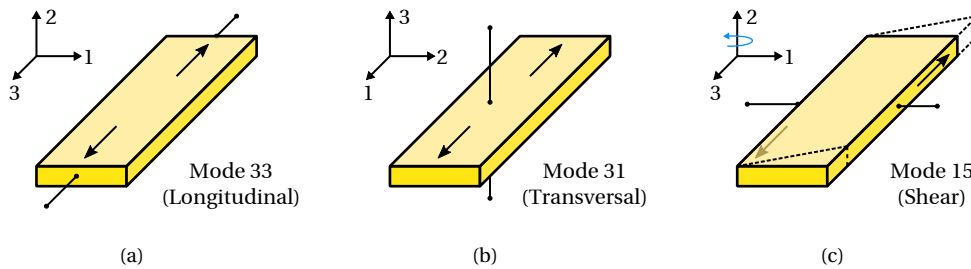


FIGURE A.2: Principals modes of operation of a piezoelectric ceramic material, (a) Longitudinal mode: electrodes are in the same direction of the applied load and polarization. (b) Transversal mode: electrodes and polarization are in the same direction but they are orthogonal to the applied load. (c) Shear mode: lateral forces are applied and the electrodes are perpendicular to the polarization direction.

## Appendix B

# Mounting fixture design

This appendix presents the design drawings of the fixture for mounting the first generation prototypes. All dimensions are in mm.

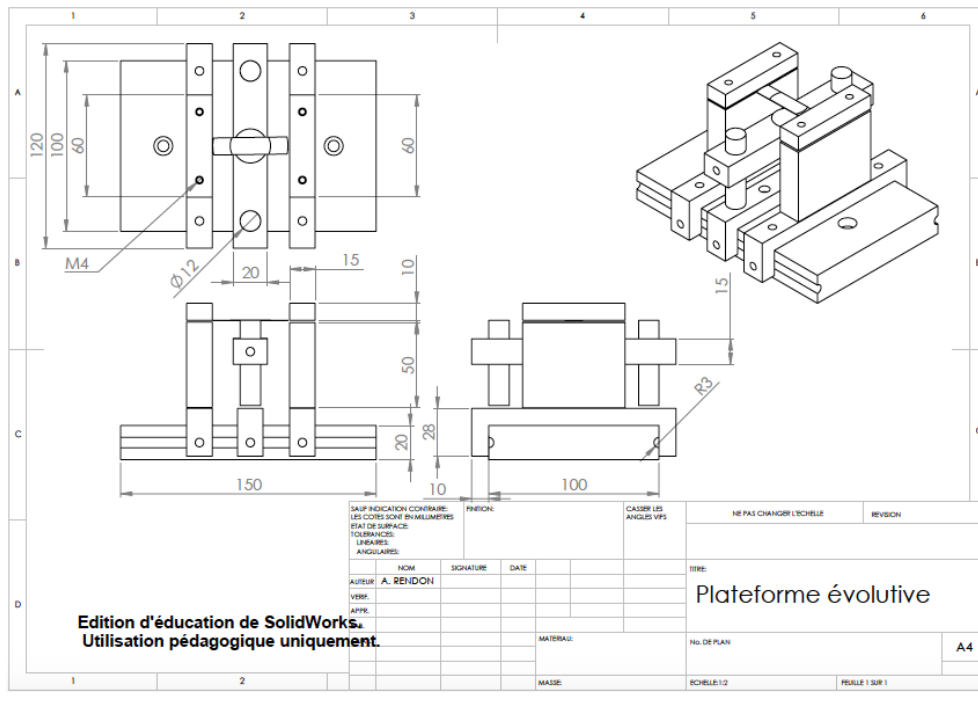


FIGURE B.1: Overall view of the design drawings of the fixture for mounting the first generation prototypes.

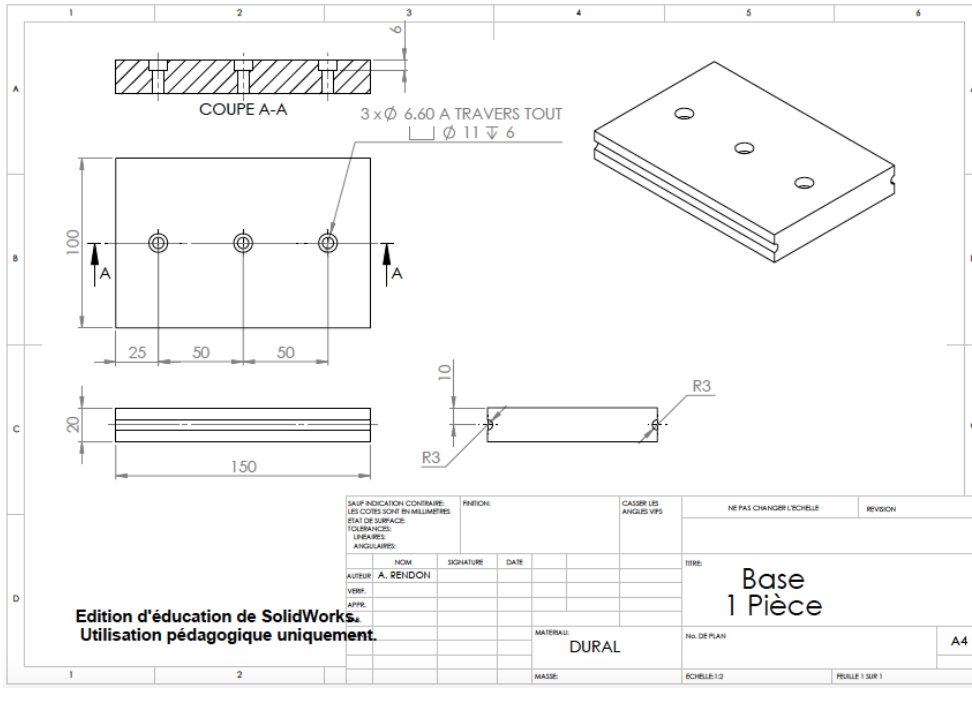


FIGURE B.2: Base support design drawing.

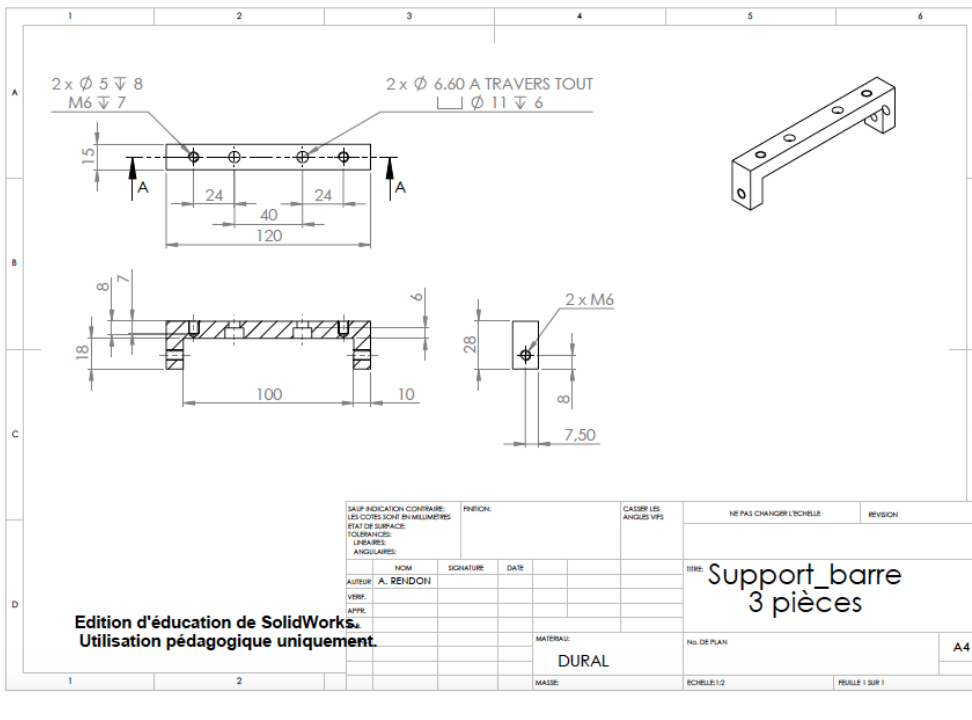


FIGURE B.3: Bar support design drawing.

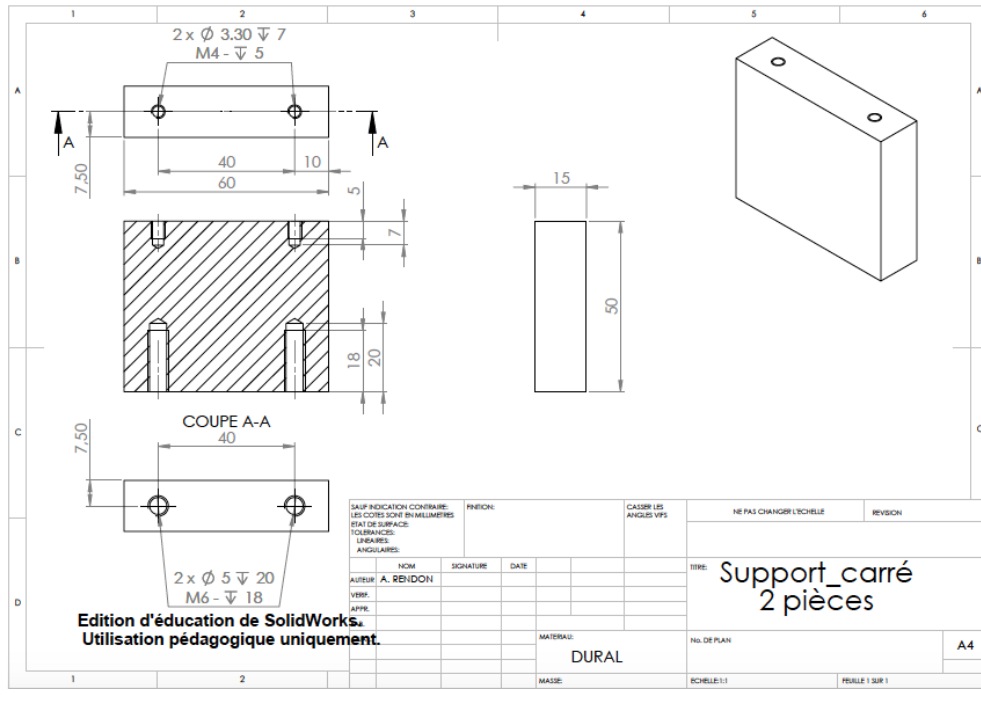


FIGURE B.4: Block support design drawing.

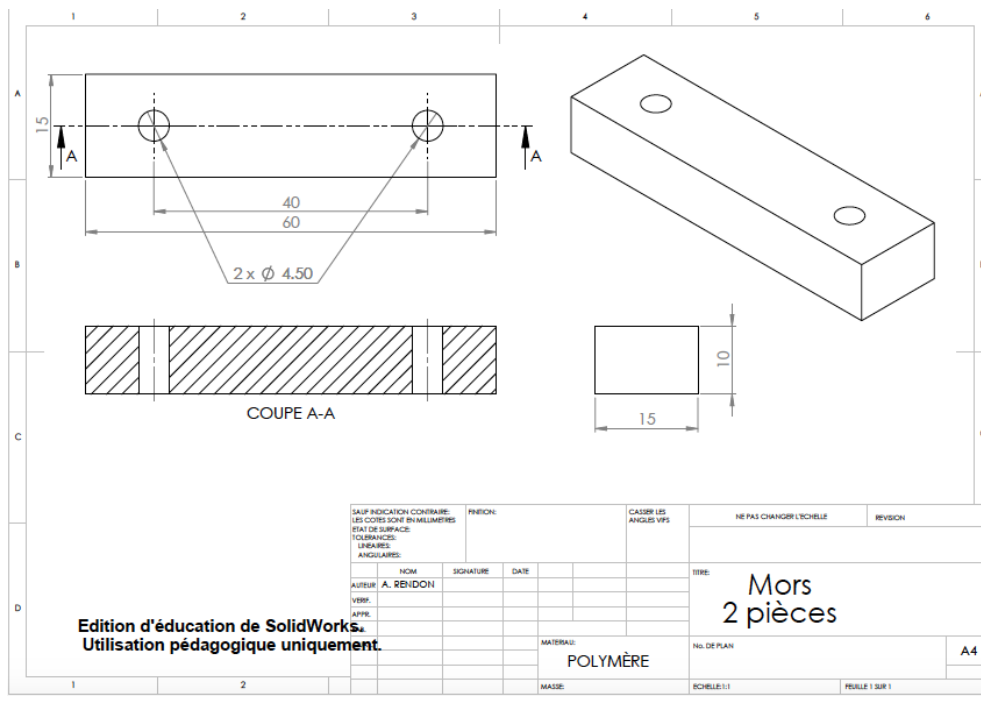


FIGURE B.5: Jaws design drawing.

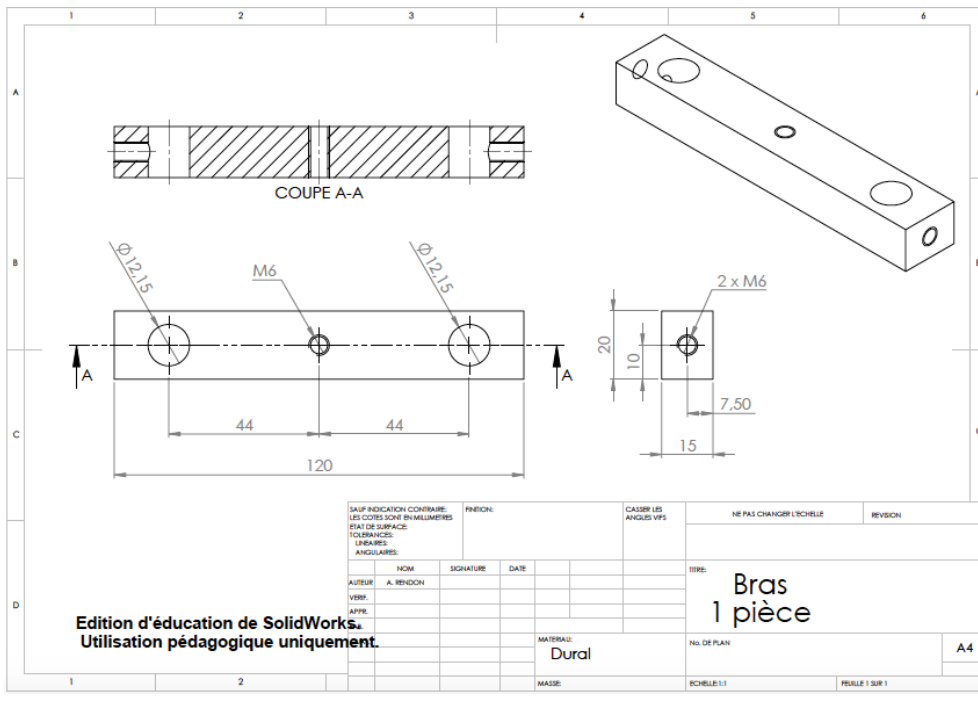


FIGURE B.6: Central bar design drawing.

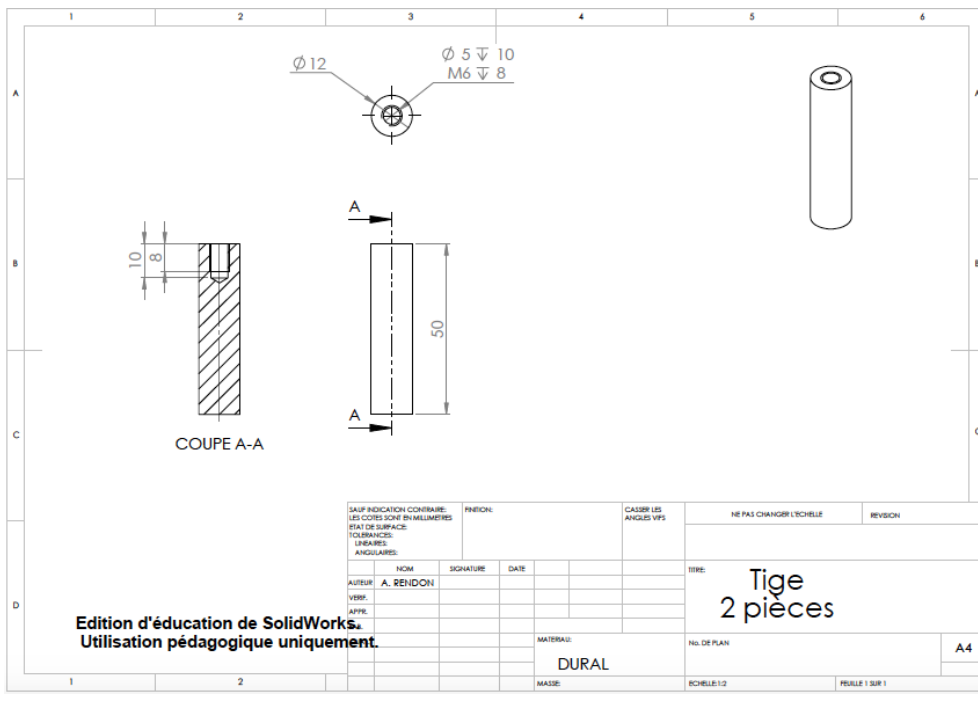


FIGURE B.7: Vertical support bar design drawing.

## Appendix C

# Implementing losses in PSpice

The losses elements, implemented in PSpice through GLAPLACE and ELAPLACE elements (i.e., G1, G2, E2, and E3), can be described as follows:

$$G_1 = s q r t(-s * s) C_b \tan \delta_d \quad (\text{C.1})$$

$$G_2 = s q r t(-s * s) C_k \tan \delta_m \quad (\text{C.2})$$

$$E_2 = \frac{s}{a b s(s)} k^* k^{**} C \quad (\text{C.3})$$

$$E_3 = s q r t(-s * s) k^* k^{**} m \quad (\text{C.4})$$

Where  $\delta_d$  and  $\delta_m$  are the dielectric and mechanical losses tangents, respectively.



# Bibliography

- [1] X. y Xiong, F. Wei, J. w Li, M. Han, and D. h Guan. Vibration monitoring system of ships using wireless sensor networks. In *2014 IEEE International Conference on Mechatronics and Automation*, pages 90–94, August 2014. doi: 10.1109/ICMA.2014.6885677.
- [2] C. Abreu and P. Mendes. Wireless sensor networks for biomedical applications. pages 1–4. IEEE, February 2013. ISBN 978-1-4673-4859-1. doi: 10.1109/ENBENG.2013.6518413. URL <http://ieeexplore.ieee.org/document/6518413/>.
- [3] Timilehin Labeodan, Christel De Bakker, Alexander Rosemann, and Wim Zeiler. On the application of wireless sensors and actuators network in existing buildings for occupancy detection and occupancy-driven lighting control. *Energy and Buildings*, 127:75–83, September 2016. ISSN 03787788. doi: 10.1016/j.enbuild.2016.05.077. URL <http://linkinghub.elsevier.com/retrieve/pii/S0378778816304558>.
- [4] Jen King. Smart Buildings: Using Smart Technology to Save Energy in Existing Buildings. *SMART BUILDINGS*, page 55.
- [5] Huidong Li, Chuan Tian, and Z. Daniel Deng. Energy harvesting from low frequency applications using piezoelectric materials. *Applied Physics Reviews*, 1(4): 041301, December 2014. ISSN 1931-9401. doi: 10.1063/1.4900845. URL <http://aip.scitation.org/doi/10.1063/1.4900845>.
- [6] Heung Soo Kim, Joo-Hyong Kim, and Jaehwan Kim. A review of piezoelectric energy harvesting based on vibration. *International Journal of Precision Engineering and Manufacturing*, 12(6):1129–1141, December 2011. ISSN 1229-8557, 2005-4602. doi: 10.1007/s12541-011-0151-3. URL <http://link.springer.com/10.1007/s12541-011-0151-3>.
- [7] Steven R Anton and Henry A Sodano. A review of power harvesting using piezoelectric materials (2003–2006). *Smart Materials and Structures*, 16(3): R1–R21, June 2007. ISSN 0964-1726, 1361-665X. doi: 10.1088/0964-1726/16/3/R01. URL <http://stacks.iop.org/0964-1726/16/i=3/a=R01?key=crossref.2c5609f4e60f2ce4b89d0db98aedfe93>.
- [8] Shad Roundy, Paul Kenneth Wright, and Jan M. Rabaey. *Energy Scavenging for Wireless Sensor Networks*. Springer US, Boston, MA, 2004. ISBN 978-1-4613-5100-9 978-1-4615-0485-6. doi: 10.1007/978-1-4615-0485-6. URL <http://link.springer.com/10.1007/978-1-4615-0485-6>.
- [9] Kris Lokere. Product How-to: Precise wireless temperature sensor powers itself. page 9.

- [10] Energy Harvesting Wireless Products in 868 MHz for Europe | EnOcean - Products, . URL [https://www.enocean.com/en/enocean\\_modules/stm-330/](https://www.enocean.com/en/enocean_modules/stm-330/).
- [11] Monnit Wireless Temperature Sensor - Commercial Coin Cell Powered | MNS-9-W1-TS-ST, . URL <https://www.monnit.com/Products/Wireless-Sensors/Coin-Cell/Wireless-Temperature-Sensors>.
- [12] Sun Labs. Sun™ Small Programmable Object Technology (Sun SPOT) Theory of Operation. page 32.
- [13] Memsic news, . URL <http://www.memsic.com/about-memsic/news-room.cfm?nid=MEMSIC%20Introduces%20LOTUS%20%E2%80%93%20Next%20Generation%20Mote%20Platform%20for%20High%20Performance%20Wireless%20Sensor%20Networks&newsyear=2011>.
- [14] MTM-CM5000-MSP 802.15.4 TelosB mote Module | IoT Hardware Platforms, . URL <https://www.advanticsys.com/shop/mtmcm5000msp-p-14.html>.
- [15] Nurul Amirah Ali, Micheal Drieberg, and Patrick Sebastian. Deployment of MICAz mote for Wireless Sensor Network applications. pages 303–308. IEEE, December 2011. ISBN 978-1-4577-2059-8 978-1-4577-2058-1 978-1-4577-2057-4. doi: 10.1109/ICCAIE.2011.6162150. URL <http://ieeexplore.ieee.org/document/6162150/>.
- [16] Wenhua Zuo, Ruizhi Li, Cheng Zhou, Yuanyuan Li, Jianlong Xia, and Jinping Liu. Battery-Supercapacitor Hybrid Devices: Recent Progress and Future Prospects. *Advanced Science*, 4(7):1600539, July 2017. ISSN 21983844. doi: 10.1002/advs.201600539. URL <http://doi.wiley.com/10.1002/advs.201600539>.
- [17] A.W. Avent and C.R. Bowen. Principles of thermoacoustic energy harvesting. *The European Physical Journal Special Topics*, 224(14-15):2967–2992, November 2015. ISSN 1951-6355, 1951-6401. doi: 10.1140/epjst/e2015-02601-x. URL <http://link.springer.com/10.1140/epjst/e2015-02601-x>.
- [18] Mohammad Amin Askari Farsangi, Francesco Cottone, Hassan Sayyaadi, Mohammad Reza Zakerzadeh, Francesco Orfei, and Luca Gammaitoni. Energy harvesting from structural vibrations of magnetic shape memory alloys. *Applied Physics Letters*, 110(10):103905, March 2017. ISSN 0003-6951, 1077-3118. doi: 10.1063/1.4978258. URL <http://aip.scitation.org/doi/10.1063/1.4978258>.
- [19] E. Trioux, S. Monfray, and S. Basrou. Butterfly micro bilayer thermal energy harvester geometry with improved performances. *Journal of Physics: Conference Series*, 773:012094, November 2016. ISSN 1742-6588, 1742-6596. doi: 10.1088/1742-6596/773/1/012094. URL <http://stacks.iop.org/1742-6596/773/i=1/a=012094?key=crossref.f27a64f030cac3d6af2bc6d6ff9e4c07>.
- [20] O. Puscasu, S. Monfray, C. Maître, P.J. Cottinet, D. Rapisarda, G. Savelli, F. Gaillard, G. Ricotti, P. Ancey, F. Boeuf, D. Guyomar, and T. Skotnicki. A disruptive technology for thermal to electrical energy conversion. *Microelectronics Journal*, 45(5):554–558, May 2014. ISSN 00262692. doi: 10.1016/j.mejo.2013.12.003. URL <http://linkinghub.elsevier.com/retrieve/pii/S0026269213003066>.

- [21] Morgan Almanza, Alexandre Pasko, Frédéric Mazaleyrat, and Martino LoBue. Numerical study of thermomagnetic cycle. *Journal of Magnetism and Magnetic Materials*, 426:64–69, 2017.
- [22] M. Gueltig, H. Ossmer, M. Ohtsuka, H. Miki, K. Tsuchiya, T. Takagi, and M. Kohl. Thermomagnetic Actuation by Low Hysteresis Metamagnetic Ni-Co-Mn-In Films. *Materials Today: Proceedings*, 2:S883–S886, 2015. ISSN 22147853. doi: 10.1016/j.matpr.2015.07.423. URL <http://linkinghub.elsevier.com/retrieve/pii/S2214785315006689>.
- [23] L. Carlioz, J. Delamare, and S. Basrour. Temperature threshold tuning of a thermal harvesting switch. In *Solid-State Sensors, Actuators and Microsystems Conference, 2009. TRANSDUCERS 2009. International*, pages 1385–1388. IEEE, 2009.
- [24] Louis Carlioz. *Générateur piézoélectrique à déclenchement thermo-magnétique*. PhD Thesis, Institut National Polytechnique de Grenoble-INPG, 2009.
- [25] Jinsung Chun, Hyun-Cheol Song, Min-Gyu Kang, Han Byul Kang, Ravi Anant Kishore, and Shashank Priya. Thermo-Magneto-Electric Generator Arrays for Active Heat Recovery System. *Scientific Reports*, 7:41383, February 2017. ISSN 2045-2322. doi: 10.1038/srep41383. URL <http://www.nature.com/articles/srep41383>.
- [26] J. M. Rabaey, M. J. Ammer, J. L. da Silva, D. Patel, and S. Roundy. PicoRadio supports ad hoc ultra-low power wireless networking. *Computer*, 33(7):42–48, July 2000. ISSN 0018-9162. doi: 10.1109/2.869369.
- [27] Aneta Prijic, Ljubomir Vracar, Dusan Vuckovic, Dejan Milic, and Zoran Prijic. Thermal Energy Harvesting Wireless Sensor Node in Aluminum Core PCB Technology. *IEEE Sensors Journal*, 15(1):337–345, January 2015. ISSN 1530-437X, 1558-1748, 2379-9153. doi: 10.1109/JSEN.2014.2343932. URL <http://ieeexplore.ieee.org/document/6867292/>.
- [28] Hubregt J. Visser, Adrianus C. F. Reniers, and Jeroen A. C. Theeuwes. Ambient RF Energy Scavenging: GSM and WLAN Power Density Measurements. pages 721–724. IEEE, October 2008. ISBN 978-2-87487-006-4. doi: 10.1109/EUMC.2008.4751554. URL <http://ieeexplore.ieee.org/document/4751554/>.
- [29] Suna Ju and Chang-Hyeon Ji. Impact-based piezoelectric vibration energy harvester. *Applied Energy*, 214:139–151, March 2018. ISSN 03062619. doi: 10.1016/j.apenergy.2018.01.076. URL <http://linkinghub.elsevier.com/retrieve/pii/S0306261918300904>.
- [30] Y. Houdas and E. F. J. Ring. *Human Body Temperature*. Springer US, Boston, MA, 1982. ISBN 978-1-4899-0347-1 978-1-4899-0345-7. doi: 10.1007/978-1-4899-0345-7. URL <http://link.springer.com/10.1007/978-1-4899-0345-7>.
- [31] Yen Kheng Tan. *Energy harvesting autonomous sensor systems: design, analysis, and practical implementation*. CRC Press, 2013.
- [32] Greg P. Carman, Kyle Wetzlar, Ray Hsu, and Sam Sandoval. Energy Harvesting A Nano-Scale Based Magnetothermal-Electric Element. Technical report, CALIFORNIA UNIV LOS ANGELES, 2015.

- [33] Ian Salmon McKay and Evelyn N. Wang. Thermal pulse energy harvesting. *Energy*, 57:632–640, August 2013. ISSN 03605442. doi: 10.1016/j.energy.2013.05.045. URL <http://linkinghub.elsevier.com/retrieve/pii/S0360544213004635>.
- [34] Ling Bing Kong, Tao Li, Huey Hoon Hng, Freddy Boey, Tianshu Zhang, and Sean Li. *Waste Energy Harvesting*, volume 24 of *Lecture Notes in Energy*. Springer Berlin Heidelberg, Berlin, Heidelberg, 2014. ISBN 978-3-642-54633-4 978-3-642-54634-1. doi: 10.1007/978-3-642-54634-1. URL <http://link.springer.com/10.1007/978-3-642-54634-1>.
- [35] James P. Thomas, Muhammad A. Qidwai, and James C. Kellogg. Energy scavenging for small-scale unmanned systems. *Journal of Power Sources*, 159(2):1494–1509, September 2006. ISSN 03787753. doi: 10.1016/j.jpowsour.2005.12.084. URL <http://linkinghub.elsevier.com/retrieve/pii/S0378775306001121>.
- [36] Elena Blokhina, Abdelali El Aroudi, Eduard Alarcon, and Dimitri Galayko, editors. *Nonlinearity in Energy Harvesting Systems*. Springer International Publishing, Cham, 2016. ISBN 978-3-319-20354-6 978-3-319-20355-3. doi: 10.1007/978-3-319-20355-3. URL <http://link.springer.com/10.1007/978-3-319-20355-3>.
- [37] C B Williams and R B Yates. Analysis of a micro-electric generator for microsystems. page 4.
- [38] Xihai Zhang, Jiali Du, Chengguo Fan, Dong Liu, Junlong Fang, and Lingshu Wang. A Wireless Sensor Monitoring Node Based on Automatic Tracking Solar-Powered Panel for Paddy Field Environment. *IEEE Internet of Things Journal*, 4(5):1304–1311, October 2017. ISSN 2327-4662. doi: 10.1109/JIOT.2017.2706418. URL <http://ieeexplore.ieee.org/document/7932071/>.
- [39] Christoph J. Brabec. Organic photovoltaics: technology and market. *Solar Energy Materials and Solar Cells*, 83(2-3):273–292, June 2004. ISSN 09270248. doi: 10.1016/j.solmat.2004.02.030. URL <http://linkinghub.elsevier.com/retrieve/pii/S092702480400100X>.
- [40] Jose Luz Silveira, Celso Eduardo Tuna, and Wendell de Queiroz Lamas. The need of subsidy for the implementation of photovoltaic solar energy as supporting of decentralized electrical power generation in Brazil. *Renewable and Sustainable Energy Reviews*, 20:133–141, April 2013. ISSN 13640321. doi: 10.1016/j.rser.2012.11.054. URL <http://linkinghub.elsevier.com/retrieve/pii/S1364032112006685>.
- [41] Priscila Gonçalves Vasconcelos Sampaio and Mario Orestes Aguirre González. Photovoltaic solar energy: Conceptual framework. *Renewable and Sustainable Energy Reviews*, 74:590–601, July 2017. ISSN 13640321. doi: 10.1016/j.rser.2017.02.081. URL <http://linkinghub.elsevier.com/retrieve/pii/S1364032117303076>.
- [42] Björn Sothmann, Rafael Sánchez, and Andrew N Jordan. Thermoelectric energy harvesting with quantum dots. *Nanotechnology*, 26(3):032001, January 2015. ISSN 0957-4484, 1361-6528. doi: 10.1088/0957-4484/26/3/032001. URL <http://stacks.iop.org/0957-4484/26/i=3/a=032001?key=crossref.dee5f1264e691b92bad78293e1d324af>.

- [43] Ming-Zhi Yang, Chyan-Chyi Wu, Ching-Liang Dai, and Wen-Jung Tsai. Energy Harvesting Thermoelectric Generators Manufactured Using the Complementary Metal Oxide Semiconductor Process. *Sensors*, 13(2):2359–2367, February 2013. ISSN 1424-8220. doi: 10.3390/s130202359. URL <http://www.mdpi.com/1424-8220/13/2/2359/>.
- [44] A. Cuadras, M. Gasulla, and V. Ferrari. Thermal energy harvesting through pyroelectricity. *Sensors and Actuators A: Physical*, 158(1):132–139, March 2010. ISSN 09244247. doi: 10.1016/j.sna.2009.12.018. URL <http://linkinghub.elsevier.com/retrieve/pii/S0924424709005445>.
- [45] Harrison Hoon Seok Chang and Zhaorong Huang. Laminate composites with enhanced pyroelectric effects for energy harvesting. *Smart Materials and Structures*, 19(6):065018, 2010.
- [46] Kamarul Aizat Abdul Khalid, Thye Jien Leong, and Khairudin Mohamed. Review on Thermionic Energy Converters. *IEEE Transactions on Electron Devices*, 63(6):2231–2241, June 2016. ISSN 0018-9383, 1557-9646. doi: 10.1109/TED.2016.2556751. URL <http://ieeexplore.ieee.org/document/7463074/>.
- [47] Applications of JTEC, . URL <http://johnsonems.com/our-technology/applications/>.
- [48] David M. Bierman, Andrej Lenert, Walker R. Chan, Bikram Bhatia, Ivan Celanović, Marin Soljačić, and Evelyn N. Wang. Enhanced photovoltaic energy conversion using thermally based spectral shaping. *Nature Energy*, 1(6):16068, May 2016. ISSN 2058-7546. doi: 10.1038/nenergy.2016.68. URL <http://www.nature.com/articles/nenergy201668>.
- [49] Shishir Pandya, Joshua Wilbur, Jieun Kim, Ran Gao, Arvind Dasgupta, Chris Dames, and Lane W. Martin. Pyroelectric energy conversion with large energy and power density in relaxor ferroelectric thin films. *Nature Materials*, 17(5):432–438, May 2018. ISSN 1476-1122, 1476-4660. doi: 10.1038/s41563-018-0059-8. URL <http://www.nature.com/articles/s41563-018-0059-8>.
- [50] D. Zabek, J. Taylor, V. Ayel, Y. Bertin, C. Romestant, and C. R. Bowen. A novel pyroelectric generator utilising naturally driven temperature fluctuations from oscillating heat pipes for waste heat recovery and thermal energy harvesting. *Journal of Applied Physics*, 120(2):024505, July 2016. ISSN 0021-8979, 1089-7550. doi: 10.1063/1.4958338. URL <http://aip.scitation.org/doi/10.1063/1.4958338>.
- [51] Shashank Priya and Daniel J. Inman, editors. *Energy Harvesting Technologies*. Springer US, Boston, MA, 2009. ISBN 978-0-387-76463-4 978-0-387-76464-1. doi: 10.1007/978-0-387-76464-1. URL <http://link.springer.com/10.1007/978-0-387-76464-1>.
- [52] Santosh Kulkarni, Elena Koukharenko, Russell Torah, John Tudor, Steve Beeby, Terence O’Donnell, and Saibal Roy. Design, fabrication and test of integrated micro-scale vibration-based electromagnetic generator. *Sensors and Actuators A: Physical*, 145-146:336–342, July 2008. ISSN 09244247. doi: 10.1016/j.sna.2007.09.014. URL <http://linkinghub.elsevier.com/retrieve/pii/S0924424707006991>.

- [53] S P Beeby, R N Torah, M J Tudor, P Glynne-Jones, T O'Donnell, C R Saha, and S Roy. A micro electromagnetic generator for vibration energy harvesting. *Journal of Micromechanics and Microengineering*, 17(7):1257–1265, July 2007. ISSN 0960-1317, 1361-6439. doi: 10.1088/0960-1317/17/7/007. URL <http://stacks.iop.org/0960-1317/17/i=7/a=007?key=crossref.5d7c04072bd76fa6cefe33d201542bc1>.
- [54] A Erturk and D J Inman. An experimentally validated bimorph cantilever model for piezoelectric energy harvesting from base excitations. *Smart Materials and Structures*, 18(2):025009, February 2009. ISSN 0964-1726, 1361-665X. doi: 10.1088/0964-1726/18/2/025009. URL <http://stacks.iop.org/0964-1726/18/i=2/a=025009?key=crossref.cda51e54de24aaa048d7a3018d369082>.
- [55] Christopher R. Bowen, Vitaly Yu. Topolov, and Hyunsun Alicia Kim. *Modern Piezoelectric Energy-Harvesting Materials*, volume 238 of *Springer Series in Materials Science*. Springer International Publishing, Cham, 2016. ISBN 978-3-319-29141-3 978-3-319-29143-7. doi: 10.1007/978-3-319-29143-7. URL <http://link.springer.com/10.1007/978-3-319-29143-7>.
- [56] Marcin Marzencki, Yasser Ammar, and Skandar Basrour. Integrated power harvesting system including a MEMS generator and a power management circuit. *Sensors and Actuators A: Physical*, 145-146:363–370, July 2008. ISSN 09244247. doi: 10.1016/j.sna.2007.10.073. URL <http://linkinghub.elsevier.com/retrieve/pii/S0924424707008047>.
- [57] S. Basrour, B. Charlot, M. Marzencki, A. Grasso, M. Colin, and L. Valbin. Design and fabrication of piezoelectric micro power generators for autonomous microsystems. pages 299–302. TIMA, 2005. URL <https://hal.archives-ouvertes.fr/hal-00009215>.
- [58] Marzencki et al. - 2008 - Design, Fabrication and Characterization of a Piez.pdf. Lausanne, 2002. EPFL, Swiss Federal Institute of Technology. ISBN 978-2-9700346-0-5. OCLC: 248494715.
- [59] Maisam Wahbah, Mohammad Alhawari, Baker Mohammad, Hani Saleh, and Mohammed Ismail. Characterization of Human Body-Based Thermal and Vibration Energy Harvesting for Wearable Devices. *IEEE Journal on Emerging and Selected Topics in Circuits and Systems*, 4(3):354–363, September 2014. ISSN 2156-3357, 2156-3365. doi: 10.1109/JETCAS.2014.2337195. URL <http://ieeexplore.ieee.org/document/6866930/>.
- [60] D.M. Rowe and Gao Min. Evaluation of thermoelectric modules for power generation. *Journal of Power Sources*, 73(2):193–198, June 1998. ISSN 03787753. doi: 10.1016/S0378-7753(97)02801-2. URL <http://linkinghub.elsevier.com/retrieve/pii/S0378775397028012>.
- [61] A Hadni. Applications of the pyroelectric effect. *Journal of Physics E: Scientific Instruments*, 14(11):1233–1240, November 1981. ISSN 0022-3735. doi: 10.1088/0022-3735/14/11/002. URL <http://stacks.iop.org/0022-3735/14/i=11/a=002?key=crossref.f56c5e1bf58113b9c1322f75c4ee651c>.

- [62] An-Shen Siao, Ching-Kong Chao, and Chun-Ching Hsiao. Study on Pyroelectric Harvesters with Various Geometry. *Sensors*, 15(8):19633–19648, August 2015. ISSN 1424-8220. doi: 10.3390/s150819633. URL <http://www.mdpi.com/1424-8220/15/8/19633>.
- [63] M. Nouh, O. Aldraihem, and A. Baz. Energy Harvesting of Thermoacoustic-Piezo Systems With a Dynamic Magnifier. *Journal of Vibration and Acoustics*, 134(6):061015, October 2012. ISSN 0739-3717. doi: 10.1115/1.4005834. URL <http://vibrationacoustics.asmedigitalcollection.asme.org/article.aspx?doi=10.1115/1.4005834>.
- [64] R Hernandez, S Jung, and K I Matveev. Acoustic energy harvesting from vortex-induced tonal sound in a baffled pipe. *Proceedings of the Institution of Mechanical Engineers, Part C: Journal of Mechanical Engineering Science*, 225(8):1847–1850, August 2011. ISSN 0954-4062, 2041-2983. doi: 10.1177/0954406211406017. URL <http://journals.sagepub.com/doi/10.1177/0954406211406017>.
- [65] Marcel Gueltig, Hinnerk Ossmer, Makoto Ohtsuka, Hiroyuki Miki, Koki Tsuchiya, Toshiyuki Takagi, and Manfred Kohl. High Frequency Thermal Energy Harvesting Using Magnetic Shape Memory Films. *Advanced Energy Materials*, 4(17):1400751, December 2014. ISSN 16146832. doi: 10.1002/aenm.201400751. URL <http://doi.wiley.com/10.1002/aenm.201400751>.
- [66] Dragan Avirovik, Ravi A. Kishore, Dushan Vuckovic, and Shashank Priya. Miniature Shape Memory Alloy Heat Engine for Powering Wireless Sensor Nodes. *Energy Harvesting and Systems*, 1(1-2), January 2014. ISSN 2329-8774, 2329-8766. doi: 10.1515/ehs-2013-0003. URL <https://www.degruyter.com/view/j/ehs.2014.1.issue-1-2/ehs-2013-0003/ehs-2013-0003.xml>.
- [67] E Trioux, S Monfray, and S Basrour. Micro thermal energy harvester design optimization. *Journal of Micromechanics and Microengineering*, 27(11):114001, November 2017. ISSN 0960-1317, 1361-6439. doi: 10.1088/1361-6439/aa7dfe. URL <http://stacks.iop.org/0960-1317/27/i=11/a=114001?key=crossref.41fc6dedbe52f3fc56393ce113aec2a7>.
- [68] M. Ujihara, G. P. Carman, and D. G. Lee. Thermal energy harvesting device using ferromagnetic materials. *Applied Physics Letters*, 91(9):093508, August 2007. ISSN 0003-6951, 1077-3118. doi: 10.1063/1.2775096. URL <http://aip.scitation.org/doi/10.1063/1.2775096>.
- [69] Louis Carlioz, Jerome Delamare, Skandar Basrour, and Orphee Cugat. Energy scavenging using hybrid thermo-magnetic / PZT structure. *Journal of Magnetism and Magnetic Materials*, page 3, 2008.
- [70] Katherine E. Bulgrin, Y. Sungtaek Ju, Greg P. Carman, and Adrienne S. Lavine. An investigation of a tunable magnetomechanical thermal switch. *Journal of Heat Transfer*, 133(10):101401, 2011.
- [71] Alexander Post, Chris Knight, and Erich Kisi. Thermomagnetic energy harvesting with first order phase change materials. *Journal of Applied Physics*, 114(3):033915, July 2013. ISSN 0021-8979, 1089-7550. doi: 10.1063/1.4815933. URL <http://aip.scitation.org/doi/10.1063/1.4815933>.

- [72] C. R. Bowen, J. Taylor, E. LeBoulbar, D. Zabek, A. Chauhan, and R. Vaish. Pyroelectric materials and devices for energy harvesting applications. *Energy Environ. Sci.*, 7(12): 3836–3856, 2014. ISSN 1754-5692, 1754-5706. doi: 10.1039/C4EE01759E. URL <http://xlink.rsc.org/?DOI=C4EE01759E>.
- [73] Chin-Chung Chen, Tien-Kan Chung, Chia-Yuan Tseng, Chiao-Fang Hung, Po-Chen Yeh, and Chih-Cheng Cheng. A Miniature Magnetic-Piezoelectric Thermal Energy Harvester. *IEEE Transactions on Magnetics*, 51(7):1–9, July 2015. ISSN 0018-9464, 1941-0069. doi: 10.1109/TMAG.2015.2395385. URL <http://ieeexplore.ieee.org/document/7017505/>.
- [74] O. Puscasu, S. Monfray, J. Boughaleb, P.J. Cottinet, D. Rapisarda, E. Rouvière, G. Delepierre, G.Pitone, C. Maître, F. Boeuf, D. Guyomar, and T. Skotnicki. Flexible bimetal and piezoelectric based thermal to electrical energy converters. *Sensors and Actuators A: Physical*, 214:7–14, August 2014. ISSN 09244247. doi: 10.1016/j.sna.2014.03.027. URL <http://linkinghub.elsevier.com/retrieve/pii/S0924424714001526>.
- [75] Chin-Chung Chen, Tien-Kan Chung, Chi-Cheng Cheng, and Chia-Yuan Tseng. A novel miniature thermomagnetic energy harvester. page 90570X, March 2014. doi: 10.1117/12.2045294. URL <http://proceedings.spiedigitallibrary.org/proceeding.aspx?doi=10.1117/12.2045294>.
- [76] Tien-Kan Chung, Ujjwal Shukla, Chia-Yuan Tseng, Chin-Chung Chen, and Chieh-Min Wang. A magnetic/piezoelectric-based thermal energy harvester. page 86880M, April 2013. doi: 10.1117/12.2009434. URL <http://proceedings.spiedigitallibrary.org/proceeding.aspx?doi=10.1117/12.2009434>.
- [77] T. Huesgen, J. Ruhhammer, G. Biancuzzi, and P. Woias. Detailed study of a micro heat engine for thermal energy harvesting. *Journal of micromechanics and microengineering*, 20(10):104004, 2010.
- [78] Katherine E. Bulgrin, Y. Sungtaek Ju, Greg P. Carman, and Adrienne S. Lavine. A coupled thermal and mechanical model of a thermal energy harvesting device. In *ASME 2009 International Mechanical Engineering Congress & Exposition. Lake Buena Vista, FL*, pages 327–335, 2009.
- [79] Samuel J. Rosenberg. Nickel and its alloys. Technical report, NATIONAL BUREAU OF STANDARDS GAITHERSBURG MD, 1968.
- [80] Oualid Messal. *Caractérisation et modélisation du comportement thermomagnétique d'alliages FeNi pour le prototypage virtuel*. PhD Thesis, Université Claude Bernard-Lyon I, 2013.
- [81] W S N TRIMMER. MICROROBOTS AND MICROMECHANICAL SYSTEMS. page 21.
- [82] Disques magnétiques en néodyme : des condensés de puissance, . URL <https://www.supermagnete.fr/aimants-disques-neodyme-petits?length-or-diameter=1.00,5.00>.
- [83] Edward P. Furlani. *Permanent magnet and electromechanical devices: materials, analysis, and applications*. Academic press, 2001.

- [84] A. Raghunathan, Y. Melikhov, J. E. Snyder, and D. C. Jiles. Theoretical Model of Temperature Dependence of Hysteresis Based on Mean Field Theory. *IEEE Transactions on Magnetics*, 46(6):1507–1510, June 2010. ISSN 0018-9464. doi: 10.1109/TMAG.2010.2045351. URL <http://ieeexplore.ieee.org/document/5467478/>.
- [85] Diana Mavrudieva, Jean-Yves Voyant, Afef Kedous-Lebouc, and Jean-Paul Yonnet. Magnetic structures for contactless temperature sensor. *Sensors and Actuators A: Physical*, 142(2):464–467, April 2008. ISSN 0924-4247. doi: 10.1016/j.sna.2007.06.015. URL <http://www.sciencedirect.com/science/article/pii/S0924424707004591>.
- [86] Aperam - Alloys - Imphy, . URL <http://www.aperam.com/alloys-imphy/telechargement/fiches-techniques/>.
- [87] Marco P. Soares dos Santos, Jorge A. F. Ferreira, José A. O. Simões, Ricardo Pascoal, João Torrão, Xiaozheng Xue, and Edward P. Furlani. Magnetic levitation-based electromagnetic energy harvesting: a semi-analytical non-linear model for energy transduction. *Scientific Reports*, 6(1), May 2016. ISSN 2045-2322. doi: 10.1038/srep18579. URL <http://www.nature.com/articles/srep18579>.
- [88] J. G. Korvink and Oliver Paul, editors. *MEMS: a practical guide to design, analysis, and applications*. W. Andrew Pub. ; Springer, Norwich, NY : Heidelberg, Germany, 2006. ISBN 978-0-8155-1497-8 978-3-540-21117-4. OCLC: ocm61362695.
- [89] D. Guyomar and A. Badel. Nonlinear semi-passive multimodal vibration damping: An efficient probabilistic approach. *Journal of Sound and Vibration*, 294(1-2): 249–268, June 2006. ISSN 0022460X. doi: 10.1016/j.jsv.2005.11.010. URL <http://linkinghub.elsevier.com/retrieve/pii/S0022460X05007224>.
- [90] Roderic S Lakes. *Viscoelastic materials*. Cambridge University Press, Cambridge; New York, 2009. ISBN 978-0-511-57995-0 978-0-511-65052-9 978-0-511-57921-9 978-0-511-62672-2 978-0-511-57847-2. URL <http://public.eblib.com/choice/publicfullrecord.aspx?p=451997>. OCLC: 642690021.
- [91] David Jiles. *Introduction to magnetism and magnetic materials*. Chapman & Hall, London, repr edition, 1996. ISBN 978-0-412-38640-4 978-0-412-38630-5.
- [92] Bernard Dennis Cullity and Chad D. Graham. *Introduction to magnetic materials*. IEEE Press, Piscataway, NJ, 2. ed edition, 2009. ISBN 978-0-471-47741-9. OCLC: 255009181.
- [93] Shad Roundy, Eli S. Leland, Jessy Baker, Eric Carleton, Elizabeth Reilly, Elaine Lai, Brian Otis, Jan M. Rabaey, Paul K. Wright, and V. Sundararajan. Improving power output for vibration-based energy scavengers. *IEEE Pervasive computing*, 4(1):28–36, 2005.
- [94] Herbert W. Behlow, Deepika Saini, Bevan Elliott, Steven. M. Serkiz, Malcolm. J. Skove, and A. M. Rao. Ringdown sensing method. pages 456–459. IEEE, August 2014. ISBN 978-1-4799-5622-7. doi: 10.1109/NANO.2014.6968178. URL <http://ieeexplore.ieee.org/document/6968178/>.

- 
- [95] Piezo Systems: Piezoceramic, PZT, Piezoelectric Transducers, Piezoelectric Actuators and Sensors, Piezoelectric Fans, Piezoelectric Amplifiers, Piezoelectric Engineering, Ultrasonic Transducers, and Energy Harvesters, . URL <http://piezo.com/>.
- [96] S Roundy and P K Wright. A piezoelectric vibration based generator for wireless electronics. *Smart Materials and Structures*, 13(5):1131–1142, October 2004. ISSN 0964-1726, 1361-665X. doi: 10.1088/0964-1726/13/5/018. URL <http://stacks.iop.org/0964-1726/13/i=5/a=018?key=crossref.8cb539ef2c04efdc61df2fae9dc8e48c>.
- [97] R. Dahiya, M. Valle, and L. Lorenzelli. SPICE model for lossy piezoelectric polymers. *IEEE Transactions on Ultrasonics, Ferroelectrics and Frequency Control*, 56(2): 387–395, February 2009. ISSN 0885-3010. doi: 10.1109/TUFFC.2009.1048. URL <http://ieeexplore.ieee.org/document/4787191/>.
- [98] Ping Li, Yumei Wen, Pangang Liu, Xinshen Li, and Chaobo Jia. A magnetoelectric energy harvester and management circuit for wireless sensor network. *Sensors and Actuators A: Physical*, 157(1):100–106, January 2010. ISSN 09244247. doi: 10.1016/j.sna.2009.11.007. URL <http://linkinghub.elsevier.com/retrieve/pii/S0924424709004798>.
- [99] A. Tabesh and L.G. Frechette. A Low-Power Stand-Alone Adaptive Circuit for Harvesting Energy From a Piezoelectric Micropower Generator. *IEEE Transactions on Industrial Electronics*, 57(3):840–849, March 2010. ISSN 0278-0046. doi: 10.1109/TIE.2009.2037648. URL <http://ieeexplore.ieee.org/document/5345727/>.
- [100] IEEE Standard on Piezoelectricity. *ANSI/IEEE Std 176-1987*, pages 0\_1–, 1988. doi: 10.1109/IEEESTD.1988.79638.

# List of publications

## International conferences

1. Adrian A. Rendon-Hernandez, Marco Ferrari, Skandar Basrour, and Vittorio Ferrari “**Electrical modeling and characterization of a Thermo-Magnetically Activated Piezoelectric Generator (TMAPG)**”, accepted for PowerMEMS Daytona Beach, USA, Journal of Physics: Conference Series, (2018).
2. Adrian A. Rendon-Hernandez, Skandar Basrour, “**On the design guidelines for miniaturizing thermo-magnetically activated piezoelectric energy generator**”, in Proc. PowerMEMS Kanazawa, Japan, Journal of Physics: Conference Series, vol. 1052, 012053, (2017), [doi: 10.1088/1742-6596/1052/1/012053](https://doi.org/10.1088/1742-6596/1052/1/012053).
3. Adrian A. Rendon-Hernandez, Skandar Basrour, “**Coupled multiphysics finite element model and experimental testing of a thermo-magnetically triggered piezoelectric generator**”, in Proc. PowerMEMS Paris, France, Journal of Physics: Conference Series, vol. 773, 012024, (2016), [doi: 10.1088/1742-6596/773/1/012024](https://doi.org/10.1088/1742-6596/773/1/012024).

## National conferences

1. Adrian A. Rendon-Hernandez, Skandar Basrour, “**A PSpice model of a thermomagnetically triggered piezoelectric generator**”, 8ème Journées Nationales sur la Récupération et le Stockage d’Énergie, Besançon, France, (2018), [Poster presentation](#).
2. Adrian A. Rendon-Hernandez, Skandar Basrour, “**Modeling and operating temperature tuning of a thermally activated piezoelectric generator**”, 7ème Journées Nationales sur la Récupération et le Stockage d’Énergie, Lyon, France, (2017), [best paper and presentation award](#).
3. Adrian A. Rendon-Hernandez, Skandar Basrour, “**Desing and optimization of a thermomagnetically triggered piezoelectric generator**”, 6ème Journées Nationales sur la Récupération et le Stockage d’Energie, Bordeaux, France, (2016), [poster presentation](#).
4. Adrian A. Rendon-Hernandez, Skandar Basrour, “**Conception et optimisation d’un microgénérateur piézoélectrique à déclenchement thermomagnétique pour des capteurs autonomes**”, 19ème Journées Nationales du Réseau Doctoral en Micro et Nano Electronique, Toulouse, France, (2016), [oral presentation](#).
5. Adrian A. Rendon-Hernandez, Skandar Basrour, “**Study of a piezoelectric microgenerator thermo-magnetically triggered**”, Journées Nationales sur la Récupération et le Stockage d’Energie, Orsay, France, (2015), [poster presentation](#), pp. 59-60.



# Résumé en français

*Cette section présente un résumé en français par chapitre du manuscrit de ma thèse. Cette étude se positionne dans le cadre général du développement de dispositifs pour la récupération d'énergie afin de satisfaire en énergie des réseaux de capteurs. Ces travaux se focalisent sur la récupération d'énergie thermique basse échelle, et plus particulièrement sur l'énergie disponible à partir de variations lentes de la température afin de répondre à la demande actuelle d'énergie nomade, toute en adressant les problèmes des systèmes de conversion conventionnels de l'énergie thermique (forte conductivité thermique des éléments thermoélectriques) limitant leurs capacités de récupération. Dans ce manuscrit, je me propose de répondre à cet objectifs ambitieux par l'étude, la modélisation et la réalisation de prototypes de récupération d'énergie par une méthode indirecte.*

Ce manuscrit est organisé en sept chapitres. Dans le premier chapitre, une introduction générale sur des dispositifs récupérant l'énergie ambiante est présentée, avec une étude sur la consommation énergétique des systèmes communicants. La justification de ce travail ainsi que sa motivation principale sont également énoncés.

Le deuxième chapitre décrit les principales techniques de récupération d'énergie ainsi que les mécanismes impliqués dans les différents types de transduction. Des méthodes directes et indirectes de conversion d'énergie thermique en électricité sont énoncées. Nous nous focalisons principalement sur des dispositifs de récupération d'énergie thermique à basse échelle.

Le troisième chapitre présente la modélisation du générateur proposé avec une étude montrant la simplification du système. Cette simplification proposée tient compte des sous-systèmes impliqués, par exemple la modélisation thermo-magnétique, la modélisation du couplage électro-mécanique et la modélisation du comportement dynamique du générateur. Des règles de conception du générateur vers sa miniaturisation sont également présentées.

Le quatrième chapitre porte sur la modélisation par éléments finis du générateur. Une approche en 3D est adoptée afin de mieux comprendre le comportement global du dispositif.

Le cinquième chapitre montre une étude expérimentale des prototypes du générateur. Une comparaison des résultats du fonctionnement de ces prototypes confirme les informations sur les règles de miniaturisation du générateur. Des prototypes d'une seconde génération de générateur sont présentés. Le but est de corroborer la possibilité de faire descendre les températures d'opération du dispositif, c'est-à-dire la température d'ouverture et celle de fermeture.

Le sixième chapitre décrit une étude sur l'optimisation de la conception du générateur. Dans un premier temps, le sous-système transducteur du générateur, c'est-à-dire le bimorphe piézoélectrique est considéré. Une force constante est considéré en bout de poutre comme paramètre d'entrée du système. Dans un second temps, l'inclusion de la dépendance thermique de l'aimantation du matériaux magnétique doux au modèle simplifié du générateur, permet de considérer des changements de température comme le signal d'entrée, ce qui rend possible l'inclusion d'autres paramètres de conception, tel est le cas de l'entrefer entre l'aimant permanent et l'alliage thermo-magnétique.

Le septième chapitre présente une conclusion générale résumant tous les résultats importants obtenus durant cette étude ainsi que les pistes d'amélioration et de continuation de ce projet. Une liste de contributions de ce travail est aussi énoncée.

## Chapitre 1 : Introduction

La récupération d'énergie est souvent définie comme l'action de tirer profit de l'énergie présente dans notre environnement proche et de la convertir en énergie électrique. Ces systèmes sont conçus pour alimenter de petits dispositifs avec une consommation faible de puissance de manière à le rendre autonome d'un point de vue énergétique.

Des réseaux de dispositifs communicants peuvent être utilisés pour surveiller des machines électriques afin de détecter des pannes [1], pour surveiller des signaux médicaux (ECG) [2], dans des systèmes de contrôle du chauffage et de l'éclairage des bâtiments [3], etcétera. Le coût de l'installer des capteurs à câble dans un bâtiment commercial a été estimé à \$100 par capteur + \$1,6 per pie lineal de câble [4]. Par conséquent, lorsqu'une application exige des centaines de capteurs communicants, des solutions totalement câblées deviennent moins rentables.

Depuis une décennie d'années, il y a eu un intérêt croissant sur des récupérateurs d'énergie utilisant des matériaux piézoélectriques [5–7]. Des alternatives pour alimenter des capteurs communicants, comme la récupération d'énergie, sont séduisantes. Grâce à qu'elles offrent la possibilité de rendre autonomes en énergie un capteur communicant, selon les sources d'énergie disponibles (c'est-à-dire, des vibrations mécaniques, de l'énergie thermique).

Les parties principales comprenant un capteur communicant sont illustrées dans la [Figure 1.1](#). Le bloc de gestion d'énergie a la fonction d'appairer à la source de puissance aux conditions d'alimentation en énergie électrique de la charge, par exemple, le micro processeur et l'émetteur-récepteur de communication. Dans ces travaux, nous sommes principalement intéressés par le bloc de ressource énergétique aussi bien qu'à son système de gestion d'énergie. Nous visons à développer tant le système de récupération d'énergie qu'à son système de gestion d'énergie. Le but est d'alimenter un capteur communicant déjà existant dans le marché des capteurs.

Des caractéristiques comme le facteur de forme et la faible consommation d'un capteur communicant les rendent fortement appropriés à être utiles pour des nombreuses applications, y compris la surveillance de signaux médicaux, la surveillance de l'environnement,

etcétera. Un récapitulatif des quelques exemples de capteurs communicants est présenté dans le Tableau 1.1.

Parmi les techniques classiques de conversion de l'énergie thermique, soit sous la forme de gradients de température ou sous la forme de variations temporelles de température incluent, respectivement, des thermo-générateurs et des générateurs pyro-électriques. Ces techniques offrent une efficacité relativement faible lorsque des dispositifs à petite échelle sont nécessaires (cela en raison du lien direct avec la taille de la surface des électrodes ou de la taille de la surface active des matériaux thermoélectriques) et lorsque de faibles gradients thermiques ou de faibles variations temporelles de température sont sensés à être la source d'énergie pour de tels systèmes. Donc, nous proposons un nouveau générateur capable de convertir de faibles et de lentes variations temporelles de température en électricité.

Cette thèse a aussi pour but de proposer des lignes directrices de conception d'un système de récupération d'énergie. En outre, un modèle analytique est proposé pour mieux comprendre le comportement quasi-statique et dynamique du dispositif. Des simulations par éléments finis ont été menées pour explorer de différentes architectures. Des prototypes expérimentaux ont été aussi conçus afin de valider les modèles simplifiés et d'explorer aussi la faisabilité du concept de récupération d'énergie en utilisant l'effet thermo-magnétique couplé à la transduction piézoélectrique.

Le principe fondamental de la conversion d'énergie thermique en énergie électrique réside dans le fait qu'il existe une propriété réversible et thermiquement dépendante, à savoir la dilatation des gaz (récupération de l'énergie thermoacoustique [17]), la déformation (des alliages à mémoire de forme [18]), le flambement thermique [19, 20] et le ferromagnétisme (la thermo-magnétisation [21–23]).

Récemment, au sein de notre groupe de recherche, l'effet thermo-magnétique a été étudié avec une transduction piézoélectrique afin de récupérer de l'énergie thermique [24, 25]. Ces dispositifs ont une puissance de sortie élevée par rapport à ceux utilisant la conversion directe de l'énergie thermique, à savoir des générateurs thermo-électriques ou des générateurs pyro-électriques. En plus, ils bénéficient d'un coût faible et d'un choix plus large au niveau de matériaux de fabrication.

Cette thèse présente les premières étapes de la conception ainsi que de la modélisation de tels dispositifs, permettant de prédire avec une bonne précision le comportement d'un générateur piézoélectrique à déclenchement thermo-magnétique. Les objectifs de cette thèse sont décrits comme suit :

1. Fournir la théorie et la méthodologie pour l'analyse de la conception d'un tel générateur en utilisant des structures bimorphes piézoélectriques, des aimants permanents et des alliages fer-nickel. Le pair alliage fer-nickel et aimant permanent formant le système de déclenchement convertit des variations temporelles de température en énergie mécanique. Le bimorphe piézoélectrique comprenant le système transducteur qui convertit l'énergie mécanique en électricité.
2. Développer un outil de conception rapide pour un tel type de générateur piézo-électrique à déclenchement thermo-magnétique afin d'améliorer son fonctionnement dynamique.

3. Développer un circuit d'extraction d'énergie capable d'extraire le maximum d'énergie générée. Ce circuit devrait pouvoir stocker l'énergie récupérée et la fournir au capteur communicant.
4. Vérifier expérimentalement le modèle analytique du système tenant compte le choix des matériaux disponibles; comme par exemple des alliages fer-nickel possédant point de Curie proche de la température ambiante et des piézo-ceramiques avec une couche de renforcement en laiton.

Notre motivation vient de la vision de fournir des alternatives à la conversion directe de l'énergie thermique en électricité. Cette nouvelle alternative devrait pouvoir surmonter la dépendance des changements rapides de température et des grands gradients thermiques, comme exigences des solutions classiques, telles que les générateurs pyroélectricité et thermoélectriques, respectivement. La [Figure 1.2](#) montre la variation temporelle de la température du corps humain, alors, lorsqu'on envisage d'alimenter des capteurs portables ou d'autres dispositifs portables, il est évident qu'il est nécessaire de récupérer de l'énergie thermique. En outre, nous pensons que si de nouvelles solutions de récupération de l'énergie thermique peuvent fonctionner à proximité de la plage de température du corps humain, elles peuvent convenir aux dispositifs portables.

Des études empiriques rapportées ont soutenu la récupération d'énergie à partir d'énergie thermique ambiante sous la forme de variations de température [31–33]. Finalement, des entreprises, telles que [Perpetuum](#), [SolePower](#), [EnOcean](#), [greenTEG](#) et [Pavegen](#) font de la recherche sur la récupération d'énergie pour répondre à la demande croissante d'alternatives d'alimentation en réseaux de capteurs sans fil.

Une attention particulière est accordée à la récupération de l'énergie thermique sous la forme de variations de température dans la plage de température basse indiquée dans le [Tableau 1.3](#). Dans un souci de modularité, la première étape de conversion de l'énergie thermo-mécanique a laissé la possibilité de combiner différentes techniques de conversion de la vibration mécanique en électricité.

## Chapitre 2 : Veille technologique sur la récupération d'énergie et l'état de l'art sur la récupération d'énergie thermique

Des nombreuses sources d'énergie ambiante peuvent être exploitées pour alimenter des systèmes à petite échelle [35]. Nous avons classé ces sources d'énergie en trois types principaux : énergie mécanique (vibrations et mouvement cinétique), énergie radiante (lumière solaire et ondes RF) et énergie thermique (gradients thermiques et variations de température). Le choix de la source d'énergie à récupérer dépend de sa disponibilité ainsi que de l'application finale.

L'énergie mécanique est l'une des sources d'énergie les plus omniprésentes autour de nous. Il peut être disponible sous plusieurs formes, notamment le mouvement humain, le rythme cardiaque, le mouvement du véhicule et les vibrations. Cela peut être le résultat de la conversion d'une autre sorte d'énergie; l'énergie stockée dans le carburant est convertie en énergie mécanique en brûlant le carburant en cas de mouvement des voitures.

La fréquence d'une excitation mécanique dépend de sa source de vibration. Il peut aller de moins de 10Hz à 200Hz, pour les cas de mouvement humain et les environnements industriels, respectivement [36]. Roundy *et al.* [8] ont entrepris plusieurs travaux sur cette source d'énergie et ont démontré qu'une combinaison de théorie et d'expériences suggère qu'environ 300 $\mu$ W pourraient être générés à partir de sources de vibrations.

Afin de déterminer quelle quantité d'énergie peut être convertie à partir des vibrations, un modèle général de conversion d'énergie de vibrations en électricité présenté par Williams et Yates [37] peut être utilisé. Le modèle est présenté dans la Figure 2.2.

L'énergie radiante est généralement émise sous forme d'ondes électromagnétiques. Un exemple de ce type d'énergie est l'énergie solaire. Elle est une sorte d'énergie rayonnante, on l'appelle aussi énergie optique. Ce type d'énergie rend compte de la partie du spectre électromagnétique transmettant l'énergie infrarouge à la lumière ultraviolette.

La densité de la puissance de l'éclairage dans les environnements intérieurs tels que les bureaux éclairés chute considérablement, presque 100mW cm<sup>-2</sup>. Il existe deux technologies différentes pour générer de l'électricité à partir de la lumière solaire; photovoltaïque et solaire thermique. La conversion photovoltaïque est la conversion directe de la lumière solaire en électricité sans aucun moteur thermique pour interférer. Les dispositifs photovoltaïques sont robustes et de conception simple, ne nécessitant que très peu d'entretien. Leur principal avantage est leur construction en tant que systèmes autonomes permettant de fournir des rendements allant de micro-watts à mégawatts.

Une des plus grandes avantages de ces deux types de technologies solaires est qu'elles ne génèrent aucune émission. Cependant, certains fabricants de cellules photovoltaïques génèrent des matériaux dangereux qui doivent être traités avec précaution afin de minimiser les risques d'exposition humaine et ambiante.

L'énergie des radiofréquences est présente dans l'environnement sous la forme de signaux qui sont délibérément émis par les antennes des stations de radiodiffusion et des antennes de téléphones portables. Ces émetteurs sont capables de générer des champs électromagnétiques puissants. Par conséquent, les récupérateurs d'énergie RF peuvent convertir ces ondes radiantes en électricité. Néanmoins, les très faibles niveaux de densité de puissance constituent une limitation majeure. La densité de puissance attendue autour de 25m d'une station de base du système mondial pour les communications mobiles (GSM) est inférieure à 1mW m<sup>-2</sup> [28].

L'énergie thermique est présente tout autour de nous, sous forme de gradients thermiques spatiaux ou de changements temporels de température. Et chaque processus énergétique, quelle que soit sa nature initiale, à savoir cinétique, électrique ou chimique, finit souvent par de la chaleur qui est ensuite renvoyée dans l'environnement. L'énergie thermique ambiante suscite donc l'intérêt des chercheurs pour la mise au point de nouvelles méthodes de conversion de l'énergie thermique en électricité.

De nombreuses techniques permettant de convertir directement l'énergie thermique en électricité ont été étudiées, notamment la génération thermoélectrique (l'effet Seebeck nécessitant un dissipateur thermique faisant face à une problématique pour maintenir un gradient thermique exploitable) et la pyroélectricité [27, 42–45]. Même si ces techniques ont l'avantage d'être des méthodes de conversion directes suggérant moins de pertes de

conversion (car ayant moins d'étapes de conversion d'énergie), elles présentent certains inconvénients lorsque la miniaturisation fait partie des prémisses de la conception.

L'énergie thermique sous forme de gradients thermiques spatiaux peut être convertie en énergie électrique par plusieurs méthodes, notamment des générateurs Seebeck (générateurs thermoélectriques), des générateurs thermoélectriques (également connus sous le nom d'effet Edison), des convertisseurs thermo-électrochimiques Johnson et des collecteurs infrarouges.

Quels que soient les matériaux, les coefficients de performance des réfrigérateurs thermoélectriques disponibles dans le commerce sont compris entre 0,3 et 0,6, soit un sixième de la valeur des réfrigérateurs traditionnels à compression de vapeur [34].

L'émission thermoionique est une autre méthode directe de conversion de l'énergie thermique en électricité. Il est également connu sous le nom d'effet Edison. Lorsque les électrons d'un matériau chauffé reçoivent de l'énergie thermique, ils ont la possibilité de s'échapper de la surface du matériau. L'énergie perdue dans ce processus est appelée la fonction de travail. La fonction de travail est une propriété de la surface émettrice et est généralement de l'ordre de plusieurs électron-volts de magnitude [46].

Une autre méthode de conversion de l'énergie thermique est le convertisseur thermo-électrochimique Johnson (JTEC) développé par la société Johnson ElectroMechanical Systems [47]. Le JTEC génère de l'énergie car l'hydrogène est comprimé en permanence à basse température et détendu à haute température. Une partie de la puissance à la sortie du dispositif est consommée lors du pompage à basse température de l'hydrogène à haute pression, la chaleur étant rejetée. Enfin, nous pouvons utiliser des systèmes thermo-photovoltaïques pour convertir l'énergie thermique en électricité au moyen de photons à rayonnement thermique. Une limitation de l'effet photovoltaïque est due à la bande interdite spécifique des matériaux photovoltaïques.

Les variations de température peuvent être converties en énergie électrique à l'aide de matériaux sensibles aux variations de température. Electrical current generation from time-dependent temperature variations has revealed useful in sensing applications [44]. En ce qui concerne les générateurs pyroélectriques, premièrement, ils ne nécessitent pas des températures de source élevées requises par les générateurs thermoélectriques traditionnels. Deuxièmement, la combinaison de températures de fonctionnement faibles offre le potentiel d'un système de production d'énergie avec une bonne fiabilité. Bien que la chaleur libérée crée plus probablement des gradients spatiaux que des variations temporelles, l'efficacité de la conversion, définie comme le rapport entre l'énergie nette récupérée et la chaleur extraite du réservoir chaud, est beaucoup plus élevée lorsque la récupération d'énergie pyroélectrique est utilisée.

Comme nous nous intéressons à la conversion de l'énergie thermique sous la forme de variations de température, nous allons décrire les techniques de transduction les plus classiques pour ces sources d'énergie. La transduction électromagnétique consiste en un noyau magnétique et une bobine, dont l'un est couplé au résonateur mécanique et l'autre reste statique. Le principe est la loi d'induction de Faraday, lorsque le résonateur vibre, le déplacement relatif de l'aimant sur la bobine induit une tension alternative. La Figure 2.8 montre le schéma de la transduction électromagnétique.

D'autres types de transducteurs d'énergie pour les vibrations mécaniques sont basés sur un effet électrostatique. Ces dispositifs peuvent convertir l'énergie mécanique en énergie électrique en utilisant l'énergie mécanique d'entrée pour modifier la capacité du générateur entre une valeur élevée et une valeur faible. Le plus souvent, la capacité est réduite en augmentant la distance (c'est-à-dire un entrefer) entre les plaques du condensateur ou en réduisant la zone de chevauchement des plaques. La [Figure 2.9](#) montre le schématique de la transduction électrostatique.

La transduction piézoélectrique est l'une des stratégies les plus populaires de récupération de l'énergie mécanique ambiante. Il est basé sur la propriété bien connue du matériau appelée piézoélectricité. L'effet piézoélectrique direct lie une action mécanique (contrainte ou déformation) à une réponse électrique (champ électrique, déplacement électrique ou polarisation). Cet effet a été étudié pour la première fois par les frères P. Curie et J. Curie dans le cadre de travaux expérimentaux (1880) sur le comportement de monocristaux de quartz soumis à une contrainte mécanique externe [55]. Dans la majorité des scénarios, les récupérateurs piézoélectriques fonctionnent en mode latéral 31. En effet, l'élément piézoélectrique est souvent lié à la surface d'un ressort mécanique, élément qui convertit les déplacements verticaux en une contrainte latérale à travers l'élément piézoélectrique. Certains modèles peuvent fonctionner en mode compressif et ceux-ci ont l'avantage d'exploiter les 33 constantes, qui sont généralement supérieures à 31 équivalents. Parmi les modes de fonctionnement pouvant être employés pour les générateurs piézoélectriques, le mode 31 est plus approprié pour les poutres en porte-à-faux piézoélectriques avec une masse sismique à l'extrémité libre, comme illustré dans [Figure 2.10](#).

Le [Tableau 2.1](#) résume la densité d'énergie maximale pour ces trois types de convertisseurs.

Plusieurs méthodes sont actuellement utilisées pour la récupération de l'énergie thermique. Dans cette section, une partie de la conversion directe de l'énergie thermique en électricité et de la conversion indirecte, à savoir la conversion de l'énergie thermique vers l'énergie mécanique et ensuite vers l'énergie électrique, est détaillée. Lorsqu'il s'agit de la conversion de l'énergie thermique, les solutions les plus courantes pour convertir les fluctuations de température (à l'aide de convertisseurs pyroélectriques) ou les gradients thermiques thermoélectriques) directement dans l'électricité dépendent fortement du taux de changement de température ou avec de grands gradients thermiques afin d'avoir de grandes puissances de sortie. C'est pourquoi différentes méthodes de conversion ont fait l'objet de plusieurs travaux.

Un moteur thermique thermo-acoustique est un moteur thermique externe qui génère de l'énergie mécanique sous la forme d'une onde acoustique oscillante dans le fluide moteur du moteur. Ils peuvent fonctionner en sens inverse pour convertir l'énergie mécanique en différence thermique pour les refroidisseurs cryogéniques. Les moteurs thermiques à ondes stationnaires thermo-acoustiques suivent le cycle de Stirling. Il a les composants suivants; compresseur, échangeur de chaleur, détenteur et régénérateur. En utilisant un tube et une pression acoustique, un gradient thermique est créé dans le mur le long du moteur. Les figures [2.14\(a\)](#) et [2.14\(b\)](#) montrent, respectivement, le schéma et la photographie d'un moteur thermique thermoacoustique à onde stationnaire couplé à une transduction piézoélectrique.

Une autre conversion indirecte d'énergie thermique en électricité est constituée par les moteurs thermiques en alliage à mémoire de forme. Les alliages à mémoire de forme (SMA) sont des matériaux qui retrouvent leur forme initiale après avoir été déformés par chauffage ou refroidissement. Gueltig *et al.* [65] ont développé un générateur utilisant des alliages à mémoire de forme magnétique. En utilisant le changement de magnétisation induit thermiquement ainsi que la capacité d'activation d'alliages à mémoire de forme magnétique, un récupérateur d'énergie atteignant des densités de puissance moyennes de  $0,5\text{mW cm}^{-3}$  pour un changement de température de  $0\text{K}$  est présenté. Le dispositif comprend les composants de base suivants : film d'alliage à mémoire de forme magnétique, interface thermique avec une source de chaleur externe, mécanisme de déclenchement ou de réinitialisation et unité de conversion d'énergie. Dans ce dispositif, l'interface thermique est conçue pour s'adapter à la forme du porte-à-faux après une déformation hors du plan.

Avirovik *et al.* [66] ont construit un moteur thermique utilisant le SMA pour convertir d'abord la chaleur environnementale en énergie mécanique, puis en énergie électrique à l'aide d'une microturbine. Les résultats expérimentaux ont montré que  $0,12\text{g}$  de fil SMA produisait  $2,6\text{mW}$  de puissance mécanique qui était ensuite utilisé pour entraîner un générateur électromagnétique miniature produisant  $1,7\text{mW}$  de puissance électrique. L'énergie électrique générée a été utilisée pour alimenter un nœud de capteur sans fil. La [Figure 2.16](#) montre la description schématique du générateur.

Puscasu *et al.* [20] ont présenté un ensemble de récupérateurs d'énergie basés sur ce principe. Un bilame thermique est une double couche constituée d'un matériau à coefficient de dilatation thermique élevé et l'autre à coefficient de dilatation thermique inférieur. Il en résulte une forme concave du matériau composite afin de le faire claquer sous l'effet de l'augmentation ou de la diminution de sa température. Cette technique convertit les gradients thermiques en énergie mécanique et en attachant une couche piézoélectrique à l'un des matériaux, de l'énergie électrique peut être extraite.

A l'échelle des MEMS, au sein de notre groupe de recherche, Trioux *et al.* [67] ont développé un récupérateur d'énergie thermique. Cela implique une transduction en deux étapes par le flambage thermique d'une bicouche en nitrure d'aluminium et en aluminium pour la conversion de l'énergie thermique en énergie mécanique. En utilisant la transduction piézoélectrique, l'énergie électrique est ensuite extraite. Des progrès dans la géométrie de la bicouche ont été réalisés afin d'améliorer la puissance de sortie du générateur.

La récupération d'énergie thermo-magnétique est une autre alternative à la conversion d'énergie thermique. Cette méthode de production d'électricité repose sur une modification des propriétés magnétiques résultant de la modification de la température de certains matériaux. Si un matériau présentant une aimantation thermiquement dépendante est soumis à un champ magnétique externe constant et soumis à un cycle de température, son aimantation cycle aussi. Ujihara *et al.* [68] ont rapporté un dispositif de récupération d'énergie thermique utilisant des matériaux ferromagnétiques (voir [Figure 2.19](#)). Dans ce récupérateur d'énergie, un actionneur thermo-mécanique convertit l'énergie thermique en énergie mécanique. Le principe du générateur repose sur une transition de phase du second ordre induite thermiquement, produisant de l'énergie mécanique.

Dans le passé, au sein de notre groupe de recherche, Carlioz *et al.* [69] ont proposé une approche différente pour convertir les fluctuations de température en électricité. Technique basée sur l'hybridation d'un ensemble d'aimants permanents - matériaux magnétiques doux et transduction piézoélectrique. Le système fonctionne comme une sorte d'interrupteur thermique. Lorsque la température du matériau magnétique doux est inférieure à sa température de Curie. Par conséquent, il présente une force d'attraction entre les aimants mobiles. Inversement, à des températures supérieures à la température de Curie, le matériau magnétique doux devient paramagnétique. Par conséquent, l'aimant permanent est libéré. Le matériau piézoélectrique convertit ces mouvements mécaniques en électricité. Les figures 2.20(a) and 2.20(b) illustrent le schéma de ce générateur thermo-magnétique et de son prototype peu coûteux, respectivement.

Une comparaison détaillée des récupérateurs d'énergie thermique est répertorié dans le Tableau 2.2.

Le générateur de courant comporte deux sections principales, selon leurs fonctions respectives : le transducteur d'énergie et le système de déclenchement comme représenté sur la figure 2.22(a). Le générateur a deux positions stables : la position fermée et la position ouverte. Dans l'état initial, à une température froide, le matériau magnétique doux est magnétisé de sorte que le faisceau en porte-à-faux est abaissé sous l'effet d'une force magnétique. Ensuite, lorsque la température ambiante augmente, les propriétés magnétiques du matériau magnétique doux changent de ferromagnétique à paramagnétique, entraînant une diminution de la force magnétique. Le faisceau est ramené à son état initial en raison de la force de rappel du faisceau. Cette action d'attirer et relâcher la poutre est répétée périodiquement tant que le récupérateur d'énergie est placé dans un environnement avec des variations cycliques de température.

### Chapitre 3 : Conception et modélisation du générateur proposé

À l'état pur, le fer et le nickel sont des matériaux ferromagnétiques à température ambiante. Lorsqu'ils sont combinés pour former des alliages, le produit peut également présenter cette propriété. Cependant, selon la stœchiométrie de ce binaire, le comportement magnétique peut présenter une grande diversité. Les alliages FeNi ne sont utilisés que pour leurs propriétés magnétiques pour des teneurs en nickel supérieures à 28%. Et leur structure est cubique avec des faces centrées et ils ne présentent pas de transformation de phase à l'état solide. Par conséquent, ces deux propriétés leur confèrent une bonne facilité de laminage à froid (jusqu'à 10 $\mu$ m) et un traitement thermique permettant de développer au mieux leurs propriétés magnétiques [79]. Typiquement, une courbe thermo-magnétique d'un matériau est une représentation de sa polarisation magnétique en fonction de la température, comme indiqué dans la Figure 3.1.

La Figure 3.4 montre le schéma d'une architecture possible du micro-générateur proposé à activation thermo-magnétique. Dans cette configuration, le générateur peut être divisé en deux sous-systèmes principaux : le système de déclenchement et le système de transduction. Le principe de fonctionnement du générateur est décrit comme suit :

1. Dans l'état initial, la température de l'alliage magnétique doux est inférieure à sa température de Curie  $\theta_C$  ; d'où une force magnétique d'attraction  $F_{mag}$  est exercée en

raison d'une paire d'aimants permanents. Ainsi, les aimants permanents sont attirés vers l'alliage magnétique doux et l'extrémité libre de la poutre se déplace vers la surface du matériau magnétique doux en contact l'un contre l'autre sous des forces magnétiques et inertielles. A cet instant, le générateur est en position fermée (Figure 3.4b)).

2. Une fois que la température ambiante augmente; le matériau magnétique doux est maintenant chauffé par conduction et perd son magnétisme au-dessus de sa température de Curie. Au moment où la température de l'alliage magnétique doux approche de sa température de Curie, la force magnétique d'attraction diminue considérablement (c'est-à-dire  $F_{mag} \leq F_{mec}$ ). Après cela, la force de réaction  $F_{mec}$  de la poutre en porte-à-faux l'éloigne de l'alliage magnétique. A cet instant, le générateur est en position ouverte (Figure 3.4c)).
3. Ensuite, lorsque la température ambiante diminue en dessous de la température de Curie de l'alliage magnétique doux, l'alliage magnétique doux retrouve son aimantation spontanée. Après avoir retrouvé l'aimantation, les aimants permanents sont attirés vers le matériau magnétique doux et se déplacent vers la surface du matériau magnétique doux qui se touchent. Les fluctuations de température sur l'alliage magnétique doux commandent le générateur dans ses deux positions de fonctionnement stables.

La modélisation de l'ensemble du cycle de récupération peut être divisée en 3 phases distinctes comme suit :

- Phase I : l'aimant permanent inférieur est en contact avec la surface de l'alliage magnétique doux, le générateur est donc en position fermée.
- Phase II : une montée en température de l'alliage magnétique doux lui fait perdre son aimantation spontanée jusqu'à atteindre le seuil d'ouverture du système, ainsi la commutation d'ouverture est atteinte entraînant un mouvement oscillant de la poutre.
- Phase III : la poutre en porte-à-faux est maintenant à sa position horizontale, une diminution de la température du matériau magnétique doux lui permet de retrouver son aimantation spontanée jusqu'à atteindre le seuil de fermeture du système.

Un transfert de chaleur se produit lors du chauffage et du refroidissement de l'alliage magnétique doux. Initialement, en position fermée du générateur, le chauffage se produit à la source de chaleur où l'alliage magnétique doux et la pointe de faisceau en porte-à-faux sont chauffés par contact direct (c'est-à-dire par conduction). Ensuite, en position ouverte du générateur, le refroidissement du système est obtenu par convection naturelle ou forcée par un mouvement oscillant dans l'air (c'est-à-dire par convection). Des équations pour la température en fonction du temps sur la face supérieure de l'alliage magnétique doux sont formulées afin de décrire les processus de chauffage et de refroidissement.

En phase I, le système est proche de son état de déplacement maximal. Dans cet état, la conductance de contact thermique domine la physique du transfert de chaleur. En phase II; le rôle de la conductance de contact thermique est négligeable et la distribution de la

température change uniquement en raison de la diffusion interne. La pression de contact est absente et la vibration est donc régie par la force magnétique et la force de rappel du ressort. La modélisation du transfert de chaleur ayant pour objet de calculer la température dans un alliage magnétique doux et la force magnétique correspondante, le transfert de chaleur peut être divisé en deux parties : réchauffement et refroidissement.

Pour produire des variations de température sur notre échantillon de matériau magnétique doux, nous avons supposé qu'il était toujours en contact avec une source de chaleur. Cette source de chaleur consiste en la conversion d'énergie électrique en chaleur. Nous trouvons l'équation dominante du système pendant la phase de chauffage [Equation 3.3](#).

Ensuite, l'expression dominante pour la phase de refroidissement avec convection forcée est décrit par l'[Equation 3.5](#).

L'aimant néodyme-fer-bore est de configuration cylindrique comme indiqué dans la [Figure 3.8](#). Selon la température à l'intérieur du matériau, l'alliage magnétique doux suit une distribution de magnétisation correspondante. L'estimation de l'aimantation d'un matériau magnétique doux nécessite la résolution de l'équation donnée [84].

Les commutations du générateur sont conduites par l'interaction de la force mécanique de restauration, créée par la poutre piézoélectrique en porte-à-faux, et de la force d'attraction magnétique agissant sur le matériau magnétique doux, créée par le champ magnétique appliqué.

L'équation résultante pour calculer la force axiale est décrite par l'[Equation 3.10](#). À ce stade, nous pouvons déduire les seuils thermiques donnés pour une conception initiale du générateur (c'est-à-dire la position initiale du transducteur, sa rigidité mécanique et ses dimensions). Pour mieux comprendre le comportement quasi statique du générateur, nous avons effectué des mesures expérimentales sur un prototype pour lequel nous avons fixé des paramètres tels que les dimensions du matériau magnétique doux, du transducteur bimorphe et de l'aimant permanent.

Par une technique de triangulation utilisant un capteur laser, nous avons surveillé le déplacement vertical à l'extrémité libre du faisceau en porte-à-faux tout le temps pendant l'expérience. Ces premières expériences ont confirmé l'impact de la distance d'écart initiale sur les températures de fonctionnement et l'hystérésis thermique.

Il est plausible qu'un certain nombre de limitations aient pu influencer les résultats obtenus. Premièrement, les hypothèses considérées sur la caractérisation de la force d'attraction magnétique sur le système de déclenchement; en supposant que le volume magnétique soit perpendiculaire à l'axe de symétrie de l'aimant permanent, ce qui n'est pas toujours le cas dans les expériences pratiques (c'est-à-dire que l'angle de flexion de la poutre tend à être important lorsque de grandes déformations sont visibles).

Une autre source d'erreur possible est la caractérisation du matériau magnétique doux, qui influence directement la réponse du générateur. Malheureusement, nous n'avons pas pu étudier les paramètres thermo-magnétiques de notre échantillon de fer-nickel directement auprès du fabricant. Une collecte de données supplémentaire serait nécessaire pour déterminer exactement les paramètres thermo-magnétiques de l'alliage magnétique doux.

Nous pensons que la réduction du volume du matériau magnétique doux peut réduire considérablement la réponse thermique du générateur, autrement dit le délai entre les commutations. En effectuant un bilan de conversion d'énergie du système, il peut être évident que la déviation initiale de la poutre représente l'énergie de sortie maximale possible qui peut être convertie en électricité. Par conséquent, de plus grands entrefers initiaux sont souhaités. Ajouté à cela ; une hystérésis thermique plus faible est attendue afin de réduire la période de transition entre les commutations. C'est la raison pour laquelle nous pensons que nous avons trouvé un modèle analytique d'un tel système capable de prédire ses comportements quasi statiques et dynamiques en réponse à sa conception.

La vibration de la poutre piézoélectrique sous la force magnétique d'attraction peut être décrite comme un système amortisseur masse-ressort de second ordre, ainsi qu'un élément piézoélectrique connecté en parallèle à l'amortisseur. Le comportement électromécanique du micro-générateur peut être décrit avec une bonne approximation par un modèle à un paramètre à dimension localisée.

En position ouverte du générateur, même si elle atteint sa position stable, il existe une contrainte mécanique dans le bimorphe piézoélectrique due à la présence d'une force magnétique faible dans le système. Cependant, le faisceau en porte-à-faux n'a pas de vitesse et donc aucun potentiel généré. En refroidissant un matériau ferromagnétique doux, il reprend son aimantation en raison de la densité de flux externe de l'aimant permanent.

Le comportement statique du générateur comprend l'opération pour laquelle le système passe de la position fermée à la position ouverte et inversement. Cela est essentiel pour concevoir et donner une première estimation des performances pouvant être atteintes par le périphérique dans un scénario spécifique. En réduisant la quantité de matériau magnétique doux, la force magnétique est également réduite, cependant, cela implique des constantes de temps plus courtes pour la réponse transitoire du dispositif à la température.

Compte tenu des propriétés du matériau répertoriées dans le Tableau 3.4, nous avons calculé la rigidité équivalente du système. Après l'achèvement de cette étape, le comportement statique et dynamique du générateur peut être exploré. L'architecture présentée du transducteur (c'est-à-dire bimorphe piézoélectrique) n'est qu'une possibilité parmi d'autres. Afin d'explorer les capacités de récupération d'énergie de différentes configurations du transducteur piézoélectrique, nous avons choisi de développer un modèle mathématique décrivant le comportement du transducteur piézoélectrique pour lequel les couches piézoélectriques peuvent être déposées sur toute la longueur de la couche de cale d'épaisseur ou sur une partie seulement, comme par exemple un patch piézoélectrique.

En conclusion, disposer d'un modèle analytique pour ce type de générateur est avantageux pour effectuer des prévisions utiles en termes de performances et d'efficacité. Et avoir une expression mathématique est utile pour faire une analyse factorielle. L'un des objectifs de cette thèse étant d'étudier la faisabilité de miniaturiser notre générateur présenté, nous avons d'abord décidé de présenter certaines règles de conception à prendre en compte lors de la conception d'un tel type d'appareil. Ensuite, une analyse de réduction du facteur d'échelle est présentée et répertoriée dans le Tableau 3.6, tandis qu'un bilan global des paramètres de conception est répertorié dans le Tableau 3.7.

La modélisation d'un micro-générateur à activation thermo-magnétique a été présentée. La réponse du générateur pour un scénario particulier a été étudiée. Cette méthode de prévision représente une alternative viable à la conception rapide de micro-générateurs.

Le modèle numérique multi-physique que nous avons présenté ici est capable de prédire une gamme de différents scénarios de fluctuations de température pour lesquels le générateur est censé travailler. De plus, cela permet également d'étudier l'influence des paramètres de l'appareil sur les performances dynamiques du générateur. Le cadre théorique du générateur a été formulé et un outil de conception rapide a été développé avec Matlab. L'objectif principal de cet outil est de mieux comprendre le comportement quasi statique (c'est-à-dire l'identification des températures de fonctionnement pour une conception spécifique du générateur) et le comportement dynamique du générateur.

Il a été prouvé que la densité de puissance de sortie du générateur peut être augmentée lorsqu'une miniaturisation efficace du dispositif est effectuée.

Certaines des conclusions sont que l'augmentation de la distance de séparation initiale du système de déclenchement peut entraîner une plus grande énergie élastique stockée initialement sur la poutre en porte-à-faux. Ainsi, aboutissant à de plus grandes capacités de récupération d'énergie. Cependant, avec des distances de séparation initiales plus grandes, la force de contre-réaction augmente également ; par conséquent, la force magnétique d'attraction requise pour assurer la position fermée est également plus grande ; qui peut facilement dépasser les propriétés magnétiques du système de déclenchement. Cette découverte suggère une conception optimale pour laquelle le bilan énergétique pourrait être maximisé.

En ce qui concerne les températures de fonctionnement du générateur, elles dépendent des paramètres de conception, essentiellement du système de déclenchement, y compris la position initiale et de la rigidité effective de la poutre en porte à faux qui en résulte. Il est donc possible d'ajuster ces seuils thermiques en modifiant les paramètres de conception tels que les dimensions du générateur ou la position initiale du transducteur, ce qui peut constituer un avantage si la sélection du matériau est correcte.

Le micro-générateur piézoélectrique à activation thermo-magnétique décrit ici montre une approche prometteuse. Il peut fonctionner par les fluctuations de la température ambiante ou industrielle, des variations de la température ambiante en fonction de l'adaptation de leurs seuils thermiques. Il pourrait aussi récupérer de l'énergie à partir de petites et lentes fluctuations de température présentes autour de nous : parois de canalisations transportant des fluides chauds, machines industrielles, radiateurs d'automobiles ; pour n'en nommer que quelques uns. De plus, il peut jouer un second rôle. comme interrupteur thermique. L'outil de conception rapide que nous avons présenté sera comparé et validé avec des simulations d'éléments finis dans le prochain chapitre de cette thèse.

## **Chapitre 4 : Modélisation par éléments finis du générateur**

La polyvalence de la méthode des éléments finis réside dans sa capacité à modéliser des structures de forme arbitraire, à utiliser des matériaux complexes, et à appliquer plusieurs types de charges ainsi que des conditions aux limites. La méthode des éléments finis peut également être adaptée à différents ensembles d'équations constitutives, c'est-à-dire le principal attrait de la simulation en physique couplée.

Le logiciel ANSYS éléments finis dispose d'une vaste bibliothèque de types d'éléments prenant en charge les analyses structurelles, thermiques et électromagnétiques, ainsi que

les éléments de champs couplés, notamment piézoélectriques, électromagnétiques thermiques et thermo-structuraux, qui simulent les interactions entre les champs susmentionnés. Dans notre cas particulier, en raison de la nature multi-physique du système de conversion indirecte de l'énergie thermique, nous sommes intéressés à explorer le comportement thermique du système dans un premier temps.

Nous avons utilisé la méthode des éléments finis pour concevoir et prédire le comportement dynamique du périphérique. Ce modèle prend en compte différentes étapes de la conversion d'énergie : la réponse en température du récupérateur d'énergie, l'aimantation de son système de déclenchement en fonction de la température et la transduction piézoélectrique jusqu'à la dissipation de la puissance de sortie à travers la résistance de charge.

Les conditions initiales de la simulation sont les suivantes : lorsque le générateur est en position fermée, une charge thermique est appliquée sur la face inférieure du matériau magnétique doux en utilisant un élément chauffant.

Pour prendre en compte le transfert de chaleur entre le matériau magnétique doux et son équivalent (l'aimant permanent inférieur), nous avons opté pour l'approche Pinball Region proposée par ANSYS Workbench. La Pinball Region, également connue sous le nom Pinball Radius, est impliquée dans l'élément de contact de forme à distance pour cibler l'élément dans une région de contact donnée. En dehors de cette région, ANSYS ne cherche pas à savoir si les éléments situés de part et d'autre de la région de contact se touchent ou non. Le logiciel suppose qu'ils sont loin de chaque autre et ne s'inquiète pas des calculs supplémentaires pour l'analyse.

Afin d'évaluer la réponse en température du système en position fermée, il est nécessaire de régler le boulet à rayon supérieur à la distance de séparation initiale. De cette manière, le logiciel considère le contact limité sur la paire d'aimants permanents FeNi. Les principaux paramètres du système sont répertoriés dans le Tableau 4.1.

Le contact thermique dans le système de déclenchement est pris en compte au début de la simulation. Dès que la température de l'alliage FeNi atteint le seuil d'ouverture, le contact thermique n'est plus pris en compte. Ce comportement est illustré par la courbe de température de l'alliage FeNi et de l'aimant permanent.

Certains résultats de cette simulation sont illustrés dans la Figure 4.6. A partir de ces résultats de simulation, on peut constater qu'au moment initial, le flux thermique est appliqué. Le but principal de cette étude est de voir la température réponse de l'appareil en tenant compte des deux conditions de fonctionnement

Il est également essentiel de garder à l'esprit que le scénario d'entrée est prédominant sur les performances du générateur. Pour les scénarios où les variations de température sont sporadiques, la meilleure conception de ce type de générateur pourrait ne pas avoir en priorité la réponse thermique, mais les capacités de conversion électromécanique de l'énergie. Inversement, pour les scénarios dans lesquels les variations de température sont fréquentes, il convient de porter une attention particulière à la réponse thermique du dispositif afin d'assurer des commutations thermiques efficaces (c'est-à-dire dont les périodes thermiques sont aussi courtes que possible).

La magnétisation dépendante de la température des matériaux magnétiques doux est la propriété clé du principe de fonctionnement de ce type de générateurs. Ceci est une propriété réversible qui dépend de la stoechiométrie de l'échantillon. L'analyse magnétique du système visait à explorer la force magnétique dans le circuit de déclenchement, à savoir le couple à aimant permanent et l'alliage FeNi. La polarisation magnétique pour un aimant permanent, le logiciel Maxwell est considéré comme étant le long de l'axe des x, nous avons créé un système de coordonnées en rotation, dont l'axe des x est orienté vers la position verticale (c'est-à-dire l'axe z du système de coordonnées global).

Nous avons découvert expérimentalement que l'alignement vertical entre l'aimant permanent et le spécimen magnétique doux est crucial pour avoir une force d'attraction magnétique efficace. Pour explorer l'influence de cet alignement sur la force magnétique résultante, avec une distance de séparation initiale constante, nous avons effectué une analyse paramétrique.

Par souci de validité, nous avons mené une étude comparative entre les modèles analytiques et la simulation par éléments finis pour le système de déclenchement. Dans cette étude, nous avons réalisé un cas de référence avec le calculateur de force adhésive du calculateur supermagnete afin d'avoir une idée de ce que les fabricants d'aimants permanents fournissent pour la force adhésive entre un aimant permanent et un matériau aimanté. Le schéma du modèle est présenté dans [Figure 4.17](#) et les résultats sont montrés dans [Figure 4.18](#).

Les paramètres généraux du modèle sont présentés dans le [Tableau 4.3](#).

Les éléments mécaniques structurels ont été modélisés via SOLID186. Les éléments piézoélectriques ont été modélisés avec le type d'élément SOLID226. Pour illustrer la puissance dissipée due à la conversion piézoélectrique, une résistance de charge modélisée avec le type d'élément CIRCU94 est directement connectée aux électrodes du bimorphe.

Premièrement, nous avons fixé la face inférieure du FeNi. En outre, une section de 15mm du transducteur est fixée. En effet, le montage de la poutre en porte-à-faux a la même longueur. Nous avons donc voulu reproduire des conditions similaires à celles du modèle. Deuxièmement, les électrodes supérieure et inférieure des faisceaux piézoélectriques sont connectées à une résistance de charge de sortie (sauf pour les simulations statiques car elle n'accepte pas ce type d'éléments). La connexion électrique entre les couches piézoélectriques est en série, de sorte qu'une flexion vers le FeNi produise une tension négative, tandis qu'une tension de sortie positive est obtenue par des flexions vers le haut. La force magnétique agit sur l'aimant inférieur vers l'alliage FeNi.

Un aspect très important que nous avons réalisé lors des expérimentations est le contact mécanique entre l'alliage FeNi et l'aimant permanent fixé au transducteur. Effectivement, la position de fermeture du générateur consiste en le contact mécanique de ces éléments. Nous avons donc dû prendre en compte ce contact sur le modèle.

Les éléments de contact TARGE170 et CONTA174 ont été mis en œuvre à la surface impliquée dans cette étape. La surface cible est la face supérieure de l'alliage FeNi. Comme ce volume est fixe et qu'il recevra l'impact du faisceau du transducteur en mouvement, il est décidé de l'affecter à la surface cible. La face inférieure de l'aimant permanent attaché au faisceau est sélectionnée comme surface de contact.

L'analyse harmonique s'explique par le fait que le générateur peut également être conçu pour fonctionner dans des environnements soumis à des vibrations. Autrement dit, non seulement les variations de température sont présentes mais il est également courant de les trouver dans les applications industrielles, telles que les machines qui gaspillent de la chaleur et génèrent des vibrations lors de leur fonctionnement. Il est souhaitable de connaître les performances du système sous une entrée harmonique telle que des vibrations. Il est évident que le générateur devrait exploiter les vibrations une fois qu'il est en position ouverte.

L'analyse harmonique est généralement utilisée pour déterminer la réponse en régime permanent d'une structure linéaire à des charges qui varient de manière sinusoïdale (c'est-à-dire harmoniquement) avec le temps. L'idée est de calculer la réponse de la structure à plusieurs fréquences et d'obtenir un graphique représentant une certaine quantité de réponse (généralement des déplacements) en fonction de la fréquence.

Comme nous le savons déjà, à partir de la simulation modale, de la fréquence propre du système, nous pouvons affiner la plage de fréquences proche de cette fréquence de résonance du système. Le terme d'amortissement est crucial pour être identifié dans cette étude. Nous avons opté pour une étude paramétrique exploitant le modèle d'éléments finis afin d'explorer l'influence du coefficient d'amortissement  $C$  sur la puissance du générateur.

Sous ANSYS, il est possible d'introduire divers termes d'amortissement, notamment l'amortissement Rayleigh, le coefficient d'amortissement, l'amortissement dépendant du matériau, le rapport global d'amortissement, etc. analyses. L'étude harmonique que nous avons menée est décrite comme suit : pour trois prototypes d'architecture, l'accélération a été appliquée à l'origine du système de coordonnées.

L'analyse des harmoniques peut être avantageuse lorsque des récupérateurs d'énergie par inertie sont ciblés. Même si notre générateur n'est pas censé fonctionner dans des environnements vibratoires, il n'est pas interdit de concevoir avec de telles capacités. C'est pourquoi les concepteurs peuvent tirer parti de ce modèle couplé pour entreprendre une analyse harmonique. Les résultats ont révélé que l'amortissement peut être un défi à relever pour assurer de longues oscillations du faisceau du transducteur. Comme il est basé sur le traitement d'événements (commutations d'ouverture et de fermeture), plus il y a d'oscillations, plus l'énergie mécanique peut être convertie en électricité.

La polyvalence de ce type de générateurs repose sur le fait qu'ils peuvent également convertir l'énergie de vibration, une fois en position ouverte, jusqu'à ce qu'une baisse de température le ferme. En d'autres termes, supposons que le générateur soit placé dans un environnement industriel où une machine fonctionne plusieurs fois pendant une courte période (c'est-à-dire quelques minutes de fonctionnement sur une journée). Et, cette machine produit aussi des vibrations, comme dans le cas d'une perceuse, une machine à couler sous pression ou même un bloc de contacteurs de protection d'un tableau de commande de moteur triphasé. Une fois que la température a amené le générateur à sa commutation d'ouverture; le générateur peut vibrer en réponse à l'excitation de l'environnement. Par conséquent, la conception optimale doit présenter un grand intérêt pour la conception d'une bonne réponse à la température et d'une bonne capacité de conversion de l'énergie de vibration.

Une analyse dynamique transitoire est utilisée pour déterminer la réponse d'une structure soumise à une charge en fonction du temps, en tenant compte des effets d'inertie

et d'amortissement. On parle souvent d'analyse temporelle. La principale charge prise en compte dans l'analyse dynamique transitoire est la force magnétique dans le système de déclenchement.

Le scénario d'entrée déterminera la fréquence de fonctionnement du générateur. Cela signifie que si la température ne diminue pas, le générateur peut rester ouvert. Néanmoins, dans cet état; comme nous l'avons mentionné dans la section précédente, si l'environnement présente des vibrations pouvant être transmises à l'appareil.

Le but de cette simulation peut être divisé en quatre principaux domaines. Le premier concerne l'analyse modale. Aucune charge n'est considérée pour cette étude, mais le résultat est le mode de vibration de la structure. Des coefficients d'amortissement peuvent être introduits dans cette étude afin de comprendre la fréquence atténuée de la résonance. Deuxièmement, une étude statique est réalisée pour étudier le contact mécanique sur le système de déclenchement. La tension en circuit ouvert du faisceau en porte-à-faux est étudiée ici. Troisièmement, une analyse harmonique est effectuée dans le but de connaître la résistance de charge optimale lorsque le générateur est soumis à des accélérations. Bien que cette approche soit généralement utilisée pour les récupérateurs d'énergie par inertie, l'avantage de ce générateur est qu'il peut également récupérer de l'énergie quand il est en position ouverte si l'environnement génère des vibrations. Enfin, le comportement transitoire du générateur complète la phase de caractérisation. Il associe les vibrations mécaniques à l'effet piézoélectrique et la tension de sortie aux bornes d'une résistance de charge est le résultat principal de cette étude.

## Chapitre 5 : Prototypes du générateur et ses premières évaluations expérimentales

Parmi les nombreux prototypes que nous avons fabriqués, nous pouvons d'abord présenter les premiers prototypes de générateurs modélisés selon la méthode des éléments finis. Les prototypes 1, 2 et 3 illustrés aux figures 4.19(a), 4.19(c) et 4.19(e) respectivement.

Le plus important, car il contrôlera le déclenchement du générateur en fonction de la température. Il consiste en un cylindre de matériau magnétique doux. Les matériaux mous eux-mêmes n'ont aucune magnétisation, mais ils sont sensibles aux sources magnétiques externes. Cela se traduit par un champ coercitif faible. Une fois cette limite franchie, le matériau mou atteint rapidement la saturation.

Dans notre cas, nous avons choisi un alliage FeNi d'une composition particulière. En ce qui concerne cette famille de matériaux, il est possible d'ajuster facilement leur température de Curie en utilisant la composition. Ainsi, avec seulement un simple alliage FeNi  $\theta_C$ , il peut facilement passer de 0 à 200°C pour le Ni de 28 à 35% de la masse totale (voir figure 3.2(a)). L'ajout d'autres éléments tels que Cr, Mo ou Si permet également ce type de réglage. Par exemple, ajouter du Cr augmente cet effet en obtenant un  $\theta_C$  de -150 à 600°C (voir figure 3.2(b)).

Les aimants permanents utilisés consistent en une paire d'aimants durs en forme de disque NdFeB, car ils peuvent être facilement obtenus. De plus, leur aimantation rémanente est comprise entre 1,2 et 1,5T ce qui permet de magnétiser facilement à saturation le

matériau magnétique doux qui va être placé contre. En outre, il est recommandé de les utiliser à une température inférieure à 80°C, ce qui les rend adaptés à la plupart des utilisations dans l'environnement humain.

Nous avons développé une interface LabView afin de contrôler le déclenchement de l'oscilloscope puis enregistrez la tension de sortie à la commutation. L'interface est également capable d'acquérir des mesures de température à travers un thermocouple inséré dans l'échantillon FeNi. Des sondes d'oscilloscope à haute impédance ont été utilisées pour nous permettre d'utiliser une résistance de charge proche de 10MΩ. La figure [Figure 5.5](#) présente un tel enregistrement sur une période de 480s de la température du FeNi. Les résultats sont présentés dans le [Tableau 5.4](#).

Dans une deuxième phase d'expérimentation, nous avons décidé de réduire le volume magnétique permanent en utilisant les plus petits aimants permanents. Nous avons utilisé deux disques à aimants permanents de 1mm de hauteur et 2mm de diamètre. Le [Tableau 5.5](#) présente les résultats de cette deuxième étape de tests.

Ces deux étapes d'expérimentation nous ont permis de mettre en évidence la preuve de concept. Couplage thermo-aimantation d'alliages magnétiques doux, tels que FeNi binaire et transduction piézoélectrique, il est possible de convertir les fluctuations de température en électricité.

L'architecture du générateur offre un large éventail de possibilités permettant d'ajuster la plage de température pour son fonctionnement. Deux paramètres clés de conception ont été identifiés comme les principaux points à prendre en compte pour un fonctionnement efficace du dispositif; distance de séparation initiale et rigidité équivalente du faisceau du transducteur.

En réduisant le volume de l'aimant permanent, il est possible d'augmenter la fréquence de résonance du faisceau du transducteur, améliorant ainsi les capacités de conversion d'énergie. Notre objectif général étant de miniaturiser ce type de générateur, nous avons entrepris une deuxième étape de fabrication de prototypes. Cette fois, nous nous sommes concentrés sur l'utilisation d'un prototype portable et nous avons l'intention de mieux améliorer les variations de température car l'excitation d'entrée du système.

Dans une seconde génération de prototypes de générateur, le principal changement que nous avons dû faire est le dispositif de montage du prototype. Comme nous l'avons vu, le luminaire que nous avons mis au point dans une première phase d'expérimentation étant encombrant, il doit être modifié. Deuxièmement, la longueur du faisceau en porte-à-faux devrait être réduite car cela pourrait augmenter la fréquence de résonance du dispositif. Comme nous ne pouvions pas nous procurer de matériaux piézoélectriques d'épaisseur différente, nous avons décidé d'étudier la réduction de la longueur et de la largeur du faisceau du transducteur, ainsi que la taille de l'aimant permanent.

Pour cette deuxième génération de récupérateurs d'énergie, nous avons également amélioré la méthode de production des fluctuations de température. En effet, au lieu d'utiliser de la chaleur en Joule, nous avons acheté un module Peltier qui est placé au contact de l'alliage FeNi. Le module Peltier a pour but d'explorer la répétabilité des seuils de température. En accélérant les phases de réchauffement et de refroidissement, nous pensons que dans une même période de temps où nous pourrions avoir 1 cycle thermique, nous aurons plusieurs cycles thermiques. Les principales caractéristiques de ces prototypes sont montrés

dans le Tableau 5.6. Les résultats plus importants à propos de l'opération de ces prototypes sont présentés dans le Tableau 5.7.

Pour aller au-delà de la conception et de la mise en œuvre du récupérateur d'énergie, nous avons décidé de mettre en œuvre un redresseur double alternance à la place de la résistance de charge afin d'explorer le comportement du prototype de test dans de telles conditions. Le pont redresseur a été mis en œuvre à l'aide de diodes de commutation rapide à petit signal, à savoir 1N4148.

On peut constater que la distance de séparation initiale pour cette architecture était de 0,6mm. Pour la transition d'ouverture, nous pouvons voir que le premier pic atteint des valeurs de 8V. Cependant, il est fortement amorti lorsque les deuxième et troisième pics d'oscillation diminuent au-dessous de la moitié de cette amplitude maximale.

La découverte la plus importante est que les températures de fonctionnement de ce prototype d'essai sont proches de la température du corps humain (voir Figure Figure 1.2). Cela ouvre énormément d'applications potentielles pour de tels générateurs. Comme la température d'ouverture est inférieure à 40°C, cela suggère que ce dispositif peut être ouvert lorsque la chaleur du corps humain approche de 37°C.

En ce qui concerne la température de fermeture, il peut être facilement fourni par la température ambiante. En d'autres termes, imaginons que nous plaçons ce générateur portable dans un cadre de montre de telle sorte que l'alliage FeNi soit exposé au toucher. A ce moment, la température du FeNi est augmentée par le biais de la chaleur du corps humain. Le générateur s'ouvre et convertit cette fluctuation de température en électricité. Ensuite, en relâchant la main du générateur, il se refroidit par transfert de chaleur par convection (en supposant que la température ambiante soit inférieure au seuil de fermeture). A ce moment, le générateur convertit cette variation de température en électricité par la commutation de fermeture.

Concernant les prototypes portables, leur but principal est de réduire autant que possible la taille de la poutre du transducteur et d'augmenter les capacités de récupération d'énergie du dispositif. En réduisant la largeur du faisceau jusqu'à 1mm et la longueur à 8mm, nous avons pu assurer la commutation de fermeture de ce dispositif d'architecture en utilisant un seul aimant. Jusqu'à présent, il s'agit de notre plus petit prototype portable fabriqué et testé.

L'un des avantages du modèle électrique équivalent est de résoudre le problème de la mise en œuvre des pertes liées aux matériaux, par exemple les pertes diélectriques et mécaniques. Nous avons opté pour le développement d'un modèle équivalent électrique, au lieu d'utiliser le modèle précédent implémenté sur Matlab. L'utilisation d'un modèle équivalent électrique présente un autre avantage : elle permet de dépasser la conception du générateur. En d'autres termes, nous pouvons également concevoir le module de gestion de l'énergie à connecter au générateur. Avoir cette implémentation dans un même logiciel accélère considérablement le processus de conception d'un tel système.

Nous avons adapté le modèle électrique équivalent, présenté par Roundy *et al*, [96] pour décrire le système que nous proposons. En utilisant PSpice, nous avons mis en œuvre le modèle extrêmement pratique pour analyser le système complet (c'est-à-dire les composants thermo-magnétiques, mécaniques et électriques). En utilisant ce modèle équivalent, les pertes liées aux matériaux peut être mis en œuvre. La polyvalence de l'introduction de

ces pertes se reflète dans l'influence de la rupture magnétique sur les performances du générateur. En utilisant un modèle équivalent, la mise en œuvre d'un module de gestion de l'alimentation peut être adressée

## Chapitre 6 : Optimisation de la conception du générateur et son étude de variabilité

Pour cette première tentative d'optimisation de la conception, nous nous sommes concentrés sur les couches piézoélectriques ainsi que sur sa position le long de la cale du faisceau du transducteur. Nous avons donc décidé d'établir les variables de conception énumérées dans le Tableau 6.1.

En travaillant avec ces variables de conception, des modifications de la rigidité mécanique peuvent être obtenues, ce qui entraîne des changements sur la fréquence de résonance du transducteur. Il est également trivial de voir que la force d'attraction magnétique ne sera pas modifiée pour ces conceptions. Par conséquent, nous pouvons définir une force magnétique d'attraction constante qui excitera le modèle.

L'un des principaux avantages de l'utilisation de ce type de modèle est la facilité de mise en œuvre des équations. Le modèle repose sur un intégrateur de second ordre. La sortie de ce bloc est la position du transducteur et sa vitesse.

Afin de garantir que chaque conception répondra aux exigences ; nous pouvons définir une condition de signal lié en tant que réponse à une exigence du périphérique. Comme le montre la Figure 6.4. La représentation schématique du signal lié peut être interprétée comme une contrainte sur le déplacement en bout de poutre.

**Phase I** Le générateur est en position ouverte et il est statique. Nous considérons que la température est supérieure au seuil de fermeture.

**Phase II** Au cours de la phase II, la force d'attraction magnétique est appliquée à l'extrémité du faisceau et si le générateur présente sa transition de fermeture, un contact mécanique est obtenu sur le système de déclenchement. Au moment où le contact entre l'aimant permanent et l'alliage FeNi est atteint, le générateur produit un pic de tension de sortie de signe négatif et la pointe du faisceau se déplace de sa position horizontale ( $w = 0\text{mm}$ ) à l'entrefer initial ( $w = -2\text{mm}$ ).

**Phase III** la force d'attraction magnétique devenant inférieure à la force mécanique, le faisceau est libéré et l'étage oscillant est présent. Au cours de cette phase oscillatoire, le déplacement en bout de poutre se situe dans la zone autorisée. La tension de sortie a donc la même forme de signal. Toute conception qui ne répond pas à ces exigences est rejetée par l'algorithme. A la fin de chaque itération, la puissance dissipée est obtenue et en intégrant ces puissances, l'énergie électrique générée est comparée à l'itération précédente. La maximisation de cette fonction objectif est l'objectif principal de ce processus.

Lorsque il est considéré la force d'attraction magnétique et la distance de séparation initiale sur le système de déclenchement en tant que paramètres constants du processus

d'optimisation de la conception, les performances dynamiques du système de transducteurs peuvent être améliorées en modifiant la rigidité mécanique de la poutre en porte-à-faux.

Bien que ces conditions de variables de conception limitent la conception à la force magnétique nécessaire pour contrer la force mécanique, une conception optimisée sur le faisceau du transducteur est possible. Dans ces conditions de conception, il est nécessaire de connaître les températures pour lesquelles cette force magnétique peut être atteinte.

La principale exigence qui garantit les deux positions de fonctionnement du générateur est la réponse de la poutre en porte-à-faux. Les améliorations apportées au dispositif se reflètent principalement sur la réponse dynamique du faisceau du transducteur. Une augmentation de la production d'énergie pendant un cycle de fonctionnement thermique est théoriquement possible.

Concernant le second modèle d'optimisation de la conception, en incluant le bloc de système de déclenchement dans le modèle de pas de temps, il est possible de concevoir une plage de températures spécifique. Les exigences de conception sont maintenant les températures de fonctionnement du générateur. En d'autres termes, connaissant la plage de température de l'environnement où le périphérique final sera placé, il est possible de concevoir des variations de température spécifiques. Nous pouvons concevoir des générateurs qui fonctionneront dans différentes plages de température. Nous avons démontré que l'énergie de sortie peut être améliorée lors de la conception de générateurs pour une plage de température spécifique. En utilisant le modèle simplifié par pas de temps du générateur, il est possible de concevoir de manière optimale d'un tel générateur.

Nous savons tous qu'en production, il faut toujours tenir compte des tolérances de conception. Par conséquent, il existe également une variabilité entre les valeurs de paramètre qui ne permettra pas de les mêmes résultats pour chaque générateur fabriqué. Même si nous pouvons construire des milliers ou des milliards de chacune de ces pièces du générateur, il y a toujours une variabilité entre ces pièces.

En tant que concepteur, nous devons donc nous assurer que nos paramètres de conception sont robustes et tenir compte de la variabilité de la production ainsi que de celle du modèle. Avant de passer à une phase de production, nous pouvons gagner du temps et de l'argent en effectuant des simulations prenant en compte les variabilités du modèle et des paramètres de conception.

## Chapitre 7 : Conclusions et futurs travaux

Un générateur piézoélectrique à déclenchement thermo-magnétique a été présenté dans cette thèse. Nous avons conçu des prototypes de test et démontré la faisabilité de la conversion de la température fluctuations en électricité par la méthode de conversion indirecte. L'objectif était, à partir de cette énergie générée, de pouvoir alimenter un nœud de capteur afin qu'il transmette des informations.

Comme le système devait pouvoir fonctionner dans un environnement «humain», les spécifications exigeaient que la température évolue lentement, avec une faible amplitude et autour de la température ambiante.

En supposant que la température initiale soit une température «froide», le système a sa position d'équilibre en position fermée. En effet, le matériau magnétique doux se comporte comme un ferromagnétique et la force magnétique qui en résulte entre les aimants et FeNi ferme le circuit. Lorsque la température devient chaude, le FeNi perd ses propriétés magnétiques et la force mécanique de la poutre en porte-à-faux devient prépondérante, ouvrant ainsi le système. Les transitions sont abruptes car les deux forces opposées ont des caractères très différents : la mécanique est linéaire tandis que la magnétique n'est pas du tout. Les couches piézoélectriques traduisent alors ces déformations brutales en électricité.

Un modèle mathématique a été développé pour décrire les caractéristiques du générateur en fonction des paramètres de conception. Ce modèle a été divisé en quatre parties. Nous avons d'abord étudié la réponse thermique du générateur en fonction de ses dimensions, de sa position à l'équilibre et de ses propriétés matérielles.

Deuxièmement, nous avons étudié la force magnétique entre un aimant permanent et un volume magnétisé de matériau magnétique doux. Nous avons ensuite étudié la thermo-aimantation du système de déclenchement, c'est-à-dire comment le changement de température modifie la force magnétique. Troisièmement, nous avons couplé thermo-aimantation avec le comportement mécanique d'une poutre en porte-à-faux en grande déviation afin de prédire les températures de fonctionnement du transducteur du générateur en fonction de sa conception.

Quatrièmement, couplé le système entier pour obtenir un comportement transitoire du système. En couplant la piézoélectricité à l'énergie mécanique produite par les commutations du générateur, nous avons pu explorer les deux signaux de sortie du générateur. Nous avons conclu que notre modèle analytique était valable pour dimensionner rapidement un générateur.

Nous avons choisi de caractériser les performances de ces prototypes en mesurant la densité d'énergie par commutation. Nous avons fabriqué un prototype de deuxième génération, portable, capable de fonctionner avec une telle source et pouvant générer de l'électricité lorsque certains seuils sont dépassés.

Enfin, nous avons mis en place des bases théoriques afin de simuler le générateur de manière globale. Cette simulation peut à la fois servir à prédire le comportement de la structure mais aussi à réfléchir à son optimisation. Nous avons ensuite vérifié que les résultats expérimentaux concordaient avec ceux obtenus par simulation.

Nous avons validé l'exploitation des variations de température lentes en tant que «nouvelle» source utilisable pour la récupération d'énergie. Le Tableau 7.1 résume les performances des prototypes évalués dans cette thèse.

# Vita

Adrián Abdalá Rendón Hernández was born on April, 1985 in Monclova, Coahuila, México. He earned his B.Sc. degree in electronics and telecommunications engineering (with the highest honors) from the Universidad Autónoma de Nuevo León (UANL) and his M.Sc. degree in electronics engineering from the Instituto Tecnológico y de Estudios Superiores de Monterrey (ITESM), campus Monterrey, in 2008 and 2012, respectively.

During his undergraduate studies, he also attended the Institut National des Sciences Appliquées (INSA) de Lyon in France from August 2007 to June 2008, as part of a academic exchange program.

From 2008 to 2010 Mr. Rendón-Hernández worked for Alestra, the AT&T's network operator in México, as optical transmission engineer. This experience allowed him to learn about his future professional aspirations, and also permitted to enhance his understanding about technical problems through sharing his ideas and experiences with a global work team. Since 2012, Mr. Rendón-Hernández has been working for Schneider-Electric R&D as Electronic Design Engineer in Monterrey, México. His primary research interest is the energy harvesting technologies and their applications to the industry.

In 2014, Mr. Rendón-Hernández joined the research group: Design of Integrated devices, Circuits and Systems (Micro- and Nano- Systems) of the TIMA Laboratory at the Université Grenoble Alpes. In 2018, he obtained the Ph.D. degree in Nano Electronics and Nano Technologies under the supervision of Professor Skandar Basrour.

Currently, Mr. Rendón-Hernández is working for Schneider-Electric R & D as MEMS specialist. His research interests include design, modeling and evaluation of sensors and actuators based on MEMS technologies for energy harvesting applications.

Permanent address: Calle La Paz, #312  
Col. Zona centro, 25600  
Ciudad Frontera, Coahuila  
México

✉ [abdala.rendon@gmail.com](mailto:abdala.rendon@gmail.com)

🌐 [www.linkedin.com/in/adrianrendon](http://www.linkedin.com/in/adrianrendon)

The present dissertation was typeset in  $\text{\LaTeX}$  by Adrián Abdalá Rendón Hernández.

# Conception, modélisation et évaluation d'un générateur piézoélectrique à déclenchement thermo-magnétique

**Résumé** - La récupération d'énergie thermique peut être réalisée par de nombreuses techniques de transduction d'énergie. Les techniques directes de conversion d'énergie thermique en énergie électrique sont généralement les technologies les plus utilisées. Lorsque des générateurs miniaturisés sont requis, des méthodes de conversion directe présentent des difficultés, y compris la nécessité des dissipateurs de chaleur volumineux ou la forte dépendance aux fluctuations de température rapides. Par conséquent, les méthodes de conversion indirecte, comme la conversion d'énergie thermique vers la mécanique et puis la mécanique vers l'électrique, sont présentées comme des alternatives aux récupérateurs d'énergie pour alimenter des capteurs autonomes. Cette technologie ouvre un nouvel axe de recherche pour surmonter les contraintes des systèmes de récupération d'énergie thermique à petite échelle. Même si leur rendement est relativement faible en raison des pertes liées aux étapes de conversion d'énergie, les capteurs d'énergie basés sur l'effet thermo-magnétique présentent une densité de puissance élevée lors de leur miniaturisation. Ces travaux présentent la conception d'un générateur capable de convertir de faibles et lentes fluctuations de température ambiante en électricité. Ce générateur exploite l'effet thermo-magnétique d'un matériau magnétique doux, à savoir l'alliage de fer et de nickel (FeNi) ainsi que la piézoélectricité. Lorsqu'un matériau présentant une thermo-aimantation est soumis à un champ magnétique externe et constant ainsi qu'à des variations temporelles de température, une force magnétique dépendante de la température est produite ; cette force déclenche le mouvement mécanique d'une structure. Le générateur a deux positions stables : la position ouverte et la position fermée. En modifiant la température de l'alliage magnétique doux, l'interaction entre deux forces du système (forces magnétique et mécanique) amène le générateur à l'une de ses deux positions. La température de Curie du FeNi étant proche de la température ambiante, des applications comme des dispositifs connectés portables peuvent être ciblées. Un modèle analytique est développé afin de prédire les performances du générateur. En utilisant ce modèle, une conception rapide du générateur est réalisée pour répondre aux cahiers des charges tels que : la température d'opération, la plage de températures de fonctionnement, la réponse thermique, les capacités de conversion piézoélectrique, etc. Des modélisations par éléments finis sont développées sous ANSYS afin de valider notre modèle analytique simplifié. Ces modèles numériques prennent en compte le système multi-physique. Ces modèles permettent aux concepteurs d'explorer d'autres matériaux et de faire des améliorations en utilisant des processus d'optimisation de la conception.

**Mots Clés:** Récupération d'énergie, Piézoélectricité, Thermo-aimantation, Variations temporelles de température

## Design, modeling and evaluation of a thermo-magnetically activated piezoelectric generator

**Abstract** - Thermal energy harvesting can be realized by numerous techniques of energy transduction. Direct conversions of thermal to electrical energy are typically the most popular technologies used. When miniaturized generators are required, direct conversion methods present difficulties, including the need of bulky heat sinks or the strong dependence to rapid temperature fluctuations. Therefore, indirect conversion methods, like thermal-to-mechanical-to-electrical energy are presented as an alternative to thermal energy harvesters towards powering autonomous sensors. This disruptive technology opens up a new approach to overcome the limitations of miniaturized thermal energy harvesting systems. Even if having a relatively low efficiency due to losses linked to energy conversion steps, energy harvesters based on thermo-magnetic effect show a large power density upon miniaturization. This work presents the design of a generator able to convert small and slow ambient temperature fluctuations into electricity. It exploits the thermo-magnetic effect of a soft magnetic material, namely, iron nickel alloy (FeNi) and piezoelectricity. Thermo-magnetization of FeNi is driving the conversion of thermal energy, in the form of temporal fluctuations, into mechanical vibrations of a structure. The generator has two stable positions; open position and closed one. Curie temperature of FeNi being near to ambient temperature, applications like wearable connected devices may be targeted. By changing the temperature of the soft magnetic alloy, the interaction between counterbalance forces (magnetic and mechanical forces) leads the generator to one of its two commutations. Analytical model is developed in order to predict generator performance. Making use of this model, a rapid design of generator is conducted to fit custom requirements such as: temperature of operations, temperature range of operation, thermal response, piezoelectric energy conversion capabilities, etc. Additionally, main design rules were derived from the design parameters of the generator. Special attention was paid on how scaling down size affects the generator performance by using the analytical model. Finite element models are developed through ANSYS software in order to validate the analytical simplified model.

**Keywords** - Energy harvesting, Piezoelectricity, Thermo-magnetization, Temporal variations of temperature